Scuola di dottorato
Università degli studi di Milano-Bicocca

Department of Physics G. Occhialini
PhD program in Physics and Astronomy – XXXVIII cycle

A study of persistent and bursting hard X-ray emission from magnetars with the INTEGRAL satellite

Dominik Patryk Pacholski
Registration number 896545

Tutor: Prof. **Monica Colpi**
Supervisor: Dr. **Sandro Mereghetti** (INAF-IASF Milano)

Coordinator: Prof. Stefano Ragazzi

Academic year 2024/2025

To my mother

Acknowledgements

First of all, I would like to express my deepest appreciation to my supervisor, Dr. Sandro Mereghetti, for his guidance, invaluable experience, and unwavering support during my PhD. I am extremely fortunate to have had the opportunity to work under his supervision. I would also like to thank my tutor, Prof. Monica Colpi, for all her help and support.

I am grateful to everyone at INAF–IASF Milano for their support and for creating such a welcoming environment throughout my PhD. Many thanks to Andrea Belfiore for all the help with the computing infrastructure, which made the data analysis possible.

I also want to thank Prof. Andrea Santangelo and all the colleagues at the Institute for Astronomy and Astrophysics in Tübingen, as well as to Philippe Laurent, Diego Götz, and everyone at the Department of Astrophysics at CEA Paris-Saclay, for their hospitality during my visits.

Many thanks to Lorenzo Ducci and Marek Nikołajuk for supervising my Master's thesis and helping me get to this point. Special thanks to Lorenzo for continuing to work with me during my time in Tübingen.

I am grateful to everyone I worked with and met during these years for the discussions, collaborations, and all the good moments we shared.

Na koniec chciałbym podziękować mojej mamie, której dedykuję tę pracę, za jej nieustające wsparcie i wiarę we mnie przez całe życie. Bez niej to wszystko nie byłoby możliwe.

Abstract

Magnetars are a small class of neutron stars with the highest known magnetic fields, reaching up to 10^{15} G. Their emission is mainly powered by the decay and evolution of their magnetic fields, which allows them to exhibit a wide variety of phenomena, including persistent emission in the soft and hard X-ray bands, short bursts, and giant flares. In this thesis, I use archival data from the space observatory INTEGRAL spanning over 20 years to perform systematic studies of all known magnetars in our Galaxy and in the Magellanic Clouds and to study giant flares from magnetars in galaxies beyond the Local Group.

First, I present the results of a study of long-term persistent hard X-ray emission from magnetars. I report the detection of eight magnetars in the hard X-ray band, including three sources detected only during outbursts, and two sources detected with low significance during short periods.

I also report on the broadband analysis of the outburst of the magnetar Swift J1555.2–5402, which was observed simultaneously with the X-ray satellites Swift, NICER, NuSTAR, and INTEGRAL. I find that the broadband spectrum is well described by an absorbed blackbody plus two-power-law model. I observed fading of the hard X-ray emission with NuSTAR, and estimate an upper limit on the hard X-ray flux with INTEGRAL.

Next, I present the results of a systematic study of short bursts from 34 known magnetars. In a total of 1136 Ms of data, I detected 1349 bursts from 21 sources, with the majority of bursts detected from 1E 1547.0–5408, SGR 1806–20, and SGR 1935+2154. I report the timing properties for the entire sample, and spectral results for the subset of bursts with sufficient statistics.

I then report the results of the search for extragalactic magnetar giant flares in nearby galaxies and the Virgo cluster. INTEGRAL observed the Virgo cluster for about 35 Ms of exposure time, and nearby galaxies for a total of around 103 Ms. I did not locate any new giant flares. I estimate lower and upper limits on the rate of giant flares, which are consistent with previous estimates.

Finally, I report the discovery of two extragalactic magnetar candidates, one in M82 and one in PGC 86046. The former is one of the most confident detections of extragalactic magnetar candidates, as it was followed up with Swift and XMM-Newton thanks to its rapid localisation with INTEGRAL, and it is located within the galaxy. The latter candidate is less certain, as the report of the burst was delayed, not allowing us to fully exclude its origin as a short Gamma-Ray Burst (GRB). However, its position is consistent

with the galaxy, and the burst properties are similar to those of magnetar bursts. Its spectral evolution is consistent with other extragalactic magnetar candidates.

The thesis is divided into five chapters, a conclusions section, and an appendix. The structure of the thesis is as follows:

In Chapter 1, I introduce magnetars, their brief history, observational properties, and theoretical models. The brightness of magnetar giant flares enables us to observe them in nearby galaxies. I introduce the known giant flares and extragalactic candidates, along with their properties.

In Chapter 2, I introduce the INTEGRAL mission, its instruments, especially the INTEGRAL Soft Gamma-Ray Imager (ISGRI), and its performance over the mission. I briefly present basic coded mask data analysis and describe the analysis methods and software used in this thesis.

In Chapter 3, I present the results of the systematic study of the long-term persistent hard X-ray emission of magnetars using ISGRI data. In addition, I present the results of the broadband analysis of the Swift J1555.2–5402 outburst using Swift, NuSTAR, and INTEGRAL data.

In Chapter 4, I present the results of the systematic study of short bursts from magnetars using ISGRI data.

In Chapter 5, I present the results of the search for extragalactic magnetar giant flares in the Virgo cluster and nearby galaxies using ISGRI data, as well as the INTEGRAL results on two extragalactic giant flares.

The full tables containing results of the magnetar burst search, including durations and spectral parameters, are in the Appendix.

List of Publications

Parts of this thesis have been published in the following papers:

- Pacholski, D. P., Arrigoni, E., Mereghetti, S., & Salvaterra, R. (2024), *INTEGRAL search for magnetar giant flares from the Virgo Cluster and in nearby galaxies with high star formation rate*, *MNRAS*, 535, 3656-3660.
- Pacholski, D. P., Ducci, L., Topinka, M., & Mereghetti, S. (2025), *INTEGRAL Observations of Magnetars*, *Astronomische Nachrichten*, 346, e20240109.
- Pacholski, D., Mereghetti, S., & Topinka, M. (2026), *INTEGRAL IBIS catalog of magnetar bursts*, ApJ; in press.
- Rodi, J. C., Pacholski, D. P., Mereghetti, S., Arrigoni, E., Bazzano, A., Natalucci, L., Salvaterra, R., & Ubertini, P. (2025), *GRB 241107A: A Giant Flare from a Close-by Extragalactic Magnetar?*, ApJ; 979, L25.
- Mereghetti, S., Rigoselli, M., Salvaterra, R., Pacholski, D. P., Rodi, J. C., Gotz, D., Arrigoni, E., D'Avanzo, P., Adami, C., Bazzano, A., Bozzo, E., Brivio, R., Campana, S., Cappellaro, E., Chenevez, J., De Luise, F., Ducci, L., Esposito, P., Ferrigno, C., Ferro, M., Israel, G. L., Le Floc'h, E., Martin-Carrillo, A., Onori, F., Rea, N., Reguitti, A., Savchenko, V., Souami, D., Tartaglia, L., Thuillot, W., Tiengo, A., Tomasella, L., Topinka, M., Turpin, D., & Ubertini, P. (2024), *A magnetar giant flare in the nearby starburst galaxy M82*, Nature, 629, 58-61.
- Borghese, A., Coti Zelati, F., Imbrogno, M., Israel, G. L., De Grandis, D., Pacholski, D. P., Trudu, M., Burgay, M., Mereghetti, S., Rea, N., Esposito, P., Pilia, M., Possenti, A., Turolla, R., & Ducci, L. (2026), *A magnetar outburst with atypical evolution: the case of Swift J1555.2–5402*, A&A; in press.

During my PhD project I also contributed to part of the data analysis and interpretation of the following papers:

- Mereghetti, S., Rigoselli, M., Salvaterra, R., Tiengo, A., & Pacholski, D. P. (2023), *XMM-Newton and INTEGRAL Observations of the Bright GRB 230307A: Vanishing of the Local Absorption and Limits on the Dust in the Magellanic Bridge*, ApJ, 956, 97.
- Ibrahim, A. Y., Borghese, A., Coti Zelati, F., Parent, E., Marino, A., Ould-Boukattine, O. S., Rea, N., Ascenzi, S., Pacholski, D. P., Mereghetti, S., Israel,

G. L., Tiengo, A., Possenti, A., Burgay, M., Turolla, R., Zane, S., Esposito, P., Götz, D., Campana, S., Kirsten, F., Gawroński, M. P., & Hessels, J. W. T. (2024), *An X-Ray and Radio View of the 2022 Reactivation of the Magnetar SGR J1935+2154*, ApJ, 965, 87.

Contents

List of Figures

List of Tables

Chapter 1

Magnetars

Magnetars are a small class of young, isolated neutron stars with powerful magnetic fields, reaching up to 10^{15} G (e.g., Mereghetti et al. 2015; Kaspi & Beloborodov 2017). Currently, there are at least 29 confirmed magnetars (for which a spin period P and a spin period derivative $\dot{P}$ have been measured in the X-ray band) plus several candidates. Persistent emission in the hard X-ray band has been detected in approximately 12 of them. All the known magnetars are located in our Galaxy, except for two in the Magellanic Clouds. They exhibit long spin periods (2–12 s) with strong spin-down rates ranging from 10^{-13} to 10^{-10} s/s. Thus, they are located in the upper right corner of the $P - \dot{P}$ diagram (see Fig. 1.1), which shows the spin period versus its period derivative for different neutron star populations. In this diagram, lines of constant dipolar magnetic field strength (derived under the assumption that the loss of rotational energy is due to the dipole radiation emission, $B \sim 2.3 \times 10^{19}(P\dot{P})^{1/2}$ G) and characteristic age ($\tau = P/2\dot{P}$) are shown, which allows a classification of different neutron star types based on their rotational properties.

They exhibit a variety of emissions, including persistent emission in the soft (<10 keV) and hard X-ray (>10 keV) bands, short bursts (typically 10^{39}–10^{42} erg), and giant flares (up to 10^{46} erg). In addition, magnetars can enter long-term outbursts, during which their persistent emission increases by up to several orders of magnitude for weeks up to several months (e.g., Coti Zelati et al. 2018). These outbursts are often accompanied by active burst periods, with dozens to hundreds of bursts occurring in rapid succession, as observed in sources such as SGR 1806–20 (Götz et al. 2006; Younes et al. 2017a) and SGR 1935+2154 (e.g., Lin et al. 2020b; Younes et al. 2020b). In fact, most magnetars were discovered through their bursting activity, which is the most distinctive characteristic of this class of neutron stars. All this emission is powered by their powerful magnetic fields and its decay and evolution. The properties of the different emission types are described in more detail in the following sections, with a focus on the hard X-ray emission, bursts, and giant flares, which are the main subjects of this thesis.

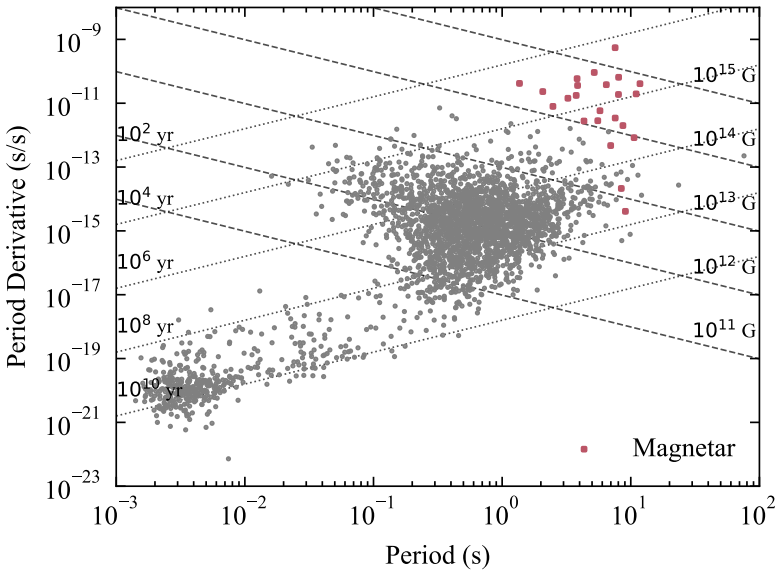

Figure 1.1: P–$\dot{P}$ diagram showing the location of magnetars in comparison to other neutron star classes. Pulsar data are from ATNF Pulsar Catalogue (Manchester et al. 2005); missing magnetar parameters were supplemented manually from the literature.

1.1 Soft Gamma-ray Repeaters and Anomalous X-ray Pulsars

Historically, two distinct classes of sources were identified: the Soft Gamma-ray Repeaters (SGRs) and the Anomalous X-ray Pulsars (AXPs). As their names suggest, SGRs were discovered through their repeating bursts in the hard X-ray and soft gamma-ray range. The first detections of SGR bursts began in 1979, although for eight years these bursts were considered a distinct class of Gamma Ray Bursts (GRB) with a softer spectrum and the peculiarity of not being one-off events, unlike the majority of other GRBs (Laros et al. 1986). We now know that GRBs are due to the collapse of massive stars or mergers of compact objects and are not related to isolated neutron stars. The first burst was discovered on January 7 as GRB 790107 (Mazets et al. 1981, 1982b); this burst was followed by about a hundred further bursts coming from the same direction in the following years showed repeating characteristics and were associated with SGR 1806-20 (Laros et al. 1987). In March of the same year, a Magnetar Giant Flare (MGF) was detected from what was later identified as SGR 0525–66 (Mazets et al. 1979b; Cline et al. 1982; Evans et al. 1980). Following this, multiple short bursts were detected from this source, which allowed it to be tied to other bursts. The association of the MGF with the supernova remnant N49 in the Large Magellanic Cloud (e.g., Cline et al. 1980) allowed to determine the distance and thus the energetics, highlighting the uniqueness of the event. The estimated energy release, of order 10^{44}–10^{45} erg, was by far greater than that of typical neutron stars and could not be explained by rotational energy or accretion processes. This event was essential to understand the nature of SGRs and led to the development of the magnetar model (see Sec. 1.3). At the end of March, three soft gamma-ray bursts from SGR 1900+14 were discovered (Mazets et al. 1979a). Soon, it

was proposed that the MGF and the distinct class of short GRBs had a common origin (Mazets et al. 1982a), and a few years later, the class of SGRs was established (Laros et al. 1986, 1987).

On 17 December 1979, the first AXP was discovered, 1E 2259+586 (Gregory & Fahlman 1980), located in supernova remnant G109.1–1.0. Its longer period, unlike that of the young pulsars in SNRs known at that time, initially suggested the presence of a companion star (Fahlman & Gregory 1981). The rotational energy loss inferred from the measurement of its spin down rate, lower than the observed luminosity, strengthened the hypothesis of the source being powered by accretion from a companion star (Koyama et al. 1987). However, as more AXPs were discovered, it became evident that they constituted a separate class. Their clustered spin periods in the range of 5–12 seconds (Mereghetti et al. 1999, 2002b), and relatively constant high spin-down rates of 10^{-13}–10^{-11} s s^{-1}, set them apart. The identification of additional sources, such as 1E 1048–5937, 4U 0142+614, and 1RXS J170849–400910, initially led to their classification as a subclass of LMXBs (Mereghetti & Stella 1995), as the high level of emission argued against the neutron star being powered by the loss of rotational energy. In the following years, further observations generally established limits on the detection of a companion star and showed that the sources had much softer spectra than those seen in X-ray binaries. Also, the sources were found in SNRs and in regions of high star formation, which suggested that they were young objects (van Paradijs et al. 1995). All these properties excluded the possibility of the sources being in binary systems and established them as a distinct class of objects (Mereghetti et al. 2002b).

Two of the three discovered SGRs were soon pinpointed to be inside supernova remnants (Evans et al. 1979, 1980; Cline et al. 1982; Kulkarni & Frail 1993; Helfand & Long 1979). Subsequent soft X-ray observations discovered emission from the quiescent counterparts of SGRs (Rothschild et al. 1994; Murakami et al. 1994). Further observations detected pulsations in the persistent emission of SGR 1806–20 (Kouveliotou et al. 1998a), confirming its nature as a neutron star. Soon after, pulsations were detected in other sources as well (e.g., Kouveliotou et al. 1999; Kulkarni et al. 2003). The spin periods were found to be in the same range as those of AXPs, with similar spin-down rates. In 2001, two SGR-like bursts were detected from AXP 1E 1048–5937 (Gavriil et al. 2002), and in 2002, 1E 2259+586 underwent an outburst emitting over 80 bursts (Kaspi et al. 2003). The identification of SGRs in the soft X-ray band and the discovery of bursts from AXPs confirmed that both classes are indeed the same type of object, now known as magnetars.

1.2 Observational properties

Soft X-ray persistent emission from magnetars was detected with the discovery of the first AXPs. The persistent luminosity in this band ranges from 10^{31} to 10^{36} erg/s. The luminosity distribution can be described as bimodal (Kaspi & Beloborodov 2017), split between persistent sources with luminosities around 10^{35} erg/s and transient sources with luminosities below 10^{33} erg/s in quiescence. The long-term luminosity level is relatively

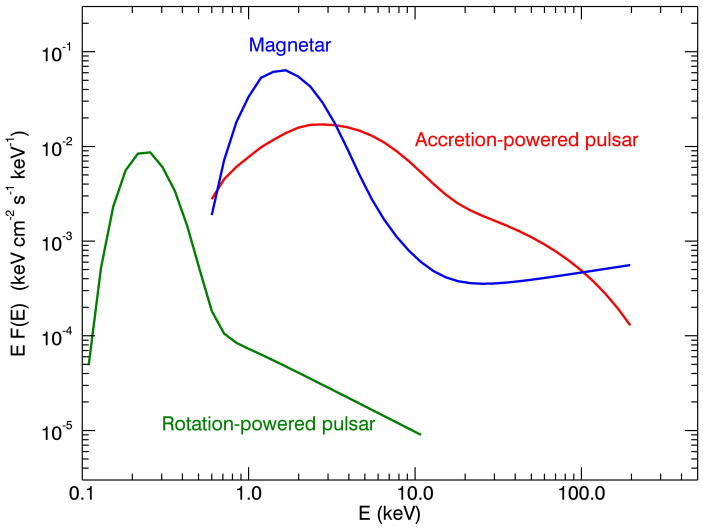

Figure 1.2: Schematic X-ray spectra of three different neutron star classes. Red: the accretion-powered binary X Persei (Di Salvo et al. 1998), Green: the rotation-powered pulsar Geminga (Jackson & Halpern 2005), Blue: the magnetar 4U 0142+614 (Rea et al. 2007). Credit: Mereghetti et al. (2015). Reproduced with permission from Springer Nature.

stable in persistent sources, while in transients, it can vary by several orders of magnitude during outbursts. The spectrum in the soft X-ray band is much softer than in other types of neutron stars powered by accretion or spin-down power (see Fig. 1.2), and it can be described by the sum of two blackbody models or a blackbody plus power-law. The blackbodies are typically found at temperatures between 0.1 and 1 keV, while the power-law photon index is in the range of 2–4 (e.g., Mereghetti et al. 2015; Kaspi & Beloborodov 2017). Due to the location of the majority of magnetars in the Galactic plane, the emission is strongly absorbed, with hydrogen column densities of 10^{22}–10^{23} cm^{-2}.

The X-ray emission from magnetars is pulsed, with pulse profile shapes varying from simple sinusoidal to complex multi-peaked profiles. The pulsed fraction varies from a few percent to 85%, generally increasing with energy (e.g., Kargaltsev et al. 2012). During outbursts variations in the pulse profiles are often observed.

The spin periods of magnetars are in the range of 2–12 seconds, with typical period derivatives of 10^{-13}–10^{-10} s/s. While all magnetars spin down, the rate is not always constant. Some sources show episodes of increased spin-down rate, while others exhibit glitches or anti-glitches (sudden increases or decreases in a period; Archibald et al. 2013), usually followed by a recovery to the previous rate. In addition, timing noise is observed in many sources, during which the spin-down rate fluctuates on timescales of months to years (e.g., Serim et al. 2012; Tsang & Gourgouliatos 2013; Ćerri-Serim et al. 2019). The inferred dipolar magnetic fields, estimated from the spin period and its derivative, are in the range of 10^{14}–10^{15} G for typical magnetars. There are, however, a few sources

with low spin-down rate, such as SGR 0418+5729 (van der Horst et al. 2010), that lead to estimated fields below 7.5×10^{12} G (Rea et al. 2010). The magnetar behavior in these sources is attributed to the higher field present in multipolar components, as it is also supported by the detection of spectral features interpreted as proton cyclotron features (Tiengo et al. 2013). In addition, two rotation-powered pulsars, PSR J1119–6127 (Archibald et al. 2016; Göğüş et al. 2016) and PSR J1846–0258 (Gavriil et al. 2008; Blumer et al. 2021; Sathyaprakash et al. 2024), exhibited magnetar-like emission, going through outbursts with luminosity exceeding the available rotational energy loss and short bursts. Their magnetic fields are estimated to be around 4–5 $\times 10^{13}$ G, which is lower than typical magnetars but still higher than most rotation-powered pulsars.

Around a third of magnetars are associated with supernova remnants (Olausen & Kaspi 2014). The ages of associated SNRs, typically a few 10^3–10^4 years, provide an estimate of the magnetar ages. In addition, a few sources are associated with star clusters (e.g., Klose et al. 2004; Muno et al. 2006), which also suggests that magnetars are young objects.

Radio emission from magnetars has only been detected in a few sources (e.g., Levin et al. 2010; Shannon & Johnston 2013), with the first detection in XTE J1810–197 (Camilo et al. 2006, 2007b). The radio emission is transient, appearing during or after outbursts. SGR J1745–2900 is the only magnetar that has shown evidence of independent radio and X-ray emission (Torne et al. 2015; Lynch et al. 2015; Kaspi & Beloborodov 2017). In addition, magnetar SGR 1935+2154 emitted a Fast Radio Burst (FRB) coincident with an X-ray burst during the April 2020 outburst (Mereghetti et al. 2020; Bochenek et al. 2020; CHIME/FRB Collaboration et al. 2020). This showed that magnetars may be the sources of at least some FRBs, as previously suggested (e.g., Popov & Postnov 2010; Beloborodov 2017). Additionally, a third of magnetars have faint optical or infrared counterparts, which can exhibit variability and, in rare cases, pulsations at the X-ray period (e.g., Kern & Martin 2002; Dhillon et al. 2005, 2011).

1.3 Magnetar model

The Giant Flare on 5 March 1979 from SGR 0525–66 provided clear evidence that SGRs are neutron stars, due to the presence of ∼8 s pulsations observed in the tail (the long, pulsed emission following the initial spike), together with the localization within a young supernova remnant (e.g., Duncan & Thompson 1992). The spin period, much longer than that normal radio pulsars, implied that only a strong dipole magnetic field could slow the rotation to such long periods within the relatively short lifetime of the SNR (about 10^4 years; Mereghetti et al. 2002b). Moreover, the energetics of SGR bursts and giant flares (and later, the high persistent luminosity of AXPs) could not be explained by rotational energy loss or accretion from a companion. Direct evidence for a strong magnetic field also comes from the tail of a giant flare, interpreted as emission from a trapped pair-photon fireball confined by the magnetosphere, as only a field of at least 10^{14} G can contain the hot plasma (kT of few tens keV) for the observed duration (Thompson & Duncan 1995). The observed periods of 2–12 seconds and high period derivatives of

10^{-13}–10^{-10} s s^{-1} again imply dipolar magnetic fields of 10^{14}–10^{15} G. This led to the proposal of the magnetar model (Duncan & Thompson 1992), in which both bursting and persistent emission are powered by the decay and evolution of their magnetic fields over timescales of 10^4–10^5 years (Kaspi & Beloborodov 2017). The subsequent unification of AXPs and SGRs extended the applicability of the magnetar model to both classes.

Beyond the external dipole, the internal magnetic field of magnetars is believed to be much stronger and more complex, composed of both poloidal and toroidal components (Braithwaite 2009), with the latter likely dominant. The evolution of the internal field causes a twist in the external field, creating strong crustal stresses through anchored magnetic field lines that can power the diverse activity observed in magnetars. These stresses can lead to sudden crustal fractures (Thompson & Duncan 1995) or plastic deformations, causing twists in the external magnetic field (Thompson & Duncan 1996).

A crustal fracture, or so-called starquake, injects magnetic energy from the interior of the neutron star into the magnetosphere. This energy release can power the short bursts observed in magnetars. Alternatively, energy can be released through magnetospheric magnetic reconnection caused by the slow deformation of the magnetosphere (Lyutikov 2003).

The formation of magnetars is believed to result from either, or both, of the following scenarios: the dynamo process or the fossil field scenario (Spruit 2009; Mereghetti et al. 2015). The dynamo process requires a proto-neutron star with an initial short spin period of about a millisecond, which would induce strong dynamo action, amplifying the magnetic field in the first few seconds after the supernova (Duncan & Thompson 1992; Thompson & Duncan 1993). As a result, the strong magnetic field would cause rapid spin-down, resulting in observed periods of a few seconds.

The fossil field scenario assumes the presence of a progenitor star with a high magnetic field (up to 10^4 G; Woltjer 1964). This magnetic field would be preserved during the collapse and also amplified due to the conservation of magnetic flux, resulting in a neutron star with a magnetic field up to 10^{14} G (Spruit 2009).

1.4 Persistent Hard X-ray Emission

The discovery of persistent emission above 20 keV occurred in 2003–2004 when INTEGRAL (Winkler et al. 2003) observed a hard tail extending up to 150 keV in SGR 1806–20 (Götz et al. 2004; Mereghetti et al. 2005a; Molkov et al. 2005). The presence of the tail was then promptly confirmed by RXTE and Suzaku X-ray satellites, and soon after, further detections were made from other sources, such as 4U 0142+614, 1RXS J170849–400910, 1E 1841–045, or 1E 1547.0–5408 (Kuiper et al. 2006; den Hartog et al. 2008b,a; Enoto et al. 2010b,a; Kuiper et al. 2004). Since then, INTEGRAL detected hard X-ray emission from a total of 8 magnetars (e.g., den Hartog et al. 2008b; Rea et al. 2009; Götz et al. 2007a; Kuiper et al. 2006).

The hard X-ray emission is generally well described by a power law with a photon index of 1–2. The INTEGRAL spectra from the initial years of the mission are shown in the Fig 1.3. The luminosity in the hard X-rays, in the range of 10^{33}–10^{36} erg/s, is

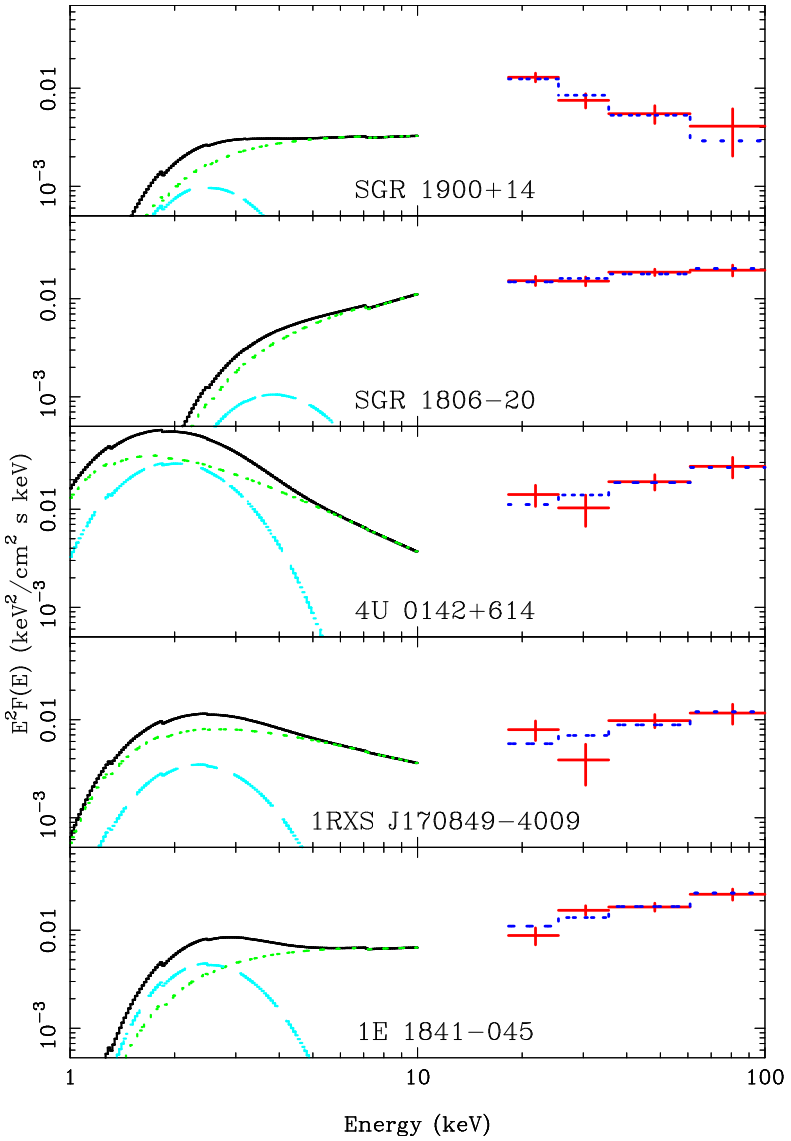

Figure 1.3: Broadband X-ray spectra of magnetars. INTEGRAL spectra above 18 keV fitted with a power law model (dotted lines). Below 10 keV, absorbed blackbody (dashed lines) with power law model (dotted lines). Soft X-ray data for sources from top to bottom: SGR 1900+14 (Woods et al. 2001), SGR 1806–20 (Mereghetti et al. 2005c), 4U 0142+614 (Göhler et al. 2005), 1RXS J170849–400910 Rea et al. (2005), and 1E 1841–045 (Morii et al. 2003). Reproduced from Götz et al. (2007b).

roughly equal to or greater than that of the soft X-ray emission. This emission in the hard X-ray was detected in only around a third of magnetars. This hard X-ray tail was also observed to appear during outbursts in some sources, such as 1E 1547.0–5408 or SGR 1935+2154, and then to fade as the outburst evolved. The fact that the hard X-ray tail is not always present, and it can appear during outbursts, may be due to sensitivity limits of the current instruments and cannot exclude the presence of faint tails in other magnetars. The decay of the magnetic field causes heating of the neutron star crust, resulting in the thermal emission observed in the soft X-ray band. While the strong and twisted magnetic field supports electric currents in the magnetosphere, which accelerate particles and lead to resonant Compton scattering of surface thermal photons

(Thompson et al. 2002). As a result, the persistent hard X-ray emission is observed in many magnetars. The enhancement of the hard X-ray emission during the outburst is thought to be caused by an increased twist in the magnetosphere, which boosts the magnetospheric currents and thus the hard X-ray emission.

The emission in the hard X-ray is strongly pulsed (den Hartog et al. 2008a,b). The pulsed fraction is observed to increase with energy, reaching up to 100% at energies around 100 keV in some sources, such as 1RXS J170849–400910, 4U 0142+614, or 1E 1048–5937 (Kuiper et al. 2006). This behaviour is expected if the hard X-ray emission arises in the magnetosphere, as the beaming of the emission would lead to a higher pulsed fraction at higher energies.

Although the spectrum is described by a hard power law in the observed range, a cutoff is expected at higher energies. However, the exact energy of the cutoff has not been determined yet, due to the limited sensitivity of the current instruments operating in the ∼MeV region. In fact, while the power law spectrum sufficiently well describes the data in most cases, the broadband analysis revealed that in some sources, such as 1E 1841–045 or 1E 2259+586, the spectrum is better described by a log-parabolic function (Rea et al. 2007; den Hartog et al. 2008b,a). In addition, upper limits in the MeV range suggest cutoffs in the range of 150–750 keV (Kuiper et al. 2006).

1.5 Burst properties

Short bursts span a wide range of durations, from a few milliseconds to a few seconds, with a distribution peaking around 100 ms. They are characterised by a short rise time (typically a few milliseconds) and a longer decay time (typically tens of milliseconds), but this is not always the case. Generally, the bursts show variety in their light curves, with some exhibiting multiple peaks or complex structures (e.g., Kaspi & Beloborodov 2017). In Fig. 1.4, examples of burst light curves from 1E 1547.0–5408 are shown, illustrating the diversity in burst profiles.

The peak luminosities of bursts are typically within 10^{39} to 10^{43} erg/s, with the lower limit set by the sensitivity of the instruments (e.g., Kaspi & Beloborodov 2017).

The short bursts can be either isolated or grouped into "storms" of tens or hundreds within a short period. The active burst periods are often associated with the outbursts, during which dozens to hundreds of bursts are observed to occur in rapid succession. In contrast, some magnetars have shown little or no bursting activity since their discovery. One example is AX J1818.8–1559, first identified through a single burst detected in 2007 (Mereghetti et al. 2012), and only one possible burst seen eight years later (Palmer et al. 2015).

The spectra of bursts are well described by cutoff power-law with an E_{peak} energy typically in the range of 20–40 keV, or by the sum of two blackbody components (e.g Younes et al. 2017a; Cai et al. 2022). In some magnetars that went through several periods of bursting activity, the spectral parameters were observed to evolve between periods (von Kienlin et al. 2012; Collazzi et al. 2015; Lin et al. 2020a). In the brighter

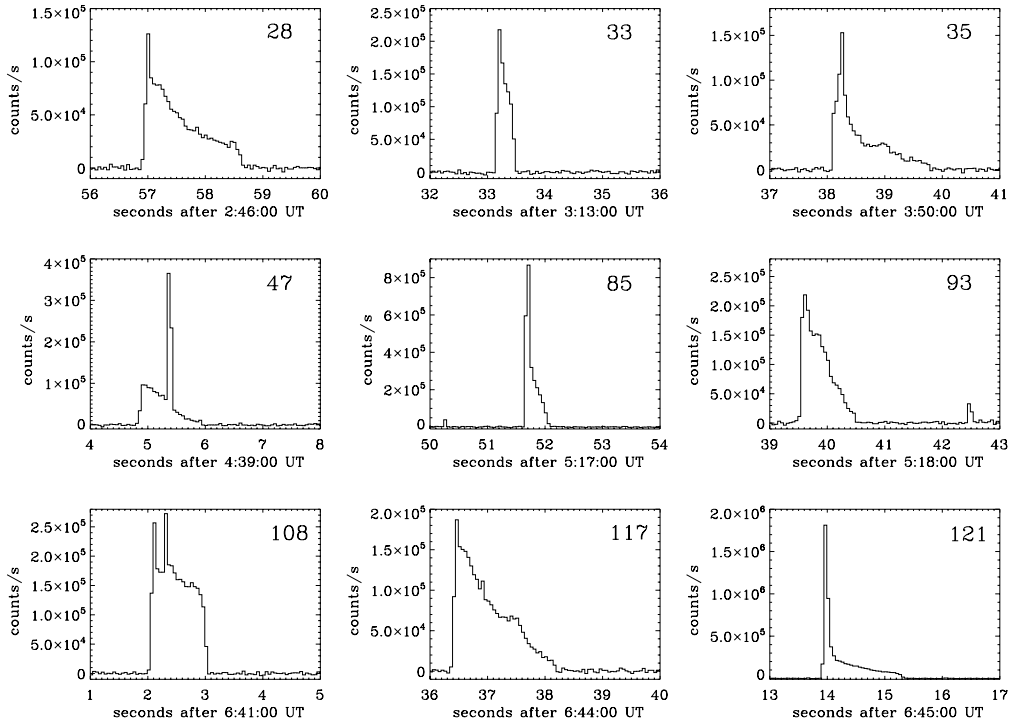

Figure 1.4: Examples of burst light curves from 1E 1547.0–5408 on 2009 January 22 observed with AntiCoincidence Shield of the SPI instrument on board INTEGRAL. Credit: Mereghetti et al. (2009), ©AAS. Reproduced with permission.

bursts, which allowed more detailed analysis, it was also possible to observe spectral evolution within a single burst (e.g., Mereghetti et al. 2020).

Some bursts can display a tail lasting up to a few hundred seconds, modulated at the spin period of the magnetar. These bursts are typically more energetic (up to $\sim 10^{42}$ erg) than the average bursts, but less powerful than the giant flares in terms of energy released (e.g., Kouveliotou et al. 2001; Olive et al. 2004). They are often referred to as "intermediate flares". Their durations are typically a few seconds, reaching up to a few tens of seconds.

The bursts fluence distribution follows a power law with a slope of about 0.6–1.0 (e.g., Collazzi et al. 2015; Younes et al. 2017b). The lower fluence cutoff is determined by the sensitivity of the instruments.

1.6 Giant Flares

Magnetar giant flares, rare explosive events releasing up to 10^{46} erg in gamma-rays in less than one second, are the most spectacular manifestation of magnetars. They are composed of an initial short ($\lesssim$0.2–0.3 s), very energetic ($E \gtrsim 10^{46}$ erg) hard X-ray pulse, always followed by a long, fainter tail of softer emission, periodically modulated at the magnetar spin period of a few seconds (Mereghetti 2008). Only three such events have been observed, all from different sources. The light curves of the three MGFs are shown in Figure 1.5.

The first such event was detected on 5 March 1979, when a bright flare from SGR

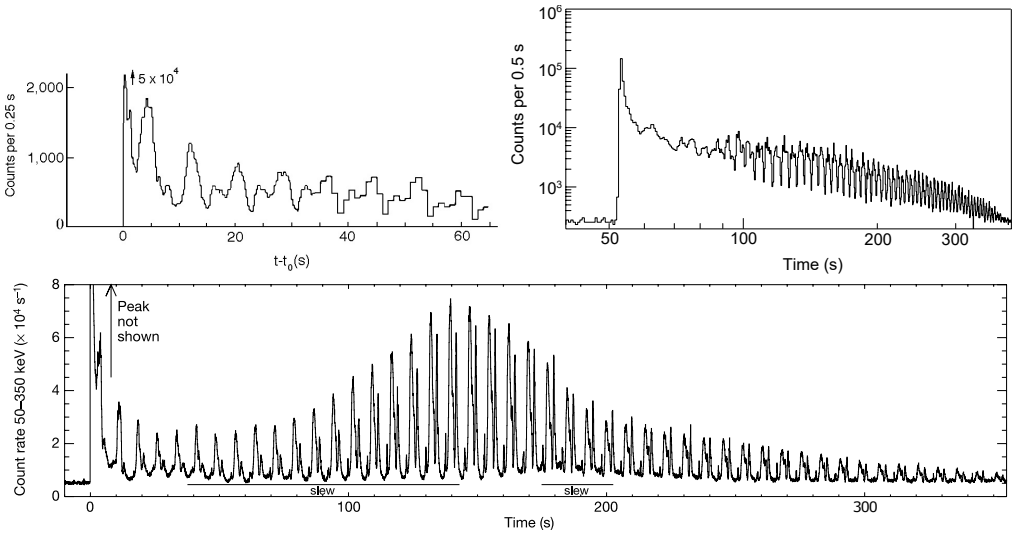

Figure 1.5: Light curves of the three observed Magnetar Giant Flares. Top left: the 1979 March 5 MGF from SGR 0525–66 observed by: Venera 12 (Mazets et al. 1979b). Top right: the 1998 August 27 MGF from SGR 1900+14 observed by Ulysses (Hurley et al. 1999). Bottom: the 2004 December 27 MGF from SGR 1806–20 observed by Swift/BAT (Palmer et al. 2005). Reproduced with permission from Springer Nature.

0525–66 in the Large Magellanic Cloud was observed by several spacecrafts (Mazets et al. 1979b; Cline et al. 1982; Evans et al. 1980). The total energy release of this event was about 10^{44} – 10^{45} erg. As mentioned in Section 1.1, it was one of the first detections of emission from magnetars. The origin was tied to young supernova remnant N49 (Evans et al. 1979, 1980; Cline et al. 1982) in the Large Magellanic Cloud.

This event remained unique for over two decades, until another MGF was detected on 27 August 1998 from SGR 1900+14 (Hurley et al. 1999; Feroci et al. 1999). The initial spike was brighter than the 1979 event, while the tail was fainter, lasting about 400 s. For comparison, the tail of the 1979 MGF lasted only about 300 s (Mazets et al. 1979b). The total energy released was estimated to be about 2×10^{44} erg, which is about five times less than the 1979 event.

The last MGF observed to date occurred on 27 December 2004 from SGR 1806–20, which had been in an active bursting period since 2003 (Mereghetti et al. 2005c). While the tail was similar to the previous two MGFs, lasting about 380 s, the initial spike was by far the brightest one, containing most of the released energy, estimated to be about 2×10^{46} erg (Mereghetti et al. 2005c) (while the tail emitted about 2×10^{44} erg). In fact, the ratio of the energy released in the initial spike to that in the tail was at least 100, while it was about 1 for the previous two MGFs (Mereghetti et al. 2005b). The brightness of the initial spike was such that it saturated all the detectors, as in the previous two MGFs. Helicon-Coronas-F, a Russian solar observatory in low Earth orbit, was in the shadow of the Earth during the flare. Still, it registered the reflected emission from the Moon (see Fig.1.6), which allowed for the reconstruction of the initial spike light curve and the estimation of its spectrum (Frederiks et al. 2007a).

The three MGFs were similar in their overall characteristics, but the initial peak of the last event (SGR 1806–20) had a total energy two orders of magnitude higher than

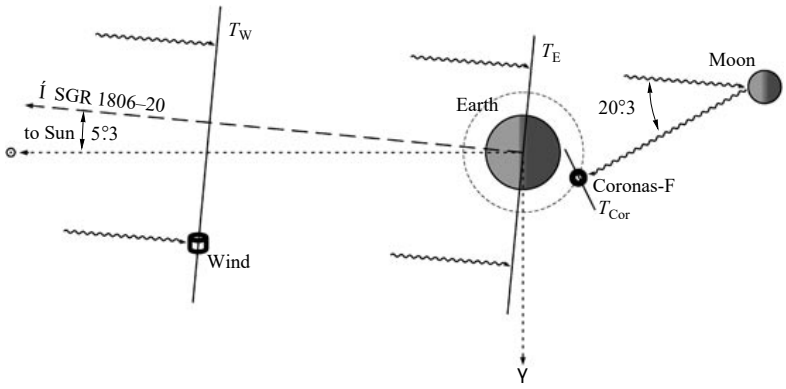

Figure 1.6: Illustration of the reflection of the MGF from SGR 1806–20 on the Moon, as observed by Helicon-Coronas-F. It also contains a second satellite, Wind, which observed the direct emission from the MGF. Credit: Frederiks et al. (2007a), reproduced with permission from Springer Nature.

the other two. However, all had a similar total energy released in the tail. All events saturated most detectors, making it difficult to study the initial spike in detail. The spectrum of the initial spike was hard, with a peak energy (E_{peak}) between 250 keV and 850 keV, while the tail had a softer spectrum with a lower peak energy. Analysis of the last MGF showed that the peak spectrum was well described by a cutoff power-law with E_{peak} of about 850 keV and a photon index α of about 0.7.

MGF, as described in Sec 1.3, are thought to be powered by the sudden reconfiguration of the magnetic field, either due to a crustal fracture or a magnetospheric reconnection event (Mereghetti 2008). The initial spike results from the rapid release of magnetic energy, while the tail is thought to be due to the cooling of a trapped pair-photon fireball confined by the strong magnetic field (Thompson & Duncan 1995). A giant flare can emit up to 10^{46} erg, which is a significant fraction of the magnetar's total magnetic energy, estimated to be around 10^{47} erg for a typical magnetar with a magnetic field of 10^{15} G (Mereghetti 2008).

1.6.1 Extragalactic MGFs

After the discovery of MGFs, it was soon realised that their luminous initial pulses could be detected up to distances of a few tens of Mpc, while the pulsed tails would remain undetectable for distances above $\sim$ 3 Mpc (Trigg et al. 2025). Thus, an MGF from a source in a distant galaxy appears very similar to, and difficult to distinguish from, short GRBs (Mazets et al. 1982a), which are much more distant and energetic (10^{50-53} erg) events originating in compact binary mergers (D'Avanzo 2015). Several studies have been conducted to determine the fraction of the short GRB population that may be due to extragalactic MGFs. However, the paucity of candidates makes the resulting estimates quite uncertain, with reported values ranging from 1% to 40% (e.g., Hurley et al. 2005; Nakar et al. 2006; Ofek 2007; Svinkin et al. 2015). Despite this difficulty, seven candidate extragalactic MGFs have been identified among short GRBs positionally consistent with nearby galaxies, often characterised by a high star formation

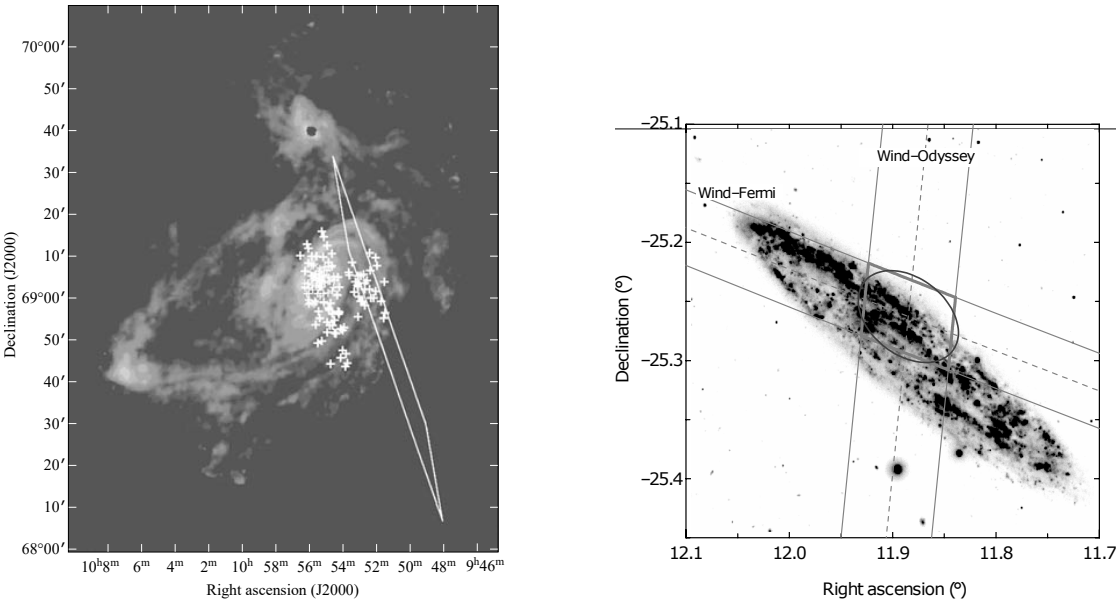

Figure 1.7: Left: The localisation of GRB 051103 (white contours) with the M81 group of galaxies overlaid (the fast radio burst discovered in a globular cluster of M81 (Kirsten et al. 2022) is outside the error region of GRB 051103). Right: The localisation of GRB 200415A overlaid on an image of NGC 253 from the GALEX. Credit: Left: Frederiks et al. (2007b, Astronomy Letters); Right: Svinkin et al. (2021, Nature). Both reproduced with permission from Springer Nature.

rate (Frederiks et al. 2007b; Mazets et al. 2008; Svinkin et al. 2021; Burns et al. 2021; Beniamini et al. 2025). However, the sample of extragalactic MGF candidates is still relatively small, considering the expected fraction of the population of short GRBs.

GRB 051103 was the first short GRB to be proposed as a possible MGF outside the Local Group (Frederiks et al. 2007b). The burst, detected with the Interplanetary Network (IPN), a network of satellites with GRB detectors, was associated with the M81 group of galaxies, located at a distance of about 3.6 Mpc. However, large localisation uncertainties (260 arcmin^2) and late follow-up observations (starting three days after the burst) could not entirely exclude the possibility of a background short GRB. The burst was characterised by a short duration (170 ms) and a hard spectrum. The energy at the distance of M81 was about 7×10^{46} erg, which is consistent with the energy of Galactic MGFs.

Two other GRBs detected by the IPN were GRB 070201 and GRB 200415A. GRB 070201 was localised in the direction of M31 with large uncertainty (error region of 446 arcmin^2; Mazets et al. 2008). The spectral parameters and the energetics of 1.5×10^{45} erg were consistent with an MGF in M31. In addition, the light curve showed a possible tail extending for about one hundred seconds after the burst. The small distance of M31 (780 kpc) would make it possible to detect bursting activity in the soft X-ray range from a magnetar in M31. Still, the large error box prevented any association (Ofek et al. 2008). GRB 200415A had a much smaller error box (20 arcmin^2) that contained the central region of NGC 253 (Roberts et al. 2021; Svinkin et al. 2021). The parameters and energetics of 1.4×10^{46} erg were also consistent with an MGF in

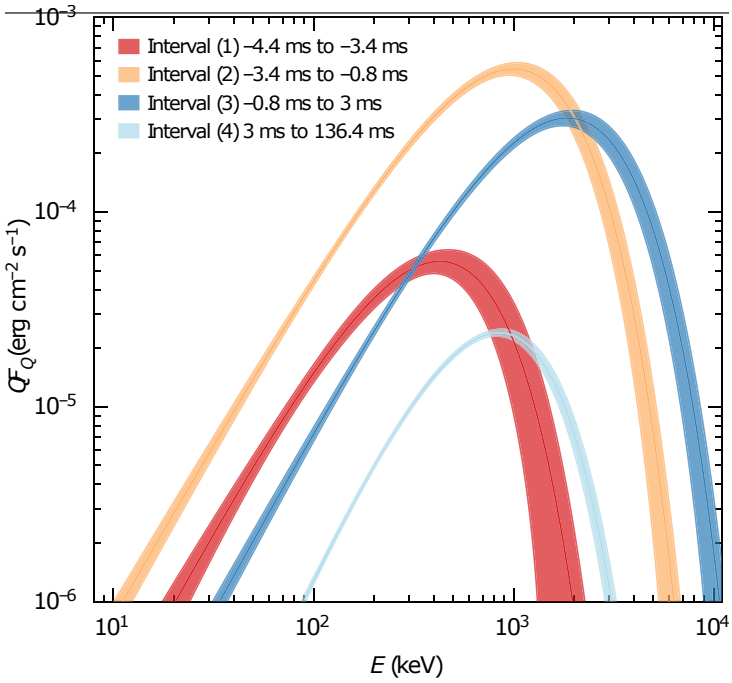

Figure 1.8: Evolution of the spectral peak, E_{peak}, during the initial spike of GRB 200415A. Credit: Roberts et al. (2021). Reproduced with permission from Springer Nature.

NGC 253, making GRB 200415A a strong extragalactic MGF candidate. Additionally, FERMI/LAT detected possible emission in the GeV range, with three photons detected up to 284 s after the initial spike (Fermi-LAT Collaboration et al. 2021). Timing analysis of the initial spike based on ASIM data (Castro-Tirado et al. 2021), which were less affected by instrumental saturation than FERMI data, revealed high-frequency quasi-periodic oscillations, providing further evidence for the magnetar origin of this transient.

The positions of the two candidates, one in M81 and the other in NGC 253, are shown in Figure 1.7, along with the localisation uncertainties. While the association with M81 is less certain due to the large error box, the association with NGC 253 is much more robust.

Also, two more candidates were found in the search of archival data from Fermi/GBM: GRB 070222, associated with M83 (Burns et al. 2021), and GRB 180128A, which could be the second giant flare in NGC 253 (Trigg et al. 2024). The two most recent additions to the extragalactic MGF sample, 231115A (Mereghetti et al. 2024c) and 241107A (Rodi et al. 2025) are part of the work described in this thesis (see Chapter 5).

The study of extragalactic MGFs revealed an additional characteristic that was not observed in the Galactic MGFs, as the peak was too bright. Specifically, the study of two MGF from NGC 253 showed the evolution of the spectral peak, E_{peak}, during the initial spike. The spectrum was initially observed to harden, reaching a peak above 1 MeV, and then gradually soften (Roberts et al. 2021; Svinkin et al. 2021; Beniamini et al. 2025; Castro-Tirado et al. 2021). An example as seen in GRB 200415A is shown in Figure 1.8.

Chapter 2

INTEGRAL & data analysis

2.1 INTEGRAL

INTEGRAL (INTErnational Gamma Ray Astrophysics Laboratory) is a space observatory of a European Space Agency mission with contributions from Russia and the USA (Winkler et al. 2003). The satellite is based on the same service module that was developed in parallel for XMM-Newton, the soft X-ray ESA's mission. INTEGRAL was launched on 17 October 2002 by a PROTON rocket from the Baikonur Cosmodrome in Kazakhstan (Jensen et al. 2003).

The wide observational energy range of INTEGRAL (from 3 keV to 10 MeV) is achieved thanks to three instruments, the Joint European X-Ray Monitor (JEM-X, Lund et al. 2003), the Imager on Board the INTEGRAL Satellite (IBIS, Ubertini et al. 2003), and the SPectrometer on INTEGRAL (SPI, Vedrenne et al. 2003) covering the energy ranges 3–35 keV, 15 keV – 1 MeV, and 18 keV – 8 MeV, respectively. In addition, the satellite is also equipped with an Optical Monitoring Camera operating in the 500 – 600 nm range. See Fig. 2.1 for an exploded view of the satellite.

Most of the INTEGRAL observations were performed using a dithering pattern in order to optimise imaging with the coded mask instruments and to improve background modelling. This means that each observation was split into individual segments, referred to as Science Windows (ScWs), typically lasting about ∼30 minutes, pointed on a grid of directions centred around the target source. A large part of the observing time was devoted to a survey of the Galactic plane, again using a predefined pattern of ScWs. The dithering pattern was optimised along the mission and, as a result, the commonly used was a 5×5 rectangular pattern with 2° steps. If longer observations were required, multiple patterns were used with a shift of 0.3° between them and an increasing roll angle between -3° and $+3^\circ$ between the patterns.

Through most of the mission, INTEGRAL was in a highly elliptical geosynchronous orbit with a period of 3 sidereal days, with a constant position above earth during the perigee. While the height and the inclination were being changed regularly with changes in the mission priorities, the orbit period was kept constant. In Figure 2.2, a visualisation of the INTEGRAL orbit is shown over the whole mission period. In 2015, four orbital manoeuvres were executed to ensure a safe deorbiting in 2029. As a result, the orbital

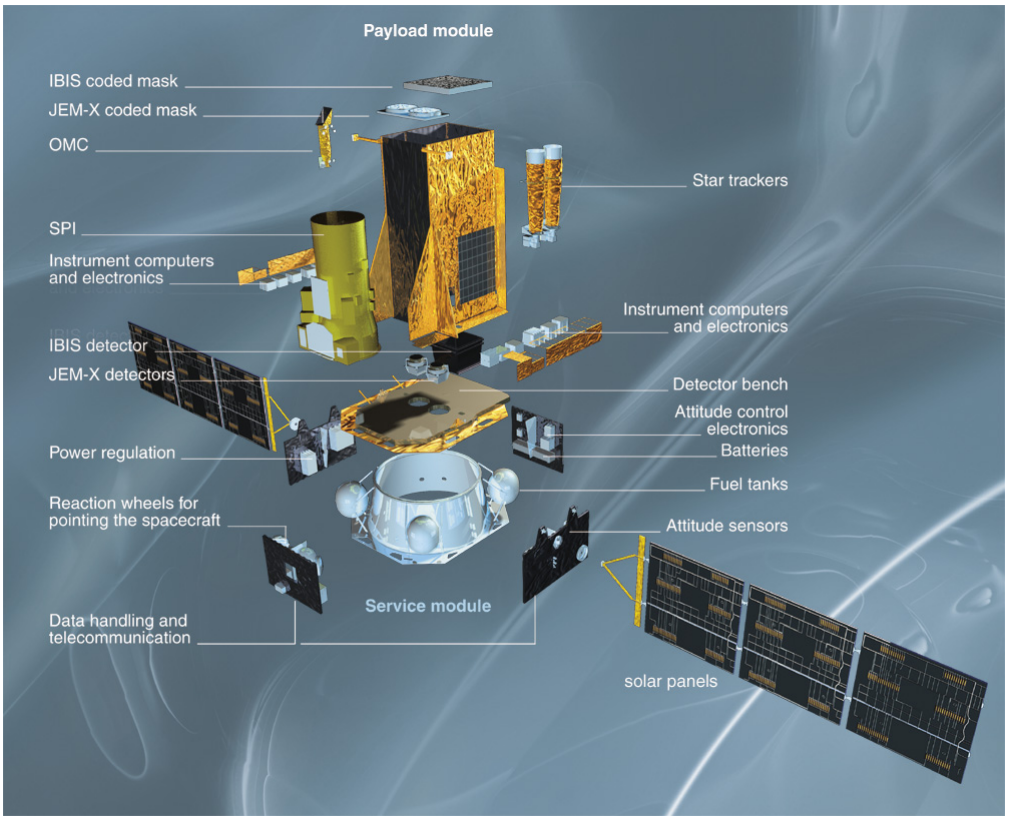

Figure 2.1: Diagram of the INTEGRAL satellite with its instruments. Credit: ESA 2002, Illustration by Medialab

period was reduced to 64 hours.

During nominal operations, the build-up of the solar radiation pressure slowly saturates the reaction wheels of the satellite that control the pointing of the spacecraft. When the reaction wheel was reaching limits, it is necessary to de-saturate it and propellers had to be used to perform this manoeuvre. However, in 2020, the satellite exhausted the stored propellant, and started to work in the so-called "z-flip mode" (De Marco et al. 2023), in which the satellite was fully controlled using reaction wheels, and solar radiation pressure was exploited to control the angular momentum of the satellite. INTEGRAL had to observe one side of the Galactic Plane for roughly half of each revolution, and when the reaction wheel was reaching its maximum rotational speed, the satellite had to flip along the z-axis to prevent saturation and was using solar radiation pressure to reduce speed of the reaction wheel. The observation schedule had to be adjusted to accommodate this new pointing strategy.

The scientific mission of INTEGRAL ended in March 2025 (Ferrigno 2025), but the satellite still continues to operate in a reduced capacity until 2029, when it is expected to re-enter the Earth's atmosphere. As of October 2025, the satellite transfers housekeeping data to the ground for about 16% of the time, which includes data from the anti-coincidence shield. Thus, it is still possible to use the satellite as part of the interplanetary network (IPN) for the localisation of gamma-ray bursts (GRBs) and other transient events.

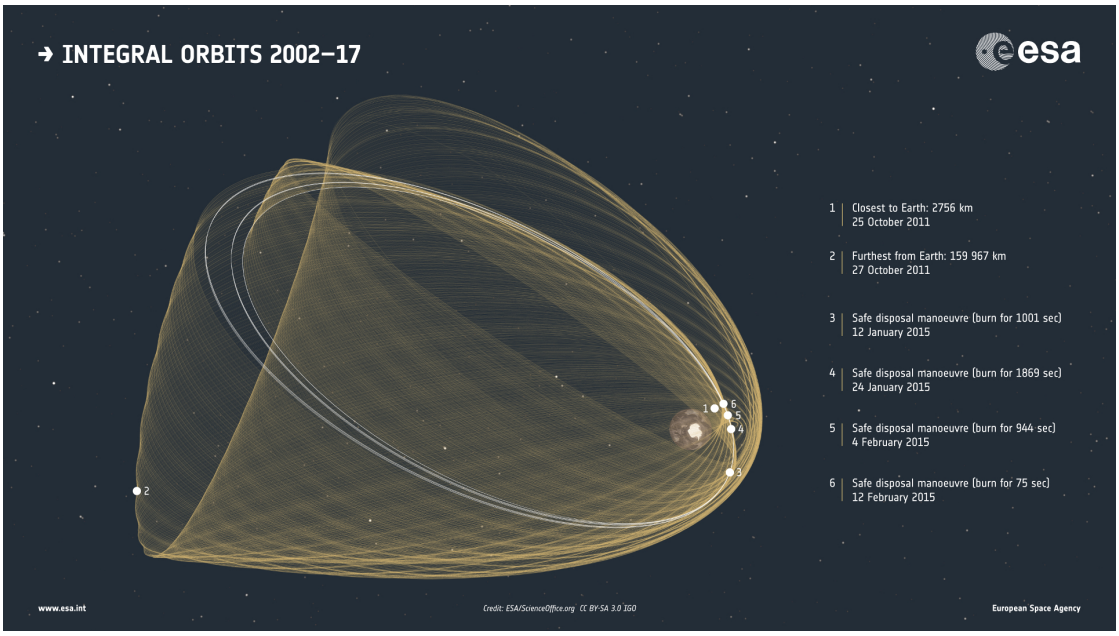

Figure 2.2: Visualisation of the INTEGRAL orbit over the 2002–2017 period with marked four deorbiting manoeuvres. Credit: ESA/ScienceOffice.org, CC BY-SA 3.0 IGO

2.1.1 IBIS/ISGRI

This work is based on data from IBIS, a coded mask imager that is composed of two detectors: lower-energy ISGRI (The INTEGRAL Soft Gamma-Ray Imager, Lebrun et al. 2003) and higher-energy PICsIT (Pixellated Imaging Caesium Iodide Telescope, Labanti et al. 2003). A schematic view of the IBIS is shown in Fig. 2.3.

ISGRI is a wide-field imager with a total Field of View (FOV) of $29.1° \times 29.4°$ including a fully coded, most sensitive FOV of $8.3° \times 8°$. The detector is composed of eight modules of 64×32 cadmium telluride (CdTe) pixels each. The pixels have a sensitive surface of 4×4 mm and are spaced by 0.6 mm. Including the spacing between the modules, a shadowgram can be represented as a matrix of 130×134 pixels. The total collecting area is about 2600 cm^2. The detector operates nominally in the 15 keV to 1 MeV range, with the maximum effective area in the 20 to 100 keV range. ISGRI provides an angular resolution of $12'$ (Full Width Half Maximum), while the sources can be located with a precision of a few arcmin, depending on their signal to noise ratio (Scaringi et al. 2010; Gros et al. 2013).

2.1.2 Coded mask

The ISGRI detection plane is located at 3.2 meters from the IBIS coded mask. The mask is composed of square gaps and fully opaque elements of tungsten with a thickness of 16 mm. The mask aperture is based on a Modified Uniformly Redundant Array, an optimal pattern that allows resolution of all sources within the field of view. The images recorded by the ISGRI detector are called shadowgrams, as they are formed by the superposition of mask shadows cast by the sources in the FoV. The analysis of the shadowgrams, through correlation with the mask pattern enables the reconstruction of the source positions.

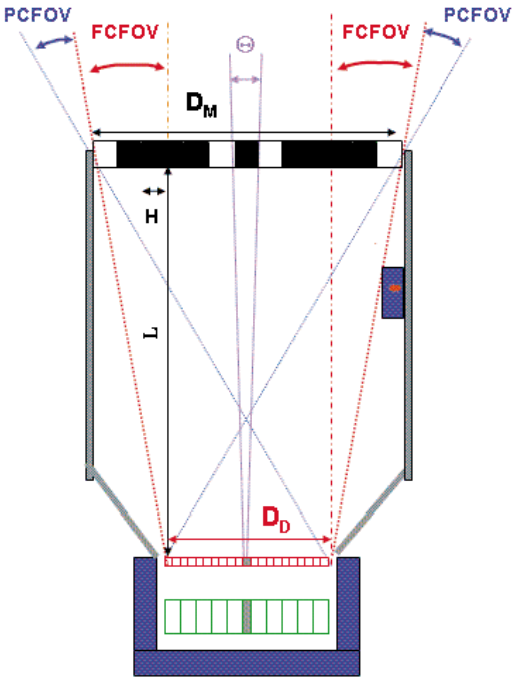

Figure 2.3: Schematic view of IBIS instrument, ISGRI, upper detector is shown in red, and PICsIT, lower detector in green. Reproduced from (Goldwurm et al. 2003)

ISGRI is able to work synchronously with PICsIT in a Compton mode (i.e. photons depositing energy in both detectors), which main objective is the measurement of polarisation. However, in this mode only the most energetic events are being registered, and total sensitivity is only a fraction of normal mode of the detector.

2.1.3 Long term evolution of the ISGRI performance

Ground tests showed that ISGRI would start losing gain when exposed to the high energy protons. The first month in the orbit showed a loss of gain of around 2.6%, which was within expectations. Additionally, a loss of gain up to 1% due to strong solar flares was observed.

While the detector was designed to operate in the energy range from 15 keV to 1 MeV, as a result of radiation damage to the CdTe pixels, the sensitivity was systematically decreasing, due to an increase in the lower threshold of the operational energy range, from less than 20 keV at the beginning of the mission to almost 40 keV at the end of the mission. In Figure 2.4 (left) I show the energy of the first percentile of the detected counts, which is a good proxy for the detection threshold of the detector. The right panel of the same figure shows the count rates in the 20-25 keV, 25-30 keV, 30-35 keV, 35-40 keV, and 35-40 keV energy bands averaged over one orbital revolution. It is clear that the sensitivity of the detector is decreasing in the lower energy bands even above the first percentile, while the sensitivity is stable above $\sim 35 - 40$ keV.

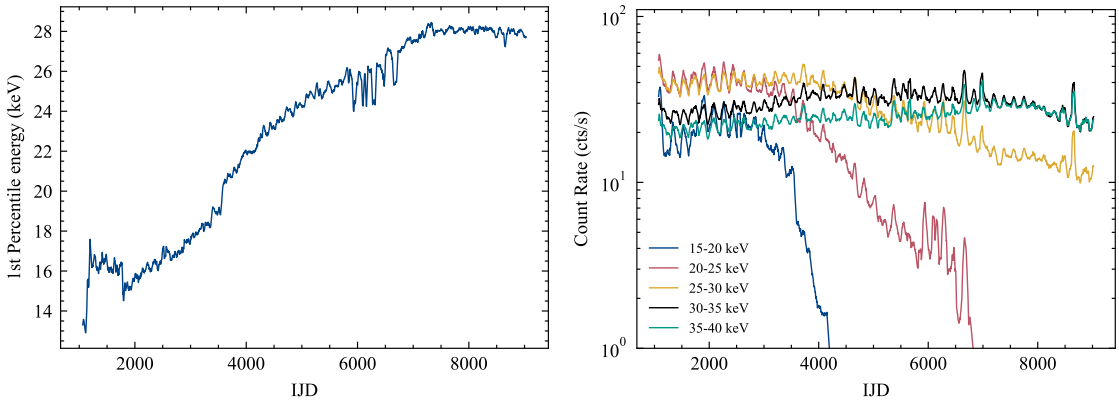

Figure 2.4: Left: Energy of the first percentile of the detected counts in ISGRI over the mission. Right: Average counts in the 20-25 keV, 25-30 keV, 30-35 keV, 35-40 keV, and 40-45 keV energy bands over the mission. Time is in INTEGRAL Julian Days, defined as IJD = MJD-51544 (IJD = 0 at 1999-12-31 23:58:55.817 UTC)

2.1.4 INTEGRAL Data analysis software

INTEGRAL Off-Line Scientific Analysis Software (OSA Goldwurm et al. 2003) is a software package developed and maintained by the INTEGRAL Science Data Centre (ISDC, Courvoisier et al. 2003). It is being used for the data reduction and analysis of the data from INTEGRAL instruments. It operates on two levels, ScW level and Observation Group (OG) level. The ScW level analysis is performed on each ScW individually. It consists of standard data reduction and analysis, including gain correction, energy reconstruction, dead time correction, good time interval (GTI) computation, shadowgram creation, image deconvolution, source detection, as well as light curve and spectrum extraction (from individual ScWs). The OG level analysis is performed on a group of ScWs, which can be created after the ScW level analysis. It allows one to create mosaics of images, and to merge light curves and spectra from multiple ScWs. The latest version of the OSA is 11.2, which was released in December 2022. This version and the newest calibration files were used for the analysis presented in this thesis.

Image reconstruction in coded mask instruments is based on the correlation of the recorded shadowgram with the mask pattern. As the detector works in photon-by-photon mode, it registers the time and energy of each detected event with the pixel position. The data are then binned in the desired time and energy intervals to create shadowgrams. The shadowgrams are first corrected for the bad and noisy pixels, and for the dead time effects, and then deconvolved using the mask pattern to reconstruct the sky image. The details of the IBIS image reconstruction are described in Goldwurm et al. (2003).

2.2 Spectral extraction

Two different methods can be used to extract spectra from the ISGRI data. In the following, I refer to them as Pixel Illumination Factor (PIF) method and imaging method. The former extracts the counts at the ScW level, by taking into account the PIF specifically computed for the source of interest, as well as all the bright sources in the FOV.

In this way, the contamination from the other sources is removed. The spectra are then averaged over the OG, taking into account the response of the instrument during each of the ScWs. However, as this method is based on single ScWs, it works best if the source is bright enough to provide a significant detection in every ScW. While this method works well for bright sources, it is not always adequate for magnetars, which are rather weak sources in the hard X-ray range. The second method of spectral extraction is based on the OG instead of single ScWs and uses imaging. It uses the count rates of the source extracted from the mosaic image obtained by properly adding the sky images of the individual ScWs. In this way, the signal-to-noise ratio of the source can be maximised before the spectral extraction is performed.

Considering the faint level of the persistent emission from magnetars and the better control over detection significance provided by the mosaic method, I selected it as the main method for spectral extraction.

The source spectra were extracted from mosaic images using the `mosaic_spec` tool. This OSA tool extracts the count rate and variance in different energy bands of the mosaic at the selected position. It fits a 2D Gaussian to the pixel distribution in the mosaic image, and the count rate is given by the centroid of the Gaussian. It can take into account the local background, by fitting a Gaussian plus a constant to the pixel distribution. The source count rate was extracted using this tool, letting the source position vary freely within a box of 5 pixels in the fit. Using the best-fit position, the fit was performed again, with fixed position and the size of 20 pixels to estimate the background contribution, with the size adjusted when necessary based on visual inspection of the mosaic.This was especially important for faint sources, where the background contribution may be significant.

2.2.1 Minimum significance

In order to assess the minimum source detection significance at which the analysis of the mosaic with `mosaic_spec` yields a reliable count rate, I performed tests decreasing the significance of the source with fixed count rate in two different ways. The first test was performed by simply measuring the total count rate in the 24–100 keV energy band, by summing the count rate in the number of spectral channels (mosaics in e.g. 24–50 keV and 50–100 keV), while increasing the number of channels from one to ten. The second test was performed by measuring the count rate in the 20–100 keV energy band, while increasing the number of ScWs used to create the mosaic.

For the first test, I selected the magnetar SGR 1900+14 and used revolutions 659-743, when the source was detected. The count rate was first extracted from a mosaic created in the full energy band, 24–100 keV, and then the number of channels (mosaics) in the 24–100 keV range was increased (mosaics in, e.g. 24–50 keV and 50–100 keV) up to a total of 12. Each time, I used the same set of ScWs and parameters for the analysis. I found that the flux derived with `mosaic_spec` increases by a factor of ~ 2 when the number of energy bins increases from 1 to 12 (see Fig. 2.5).

For the second test, I selected two bright sources, X Per and 4U 1722-30, using the

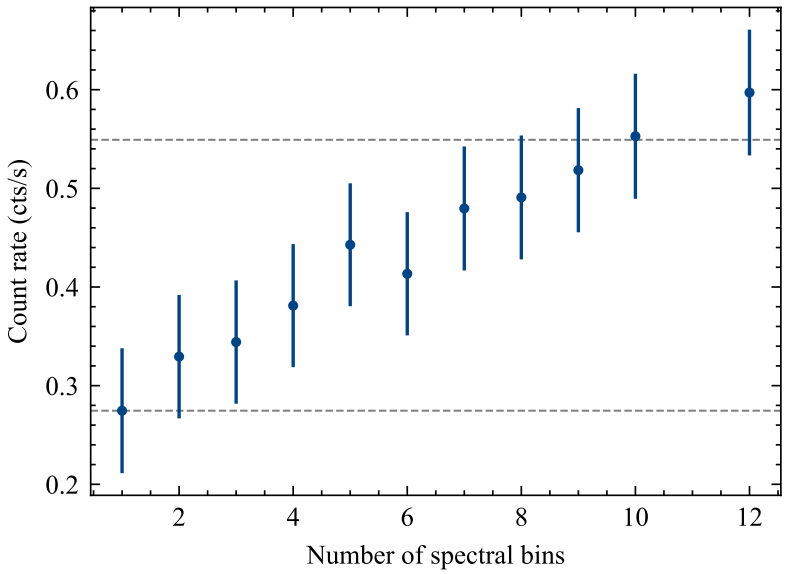

Figure 2.5: Count rate of SGR 1900+14 in the 24–100 keV energy band as a function of the number of spectral channels used to extract the count rate. The dashed lines show the count rate obtained with a single energy band (lower line) and twice this value (upper line), illustrating the systematic flux increase with finer energy binning.

ScWs in revolution 0646 and 0235, respectively. I extracted the fluxes using groups with a decreasing number of ScWs (after checking that the average of the source count rates measured in the ScWs of each group was the same). The fluxes measured with `mosaic_spec` are plotted in Figure 2.6 (left) as a function of the number of ScW.

With the decreased exposure time, the significance of the detection decreases. The count rate as a function of the detection significance in the 20–100 keV band is shown in Figure 2.6 (right). The flux has a steady level up to a detection significance of around 6–7σ in the 20–100 keV. The apparent flux increase below this limit is more pronounced with faint sources and diminishes with brighter ones.

In addition, I compared the flux of the magnetar SGR 1806–20 obtained with imaging method to that measured with the NuSTAR satellite which observed the source during the same period. I used data from 2015 February 16 to 2015 April 28 (revolutions 1508–1535), selecting the ScW pointed within 10° of the source position. I found consistent results for the flux obtained with INTEGRAL when the detection significance is at least 6–7σ in the 20–100 keV band.

All these tests indicate that in the case of faint sources, the fluxes are overestimated when their significance is below ∼6–7σ. As the hard X-ray emission from magnetars is rather faint, in the following analysis, I adopted a threshold of 7σ in each spectral channel.

2.3 Burst search

For the burst search described in Chapter 4, I used all ScWs pointed within 14.5° from the source of interest. In fact, although the ISGRI sensitivity decreases near the edges

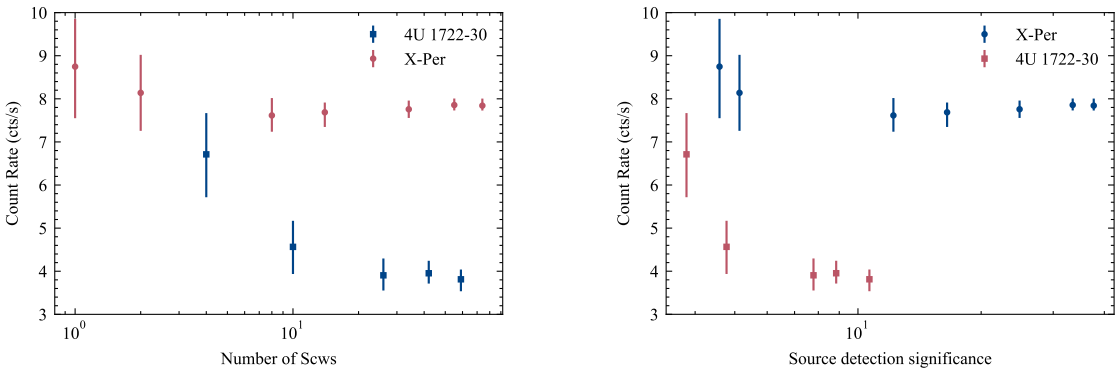

Figure 2.6: Left: Count rate of X Per and 4U 1722-30 in the 20–100 keV energy band as a function of the number of ScWs used to create the mosaic. Right: Count rate of X Per and 4U 1722-30 in the 20–100 keV energy band as a function of the detection significance in the 20–100 keV band.

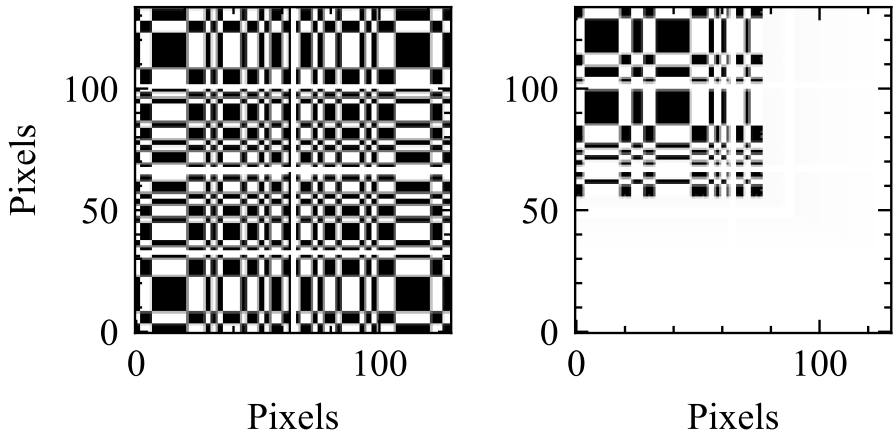

Figure 2.7: Pixel Illumination Factor matrix for the source, located in the fully coded FOV (left panel) and partially coded FOV (right panel).

of the FoV, it is still possible to detect and locate bright bursts. Each ScW was screened to eliminate those affected by strongly variable background. This was done by fitting a constant to the light-curve of the whole detector in the full energy range binned at one second, after performing 1σ clipping to exclude possible bursts. ScWs were considered to have good quality and used in the search for bursts if the fit resulted in a reduced chi square $\chi_{\rm red} \leq 1.3$.

The PIF describes the percentage by which a pixel is illuminated by a source in the sky. Selecting events based on their PIF values allows one to reduce the number of background events and thus to increase the sensitivity of the search. Before the search, the position of the source was used to create the PIF matrix for each ScW and to filter the list of events with it. In particular, I extracted the source light curves using only pixels with PIF > 0.5. Figure 2.7 shows an example of the PIF map for a source in the fully coded FOV (left panel) and in the partially coded FOV (right panel).

The burst search was performed on the selected ScWs using the following procedure. The search was done simultaneously in eight time intervals with logarithmically spaced durations between 0.01 and 1.28 s (i.e. 0.01, 0.02, 0.04, 0.08, 0.16, 0.32, 0.64, 1.28 s).

The threshold for each timescale was set at a level above the average (estimated from the sigma-clipped background level in the 1-second light curve) corresponding to a false positive probability of 10^{-3} for each ScW.

Typically, a single variability event can exceed the threshold in several timescales and time bins. After joining adjacent bins, only the trigger with the highest significance was retained.

The triggers found in the light curves were then verified by examining images of the corresponding time intervals. This was done with an interactive analysis based on the imaging software developed for the INTEGRAL Burst Alert System (IBAS, Mereghetti et al. 2003). This allowed me to eliminate triggers caused by background variations, sources outside the field of view or coming from other sources in the field of view but unrelated to the magnetar of interest.

2.3.1 Dead time corrections

To produce the final light curves of each burst and to properly derive their fluences, corrections for instrumental dead time and the coding fraction must be applied. The dead time correction also includes the effects induced by the Veto system, by the photons of the on-board calibration source, and (if enabled) by the tagging of Compton events. These three effects cause a dead time ϵ_{hk} which can be computed from the housekeeping data of each ScW. The true count rate N_{true} is then related to the observed count rate N_{rec} by the expression: $N_{true} = N_{rec} \cdot \tau_{tot}$, where τ_{tot} is given by:

$$\tau_{tot} = \exp\left(\epsilon_{hk} + \frac{N_{rec}}{M}\tau\right) \tag{2.1}$$

where $\tau = 0.114$ ms is the fixed dead time during which a pixel cannot register a new event and M is the number of modules illuminated by the source for at least 20% of their surface.

Sources in the partially coded field of view do not illuminate the whole detection plane. Therefore, their observed count rate must be corrected for the coding fraction, i.e., the fraction of the detector area exposed to the source. In the following, all reported burst fluences refer to these corrected values unless stated otherwise.

Chapter 3

Hard X-ray emission of magnetars

INTEGRAL discovered persistent (i.e., non due to the bursts) hard X-ray emission from magnetars (Götz et al. 2004; Mereghetti et al. 2005a; Molkov et al. 2005), which was later confirmed by other missions, such as Suzaku and RXTE (Kuiper et al. 2006; den Hartog et al. 2008b,a; Enoto et al. 2010b,a; Kuiper et al. 2004). During the twenty years of the INTEGRAL mission, the exposure time of the Galactic Plane increased significantly, allowing us to study the long-term behaviour of magnetars in the hard X-ray band. I present the results of a systematic study of the persistent hard X-ray emission from all known magnetars using all the available ISGRI data. I detected four magnetars and one rotation-powered pulsar that exhibited magnetar-like behaviour. In addition, three more sources were detected only during outbursts or with low statistical significance.

In this chapter, I also present the results of a 2.5 yr long multi-wavelength campaign on the outburst of the magnetar Swift J1555.2–5402. I contributed to this work not only with the INTEGRAL data, but also with the analysis of data obtained with Swift, NuSTAR, and NICER.

3.1 Observations and data analysis

As the magnetars are rather faint sources in the hard X-ray range, usually not detectable in a single ScW, the imaging method was selected for the study of their persistent emission, as described in Section 2.2.

As the majority of magnetars are located in the Galactic Plane, especially in inner regions and in directions tangential to the spiral arms, several magnetars were often observed simultaneously in a single ScWs. To optimise the data analysis, I applied the following procedure based on two stages: first, single ScW images were generated and archived in order to re-use them for the analysis of different sources; then, mosaics were produced by combining all available, non-noisy ScWs pointed within 10° from the source of interest to maximise sensitivity.

Images were created in ten logarithmic energy bands between 17 and 200 keV. The lower energy channels were successively excluded (up to 30 keV) as the lower energy threshold of ISGRI evolved with time (see Section 2.1.3). However, the sources were generally too faint for significant detections on a short timescale. Therefore, I used these

ten-bands mosaics only to derive the average spectra of the source over extended periods (typically years).

To obtain long term light curves with the best possible time resolution, the flux was measured in a single broad band $E_1 - E_2$. E_2 was kept at 80 keV for all the observations, while E_1 was varied between 18 and 30 keV, depending on the epoch of the observation. In particular, for observations before September 2007 (revolution 600), I used E_1=18 keV, between September 2007 and March 2009 (revolutions 600 and 780) E_1=22 keV, between March 2009 and October 2011 (revolutions 780 and 1100) E_1= 25 keV, between October 2011 and end of 2017 (revolutions 1100 and 1900) E_1=27 keV, and since 2018 (revolution 1900) E_1= 30 keV. These energy bands were chosen to maximise the significance of the detection for the typical spectrum of magnetars. For mosaics extending across two or more of the above periods, the energy band was selected based on the revolution of the last ScW included in the mosaic. To quantify the long-term variability, I computed the variability factor $V_f = F_{max}/F_{min}$ and fitted a constant to each light curve to test for flux stability.

As the mosaic is composed of multiple ScWs from different revolutions, the response matrix for the spectral analysis had to be created accordingly. For this, I created the weighted response matrix for each mosaic by averaging the response matrices of the individual ScWs, weighted by their exposure time.

3.2 Results

Five magnetars were detected during multiple periods and with sufficiently good statistical significance to produce long term light curves. The results of these sources (4U 0142+614, 1RXS J170849–400910, SGR 1806–20, 1E 1841–045, PSR J1846–0258) are presented in detail below. The transient 1E 1547.0–5408 was detected in the first half of 2009, with significance of 26σ, and then with a significance of 9.4σ over the next year. In addition, two sparse detections with low significance ($< 4\sigma$) were obtained between 2014 and 2019. SGR 1900+14 was detected in the first half of 2004 with a significance of 7.6, and with lower significance up to 2009 and between 2012 and 2018. Finally, SGR 0501+4516 was detected only in the second half of 2008 with significance of 3.8σ.

Fig. 3.1 shows the long-term light curves of five magnetars as derived from the count rates measured in the mosaics. Since these count rates were extracted in different energy ranges, I converted all of them to fluxes in the 20-80 keV, assuming a power law spectrum with photon index fixed to a representative value of 1.7.

As it can be seen in Fig. 3.1, SGR 1806–20 exhibited strong flux variability. Therefore, I extracted three different spectra for the time intervals 2003–2005, 2006–2011, and 2012–2023. All of them were well fit with a power law of index between 0.96 and 1.91, showing significant evidence for spectral variations (see Table 3.1). Using the count rate to flux conversion factors based on these spectra, I then computed the final light curve of SGR 1806–20 shown in Fig. 3.2. The lower panel of Fig. 3.2 shows the exposure time of each mosaic.

I proceeded in a similar way for 1E 1841–045, extracting spectra from three separate

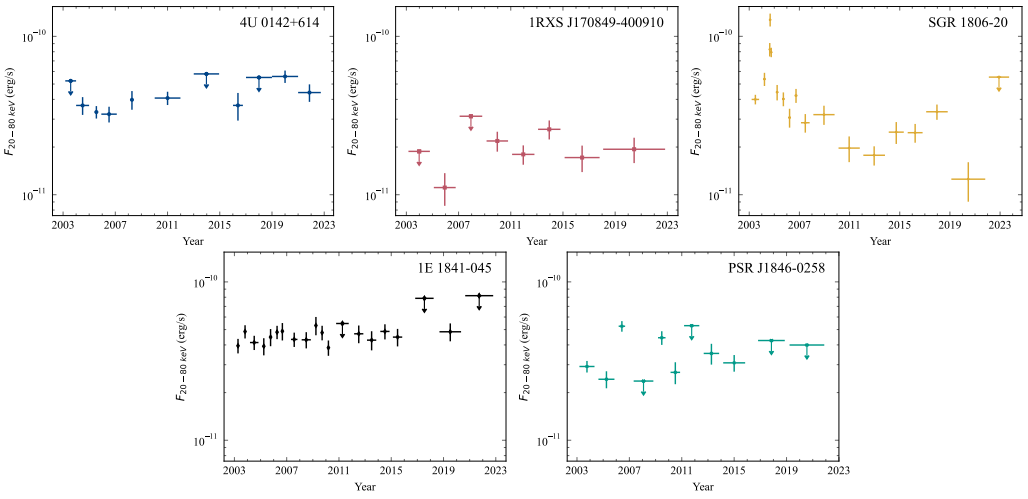

Figure 3.1: Preliminary long-term light curves of the detected magnetars. The fluxes were calculated assuming a power law with photon index $\Gamma = 1.7$ for all observations.

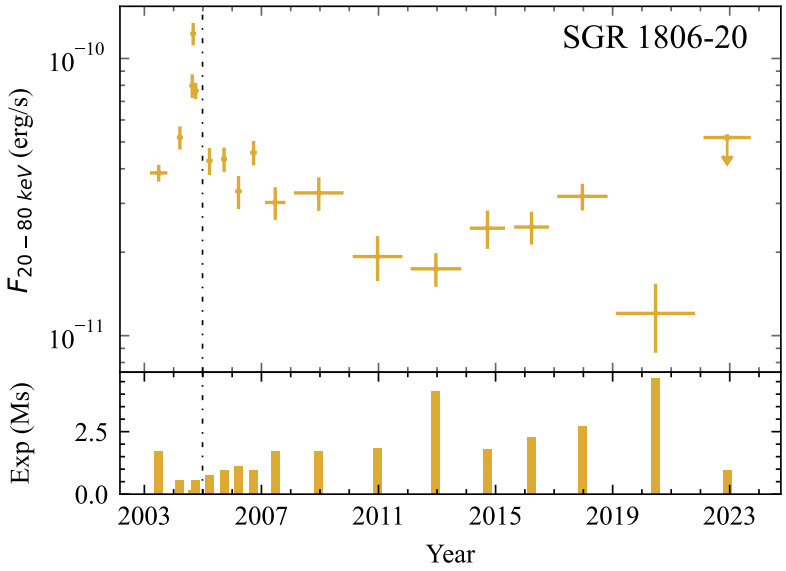

Figure 3.2: Long-term light curve of SGR 1806–20. The bottom panels show the exposure time in each bin. A vertical line marks the time of the Giant Flare on 27 December 2004.

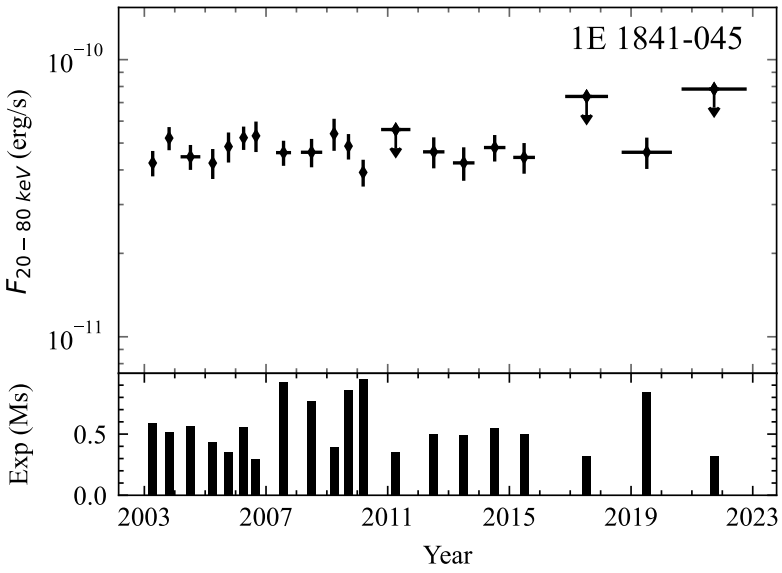

Figure 3.3: Long-term light curve of 1E 1841–045. The bottom panels show the exposure time in each bin.

time intervals. In this case they were all consistent with the same power law (see Table 3.1) therefore to produce the final light curve of Fig. 3.3 I used the photon index of the total spectrum Γ=1.18.

For PSR J1846–0258, besides the average spectrum for the whole time period, I produced two spectra for the intervals before and after the 2006 outburst. The pre-2006 spectrum was not well fitted (see Table 3.1); the post-2006 spectrum is consistent with the average one. The fluxes in Fig 3.4 have been computed with the spectra corresponding to the respective intervals.

In the case of the other two sources, 4U 0142+614 and 1RXS J170849–400910, dividing the data into two time periods reduced the detection significance below the threshold in spectral channels in the second period, so it was possible to obtain a spectrum only for the first part of the mission. These were consistent with the average spectra (Table 3.1), which were used to obtain the light curves of Fig. 3.5 and Fig. 3.6.

Table 3.2 summarizes the variability results for the five sources.

3.3 Discussion

4U 0142+614, 1RXS J170849–400910, and 1E 1841–045 are relatively stable sources, with variability factors below 2. In fact, a constant fit to the light curves yields reduced chi-square values between 0.6 and 1.8. The results obtained in this work are consistent with those of previous studies of 4U 0142+614 (Revnivtsev et al. 2004; den Hartog et al. 2006; Kuiper et al. 2006; den Hartog et al. 2007; Rea et al. 2007; den Hartog et al. 2008b; Wang et al. 2014; Weng & Göğüş 2015), 1RXS J170849–400910 (Revnivtsev et al. 2004; Kuiper et al. 2006; Götz et al. 2007a; den Hartog et al. 2008a; Guo et al. 2015; Younes et al. 2020a), and 1E 1841–045 (Kuiper et al. 2004; Molkov et al. 2004; An et al. 2013, 2015; Weng & Göğüş 2015). Most published results for these sources were based

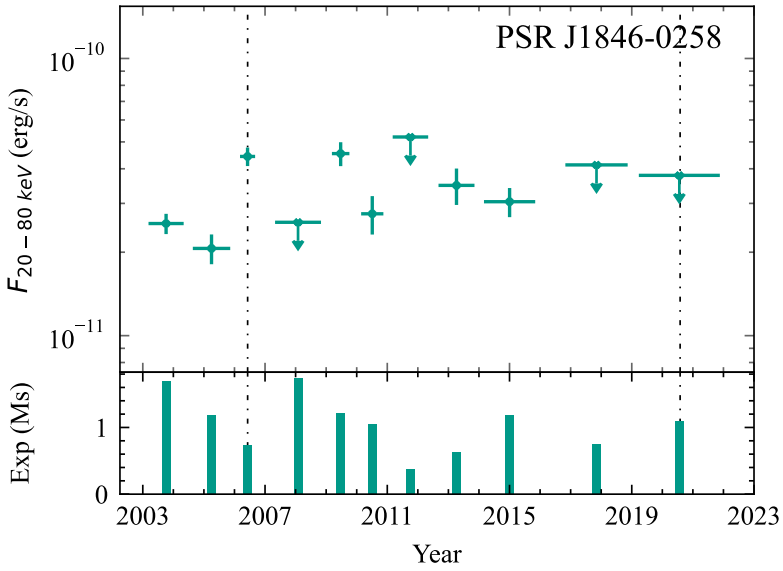

Figure 3.4: Long-term light curve of PSR J1846–0258. The bottom panels show the exposure time in each bin. Vertical lines mark the onset of the outbursts, the first one on 2006 July 7, and second one on 2020 August 1.

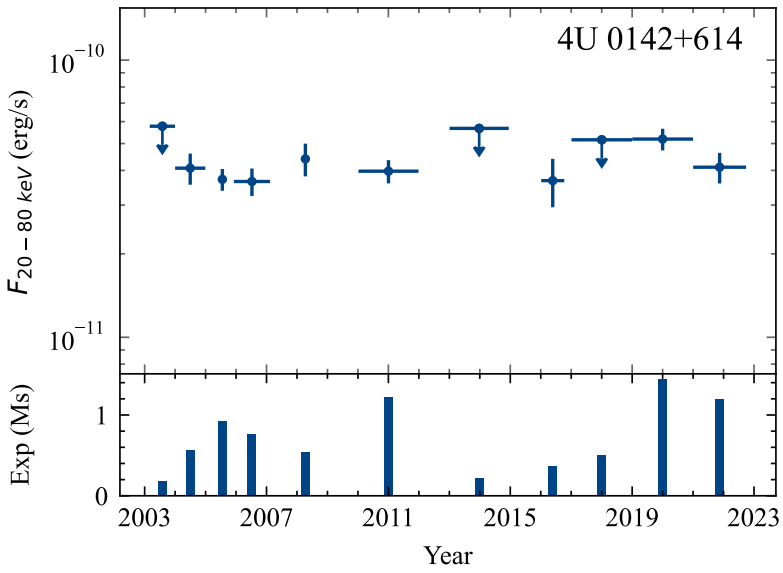

Figure 3.5: Long-term light curve of 4U 0142+614. The bottom panels show the exposure time in each bin.

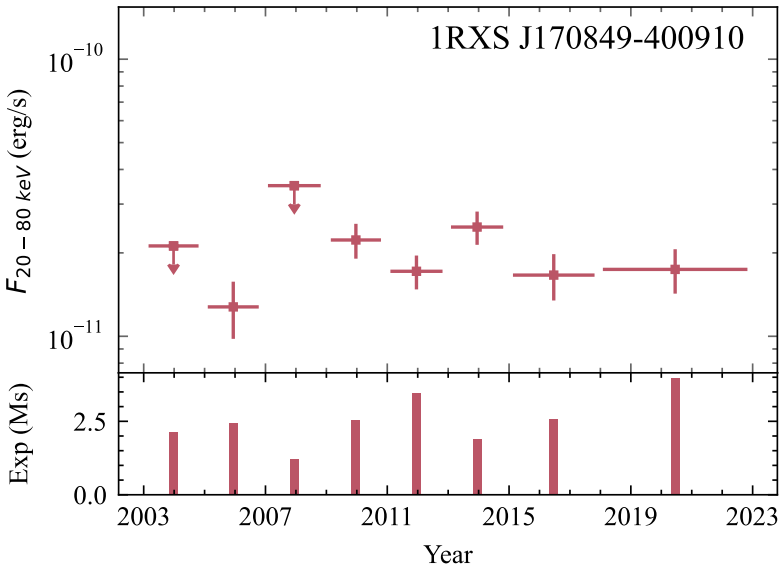

Figure 3.6: Long-term light curve of 1RXS J170849–400910. The bottom panels show the exposure time in each bin.

Table 3.1: Spectral properties of the detected magnetars

Source	Tstart	Tstop	Γ	χ^2_{red}(dof)	Flux[a]
4U 0142+614	2003-03-03	2022-09-27	0.87 ± 0.14	1.6(4)	3.9 ± 0.3
1RXS J170849–400910	2003-03-03	2022-10-30	0.55 ± 0.27	0.8(3)	1.8 ± 0.2
1E 1841–045	2003-03-10	2022-10-20	1.18 ± 0.17	0.1(2)	4.7 ± 0.3
	2003-03-10	2007-10-16	1.06 ± 0.16	1.3(4)	4.5 ± 0.3
	2007-10-16	2012-03-01	1.16 ± 0.21	0.2(3)	4.8 ± 0.4
	2012-03-01	2022-10-20	1.08 ± 0.23	0.8(3)	4.9 ± 0.4
SGR 1806–20	2003-03-03	2005-04-28	1.91 ± 0.21	0.4(3)	5.5 ± 0.4
	2005-08-16	2011-10-25	1.22 ± 0.22	1.0(3)	3.6 ± 0.3
	2012-02-05	2023-09-21	0.96 ± 0.24	1.7(3)	2.7 ± 0.3
PSR J1846–0258	2003-03-10	2005-11-10	1.08 ± 0.44	0.7(1)	2.8 ± 0.3
	2003-03-10	2006-09-04	2.59 ± 0.48	4.4(2)	2.4 ± 0.4
	2007-04-30	2015-11-03	1.18 ± 0.44	1.0(1)	3.9 ± 0.4

[a] Flux is in units of 10^{-11} erg cm^{-2} s^{-1}.

Table 3.2: List of detected magnetars with their average X-ray fluxes (F_{mean}), χ^2_{red} values of constant fit, and variability factors (V_f).

Source	$\mathbf{F}^a_{mean}$	χ^2_{red}**(dof)**	$\mathbf{V}_f$
4U 0142+61	4.1 ± 0.2	1.2(7)	1.42 ± 0.21
RXS J1708–40	1.8 ± 0.1	1.8(5)	1.94 ± 0.53
SGR 1806–20	3.3 ± 0.1	19.3(16)	10.21 ± 3.01
1E 1841–045	4.6 ± 0.1	0.6(16)	1.38 ± 0.24
PSR J1846–0258	2.9 ± 0.1	8.1(6)	2.20 ± 0.35

[a] Error weighted average flux in the $20-80$ keV energy range in units of 10^{-11} erg cm^{-2} s^{-1}, excluding upper limits.

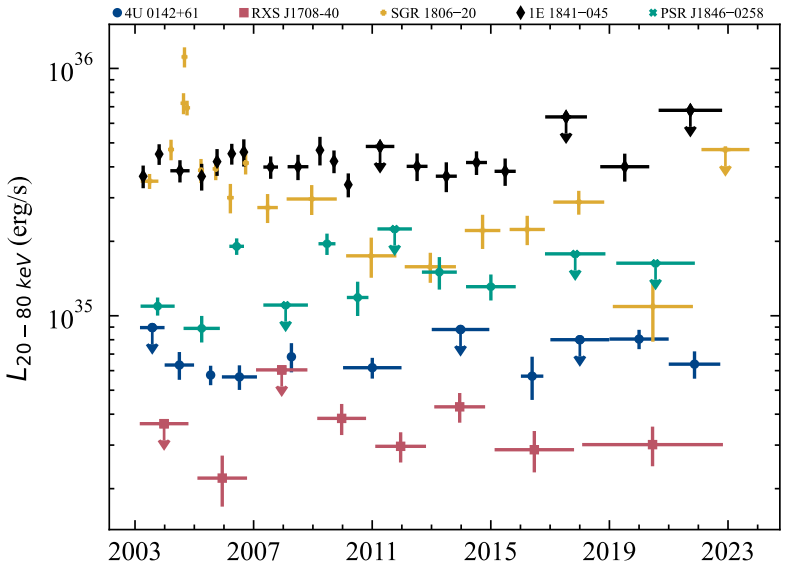

Figure 3.7: Long-term luminosity curves of the detected magnetars. The luminosity was calculated assuming distances of 3.6 kpc for 4U 0142+614, 3.8 kpc for 1RXS J170849–400910, 8.7 kpc for SGR 1806–20, 8.5 kpc for 1E 1841–045, and 6 kpc for PSR J1846–0258.

on observations with INTEGRAL (mostly up to 2012), as well as with other satellites such as Suzaku, NuSTAR, and RXTE. The three sources did not show any significant spectral variability, either because of the limited statistics (in the case of 4U 0142+614 and 1RXS J170849–400910), or because the spectra were consistent within errors (for 1E 1841–045). The spectral parameters are consistent with previously reported values. Only 1RXS J170849–400910 showed a large difference in the photon index, while I obtained a harder photon index, 0.55 ± 0.27, than previously reported measurements (0.7–1.5), it is still consistent within errors with most of them.

The two sources that showed significant variability are SGR 1806–20 ($V_f > 10$) and PSR J1846–0258 ($V_f \sim 2.2$), based on their high χ^2_{red} values (>8) indicating flux variations inconsistent with a constant level. Both sources underwent an outburst during the INTEGRAL mission, SGR 1806–20 in 2004 and PSR J1846–0258 in 2006 and 2020. Figure 3.7 shows the long-term luminosity evolution of all five sources. I discuss them separately below.

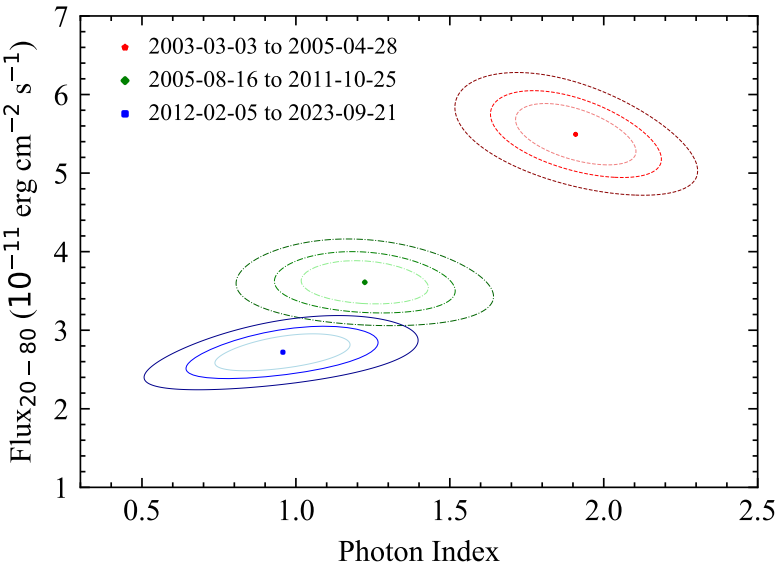

Figure 3.8: Confidence contours of spectra for three periods (2003–2005, 2005–2011, and 2012–2023) of SGR 1806–20. The contours represent confidence levels of 68%, 90%, and 99%.

3.3.1 SGR 1806–20

SGR 1806–20 has been one of the most active magnetars in the past decades, with multiple bursting episodes and a giant flare in December 2004 (Hurley et al. 2005). It is also the most variable source among those detected in hard X-ray by INTEGRAL. In September 2004, just before the giant flare, it reached a peak flux of $\sim 1.2 \times 10^{-10}$ erg cm^{-2} s^{-1}. Then, the flux started to decrease, reaching a minimum of $\sim 1.1 \times 10^{-11}$ erg cm^{-2} s^{-1}. It is also the only source for which I observed a significant long-term spectral evolution (see Fig. 3.8), with the power law slope changing from 1.91 ± 0.21 in 2003–2005, to 1.22 ± 0.22 in 2005–2011, and finally to 0.96 ± 0.24 in 2012–2023.

Due to its high activity, the source was extensively observed with INTEGRAL, Suzaku, and XMM-Newton during 2003–2011 (Molkov et al. 2005; Mereghetti et al. 2005a; Esposito et al. 2007; Gotz et al. 2008; Guo et al. 2015). Guo et al. (2015) analysed all the INTEGRAL data available until the end of 2011, split into yearly intervals, and the flux is generally consistent with what I obtained. However, when the source becomes fainter in 2010 and 2011, I report flux lower by a factor of ~ 2 at a value of 1.9×10^{-11} erg cm^{-2} s^{-1}. This difference is consistent with the flux increase seen during tests and comparison with NuSTAR in Section 2.2.1, as these values were obtained by spectral analysis using yearly data.

Younes et al. (2017a) analysed five NuSTAR observations of SGR 1806–20 taken between 2015 and 2016. The reported flux ($\sim 3 \times 10^{-11}$ erg cm^{-2} s^{-1} in the 3–79 keV range from the power-law component, which is comparable to the flux measured in the 20–80 keV band) is in agreement with the flux I obtained from INTEGRAL data in the same period. The power-law slope is slightly softer (~ 1.27–1.36) than what I obtained from INTEGRAL data (0.96 ± 0.24), but still consistent within errors.

Additionally, NuSTAR observed the source in October 2018. As the data were not

published, I analysed them myself, which yielded a flux of $\sim 1.8 \times 10^{-11}$ erg cm^{-2} s^{-1} in 20–80 keV, in agreement with the values seen in INTEGRAL data. However, NuSTAR observed the source between the flux drop in 2012–2014 and the increase in 2017–2018, and again after the flux increase, missing the evolution seen in the INTEGRAL data. A fit of a constant to the INTEGRAL data between 2008 and 2022 yields a reduced chi-square of 4.6 (6 dof), suggesting variability.

The long-term hardening of the spectrum seen in INTEGRAL the data is also consistent with previously reported results from INTEGRAL (Molkov et al. 2005; Mereghetti et al. 2005a; Esposito et al. 2007; Gotz et al. 2008; Guo et al. 2015), as well as with the NuSTAR results (Younes et al. 2017a). The spectral hardening might be due to an evolution of the magnetosphere geometry leading to increased currents.

3.3.2 PSR J1846–0258

PSR J1846–0258 was discovered in 2000 (Gotthelf et al. 2000) and was the first rotation-powered pulsar found to display a magnetar-like behaviour. In fact, during an outburst in July 2006 (and in a second one in 2020, Blumer et al. 2021; Sathyaprakash et al. 2024), it exhibited a typical magnetar-like behaviour, including a large flux increase, significant bursting activity, and a glitch. The average spectrum I obtained with INTEGRAL is hard, with a photon index of $\Gamma = 1.08 \pm 0.44$. However, the source was detected only in four energy bands (up to 50 keV), limiting the photon index constraints. To investigate spectral evolution, I extracted two separate spectra, one before the 2006 outburst and one after. The first spectrum is very soft ($\Gamma = 2.6 \pm 0.5$), but is poorly fitted, while the post-outburst spectrum is harder ($\Gamma = 1.2 \pm 0.4$) and consistent with the average spectrum within errors.

One study of this source concerns only the pre-outburst period (McBride et al. 2008), while a second one also included the period after the outburst, up until the end of 2007 (Kuiper & Hermsen 2009). For this pre-outburst period, reported results of spectral analysis with INTEGRAL were photon indices of $\Gamma = 2.0 \pm 0.02$ (McBride et al. 2008) and $\Gamma = 1.80 \pm 0.06$ (Kuiper & Hermsen 2009). While McBride et al. (2008) also studied the first observations after the outburst (90 days since onset) as outburst period and post-outburst period of the next year, including data up to 23 September 2007, during which the photon index was $\Gamma = 1.90^{+0.33}_{-0.35}$, and $\Gamma = 1.75^{+0.27}_{-0.31}$ in the outburst period. In fact, none of these results of the spectral analysis has a reflection in this analysis, as in the pre-outburst period, I obtained a much softer power law (but with a poor fit), the post-outburst and average spectrum is much harder.

This difference is also in the way data analysis is performed, from data selection where I used ScWs with pointings within 10° from the source, Kuiper & Hermsen (2009) used all which had source within FOV (14.5°), software version (OSA 11.2 vs OSA 5.1), and Kuiper & Hermsen (2009) extracted spectra in 10 energy bands between 20–300 keV (in which CR was normalized using the Crab observations) for shorter periods, for which I did not manage to obtain required significance.

However, the previously reported fluxes (Kuiper & Hermsen 2009) are in agreement

with the values obtained here. I estimated the same flux increase of ~ 2.2; however, I used data before and after the outburst in 2006 to obtain the required source detection significance, so the flux increase just after the outburst could have been higher.

As noted by Kuiper & Hermsen (2009), INTEGRAL did not observe the source until 90 days after the outburst onset. This gap means that a higher-flux phase could have been missed, or, alternatively, that the detected flux was not directly connected to the initial outburst peak. Supporting the latter interpretation, the source was detected again in 2009 at comparable or even slightly higher flux, and again in 2012/2013 (though with a lower flux by $\sim 30\%$ in this period).

During the second outburst in August 2020, INTEGRAL observed the source at the end of August and then in October and November. However, the source was not detected in any of these periods.

3.4 Broadband analysis of the 2021 outburst of Swift J1555.2–5402

On 2021 June 3 at 09:45:46 UT, Swift BAT (Gehrels et al. 2004) detected a magnetar-like burst from the new source Swift J1555.2–5402. The magnetar nature of the source was confirmed during the first month of the outburst by NICER, which measured pulsations at 3.86 s and a spin-down rate of $3.05(7) \times 10^{-11}$ s s^{-1} (Coti Zelati et al. 2021; Enoto et al. 2021). The soft X-ray flux reached 4×10^{-11} erg cm^{-2} s^{-1}, and the hard X-ray emission was detected up to $\sim$40 keV with estimated 10–60 keV flux of 9×10^{-12} erg cm^{-2} s^{-1} (Enoto et al. 2021).

Here, I present the analysis of the 29-month long outburst of Swift J1555.2–5402, which was extensively monitored by Swift, NICER, NuSTAR, and INTEGRAL. Part of this analysis has been included in the paper *A magnetar outburst with atypical evolution: the case of Swift J1555.2–5402*, by Borghese, Coti Zelati, Imbrogno, Israel, De Grandis, Pacholski, et al., A&A, in press.

3.4.1 Observations and data analysis

NuSTAR

The Nuclear Spectroscopic Telescope Array (NuSTAR, Harrison et al. 2013) observed Swift J1555.2–5402 four times for $\sim$ 144 ks (covering 3–79 keV energy range). Three times in the first month of the outburst in June and a fourth time in October (see Table 3.3). I processed the data using HEASoft 6.33 (Heasarc 2014) and the standard pipeline `nupipeline`. The Nustar-gen-utils (Grefenstette et al. 2025) package was used to select the optimal source extraction region to maximize the signal-to-noise ratio in the hard X-rays in each observation. For the background extraction region, I selected a source free area in the same module, when it was possible. The spectra were rebinned with the `ftgrouppha` tool using an optimal binning scheme (Kaastra & Bleeker 2016) with at least 25 counts per bin.

Table 3.3: NuSTAR observation of Swift J1555.2–5402, with observation time, slope of the power law and flux in 10–60 keV

ObsID	Date	Exposure (ks)	Γ	Flux (10^{-12} erg cm^{-2} s^{-1})
90701319002	2021 June 5	38.4	0.88 ± 0.11	11.1 ± 0.5
80702313002	2021 June 9	25.0	1.00 ± 0.16	10.2 ± 0.8
80702313004	2021 June 21	29.0	0.93 ± 0.15	9.9 ± 0.8
80702313006	2021 October 7	51.9	0.89 ± 0.50	$7.2^{+0.4}_{-1.4}$

NICER

The Neutron star Interior Composition Explorer (NICER, Gendreau et al. 2016) observed Swift J1555.2–5402 67 times for a total of $\sim$ 100 ks between June 2021 and the end of August 2022 in the energy range 0.2–12 keV. I processed the observations using standard procedures in HEASoft 6.33. I used the `nicerl2` command, excluding the COR 0-1.5 GeV/c range and reducing the overshooting range to 0-5 ct/s. I also excluded data from detectors 14 and 34 to minimize detector noise in the soft part of the spectrum. I extracted the spectrum of the source using `nicerl3-spect` and used SCORPEON for the background model. I inspected spectra and, if needed, I ignored counts below 0.5 keV caused by low-energy noise. In those cases, I fixed `noise_norm`, `lhb_em` and `gal_nh` parameters in the SCORPEON model.

Swift

After the source discovery, Swift performed 94 observations for a total of $\sim$ 170 ks. I used the Swift-XRT data (covering 0.2–10 keV energy range) products generator (Evans et al. 2009) to extract spectra from single or from stacked observations. Spectra were inspected and, if needed, lower energy channels (below $\sim$ 1 keV) were ignored in WT mode. The spectra were rebinned to have at least 25 counts per bin, using the optimal binning scheme (Kaastra & Bleeker 2016).

INTEGRAL

INTEGRAL observed the source for about 58.8 ks during the first 150 days of the outburst. Using the method described in Section 2.2, I created a mosaic image in the 30–80 keV energy band. The source was not detected, and I obtained a 3σ upper limit of 9.7×10^{-11} erg cm^{-2} s^{-1}. A search for bursting activity was also performed, but no bursts were found. For details see Chapter 4.

3.5 Spectral analysis

I used XSPEC version 12.14 (Arnaud 1996) for the spectral analysis. I fitted the spectra of NICER and Swift independently using an absorbed blackbody model (`tbabs*bbodyrad`). I obtained consistent results between spectra from both observatories. As seen in Fig-

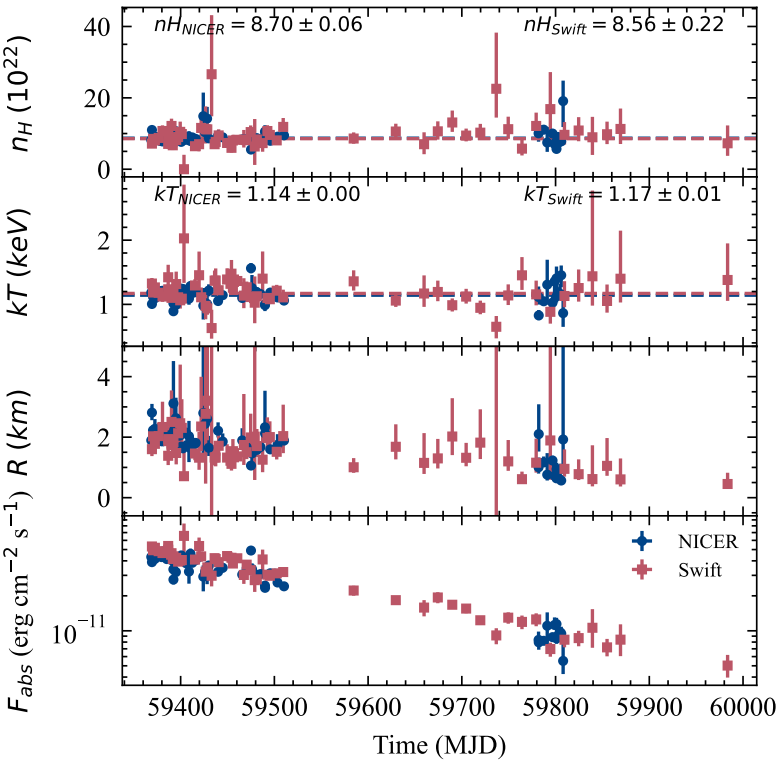

Figure 3.9: Spectral evolution of absorption, temperature, and blackbody emitting radius of Swift J1555.2–5402 derived from individual SWIFT or NICER observations. The bottom panel shows the absorbed flux in the 2–10 keV range.

ure 3.9, the absorption and the temperature of the blackbody are not variable. The error weighted average parameters are hydrogen column density $N_{\rm H} = (8.70 \pm 0.06) \times 10^{22}$ cm^{-2} and blackbody temperature $kT = 1.14 \pm 0.00$ keV for NICER, and $N_{\rm H} = (8.56 \pm 0.22) \times 10^{22}$ cm^{-2} and $kT = 1.17 \pm 0.01$ keV for Swift. However, the normalization factor (and thus the emitting radius) is not well constrained. Therefore, to reduce the errors of the parameters, I selected Swift and NICER observations performed simultaneously, or close to each other, and fitted them together. Some Swift spectra were fitted alone, as no NICER observations were performed in the same period. The derived absorption and temperature values are in agreement with the previous results (see Figure 3.10), yielding $N_{\rm H} = (8.67 \pm 0.05) \times 10^{22}$ cm^{-2} and $kT = (1.15 \pm 0.01)$ keV. When fixing the absorption to the average value, the temperature shows no significant variation (Figure 3.11).

As I observe no variability in the absorption and temperature, as well as any change due to a fixed absorption value, I fitted the spectra, fixing both absorption and temperature. The result is shown in Figure 3.12, where the top panel shows a decrease of the emitting radius from 2.15 ± 0.03 km to 0.33 ± 0.01 km (assuming a distance of 10 kpc), and the bottom panel shows a flux decrease from $(51.0 \pm 0.9) \times 10^{-12}$ erg cm$^{-2}s^{-1}$ to $(1.2 \pm 0.1) \times 10^{-12}$ erg cm$^{-2}s^{-1}$ in the 2–10 keV.

Additionally, to estimate the flux in the last SWIFT observations when the source was fainter, I obtained the count rates using the source detection in the XRT product builder. These were converted to fluxes using the energy conversion factor that I derived with `w3pimms` for the average spectral model.

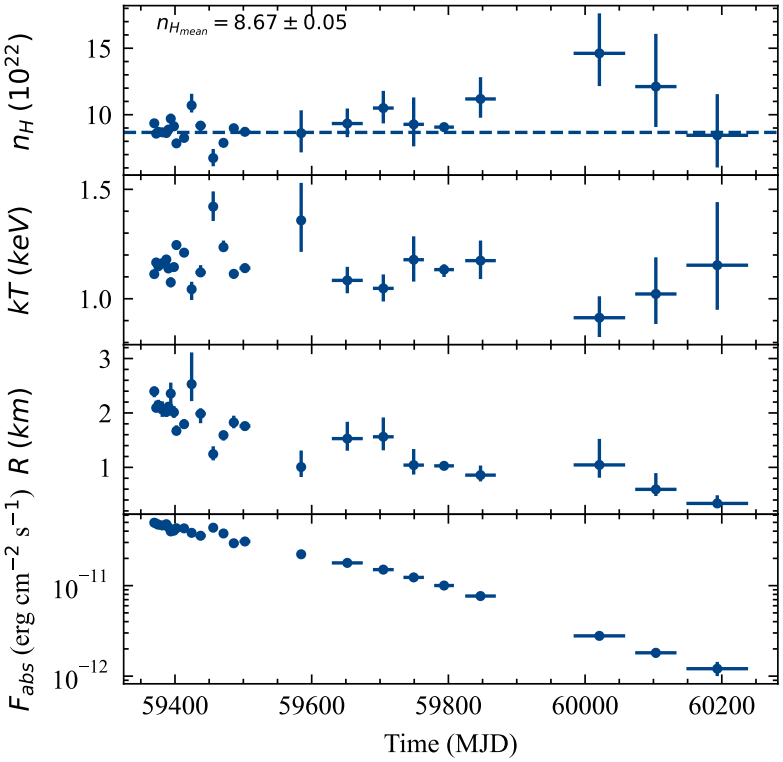

Figure 3.10: Spectral evolution of absorption, temperature, and radius of Swift J1555.2–5402 using grouped SWIFT and NICER observations. The bottom panel shows the 2–10 keV absorbed flux.

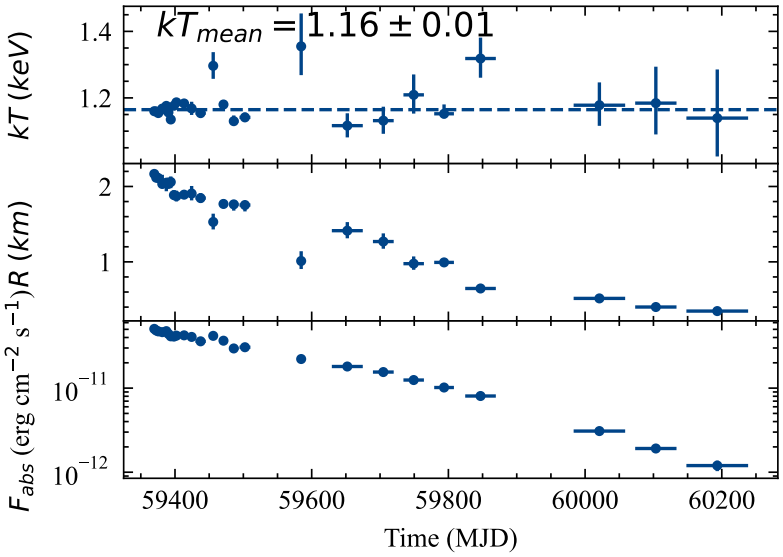

Figure 3.11: Spectral evolution of temperature, and blackbody emitting radius of Swift J1555.2–5402 using grouped SWIFT and NICER observations with a fixed absorption. The bottom panel is absorbed flux in 2–10 keV.

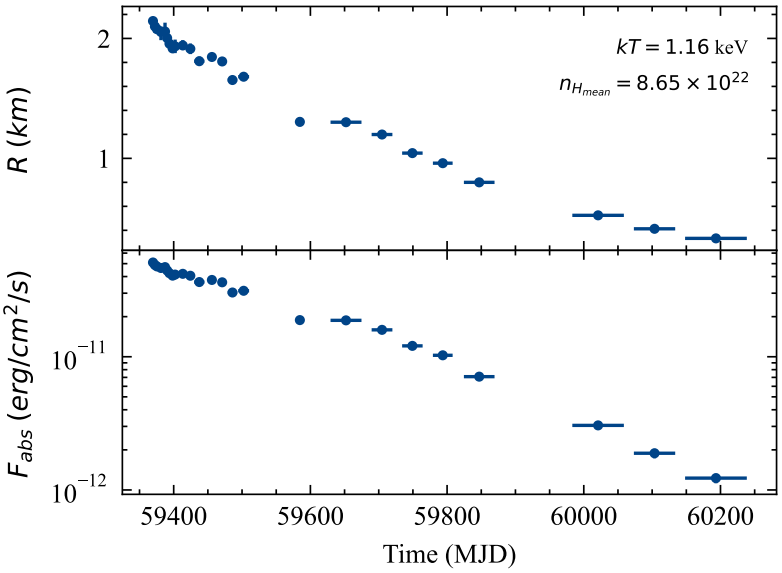

Figure 3.12: Evolution of the blackbody radius assuming a distance of 10 kpc using grouped SWIFT and NICER observations with a fixed absorption and temperature. The bottom panel gives the absorbed flux in the 2–10 keV range.

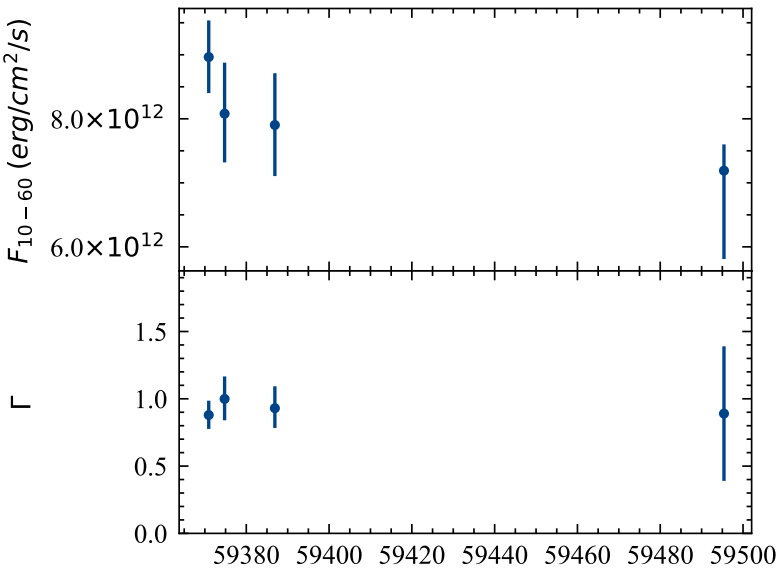

Figure 3.13: Evolution of the Swift J1555.2–5402 spectrum from NuSTAR observations. The upper panel shows the flux in 10–60 keV from the power-law component and the bottom panel shows the evolution of the photon index.

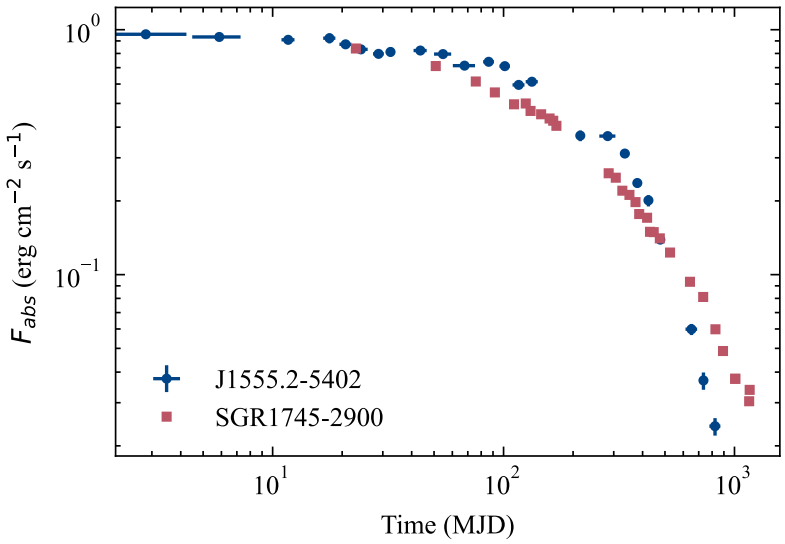

Figure 3.14: Comparison of Swift J1555.2–5402 outburst with that of SGR 1745-2900 (from the MOOC). Fluxes are normalised to 1 at the beginning of the outburst.

3.5.1 Discussion and conclusions

Swift J1555.2–5402 showed an exceptional flux evolution during the outburst. During the first month of the outburst, the source maintained a nearly constant soft X-ray flux at the level of $\sim 4 \times 10^{-11}$ erg cm^{-2} s^{-1} in the 2–10 keV band. Only then was the steep decline of the flux observed, reaching a value of $\sim 9 \times 10^{-13}$ erg cm^{-2} s^{-1} by 2023 October. The hard X-ray emission showed similar behaviour to the soft X-ray counterpart: the flux remained constant at $\sim 10 \times 10^{-12}$ erg cm^{-2} s^{-1} in the first three NuSTAR observations in June, then decreased by about 20% in October, 127 days after the source's discovery (see Figure 3.13). This delayed decay, with flux above 10^{-11} erg cm^{-2} s^{-1} for more than 500 days, is unusual but was observed previously on a less extreme scale in other magnetars such as SGR 1833–0832 and 1E 1048–5937 (Coti Zelati et al. 2018).

A comparison of the Swift J1555.2–5402 outburst with that of SGR J1745–2900, which showed similar outburst evolution, is shown in Fig 3.14.

The spectrum was well fitted by an absorbed blackbody (below 10 keV) plus a power law (above 10 keV, using NuSTAR data). Over the whole outburst, the blackbody temperature remained constant at kT$\sim$ 1.2 keV, while the hotspot radius decreased from $\sim$ 2.1 km to $\sim$ 0.3 km (assuming a distance of 10 kpc). This indicates a persistent, hot, but contracting region on the neutron star surface with sustained heating, possibly by magnetospheric currents (Beloborodov 2009), rather than cooling of the entire crust.

Such constant-temperature behaviour has been observed in only a few other magnetar outbursts, such as CXOU J164710–455216, Swift J1818.0–1607, and SGR J1830–0645. While the former kept a temperature of $\sim$ 0.7 keV for almost a year (Borghese et al. 2019), the two latter ones had higher temperatures of above 1 keV. Specifically, Swift J1818.0–1607 kept a temperature of 1.1 keV while the flux decreased by about 60% over $\sim$100 days, only with a marginal radius decrease (Hu et al. 2020). The SGR J1830–0645 spectrum was composed, in contrast, of two blackbody components with kT$_1 \sim$ 0.5 keV

and $kT_2 \sim 1.2$ keV that remained steady for over 220 days of the outburst (Younes et al. 2022).

The prolonged plateau phase suggests that heat was continuously injected into the crust for an extended period, either from a sustained dissipation mechanism or from multiple shorter heating episodes (Pons & Rea 2012). Crustal cooling model (De Grandis et al. 2025) require heat injection for a time comparable to the plateau duration itself (specifically, ∼400 days) to reproduce the observed behaviour. Magnetospheric currents from a slowly dissipating twisted magnetic bundle could provide such sustained heating (Beloborodov 2009; Beloborodov & Li 2016). If the twist is long lasting or periodically replenished, this could account for the observed prolonged brightness plateau. As the twist dissipates, the heated surface area should decrease, consistent with the observed shrinking of the emitting region.

Chapter 4

A systematic search for magnetar bursts

One of the most characteristic features of magnetars is the emission of short bursts of hard X-rays, which are typically less than one second long and have peak luminosities of $10^{38} - 10^{41}$ erg s^{-1}. They can be observed as isolated events during periods of low source activity or during active periods, when tens or hundreds of bursts are observed within a few days. In this chapter, I present results of the search for bursts from all known magnetars using ISGRI data. In total, 1349 bursts were detected from 21 sources, with the majority of them from 1E 1547.0–5408, SGR 1806–20, and SGR 1935+2154. The following sections describe the data selection, analysis methods, and the timing and spectral properties of the bursts. The results of this part of this thesis have been included in the paper *INTEGRAL IBIS catalog of magnetar bursts*, by Pacholski, Mereghetti, and Topinka on ApJ, in press.

4.1 Data selection and analysis

I considered the 34 sources listed in Table 4.1. Besides the confirmed magnetars, this sample also includes the two rotation-powered pulsars that exhibited magnetar-like emission, PSR J1119-6127 (Archibald et al. 2016; Göğüş et al. 2016) and PSR J1846-0258 (Gavriil et al. 2008; Blumer et al. 2021; Sathyaprakash et al. 2024). For each of the considered sources, I applied the procedure described in Section 2.2 to all the public ISGRI ScW centered within 14.5° from the source position. This selection resulted in a total of about 1136 Ms of data, spanning from March 2003 to October 2023. Only ISGRI data was used, as bursts have soft spectrum, and thus the majority of counts are observed below 100 keV.

4.1.1 Timing analysis

Bayesian blocks

The timing characterisation of the bursts was performed using the Bayesian Blocks (BB) method (Scargle 1998; Scargle et al. 2013), in particular to estimate their duration and

to define the time intervals for the spectral analysis. This nonparametric technique characterises intensity variations from an unbinned list of event arrival times by dividing the data into blocks, each of which shows no statistically significant variations in count rate, ensuring that each block is statistically consistent with a period of stable intensity. Only statistically significant changing points are introduced to separate the blocks, based on a parameter, p0, that represents the false-positive probability threshold used to determine the change points in the data. I used the Astropy implementation of the algorithm (Astropy Collaboration et al. 2013, 2018, 2022), setting p0 = 5%.

The list of events in a time interval $[t_0 - 15s, t_0 + 15s]$ from the trigger time is given in input to the BB algorithm. This produces a list of N blocks that represents the best estimate of the light curve and I use it to assess the burst duration.

In order to do this, it is first necessary to decide which blocks belong to the burst and which ones to the background. The first step involved selecting blocks whose durations exceeded the 15th percentile of all block durations and whose count rates were not higher than one standard deviation above the mean. Blocks with count rates above this background level and falling within a conservative 3-second window centred on the trigger time were initially classified as part of the burst.

In the second step, all blocks initially classified as part of the burst, along with adjacent background blocks immediately preceding or following them, were re-examined. This step took into account both the count rate and duration of each block. Specifically, longer blocks were required to have a higher count rate to be classified as part of the burst. Shorter blocks, however, could still be included as part of the burst even if their count rates were below the estimated background level. This method allowed for the inclusion of short, low-intensity blocks, which were necessary to account for the wide variety of burst morphologies.

The block selection criteria were determined through multiple tests on a subsample of bursts from SGR 1935+2154, ensuring accurate burst duration estimates. However, a wide range of possible burst shapes could still lead to incorrect block assignments. Therefore, each burst was visually examined to verify the accuracy of the assignments.

$\mathbf{T_{90}}$

T_{90} is a commonly used quantity to describe the duration of a burst. It is defined as the duration of the time interval containing 90% of the burst fluence. In practice, it is computed from the integral distribution of burst counts, setting T_{start} and T_{stop} at times corresponding to 5% and 95% of the counts, respectively. My calculation of T_{90} was based on the previously obtained Bayesian Blocks and the cumulative sum of the counts.

The background was estimated using two time intervals: one before and one after each burst. For both intervals, I selected the longest Bayesian Block. The counts within these blocks were accumulated and fitted with a linear function. The background levels before and after the burst were then compared and averaged.

First, I estimated the 0% and 100% levels, for which I used a step function with an additional linear component to take into account the rest of the background that had

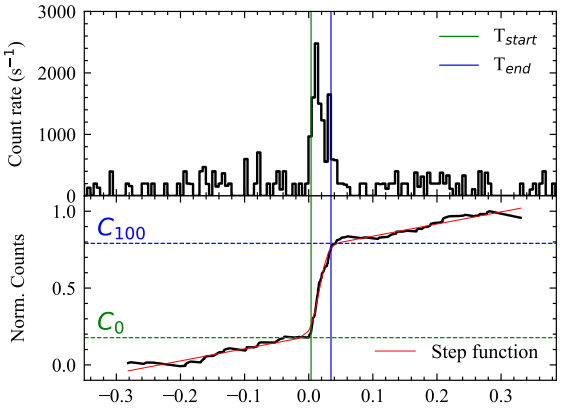

Figure 4.1: Top panel: Light curve of the burst with 5 ms binning. Bottom panel: Normalized cumulative counts (background subtracted) of the burst, with the fitted step function overlaid. The 0% and 100% levels are marked, along with the corresponding times used to calculate T_{90}, defined as the interval between the 5% and 95% levels of the burst counts.

not been removed (Gavriil et al. 2004). The function was defined as:

$$f(t, t_0, y_0, h, a, b) = y_0 + \frac{h}{2}\,\mathrm{erf}((t - t_0)a) + bt, \tag{4.1}$$

where $\mathrm{erf}(z) = \frac{2}{\sqrt{\pi}} \int_0^z e^{-t^2}\, dt$ is the error function, h and a are scaling factors, y_0 is the baseline level, and b accounts for the residual background contribution. Figure 4.1 shows an example burst, with the fitted step function and background subtracted normalised cumulative counts. The times corresponding to the levels 5% and 95% are indicated, defining the interval used to calculate T_{90}.

However, this method has its own limitations, particularly when dealing with very faint bursts or certain burst shapes, which may prevent a correct fit of the function, usually causing unnaturally large T_{90}. Thus, each burst light curve was manually inspected and was not included in the following statistical analysis in case of incorrect estimation. No alternative T_{90} estimation methods were applied to the problematic cases, to maintain consistency throughout the analysis.

4.2 Telemetry saturation

In the case of bright events, especially during periods of high background, IBIS can suffer telemetry saturation. When this occurs, the information on the detected events is not transmitted to ground, resulting in gaps in the light curves, typically on timescales shorter than a second. In the sample of detected bursts, 36 suffered in various degrees of the saturation problem.

I used BBs to find time gaps due to telemetry saturation, as they were effective in marking the boundaries of saturation periods. I estimated the count rates in the two BBs adjacent to the gap and interpolated them to the saturated period. Since the T_{90} estimate was performed on unbinned data, I estimated the required number of counts

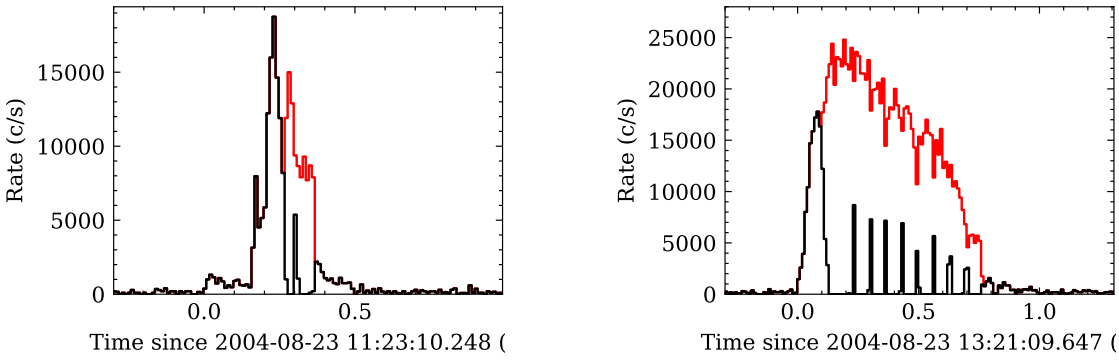

Figure 4.2: Example of two saturated bursts. The black line shows the original light curve in 10 ms bins, while the red line shows the light curve after correcting for telemetry saturation. During saturation, some 10 ms bins include intervals where no data were recorded, causing the average count rate in those bins to appear artificially low. After correction, the true count rate during the saturated periods is recovered, resulting in much higher rates in the affected intervals.

and injected them uniformly across the saturated period. With this corrected event list, I repeated the T_{90} calculation and the counts estimation. The bursts for which I applied this correction are marked as saturated, and the quantities derived from their number of counts (e.g. the fluence and average flux) should be considered as lower limits. Two examples of the corrections (in red) applied to saturated bursts are shown in Fig. 4.2.

4.2.1 Spectral analysis

I performed a spectral analysis for bursts with at least 100 observed counts in the 20–150 keV range, for bursts before January 2015, or in the 40–150 keV range after this date. For the spectral analysis, I used the pyXspec (Gordon & Arnaud 2021) version 2.1.4 with the Xspec version 12.14.1 (Arnaud 1996). Burst spectra were extracted using the standard pipeline with OSA 11.2 (Goldwurm et al. 2003) using custom-defined Good Time Intervals (GTI) that were based on the T_{BB} durations of the bursts. If a burst was affected by telemetry saturation, the saturated periods were excluded from the GTIs. The energy range E_{min}–E_{max} used for the spectral analysis depended on the date of the burst, in order to take into account the evolution of the lower energy threshold (See Section 2.1.3). I used E_{min} values between 20 and 32 keV, depending on the observation date, and E_{max} = 300 keV. The energy range was divided in 16 or in 13 logarithmic channels.

The spectra were rebinned to obtain a minimum of 20 counts in each bin, and 5% systematic errors were added to the data. I considered two models, a simple power law and a power law with exponential cut-off (often called Comptonized model in the literature), defined as follows:

- power law (PL): $F(E) = kE^{\alpha}$ ph cm^{-2} s^{-1} keV^{-1},
- cut-off power law (CPL): $F(E) = kE^{\alpha}\exp(-(E(2+\alpha)/E_{peak}))$ ph cm^{-2} s^{-1} keV^{-1}.

For the bursts with the highest number of counts I performed also a time-resolved

analysis by extracting spectra from different time intervals (15 from SGR 1935+2154 and 6 from SGR 1806–20). The analysis was done as described above, using the 20–300 keV and 32–300 keV energy ranges, for SGR 1806–20 and SGR 1935+2154, respectively, divided in 13 energy bins.

The selection of the burst segments was based on the Bayesian Blocks; however, in some cases, the segmentation was done manually only based on the visual inspection of the light curve and Bayesian block structure. If the block contained sufficient counts, it was divided into segments of approximately equal duration; conversely, adjacent blocks were merged when individual segments lacked sufficient statistics.

4.3 Results

1349 magnetar bursts were confirmed among more than 75,000 potential triggers found in the light curves search. A summary of the number of bursts and analysed exposure time for each source is provided in Table 4.1. The largest number of bursts originated from SGR 1806–20 (Table 4.3), followed by SGR 1935+2154 (Table 4.4), and 1E 1547.0–5408 (Table 4.2). Additionally, 37 bursts were detected from 18 other magnetars (Table 4.5). These tables gives the unique number identifier for each burst, the timing information (see below), the coding fraction (COD), and the fluences in counts (background-subtracted and corrected for the coding fraction). The time distributions of the bursts from these three sources and the analysed exposure time are shown in Fig 4.3.

4.3.1 Burst durations

The derived durations of all the bursts are given in Tables 4.2, 4.3, 4.4 and 4.5. The distributions of T_{BB} and T_{90} for 1E 1547.0–5408, SGR 1806–20, and SGR 1935+2154 are shown in the top panels of Fig. 4.4. The bottom panels of the same figure show the duration T_{BB} as a function of the number of counts. The distributions of both T_{BB} and T_{90} are well fit with log-normal curves as also confirmed using the Kolmogorov-Smirnov test. Two particularly long bursts emitted by SGR 1806–20 on 2004 October 5 (n.387 and n.414) have been excluded from this analysis, because they were affected by telemetry saturation and most likely involved the superposition of several bursts. They have been analysed in detail by Götz et al. (2006) using ACS. The average durations and the best fit parameters of the lognormal fits (mean μ and standard deviation σ) for the three sources and for the whole sample are given in Table 4.6.

T_{90} was estimated for 691 bursts and, similarly to T_{BB}, follows a log-normal distribution, as shown in Fig. 4.4. Note that T_{90} could not be reliably measured for the fainter bursts, therefore a direct comparison between the average T_{90} and T_{BB} is not straightforward because they refer to different samples. As it is shown in Fig. 4.4, T_{BB} is generally longer than T_{90}.

Table 4.1: List of the magnetars with coordinates, exposure time and number of found bursts.

Source	RA (J2000)	DEC (J2000)	Exposure (Ms)	NoBursts
CXO 0100–7211	01:00:43.1	-72:11:33.8	7.96	1
4U 0142+614	01:46:22.4	61:45:03.2	21.35	0
SGR 0418+5729	04:18:33.9	57:32:22.9	8.90	0
4XMM J045626.3–694723	04:56:26.4	-69:47:23.1	14.15	0
SGR 0501+4516	05:01:06.7	45:16:33.9	9.21	8
SGR 0525–66	05:26:00.9	-66:04:36.3	11.94	2
SGR 0755–2933	07:55:42.5	-29:33:49.2	9.55	0
1E 1048–5937	10:50:07.1	-59:53:21.4	23.75	2
PSR J1119–6127	11:19:14.3	-61:27:49.3	25.13	1
1E 1547.0–5408	15:50:54.1	-54:18:24.1	27.09	146
Swift J1555.2–5402	15:55:08.7	-54:03:41.1	27.43	0
PSR J1622–4950	16:22:44.9	-49:50:52.7	28.55	0
SGR 1627–41	16:35:51.8	-47:35:23.3	29.04	2
CXOU J164710–455216	16:47:10.2	-45:52:16.9	31.60	3
1RXS J170849–400910	17:08:46.9	-40:08:52.4	61.82	2
CXOU J171405–381031	17:14:05.7	-38:10:30.9	66.88	1
SGR J1745–2900	17:45:40.2	-29:00:29.8	67.93	0
SGR 1801–23	18:00:58.9	-22:56:48.5	67.04	2
SGR 1806–20	18:08:39.3	-20:24:39.9	65.23	934
XTE J1810–197	18:09:51.1	-19:43:51.9	64.44	3
Swift J1818.0–1607	18:18:03.7	-16:07:31.8	52.89	1
AX J1818.8–1559	18:18:51.4	-15:59:22.6	52.12	1
Swift J1822.3–1606	18:22:18.0	-16:04:26.8	52.20	1
SGR J1830–0645	18:30:41.6	-06:45:16.9	25.28	0
SGR 1833–0832	18:33:44.4	-08:31:07.5	25.50	3
Swift J1834.9–0846	18:34:52.1	-08:45:56.0	25.62	0
1E 1841–045	18:41:19.3	-04:56:11.2	28.21	1
AX J1845.0–0258	18:44:54.7	-02:56:53.1	30.51	0
PSR J1846–0258	18:46:24.9	-02:58:30.1	30.57	2
3XMM J185246.6+003317	18:52:46.7	00:33:17.8	31.18	0
SGR 1900+14	19:07:14.3	09:19:20.1	27.57	1
SGR 1935+2154	19:34:55.6	21:53:48.0	32.90	232
SGR 2013+34	20:13:56.9	34:19:48.0	27.98	0
1E 2259+586	23:01:08.3	58:52:44.5	25.24	0

Table 4.2: Bursts from 1E 1547.0–5408.

No	T_{start} (UTC)	T_{BB} (ms)	T_{90} (ms)	COD	CTS[a]	CTS[b]	CTS[c]
0	2003-03-14 00:09:42.553	68.0	—	0.74	1.7	39.0	16.5
934	2008-10-09 07:24:59.094	16.4	—	0.97	40.5	31.3	0.0
935	2009-01-24 15:41:14.098	85.3	—	0.89	37.9	30.6	2.3
936	2009-01-24 15:48:32.241	280.5	—	0.89	179.1	86.4	15.4
937	2009-01-24 16:28:28.556	278.1	—	1.00	31.7	35.0	5.0
938	2009-01-24 16:28:31.640	1665.5	—	1.00	148.0	116.8	26.6
939	2009-01-24 16:48:19.454	50.3	—	0.98	39.0	63.8	7.4
940	2009-01-24 18:44:30.202	232.7	—	1.00	46.2	71.1	1.5
941	2009-01-24 22:29:42.471	124.3	109.7	1.00	88.5	137.7	23.8
942	2009-01-24 22:39:38.976	9.8	—	1.00	8.9	12.4	3.7

Table 4.2 is included in the full form in the Appendix as Table A.1. A portion is shown here as an example regarding its form and content.
[a] Counts in 20–40 keV
[b] Counts in 40–100 keV
[c] Counts in 100–150 keV

Table 4.3: Bursts from SGR 1806–20.

No	T_{start} (UTC)	T_{BB} (ms)	T_{90} (ms)	COD	CTS[a]	CTS[b]	CTS[c]
5	2003-08-23 17:32:11.718	216.1	121.8	0.73	104.0	190.8	29.8
6	2003-08-23 22:05:01.450	129.5	91.3	0.40	171.2	138.1	4.8
7	2003-08-23 22:05:01.776	87.6	—	0.40	85.5	97.6	10.1
8	2003-08-24 15:01:11.846	213.0	189.9	0.86	48.4	55.7	11.8
9	2003-08-24 15:30:44.152	254.8	177.2	0.86	240.0	172.6	19.8
10	2003-08-24 15:57:14.658	123.8	—	0.96	30.3	44.4	0.2
11	2003-08-24 16:33:24.855	293.2	112.4	0.96	42.6	52.0	17.6
12	2003-08-24 17:50:20.050	224.4	159.7	0.97	292.8	196.4	11.1
13	2003-08-24 17:56:31.863	201.2	—	0.78	43.5	64.8	1.4
14	2003-08-24 19:03:48.664	101.7	87.2	0.78	129.4	93.7	2.7

Table 4.3 is included in the full form in the Appendix as Table A.2. A portion is shown here as an example regarding its form and content.
[a] Counts in 20–40 keV
[b] Counts in 40–100 keV
[c] Counts in 100–150 keV

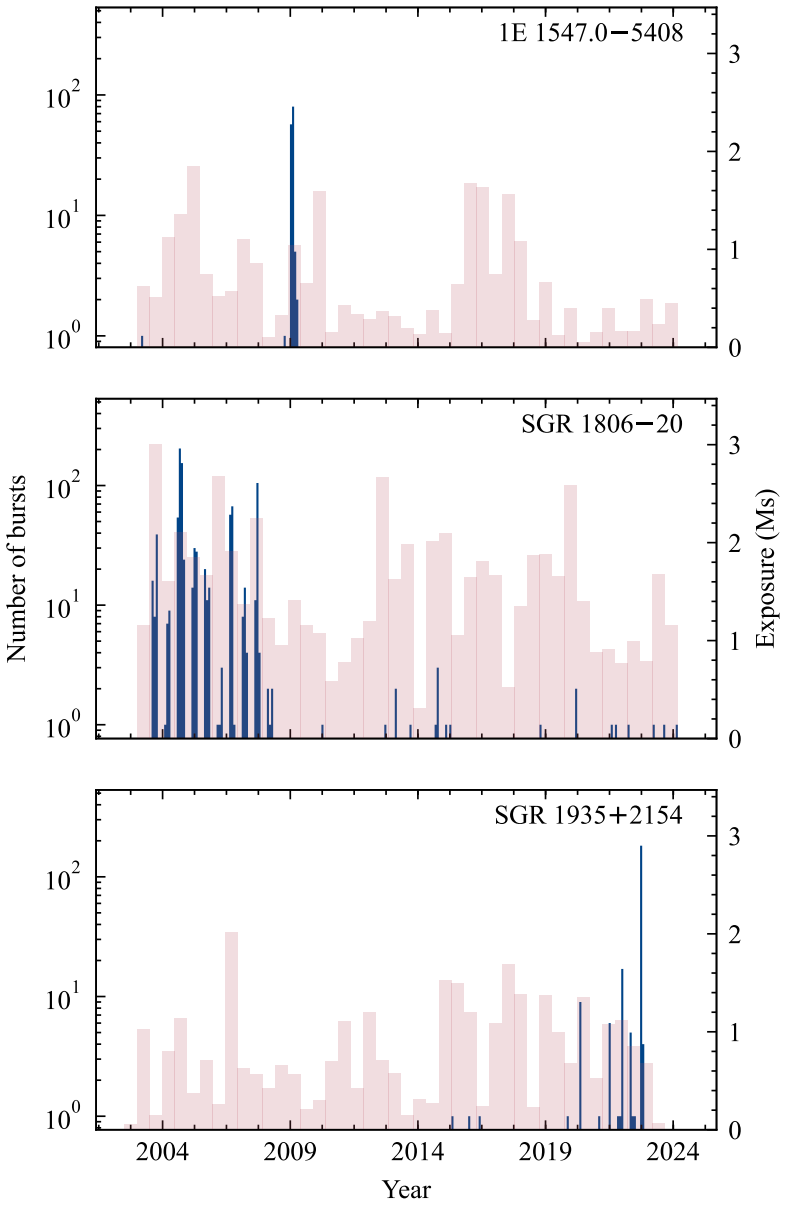

Figure 4.3: Time distribution of the bursts (blue histogram) and exposure time (red histogram) of 1E 1547.0–5408 (top), SGR 1806–20 (middle), and SGR 1935+2154 (bottom). The bursts are in bins of 30 days, while the exposure is for bins of 180 days.

4.3.2 Burst spectra

In total, 535 bursts had enough counts for spectral analysis. The results of the spectral fits for each burst are listed in Tables 4.7, 4.8, and 4.9 for 1E 1547.0–5408, SGR 1806–20, and SGR 1935+2154. The power law model provided an acceptable fit for 313 bursts, while a CPL was required in 114 cases. The other bursts could not be well fitted with either model (due to saturation problems or because the fit parameters were completely unconstrained). For 54 of the bursts adequately fit by a PL, the addition of a cut-off provided a statistically significant improvement, as determined by an F-test with a p-value below 0.15. Thus, in summary, I have a sample of 168 bursts for which α and E_{peak} could be derived, although for some of them (30), the peak energy E_{peak} was poorly

Table 4.4: Bursts from SGR 1935+2154.

No	T_{start} (UTC)	T_{BB} (ms)	T_{90} (ms)	COD	CTS[a]	CTS[b]	CTS[c]
1100	2015-05-11 01:31:20.484	630.3	—	0.71	—	24.1	43.2
1101	2015-12-21 02:51:12.494	85.4	38.1	0.78	—	347.8	28.6
1102	2016-05-30 00:46:25.402	273.7	156.4	0.20	—	336.8	63.2
1109	2019-11-14 00:30:46.498	50.2	—	0.27	—	63.5	14.5
1112	2020-04-28 03:47:52.135	47.0	27.4	0.11	—	203.0	34.2
1113	2020-04-28 04:09:47.290	73.3	42.6	0.11	—	230.9	43.8
1114	2020-04-28 05:56:30.451	114.8	37.2	0.29	—	268.0	70.2
1115	2020-04-28 06:07:46.818	156.6	—	0.29	—	205.8	41.6
1116	2020-04-28 08:03:34.210	116.4	84.4	0.15	—	87.0	7.8
1117	2020-04-28 09:51:04.730	371.4	174.5	0.48	—	192.3	25.0
1118	2020-04-28 14:34:24.002	728.1	205.8	0.72	—	1302.9	533.3

Table 4.4 is included in the full form in the Appendix as Table A.3. A portion is shown here as an example regarding its form and content.
[a] Counts in 20–40 keV
[b] Counts in 40–100 keV
[c] Counts in 100–150 keV

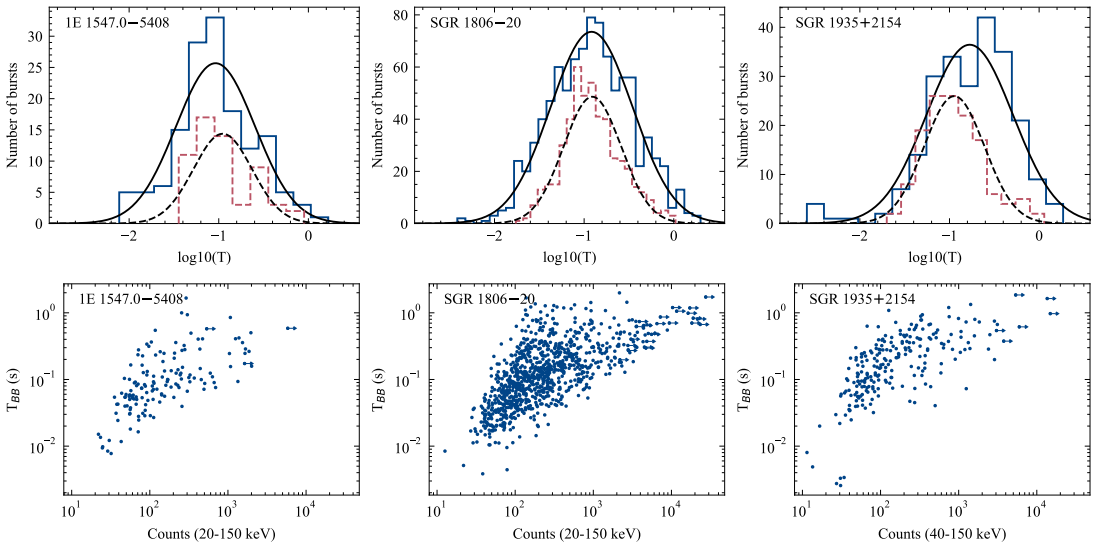

Figure 4.4: Top panels: Distributions of the burst durations T_{BB} for 1E 1547.0–5408 (left), SGR 1806–20 (middle), and SGR 1935+2154 (right). Solid lines refer to T_{BB} and dashed lines to T_{90}. Bottom panels: T_{BB} duration as a function of the number of counts for the same three magnetars.

constrained (the lower bound of its confidence interval was below 10 keV).

I computed the error-weighted average values of the best fit spectral parameters. The average values of the CPL model were then used to estimate Energy Conversion Factors (ECFs) from the count rates ($20-150$ keV and $40-150$ keV) to the $30-150$ keV flux in physical units. The average spectral parameters and the ECFs are listed in Table 4.10. The relation between α and E_{peak} is plotted in the top panels of Fig. 4.6, while the bottom panels show how the spectral parameters depend on the burst fluence.

These figures show evidence for some correlations between the parameters. To quantify this taking into account the measurement errors, I computed the Spearman's rank

Table 4.5: Bursts of magnetars not included in the previous tables.

No	Source	T_{start} (UTC)	T_{BB} (ms)	T_{90} (ms)	COD	CTS[a]	CTS[b]	CTS[c]
1	SGR 1627-41	2003-03-25 02:45:59.024	111.7	—	1.00	0.0	27.0	19.7
2	1RXS J1708-40	2003-03-26 05:48:55.080	121.9	—	0.98	4.3	33.3	18.3
3	SGR 1833-0832	2003-04-26 11:34:19.751	532.9	—	0.67	26.8	50.6	9.1
4	1E 1048-5937	2003-07-04 01:53:56.652	2303.3	142.3	1.00	33.5	70.8	18.2
69	1RXS J1708-40	2004-02-23 05:54:01.936	352.6	—	0.66	11.7	45.3	16.1
86	SGR 1627-41	2004-08-12 05:10:48.867	563.3	—	1.00	21.7	47.0	8.8
642	SGR 1900+14	2006-04-02 17:48:24.812	12.6	—	1.00	23.1	21.7	0.0
643	Swift J1822-16	2006-04-21 18:07:58.972	359.7	—	0.80	11.4	45.8	11.7
779	CXOU J1714-381	2007-03-05 19:51:06.905	91.8	—	0.46	1.3	43.4	7.7
909	XTE J1810-197	2007-09-30 19:53:21.119	598.2	—	1.00	23.7	40.6	14.0
917	AX J1818.8-1559	2007-10-17 00:58:08.596	111.3	—	0.71	205.7	89.4	7.9
926	SGR 0501+4516	2008-08-27 10:37:13.874	37.1	—	1.00	19.2	17.6	0.0
927	SGR 0501+4516	2008-08-27 14:08:25.210	47.2	—	0.96	38.1	24.1	3.9
928	SGR 0501+4516	2008-08-27 16:25:13.411	17.5	—	1.00	14.3	19.5	1.6
929	SGR 0501+4516	2008-08-27 22:25:57.677	98.4	—	1.00	47.9	29.2	9.9
930	SGR 0501+4516	2008-08-27 22:29:30.079	64.1	—	1.00	22.4	41.4	2.1
931	SGR 0501+4516	2008-08-28 03:32:28.353	193.4	176.9	1.00	167.4	100.5	3.4
932	SGR 0501+4516	2008-08-28 20:59:41.898	46.7	—	0.89	75.3	55.3	11.2
933	SGR 0501+4516	2008-09-05 10:40:11.183	61.7	42.5	1.00	47.8	58.6	3.4
1079	PSR J1846-0258	2009-08-30 05:47:28.421	35.7	29.9	0.97	25.8	28.5	9.4
1080	SGR 1833-0832	2010-03-19 18:34:50.885	15.8	—	1.00	28.0	32.0	3.1
1082	SGR 0525-66	2011-04-07 22:38:31.212	385.9	—	0.73	29.0	19.8	29.7
1083	1E 1841-045	2011-04-24 06:51:41.781	7.3	—	0.26	38.2	48.7	0.0
1084	SGR 0525-66	2011-07-08 07:46:39.110	268.8	—	1.00	11.0	24.0	17.9
1085	SGR 1801-23	2012-09-19 05:13:56.529	127.0	—	1.00	9.2	23.1	9.7
1091	SGR 1833-0832	2014-09-27 16:18:02.334	3411.1	2082.5	0.77	54.0	76.6	40.8
1093	SGR 1801-23	2014-09-28 14:59:06.815	788.6	—	0.67	34.4	51.5	26.3
1094	XTE J1810-197	2014-10-13 22:36:31.026	345.8	—	0.77	16.5	30.4	9.8
1097	CXO 0100-7211	2014-10-29 22:15:48.274	899.3	—	1.00	22.8	37.0	14.8
1103	PSR J1119-6127	2016-11-12 21:28:56.307	10.8	—	0.60	—	33.5	1.6
1104	CXOU J1647-45	2018-02-06 00:33:19.122	25.7	21.8	0.84	—	64.2	12.9
1105	CXOU J1647-45	2018-02-06 07:25:56.408	25.2	19.1	1.00	—	102.6	7.2
1106	CXOU J1647-45	2018-02-06 12:33:34.121	151.6	116.2	1.00	—	134.9	29.0
1107	1E 1048-5937	2018-06-11 07:16:44.721	282.5	—	0.81	—	29.5	19.8
1121	PSR J1846-0258	2020-05-05 07:05:53.836	267.2	220.9	1.00	—	29.3	17.4
1151	Swift J1818-16	2022-04-17 17:59:22.174	643.1	293.5	0.74	—	38.3	39.0
1346	XTE J1810-197	2023-08-31 02:00:26.963	190.0	179.6	0.85	—	36.9	9.7

[a] Counts in 20–40 keV
[b] Counts in 40–100 keV
[c] Counts in 100–150 keV

correlation coefficient ρ with a Monte Carlo approach that combines bootstrap resampling with perturbations (Curran 2014) drawn from the split-normal error distributions for each data point. I found a very significant anti-correlation between E_{peak} and fluence for SGR 1806–20, with a mean $\rho = -0.48 \pm 0.07$ and a mean z-score of 7.1 ± 1.0 from 100,000 Monte Carlo tests. For this source, there is also marginal evidence for a correlation between α and E_{peak} ($\rho = -0.31 \pm 0.09$, z-score$=3.4 \pm 1.1$). These correlations are less significant for the other two magnetars (see the ρ and z-score values in Table 4.12).

I performed time-resolved spectral analysis for 21 bursts (15 from SGR 1935+2154 and 6 from SGR 1806–20).

First I fitted the spectra with the power law model and no significant spectral evolution was observed in the photon index. In several bursts, the spectra corresponding to

Table 4.6: Properties of the burst durations.

Source		Average (ms)	10^{μ} (ms)	σ
1E 1547.0–5408	T_{BB}	157.3	92.5 ± 7.8	0.44 ± 0.03
	T_{90}	154.4	110.2 ± 10.6	0.32 ± 0.03
SGR 1806–20	T_{BB}	206.6	120.7 ± 4.2	0.46 ± 0.01
	T_{90}	165.9	123.4 ± 4.2	0.32 ± 0.01
SGR 1935+2154	T_{BB}	274.0	168.5 ± 12.3	0.48 ± 0.02
	T_{90}	159.1	113.1 ± 7.5	0.33 ± 0.02

μ and σ are the mean and standard deviation of lognormal fits to the distributions of durations.

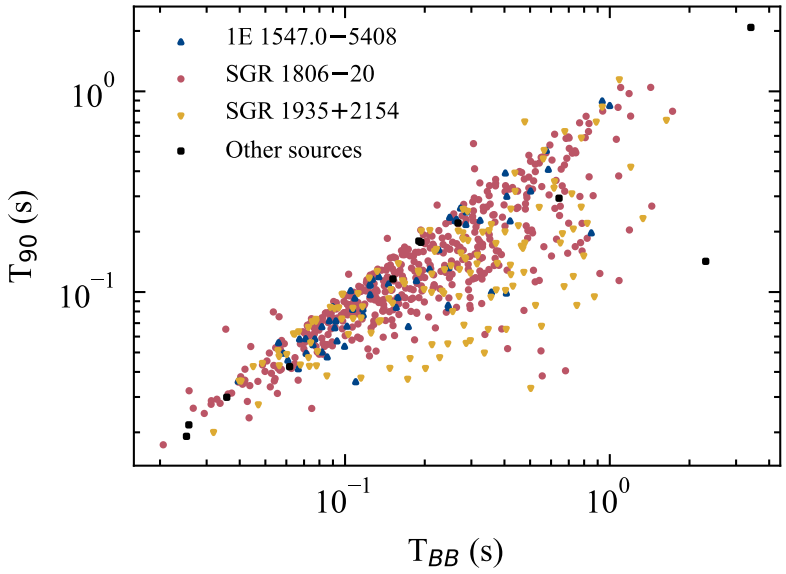

Figure 4.5: T_{90} versus T_{BB} of all the bursts for which T_{90} could be estimated.

Table 4.7: Results of the timed-averaged spectral analysis of the bursts from 1E 1547.0–5408.

	Power law			Cutoff power law			
No	α	χ^2_r(dof)	Flux	α	E_{peak}	χ^2_r(dof)	Flux
937	-2.3 ± 0.2	1.7(7)	1.2 ± 0.2	—	—	—	—
939	-2.4 ± 0.3	0.5(6)	0.3 ± 0.1	—	—	—	—
942	-1.6 ± 0.2	1.5(7)	$2.6^{+0.3}_{-0.4}$	$0.4^{+1.9}_{-0.8}$	$67.7^{+14.7}_{-11.6}$	0.7(6)	2.6 ± 0.4
951	-2.3 ± 0.1	0.3(8)	8.3 ± 0.7	$-1.8^{+0.5}_{-0.2}$	< 32.2	0.2(7)	8.2 ± 0.7
955	-1.6 ± 0.3	0.6(7)	0.8 ± 0.2	—	—	—	—
956	—	—	—	$-0.8^{+0.5}_{-0.4}$	$46.6^{+4.2}_{-1.9}$	1.1(8)	$3.8^{+0.2}_{-0.3}$
957	-2.2 ± 0.2	0.5(5)	$7.1^{+1.1}_{-1.3}$	—	—	—	—
958	-1.7 ± 0.2	1.5(7)	2.8 ± 0.4	—	—	—	—
959	—	—	—	$-0.7^{+0.5}_{-0.4}$	$41.2^{+3.3}_{-4.2}$	1.6(8)	5.2 ± 0.3
963	-1.2 ± 0.2	1.1(6)	$2.7^{+0.4}_{-0.5}$	—	—	—	—

Table 4.7 is included in the full form in the Appendix as Table A.4. A portion is shown here as an example regarding its form and content.
Flux is in units of 10^{-7} erg cm^{-2} s^{-1}.
E_{peak} is in units of keV.

the onset and to the tail of the bursts, still classified as part of the bursts by the BB,

Table 4.8: Results of the timed-averaged spectral analysis of the bursts from SGR 1806–20.

	Power law			Cutoff power law			
BurstNo	α	χ^2_r(dof)	Flux	α	E_{peak}	χ^2_r(dof)	Flux
6	-2.2 ± 0.2	1.6(8)	2.9 ± 0.4	$-0.5^{+1.3}_{-1.0}$	$46.3^{+8.6}_{-9.6}$	1.3(7)	$3.0^{+0.4}_{-0.5}$
9	—	—	—	$-0.4^{+1.0}_{-0.9}$	$40.0^{+5.2}_{-8.8}$	1.5(6)	1.6 ± 0.2
14	-2.1 ± 0.3	0.8(6)	3.3 ± 0.6	—	—	—	—
17	-2.1 ± 0.2	0.8(9)	1.6 ± 0.2	—	—	—	—
19	-2.1 ± 0.1	0.8(9)	2.1 ± 0.2	—	—	—	—
28	-2.6 ± 0.1	1.5(8)	4.4 ± 0.4	—	—	—	—
32	—	—	—	$-0.6^{+0.5}_{-0.9}$	$24.9^{+3.2}_{-10.8}$	0.6(8)	12.0 ± 0.8
34	-2.8 ± 0.2	1.4(7)	2.2 ± 0.3	—	—	—	—
35	-2.4 ± 0.2	1.3(7)	1.1 ± 0.2	—	—	—	—
36	$-2.1^{+0.3}_{-0.4}$	0.7(4)	1.3 ± 0.3	—	—	—	—

Table 4.8 is included in full form in the Appendix as Table A.5. A portion is shown here as an example regarding its form and content.
Flux is in units of 10^{-7} erg cm^{-2} s^{-1}.
E_{peak} is in units of keV.

Table 4.9: Results of the timed-averaged spectral analysis of the bursts from SGR 1935+2154.

	Power law			Cutoff power law			
BurstNo	α	χ^2_r(dof)	Flux	α	E_{peak}	χ^2_r(dof)	Flux
1102	-3.1 ± 0.2	0.6(4)	9.6 ± 0.8	—	—	—	—
1119	-2.0 ± 0.1	1.4(8)	6.1 ± 0.3	-1.1 ± 0.5	$66.4^{+11.4}_{-7.7}$	1.1(7)	6.0 ± 0.3
1123	—	—	—	< 6.3	39.8 ± 1.7	1.0(4)	$7.3^{+0.8}_{-0.9}$
1124	—	—	—	< 4.6	44.4 ± 1.6	1.3(5)	$35.3^{+2.8}_{-2.9}$
1126	—	—	—	$-0.1^{+0.9}_{-1.1}$	$31.7^{+4.4}_{-10.5}$	0.8(6)	26.9 ± 1.3
1136	-3.1 ± 0.3	1.6(5)	4.3 ± 0.4	—	—	—	—
1141	-3.7 ± 0.3	0.8(5)	$3.6^{+0.3}_{-0.4}$	—	—	—	—
1146	-3.0 ± 0.3	0.7(5)	$6.3^{+0.7}_{-0.8}$	—	—	—	—
1148	—	—	—	$0.8^{+1.5}_{-0.9}$	$30.4^{+4.8}_{-5.2}$	1.3(5)	17.7 ± 0.7
1159	-2.7 ± 0.3	0.4(5)	4.4 ± 0.5	—	—	—	—

Table 4.9 is included in the full form in the Appendix as Table A.6. A portion is shown here as an example regarding its form and content.
Flux is in units of 10^{-7} erg cm^{-2} s^{-1}.
E_{peak} is in units of keV.

but where the count rate was lower showed possible photon index variations (at 68% c.l.). However, these spectra have a low signal and the derived slopes are still marginally consistent (within the 90% c.l.). I therefore conclude that there is no evidence for time variations of the photon index. In cases when the phase-averaged spectrum was also correctly described by a power law, the slope of the subperiods was consistent with the average one.

Therefore, I then used the cutoff power law model, keeping α tied across all the time intervals of each burst, while E_{peak} and the normalization were allowed to vary independently. In the majority of cases, E_{peak} was found to be consistent within the errors, with a constant value. Only in five cases, I detected a marginally significant variation (p-value < 0.05, for bursts no 193, 1118, 1244, and 1310 and p-value < 0.1 for

Table 4.10: Average spectral parameters and Energy Conversion Factors for the cut off power law model.

Source	α_{PO}	α_{CPL}	E^a_{peak}	ECF^b_{20-150}	ECF^c_{40-150}
1E 1547.0–5408	-1.78 ± 0.03	-0.32 ± 0.11	43.3 ± 0.7	1.1	2.2
SGR 1806–20	-2.42 ± 0.01	-0.60 ± 0.07	32.4 ± 0.4	0.9	2.2
SGR 1935+2154	-2.68 ± 0.03	0.03 ± 0.25	37.7 ± 1.4	—	1.9

[a]keV
[b]from counts in the $20-150$ keV range to 10^{-10} erg cm^{-2} in the $30-150$ keV range.
[c]from counts in the $40-150$ keV range to 10^{-10} erg cm^{-2} in the $30-150$ keV range.

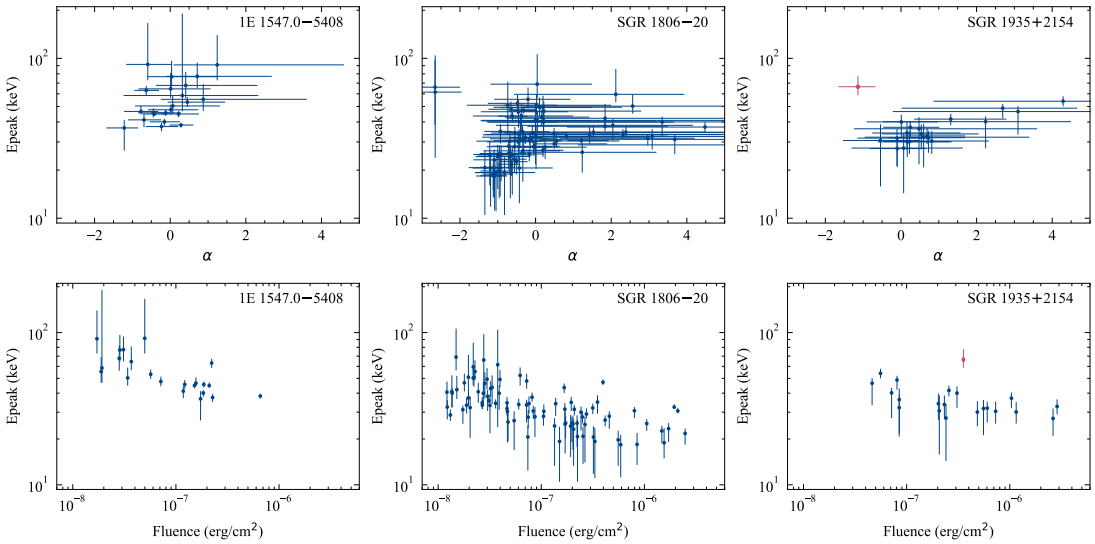

Figure 4.6: E_{peak} versus α (upper panels) and versus fluence (bottom panels) for the spectra fitted by the cut-off power law model. The figure show results for three sources: 1E 1547.0–5408 (left), SGR 1806–20 (middle), and SGR 1935+2154 (right). The fluence refers to the 30–150 keV range.

no 1260). These are shown in Fig. 4.7 and their spectral parameters are given in Table 4.11.

Table 4.11: Parameters of time-resolved spectral analysis of the selected bursts. Segments were simultaneously fitted with tied α.

ID	T_{start}[a] (s)	T_{stop}[a] (s)	α	E_{peak}[b] (keV)	Flux[c] (10^{-7} erg cm^{-2} s^{-1})
193	0.000	0.808	$0.8^{+0.6}_{-0.3}$	$32.4^{+1.5}_{-0.6}$	16.4 ± 0.6
	0.000	0.037	$2.3^{+0.3}_{-0.9}$	$31.5^{+2.7}_{-3.0}$	$7.4^{+1.1}_{-0.9}$
	0.047	0.066	—	$32.6^{+1.3}_{-1.8}$	$29.4^{+2.3}_{-2.2}$
	0.066	0.086	—	$39.6^{+1.4}_{-1.6}$	$37.9^{+2.6}_{-2.4}$
	0.086	0.120	—	$34.0^{+1.2}_{-1.5}$	$33.2^{+2.2}_{-2.1}$
	0.229	0.365	—	$31.9^{+1.8}_{-2.1}$	$19.8^{+2.0}_{-1.8}$
	0.429	0.568	—	$27.5^{+1.5}_{-2.0}$	$12.7^{+1.4}_{-1.3}$
	0.624	0.704	—	$30.3^{+2.3}_{-2.9}$	$9.0^{+1.2}_{-1.1}$
	0.760	0.808	—	$47.8^{+6.7}_{-7.6}$	$1.6^{+0.4}_{-0.3}$

Table 4.11: (continued)

ID	T_{start}[a] (s)	T_{stop}[a] (s)	α	E_{peak}[b] (keV)	Flux[c] (10^{-7} erg cm^{-2} s^{-1})
1118	0.000	0.728	-1.1 ± 0.5	$66.4^{+11.4}_{-7.7}$	6.0 ± 0.3
	0.000	0.192	$-1.1^{+0.4}_{-0.6}$	$21.6^{+4.3}_{-9.3}$	$1.5^{+0.3}_{-0.2}$
	0.192	0.255	—	$56.5^{+12.6}_{-15.9}$	$13.3^{+1.3}_{-1.2}$
	0.255	0.300	—	$70.5^{+12.9}_{-17.2}$	$29.5^{+2.2}_{-2.0}$
	0.300	0.338	—	$84.7^{+19.1}_{-45.6}$	$20.2^{+1.8}_{-1.7}$
	0.338	0.728	—	$114.0^{+40.0}_{-297.7}$	$2.5^{+0.3}_{-0.2}$
1244	0.000	0.616	$0.2^{+1.1}_{-0.7}$	30.1 ± 4.9	12.7 ± 0.4
	0.000	0.198	$0.9^{+0.6}_{-1.0}$	$60.2^{+7.3}_{-8.5}$	$1.8^{+0.3}_{-0.2}$
	0.198	0.262	—	$32.3^{+3.8}_{-4.7}$	$8.3^{+0.9}_{-0.8}$
	0.262	0.292	—	$33.7^{+2.9}_{-3.5}$	$37.9^{+2.4}_{-2.3}$
	0.292	0.322	—	$42.3^{+2.8}_{-3.3}$	$45.1^{+2.8}_{-2.6}$
	0.322	0.352	—	$37.4^{+3.0}_{-3.6}$	$38.3^{+2.4}_{-2.3}$
	0.352	0.382	—	$34.4^{+2.9}_{-3.3}$	$37.8^{+2.3}_{-2.2}$
	0.465	0.616	—	$34.5^{+3.2}_{-4.0}$	$16.9^{+1.3}_{-1.2}$
1260	0.000	1.853	$0.2^{+0.8}_{-0.7}$	$37.1^{+3.3}_{-5.0}$	3.7 ± 0.1
	0.000	0.523	$1.8^{+0.5}_{-0.8}$	$64.5^{+16.2}_{-30.1}$	0.4 ± 0.1
	0.523	1.089	—	$55.0^{+6.2}_{-7.2}$	1.0 ± 0.1
	1.089	1.377	—	$46.8^{+4.6}_{-5.0}$	1.7 ± 0.2
	1.377	1.458	—	$36.1^{+3.1}_{-3.5}$	$5.7^{+0.6}_{-0.5}$
	1.458	1.490	—	$45.2^{+2.0}_{-2.3}$	$48.2^{+2.6}_{-2.5}$
	1.490	1.522	—	$47.8^{+2.0}_{-2.2}$	$50.9^{+2.8}_{-2.7}$
	1.522	1.554	—	$44.7^{+2.0}_{-2.2}$	$47.8^{+2.6}_{-2.5}$
	1.567	1.654	—	$43.1^{+2.9}_{-3.4}$	$30.0^{+2.6}_{-2.4}$
	1.783	1.853	—	$52.0^{+6.8}_{-7.9}$	$3.1^{+0.6}_{-0.5}$
1310	0.000	0.281	$0.5^{+1.5}_{-1.0}$	$33.7^{+4.9}_{-6.7}$	6.7 ± 0.3
	0.032	0.059	$4.3^{+1.3}_{-1.7}$	$30.6^{+3.7}_{-3.8}$	$4.8^{+0.8}_{-0.7}$
	0.059	0.085	—	$45.3^{+1.7}_{-1.6}$	$38.1^{+2.3}_{-2.1}$
	0.085	0.111	—	46.3 ± 1.9	$28.6^{+2.0}_{-1.9}$
	0.111	0.281	—	$40.1^{+3.7}_{-3.8}$	1.1 ± 0.2

[a] Time in seconds since T_{start} as defined in Tables 4.3 and 4.4.

[b] E_{peak} is in units of keV.

[c] Flux is in units of 10^{-7} erg cm^{-2} s^{-1}.

4.3.3 Log N – Log S

For each of the three magnetars with a large number of detected bursts I calculated the integral distribution of burst fluences. The fluences, S, in the 30–150 keV energy range were computed from the number of counts using the ECF values reported in Tab. 4.10. These distributions (LogN-LogS) are plotted in Fig. 4.8. In order to compare these distributions with other published results, I fitted them with a power law model ($N(>$

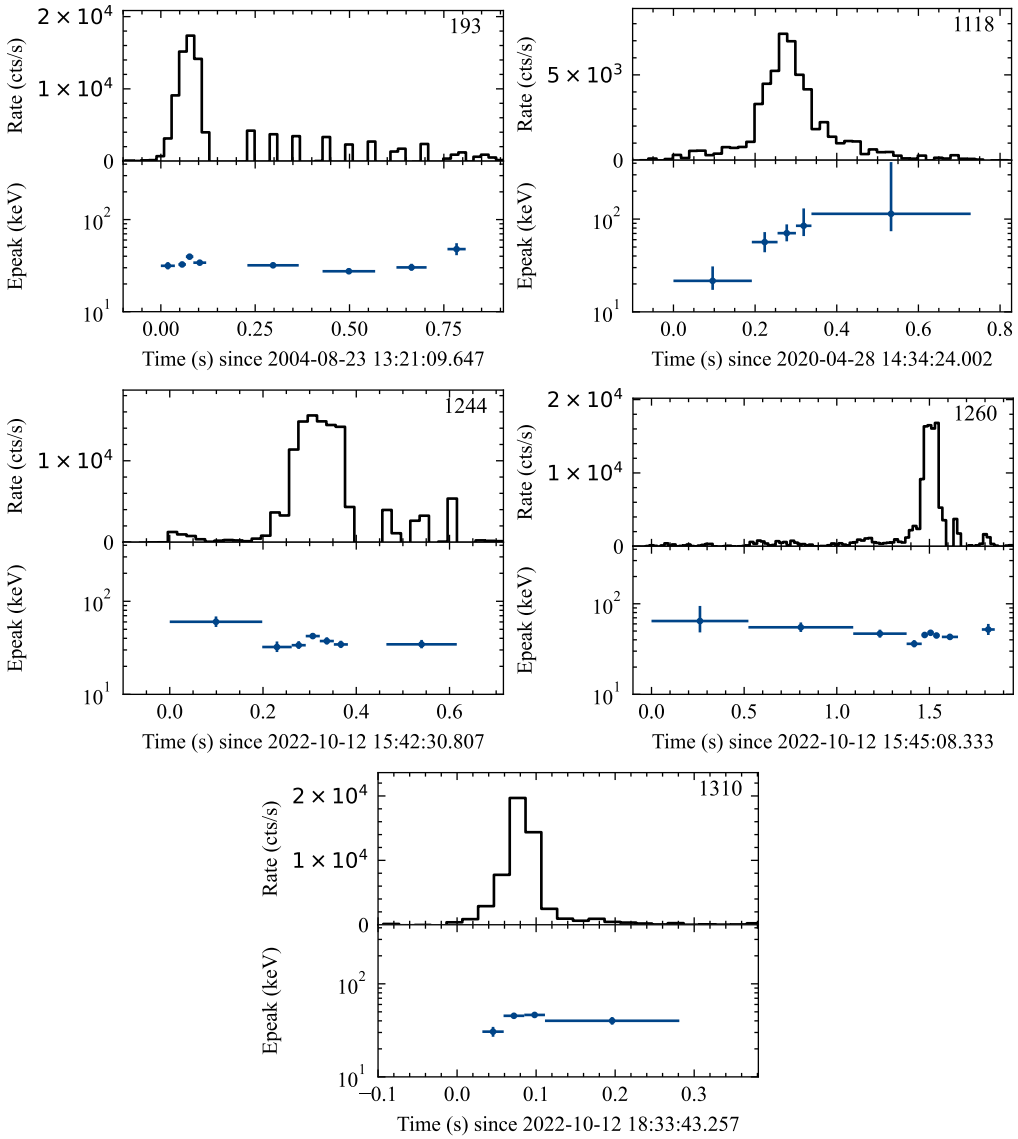

Figure 4.7: Time resolved spectral analysis of one burst (n. 193) from SGR 1806–20 and four bursts from SGR 1935+2154. The upper panel in each figure shows the background subtracted light curve of the burst, while the bottom panel shows the time evolution of E_{peak}. The gaps in the light curve of burst n. 193 are due to telemetry saturation.

$S) \propto S^{-\beta}$). To avoid potential biases resulting from least-square fitting of the binned differential distributions, I followed a maximum-likelihood approach to derive from the unbinned data the power law slope β and the minimum fluence S_{min} above which a power-law is a good description of the data (Crawford et al. 1970; Clauset et al. 2009). The results obtained for the three sources are given in Table 4.12. The deviation from a power-law trend visible at low fluences is due to the decreasing efficiency in the detection of the faintest bursts. In fact the highest S_{min} value was obtained for 1E 1547.0–5408 , that was active during the latest part of the mission, when the ISGRI sensitivity decreased.

Table 4.12: Spearman's rank correlations and best fit parameters of the fluence distributions ($N(>S) \propto S^{-\beta}$, for $S > S_{min}$)

Source	$\rho(E_p, S)$	z–score	$\rho(E_p, \alpha)$	z–score	β	S_{min}
1E 1547.0–5408	-0.51 ± 0.19	2.5 ± 1.2	0.22 ± 0.19	1.0 ± 1.1	0.76 ± 0.04	0.53
SGR 1806–20	-0.48 ± 0.07	7.1 ± 1.0	0.31 ± 0.09	3.4 ± 1.1	0.95 ± 0.06	1.89
SGR 1935+2154	-0.39 ± 0.15	2.2 ± 0.9	0.38 ± 0.17	2.1 ± 1.1	0.92 ± 0.10	3.95
SGR 1935+2154[a]	-0.45 ± 0.15	2.5 ± 1.0	0.46 ± 0.16	2.6 ± 1.1	—	—

S_{min} is in units of 10^{-8} erg cm^{-2}
[a] Excluding burst coincident with FRB 200428

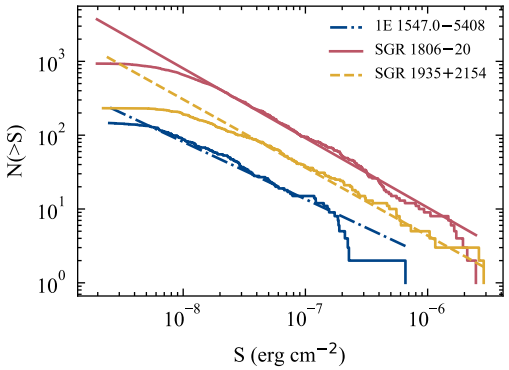

Figure 4.8: LogN-LogS distributions of bursts of 1E 1547.0–5408 (blue), SGR 1806–20 (red), and SGR 1935+2154 (yellow), with best fit power laws. The fluence S refers to the 30–150 keV energy range.

4.4 Discussion

I have carried out a comprehensive search for short bursts in data of the INTEGRAL IBIS instrument, taken in the period from end of February 2003 to October 2024. The search for bursts in the light curves provided more than 75,000 candidates. Exploiting the ISGRI imaging capability, I could verify the nature of each of them, which was especially important in the crowded region of Galactic Centre where multiple sources are present in the FOV. This led to a final sample of 1349 confirmed bursts from 21 different sources.

The total exposure across all sources amounted to 1136.8 Ms, with individual exposures ranging from ∼8 Ms for CXO0100–7211 in the Small Magellanic Cloud to nearly 68 Ms for SGRJ1745–2900, located close to the Galactic center that was extensively observed by INTEGRAL. Nine magnetars were observed for more than 50 Ms; however, only one of them, SGR 1806–20, produced a significant number of bursts. In contrast, the two next most active sources in our sample, SGR 1935+2154 and 1E 1547.0–5408, were observed for only ∼33 Ms and ∼27 Ms, respectively. This is not surprising as typically most of the magnetar bursts are produced during outbursts lasting weeks to months, and many sources were either not active during the INTEGRAL observation periods or the phases of intense activity were missed by INTEGRAL. For example, this is the case of SGR 1935+2154 that underwent multiple outbursts since 2015 (e.g., Lin et al. 2020a,b; Borghese et al. 2020; Ibrahim et al. 2024; Rehan & Ibrahim 2025), but was observed by INTEGRAL mostly during the 2022 October activity period.

Similar to previous works, the distribution of burst durations is well described by log-normal functions centred around ∼0.1 s and that the burst fluences follow power-law distributions with integral slopes β ∼0.7–1. The power law distributions of burst energies suggest that a self-organized critical system might be at the bases of the sudden energy release of the bursts (Cheng et al. 1996; Aschwanden et al. 2016).

For the bursts with sufficient statistics, I could derive time averaged spectra (about 40% of the sample), and time-resolved spectra for the 21 brightest ones. However, the spectral results suffered from the relatively limited energy range over which the bursts were detected (which also decreased with time due to the rising lower energy threshold of ISGRI). In fact, a simple power law model provided a good fit for most of the bursts (313 bursts out of 427), while the addition of a cut-off was generally required in the bursts with the highest counting statistics. In these cases, the best fit peak energies E_{peak} derived with an exponentially cut-off power law model were typically in the range ∼20-60 keV for SGR 1806–20 and SGR 1935+2154 and slightly higher for 1E 1547.0–5408 (∼35-100 keV). A time resolved spectral analysis for 21 bursts with high fluence, did not provide evidence for strong spectral evolution, with the notable exception of the SGR 1935+2154 burst with associated FRB-like radio emission.

I found a negative correlation between E_{peak} and fluence for SGR 1806–20. This confirms the reported trends of spectral softening with increasing flux (Götz et al. 2006) and fluence (Göğüş et al. 2001), that were based only on the analysis of hardness ratios. Negative correlations between E_{peak} and fluence have been seen for other magnetars, including 1E 1547.0–5408 and SGR 1935+2154, also with some evidence for a positive correlation at the highest fluences (van der Horst et al. 2012; Collazzi et al. 2015; Lin et al. 2020b, 2011a). The smaller samples of bursts from the two latter sources do not provide significant evidence for correlations, when measurement errors are properly taken into account.

4.4.1 1E 1547.0–5408

The active period of 1E 1547.0–5408 spanned from October 2008 to April 2009 and included three distinct bursting episodes (e.g. Scholz & Kaspi 2011; van der Horst et al. 2012), in which INTEGRAL detected 1, 106, and 38 bursts, respectively. Savchenko et al. (2010) studied the January 2009 activity using both the Anti-Coincidence Shield (ACS) of the spectrometer and ISGRI, reporting over 200 bursts with ACS and 84 with ISGRI. They measured a burst duration distribution centred at 68 ± 3 ms using ACS data. In comparison, my ISGRI analysis during the same period yielded a longer duration distribution, centred at 94.72 ± 3.84 ms. Although discovered several years earlier, 1E 1547.0–5408 was suggested as a magnetar candidate only in 2007, based on its association with SNR G327.24-–0.13 and the discovery of radio pulsations (Gelfand & Gaensler 2007; Camilo et al. 2007a). The first bursts from this source were reported by Swift during the 2008 October outburst (Scholz & Kaspi 2011), but a burst detected by INTEGRAL detected on 14 March 2003 (no 0 in Table 4.2) indicates that 1E 1547.0–5408 was also active at earlier times. von Kienlin et al. (2012) reported spectral evolution between the

bursts of first and third active periods. In our case, such evolution, between the second and the third period, could not be assessed due to the limited number of bursts with sufficient counts for detailed spectral fitting during the third period, as only two bursts could be fitted with the cut-off power-law model.

The fluence distribution of the 1E 1547.0–5408 bursts was previously derived using Swift/XRT data in the 1-10 keV range by Scholz & Kaspi (2011), who found a power law index $\beta = 0.6 \pm 0.1$. A similar slope was obtained at higher energies (8-200 keV, $\beta = 0.7 \pm 0.2$) with the Fermi/GBM instrument (van der Horst et al. 2012) and with the INTEGRAL SPI/ACS instrument at E>80 keV ($\beta = 0.75 \pm 0.06$, Mereghetti et al. (2009)). All these results are in agreement with the value $\beta = 0.76 \pm 0.05$ derived in our analysis.

The 1E 1547.0–5408 bursts detected by IBIS are on average harder than those seen from the other two magnetars (see Fig. 4.6 and Table 4.10). I obtained an average value of E_{peak}= 43.7±0.7 keV consistent with that obtained with Fermi/GBM during the January 2009 activity period (Lin et al. 2012), which is the one that dominates our sample (see Fig. 4.3).

4.4.2 SGR 1806–20

SGR 1806–20 was the most active source during the INTEGRAL mission, with a total of 934 bursts, providing the largest sample in the considered data, it dominates the overall burst statistics. The bursting activity of SGR 1806–20 began with a high-bursting period over a year before the Giant Flare in 2004 (Mereghetti et al. 2005c). After April 2008 only 20 bursts were detected with INTEGRAL, and also other satellites detected only sporadic bursts (Collazzi et al. 2015; Younes et al. 2017a). The fluence distribution of the bursts detected from SGR 1806–20 follows a power law of slope 0.95±0.06 for fluences above $\sim 2 \times 10^{-8}$ erg cm^{-2}. This agrees well with the previous value, $\beta = 0.91 \pm 0.09$, obtained with a smaller subset of these bursts (Götz et al. 2006). Flatter slopes ($\beta \sim 0.5$) were found for the bursts detected with the *RXTE* satellite (Prieskorn & Kaaret 2012; Göğüş et al. 2000), which operated at lower energies (2-60 keV).

4.4.3 SGR 1935+2154

All the bursts detected for SGR 1935+2154 occurred between 2015 and 2022. This sample includes the burst with associated FRB-like radio emission on 2020 April 28 (Mereghetti et al. 2020; Bochenek et al. 2020; CHIME/FRB Collaboration et al. 2020), but the period of high bursting activity that preceded this event (Younes et al. 2020b; Kaneko et al. 2021) was not observed by INTEGRAL. Most of the bursts were detected during the outburst of October 2022 (186 bursts between October 10 and 16). This outburst was also covered by the Fermi satellite, which reported 113 bursts (Rehan & Ibrahim 2025). The bursts detected by the Fermi/GBM instrument (covering the 10 keV – 40 MeV energy range) were on average shorter (log-normal distribution centred at $\sim$ 120 ms) and had lower E_{peak} values ($\sim$ 26 keV) than those observed by INTEGRAL (168.51 ± 5.34 ms and 38.1 ± 1.4 keV), but note that the two studies were based on different samples of

bursts that only partially overlapped. These authors found a fluence distribution with $\beta = 1.2 \pm 0.2$ for the October 2022 bursts, steeper than what observed with Fermi/GBM in the other activity periods of SGR 1935+2154, and consistent within the errors with the value I found ($\beta = 0.92 \pm 0.10$).

The spectral results for the April 2020 burst with associated FRB-like radio emission (burst n. 1118 in our sample, see Fig. 4.7) agree with those reported in the previous analysis of these data (Mereghetti et al. 2020), when one accounts for the different energy ranges of the reported fluxes and the slightly different integration times. In particular, I confirm that the time averaged peak energy was greater than that of bursts of similar fluence (Fig. 4.6), and that the spectrum hardened with time with E_{peak} evolving from $\sim$20 to $\sim$ 100 keV (Fig. 4.7). The peculiar spectral properties of this bursts were seen also in the data obtained with the Insight-HXMT satellite over the broad energy range of 1–250 keV (Li et al. 2021) and with Konus-Wind (Ridnaia et al. 2021). Several authors speculated that this is related to the unique radio burst emitted during this event (Bochenek et al. 2020; CHIME/FRB Collaboration et al. 2020), although a clear interpretation of such a connection is still a matter of debate (see, e.g., Ioka 2020; Li et al. 2021; Wu et al. 2025).

Radio bursts from SGR 1935+2154 were detected also on 2020 April 30 (Zhang et al. 2020), on 2020 September 2 (Alexander & Fedorova 2020), on 2020 October 8 (Good & Chime/Frb Collaboration 2020; Giri et al. 2023), on 2022 October 14 and 21 (Maan et al. 2022; Dong & Chime/Frb Collaboration 2022), and on 2022 December 1 (Giri et al. 2023), but unfortunately they were not covered by INTEGRAL data.

4.4.4 Bursts from the other magnetars

In 1011.56 Ms of data among 31 less active sources, 37 bursts were detected from 18 sources. All these bursts are on the fainter side, with a mean of only 58 counts in 40–150 keV energy range. Although these bursts are also visible in the images, I cannot exclude that some of them (especially those with the smallest number of counts) are not real bursts, but just statistical fluctuations of the background. However, I report them here for completeness and to allow cross-checks with possible detections by other instruments. Only 5 bursts exceeded the threshold of 100 observed counts required for spectral analysis. In the following sections, I present bursts from each source, including light curves and, when possible, spectral analysis results.

CXOU 0100–7211

This source, classified as a possible magnetar in 2002 (Lamb et al. 2002), is the only known magnetar in the Small Magellanic Cloud. The latest timing analysis using multiple XMM-Newton observations spanning between 2000 and 2016 done by Chatterjee et al. (2021) measured the period P = 8.0275(1) s and $\dot{P} = (1.76 \pm 0.02) \times 10^{-11}$ s s^{-1}, which was consistent with values obtained previously (McGarry et al. 2005; Tiengo et al. 2008).

No bursts were observed from CXOU 0100–7211 in the past. I found a possible burst with a signal-to-noise ratio of 3.7 (in the 0.64 s timescale) on 29 October 2014. The burst

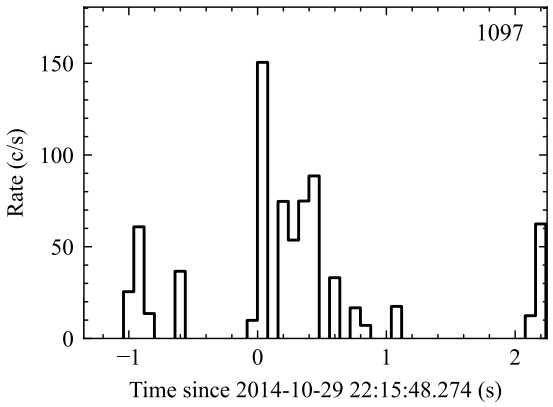

Figure 4.9: Light curve of the burst from CXOU 0100–7211.

duration is 899.3 ms. The background subtracted counts were 51.8 in the 40-150 keV energy range, which correspond to a fluence of 7.3×10^{-9} erg cm^{-2} assuming the average spectrum as in Table 4.10.

SGR 0501+4516

On On 22 August 2008, Swift BAT identified SGR 0501+4516 during an outburst (Barthelmy et al. 2008; Holland et al. 2008), leading to thorough observations by Swift BAT (Barthelmy et al. 2008; Holland et al. 2008), which were followed by extensive observations by multiple various satellites. Within a year, the magnetar's flux had dropped to roughly ~ 75 times less than its peak during the outburst (Camero et al. 2014), continuing to slight decrease until it reached a quiescent state in 2013 (Mong & Ng 2018).

Multiple bursts from the source were reported only during the first 10 days of the outburst (Lin et al. 2011c; Qu et al. 2015). I detected 8 bursts starting 5 days after the first detected burst from the source on August 27 with the last one on September 5. After the outburst, there were no bursts in about 8 Ms of INTEGRAL data. The brightest burst (no 931) was detected on 28 August 2008, six days after the first burst, with a fluence of 2.6×10^{-8} erg cm^{-2}. The burst had a duration of 193 ms (which was also the longest detected burst) and a signal-to-noise ratio of 12.4. The power law provided a good fit to the spectrum, with a photon index of -2.9 ± 0.3. The other bursts from this source of the bursts were fainter, with fluences between 8.4×10^{-9} and 1.1×10^{-8} erg cm^{-2}, and durations between 17.5 ms and 98.4 ms. The signal-to-noise ratios were between 4.6 and 9.0.

SGR 0525–66

SGR 0525–66, located in the Large Magellanic Cloud, was the first SGR ever discovered. More importantly, it is the first magnetar from which a giant flare was observed on 5 March 1979 (Mazets et al. 1979b), followed by several years of bursting activity (e.g. Golenetskii et al. 1984; Rothschild & Lingenfelter 1984). No further bursts have been reported from this source since 1983 (Tiengo et al. 2009). INTEGRAL detected the first bursts after 1983. The bursts were emitted in 2011, separated by approximately three

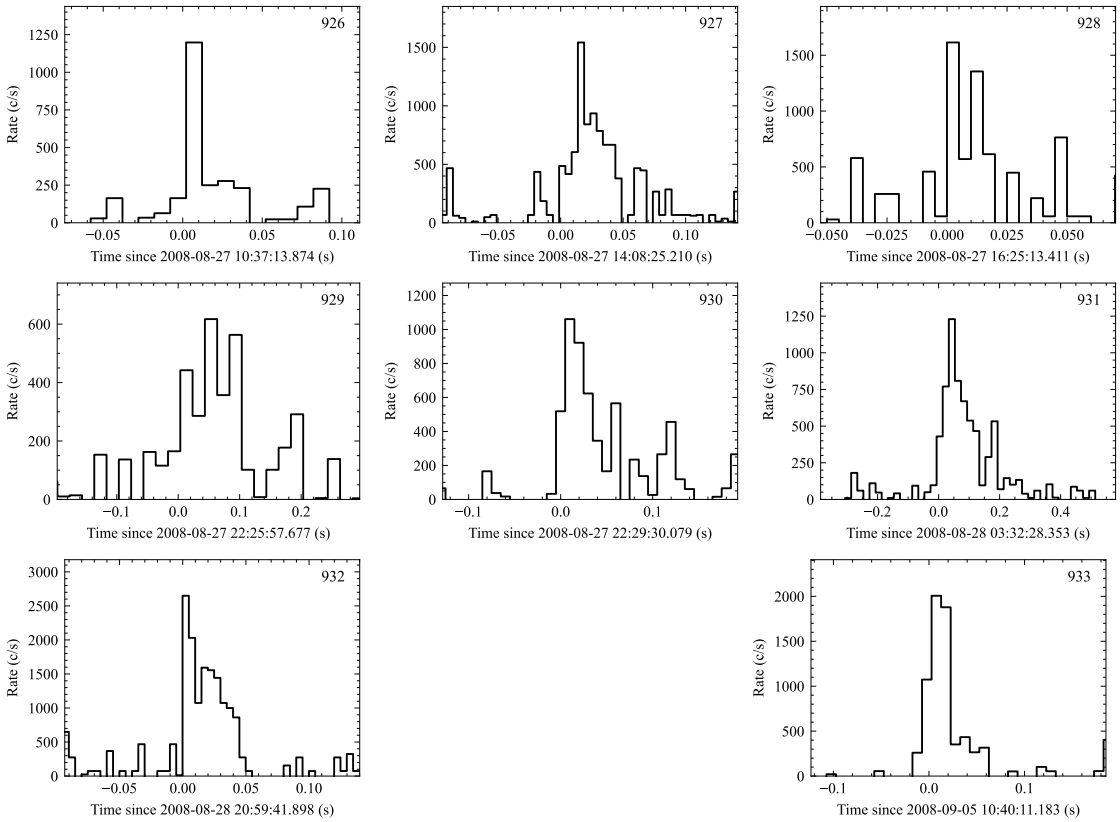

Figure 4.10: Light curves of the bursts from SGR 0501+4516.

months. Due to its sky position outside the Galactic plane, the total observation time is limited to only $\sim$ 11 Ms. Both bursts were similar, had durations of 385.9 ms and 268.8 ms, with corresponding fluences of 7.7×10^{-9} erg cm^{-2} and 5.1×10^{-9} erg cm^{-2}, respectively. The signal-to-noise ratio was also on the lower level, 4 for the first burst, and 3.4 for the second one.

1E 1048–5937

1E 1048–5937 was discovered as a persistent X-ray source with a period of 6.44 seconds (Seward et al. 1986), and several years later it was suggested as an AXP (Mereghetti & Stella 1995). Concurrent observations revealed variations in its spin-down rate (Mereghetti 1995), and in 2002, also in its X-ray flux (Mereghetti et al. 2004).

In total, 1E 1048–5937 has undergone six outbursts, all of which were accompanied by variations in the spin-down rate (Gavriil & Kaspi 2004; Dib & Kaspi 2014; Archibald et al. 2015, 2020).

The bursting activity has been sparse but significant. The first bursts were detected in 2001, marking the first such detection from an AXP and thus showing a link between AXPs and SGRs (Gavriil et al. 2002). The third and fourth bursts were detected in 2004 (Gavriil et al. 2006) and 2008 (Dib et al. 2009), respectively. The most recent bursts, eight in total, were detected in 2013 (An et al. 2014). Since then, no bursts were detected from the source.

I report the detection of two bursts, the first one on 4 July 2003, and the second one

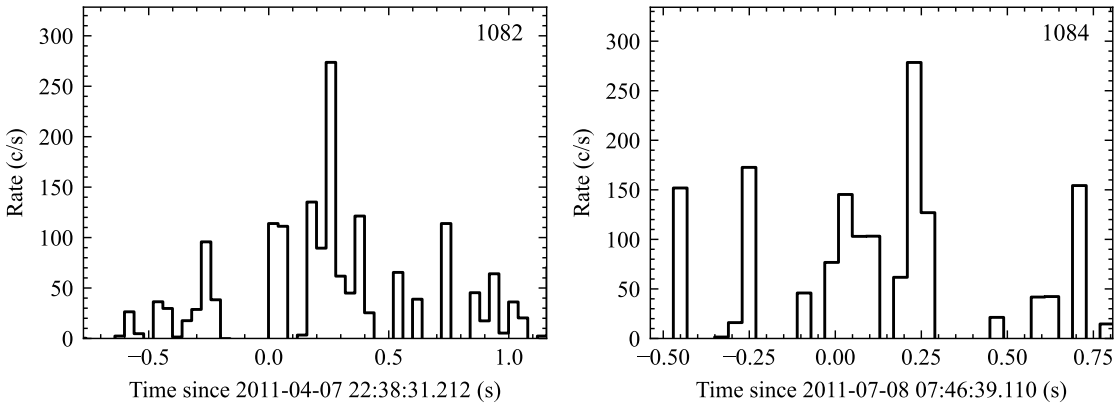

Figure 4.11: Light curves of the bursts from SGR 0525–66.

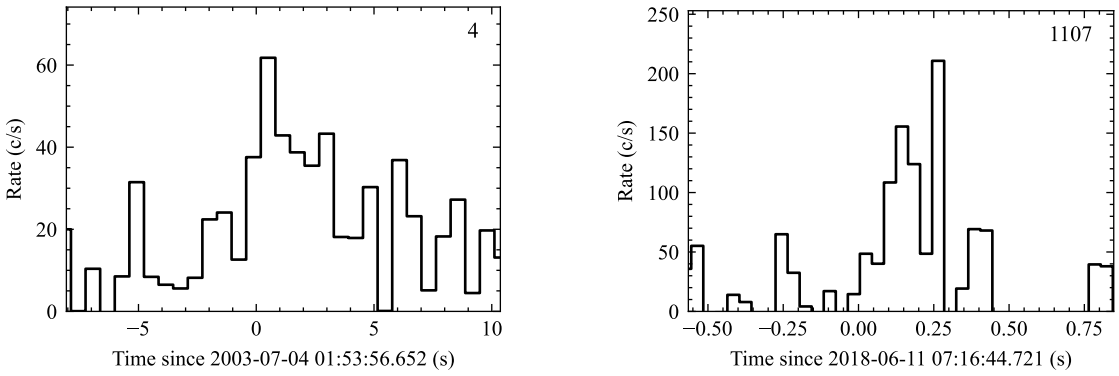

Figure 4.12: Light curves of the bursts from 1E 1048–5937.

on 11 June 2018. The 2003 burst had a signal-to-noise ratio of 4.3 (in the time scale of 1.28 s). Its duration of 2.3 s, was longer than that of typical magnetar bursts. The fluence, however, was relatively low, 1.2×10^{-8} erg cm^{-2}. The burst in 2018, was more typical of magnetar burst, but with lower signa-to-noise ratio of 3.8. It had a fluence of 1.2×10^{-8} erg cm^{-2} and duration of 282.5 ms.

PSR J1119–6127

PSR J1119–6127 is one of the two rotation-powered pulsars analysed here. It is a young, high-B ($B \sim 4 \times 10^{13}$ G) pulsar with a spin period of ~ 0.407 s and known pulsed radio emission. In July 2016, it underwent a magnetar-like outburst (Archibald et al. 2016), during which 12 short bursts were detected over a two-day period by the Fermi and Swift satellites (Göğüş et al. 2016). Radio emission disappeared during the X-ray bursts and recovered on average, about ~ 70 seconds after the bursts (Archibald et al. 2017a). In addition, a glitch was observed inducing a change in rotational frequency of $\Delta\nu \approx -4 \times 10^{-4}$ Hz (0.1 ms) (Dai et al. 2018). During the outburst, a hard X-ray tail was observed above 8 keV (Archibald et al. 2016), and pulsed radio emission was suppressed, reappearing approximately two weeks later (Burgay et al. 2016a,b).

INTEGRAL observed the source during and after the outburst for over 13 Ms (and almost 12 MS before it). The only detected burst was 5 months after the outburst, on 12 November 2016. It was a short burst of 10.83 ms with a signal-to-noise ratio of 5 and

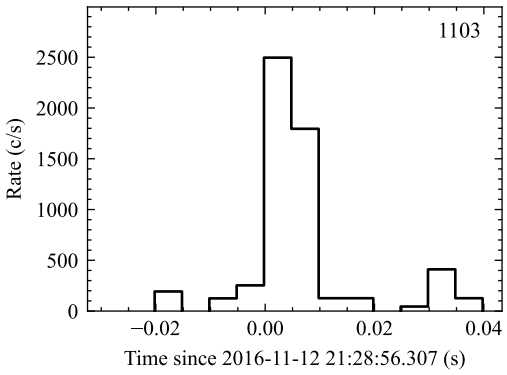

Figure 4.13: Light curve of the burst from PSR J1119–6127.

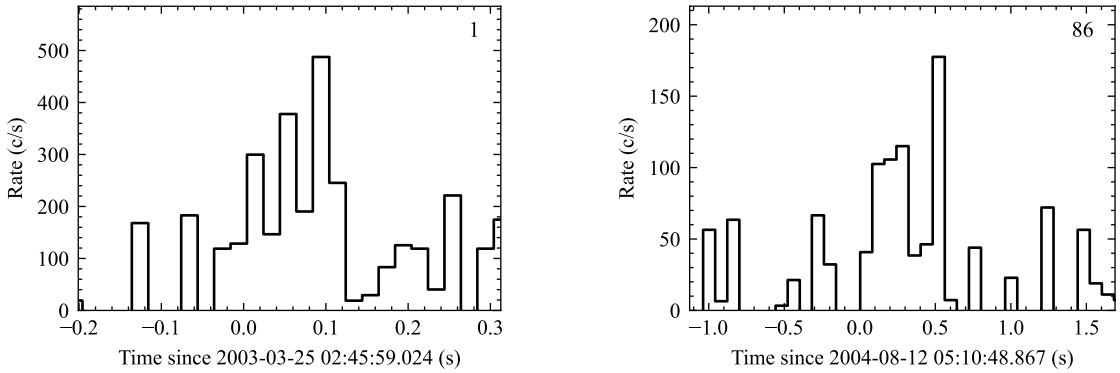

Figure 4.14: Light curves of the bursts from SGR 1627–41.

fluence of 5.2×10^{-9} erg cm^{-2}.

SGR 1627–41

SGR 1627–41 was discovered during a period of high bursting activity in 1998, when over 100 bursts were detected in a period of roughly 6 weeks (Kouveliotou et al. 1998b; Feroci et al. 1998; Woods et al. 1999; Mazets et al. 1999). After the outburst, the magnetar went into quiescence for 10 years and no more bursts were detected until the next active period (Mereghetti et al. 2006). In 2008 a second outburst occurred (Esposito et al. 2008) with high bursting activity. After this second outburst, SGR 1627–41 is again in quiescence (An et al. 2018). I report the detection of two low-count bursts detected in 2003 and 2004, between the two outbursts, with signal-to-noise ratios of 3.9 and 4.3. The first one is clearly harder, with no counts detected below 40 keV and a fluence of 4.5×10^{-9} erg cm^{-2}, while the second burst had expected, soft burst distribution and reached fluence of 7.5×10^{-9} erg cm^{-2}. Despite having similar fluences, the duration of the first one was 111.66 ms, and second of 563.26 ms.

CXOU J164710–455216

CXOU J164710–455216 was discovered in 2005 by Chandra (Muno et al. 2006), just before it went through it first outburst next year and two more outbursts were then observed in 2011 and 2017 (Borghese et al. 2019). INTEGRAL detected three bursts on

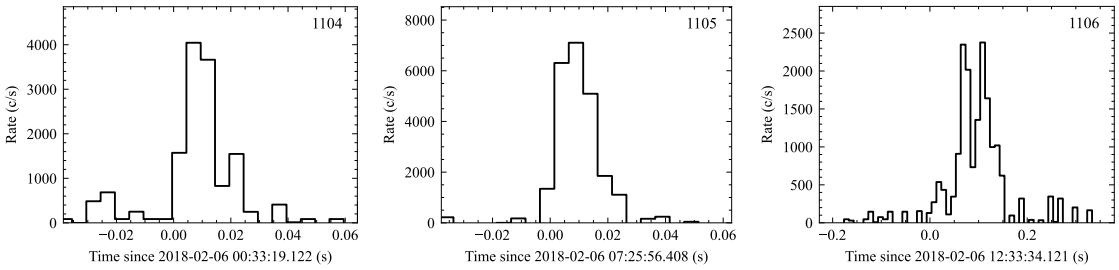

Figure 4.15: Light curves of the bursts from CXOU J164710–455216.

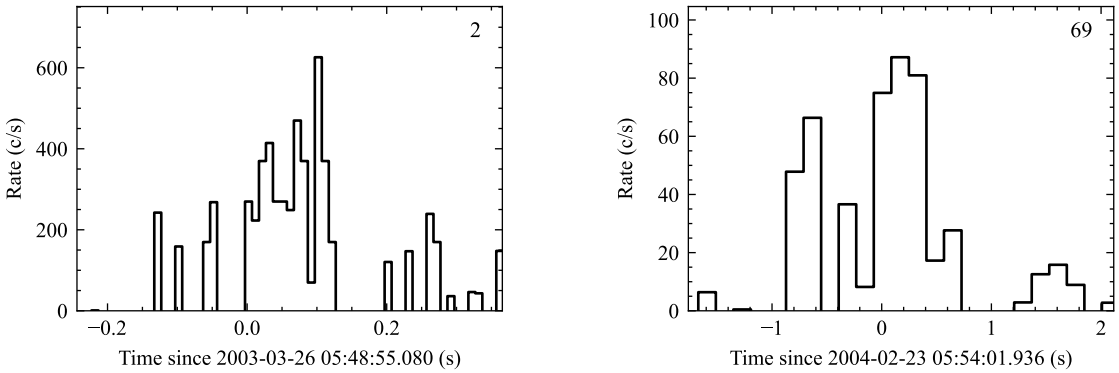

Figure 4.16: Light curves of the bursts from 1RXS J170849–400910.

6 February 2018, about a half a year when source became burst active. A day before, also a burst was detected by Swift BAT (Borghese et al. 2019). Two of three bursts were also detected in real time by IBAS (Savchenko et al. 2018). The faintest burst (first one) had fluence of 1.7×10^{-8} erg cm^{-2} the later ones (detected by IBAS) had fluences of 2.4×10^{-8} erg cm^{-2} and 3.6×10^{-8} erg cm^{-2}, respectively. The most notable difference was in signal-to-noise ratios, which were equal to 6.4,10.0, and 11.0, respectively. The last two bursts were bright enough to perform spectral analysis, which yielded a good fit with a cut-off power-law model with $\alpha \geq 6.5$ and $E_{peak} = 37.1^{+2.4}_{-2.2}$ keV for burst no 1105 and power law model with $\alpha = -1.8 \pm 0.2$ for the last burst, 1106.

1RXS J170849–400910

1RXS J170849–400910 has been a persistently active X-ray source since its discovery in 1996 (Voges et al. 1998; Sugizaki et al. 1997), and was classified as a magnetar in 1999 (Israel et al. 1999). Three rotational glitches have been confirmed in the source: the first one in 1999 (Kaspi et al. 2000), the second one in 2001 (Dall'Osso et al. 2003; Kaspi & Gavriil 2003), and the third in 2005 (Israel et al. 2007; Dib et al. 2008). Additional glitch candidates have been proposed, though they remain unconfirmed due to uncertainties in timing analysis or gaps in the coverage (Dib et al. 2008; Şaşmaz Muş & Göğüş 2013). As shown in Chapter 3, the source exhibited steady hard X-ray emission throughout the INTEGRAL mission, with flux variability remaining below a factor of two.

1RXS J170849–400910 showed no significant bursting activity. However, two bursts have been reported in recent years: one detected by Swift in 2017 (Archibald et al. 2017b), and another one in 2020, coinciding with a brief increase in the persistent flux

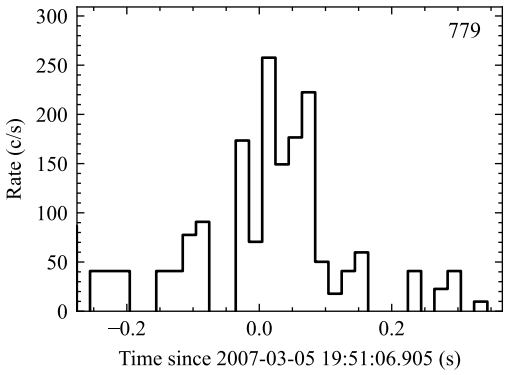

Figure 4.17: Light curve of the burst from CXOU J171405–381031.

(Younes et al. 2020a). INTEGRAL also detected two earlier bursts in 2003 and 2004, with signal-to-noise ratio of 4.4 and 3.6, respectively. The bursts had longer duration, lasting 121 ms and the second one 353 ms, and their fluences were 5.4×10^{-9} erg cm^{-2} and 7.1×10^{-9} erg cm^{-2}, respectively.

CXOU J171405–381031

CXOU J171405–381031 is one of the youngest known magnetar, with a characteristic age of approximately 950 years (Sato et al. 2010). It was discovered during an XMM-Newton observation and an archival Chandra observation was used to confirm its timing properties. Gotthelf et al. (2019b) reported a twofold increase in the spin-down rate within less than a year, which was correlated with a 50% rise in X-ray flux. Following this, the spin-down rate decreased and stabilized at a lower value. Aside from this event, the source has remained in a quiescent state, with no bursts reported since its discovery. The only burst detected by INTEGRAL was on 5th March 2007, before the source discovery. However, the burst was detected only with signal-to-noise ratio of 3.6, and with the only 18 observed counts in 40-150 keV energy range (52.4 counts after corrections, which yields 5.1×10^{-9} erg cm^{-2} in 30-150 keV energy range), which is too low for spectral analysis and despite a small excess is visible in the image. It is possible that the burst is not real.

SGR 1801–23

SGR 1801–23 was identified through the detection of two bursts in 1997 (Cline et al. 2000). In a later observation reported by Molkov et al. (2005) the source was within the INTEGRAL FOV during the monitoring of SGR 1806–20, but no persistent or bursting emission from SGR 1801–23 was detected. Since then no detection of the source was reported. I report two possible faint bursts from the direction of SGR 1801–23, in 2012 and 2014, with signal-to-noise ratio of 3.5 and 4.0, respectively. The bursts had fluences of 4.1×10^{-9} erg cm^{-2} and 1.1×10^{-8} erg cm^{-2}.

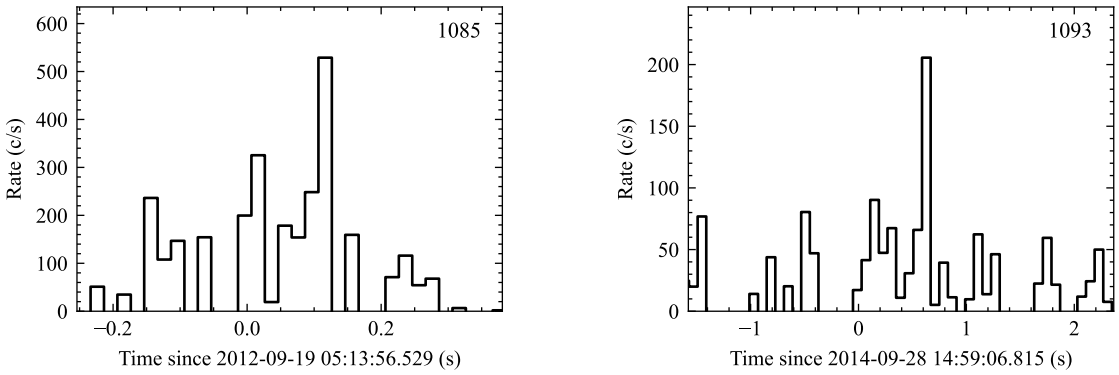

Figure 4.18: Light curves of the bursts from SGR 1801–23.

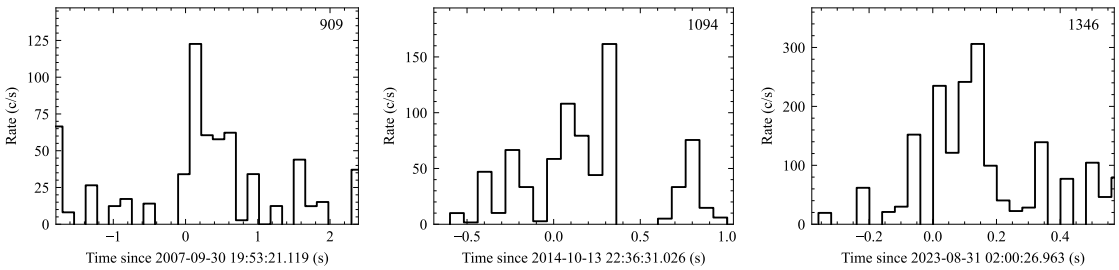

Figure 4.19: Light curves of the bursts from XTE J1810–197.

XTE J1810–197

XTE J1810–197 is a transient magnetar discovered during an outburst in 2003 (Ibrahim et al. 2004). This outburst lasted until around 2007, after which the source entered into a quiescent phase that lasted 11 years (Bernardini et al. 2009; Alford & Halpern 2016; Pintore et al. 2019). In 2018, XTE J1810–197 underwent a second outburst (Gotthelf et al. 2019a). During both outbursts, pulsed radio emission was detected while it was absent during the quiescent period (Hotan et al. 2007; Camilo et al. 2007b). Multiple X-ray and radio bursts were detected during the first outburst (Woods et al. 2005), however, no X-ray bursts were detected either during quiescence or during the second outburst. During the second outburst, radio emission was reactivated (Pearlman et al. 2020; Caleb et al. 2022).

INTEGRAL detected three faint, possible bursts with signal-to-noise ratios not exceeding 4, and fluences of 7.6×10^{-9} erg cm^{-2}, 5.5×10^{-9} erg cm^{-2}, and 1.0×10^{-8} erg cm^{-2}. These bursts occurred on 30 September 2007, 13 October 2014, and 31 August 2023, respectively.

Swift J1818.0–1607

Swift J1818.0–1607 is only the fifth known radio-loud magnetar, from which pulsed radio emission has been detected shortly after its discovery during an outburst in March 2020 (Bansal et al. 2023). The source was discovered when Swift BAT triggered on a short burst on 12 March 2020 (Evans et al. 2020; Esposito et al. 2020), followed by follow-up observations with Swift. Swift J1818.0–1607 has a short spin period of 1.36 s. The spin-down rate fluctuated significantly during the initial period of the outburst, varying

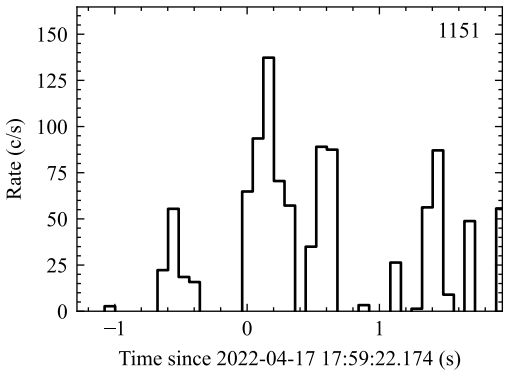

Figure 4.20: Light curve of the burst from Swift J1818.0–1607.

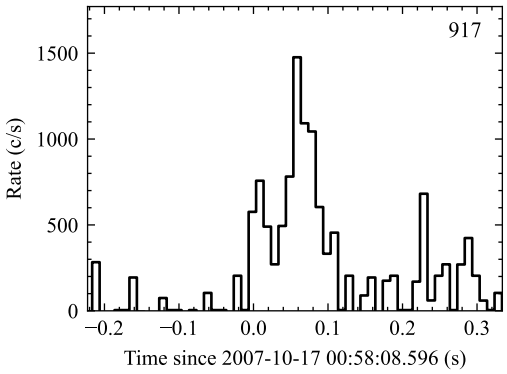

Figure 4.21: Light curve of the burst from AX J1818.8–1559.

between $(2-10)\times10^{-11}$ s s^{-1} (Champion et al. 2020), and gradually decreased over more than a year. It later stabilised at the value of $\dot{P}=2.55\times10^{-11}$ s s^{-1} (Rajwade et al. 2022), yielding a characteristic age of around $\sim$ 860 years and surface magnetic field of B$\approx 1.9\times10^{14}$ G. A limited number of bursts were detected from this source: after the first one (Evans et al. 2020; Hu et al. 2020), four faint bursts were detected by NuSTAR between March and May 2020 (Ibrahim et al. 2023). The latest burst was recently detected by SVOM on 17 August 2024 (Lanza et al. 2024; SVOM/GRM Team et al. 2024a).

INTEGRAL detected only one burst from the direction of Swift J1818.0–1607. The faint event, occurred on 17 April 2022, over 2 years after the outburst, and had signal-to-noise ratio of 3.8 and fluence of 1.7×10^{-8} erg cm^{-2}.

AX J1818.8–1559

A single burst was observed from this source on 17 October 2007, that was also detected by IBAS. This burst was investigated by Mereghetti et al. (2012), who analysed new observations from the Suzaku satellite and archival data from ROSAT, Chandra, and Swift. The analysis of available data was unable to clearly confirm the nature of the source, leaving it as a magnetar candidate. Eight years later, Swift BAT detected a single burst at a distance of 0.7 arcminutes from the source. However, due to Sun observing constraints, no follow-up observation was performed (Page et al. 2015; Palmer et al. 2015). No further activity or follow-up studies have been reported.

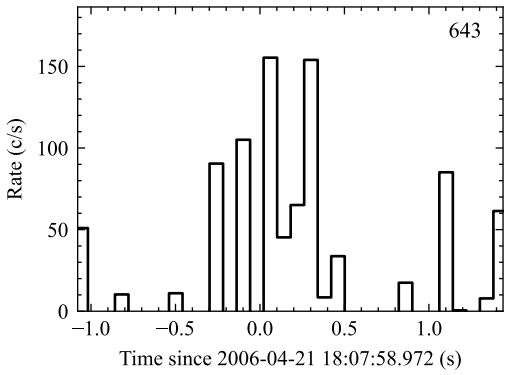

Figure 4.22: Light curve of the burst from Swift J1822.3–1606.

The burst detected by INTEGRAL is soft, with a total of 154.6 observed counts in the 20–150 keV range, including 107 counts in the 20–40 keV band and only 4 counts in the 100–150 keV energy range. The fluence in the 30–150 keV energy range was 2.9×10^{-8} erg cm^{-2}. The spectrum analysis yielded a good fit with a power law model with a photon index of -2.8 ± 0.2, which is consistent with the analysis of Mereghetti et al. (2012).

Swift J1822.3–1606

Swift J1822.3–1606 was discovered through the emission of five bursts detected by Swift /BAT on 17 July 2011 (Cummings et al. 2011). It is another transient magnetar discovered during an outburst (Livingstone et al. 2011b; Rea et al. 2012). The peak emission reached levels three orders of magnitude higher than the persistent emission found in archival ROSAT observation taken in 1993 (Scholz et al. 2012). During the outburst, Swift J1822.3–1606 likely experienced a glitch, similar to several other magnetars, as suggested from the post-outburst evolution of its spin-down rate (Scholz et al. 2014). Initially classified as a low magnetic field magnetar with $B \approx 2.7 \times 10^{13}$ G (Rea et al. 2012), a revised estimate, after 2.5 years of observations based on updated $\dot{P}$ suggested an even lower magnetic field at the level of $B \approx 1.35 \times 10^{13}$ G.

In addition to the initial bursts, six bursts were detected in RXTE observations between 19 July and 17 August 2011 (Scholz et al. 2012).

I report a possible earlier burst on 21 April 2006. This faint burst was detected with a signal-to-noise ratio of 3.3, with 41.4 observed counts in the 20–150 keV energy range, yielding a fluence of 6.7×10^{-9} erg cm^{-2}.

SGR 1833–0832

SGR 1833–0832, like many magnetars, was discovered through a burst detected by Swift BAT on 19 March 2010 during an outburst. Follow-up by Swift, RXTE, and XMM-Newton showed a steady flux level for ~ 20 days, which then faded by a factor of ~ 40 over the next 140 days (Esposito et al. 2011). During the outburst, only five additional bursts were detected by RXTE (Göğüş et al. 2010; Esposito et al. 2011), and no further bursts have been reported since.

The initial burst that triggered Swift /BAT was also detected by INTEGRAL (Kuiper

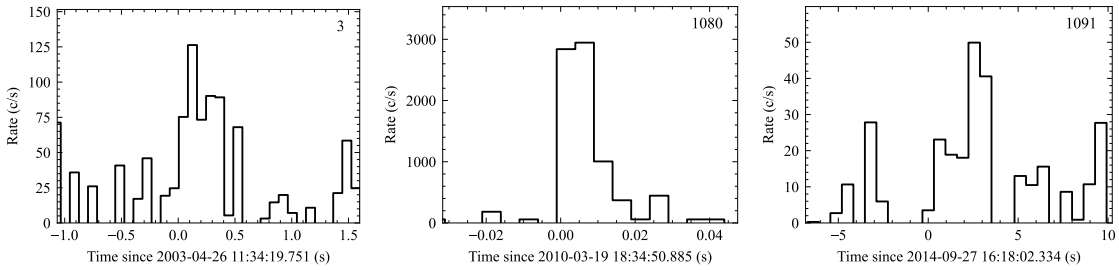

Figure 4.23: Light curves of the bursts from SGR 1833–0832.

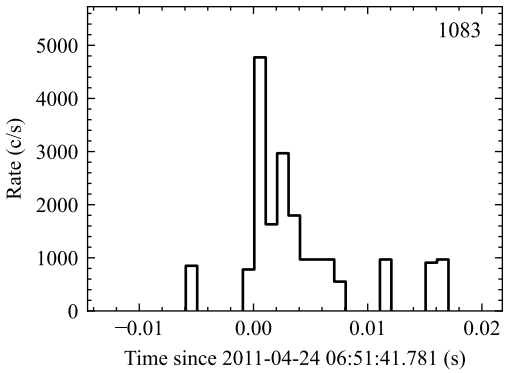

Figure 4.24: Light curve of the burst from 1E 1841–045.

& Hermsen 2010), and is included in my analysis. In addition to this burst, I report the detection of two other possible faint bursts, in 2003 and 2014. Both bursts have a low signal-to-noise ratio of 3.5 (while the one in 2010 has a 6.7) and fluences of 8.4×10^{-9} erg cm^{-2} and 6.1×10^{-09} erg cm^{-2}, respectively. However, both bursts were detected on the longer time-scales and had longer durations of 532.93 ms and 3.4 s. The longer burst (no 1091) provided enough counts for spectral analysis and simple power law model provided a good fit with a photon index of -1.1 ± 0.9.

1E 1841–045

In 1985, the Einstein Observatory detected a persistent X-ray source in the central part of SNR Kes 73 (Kriss et al. 1985). In 1997, pulsed X-ray emission was detected with a period of ~ 11.8 seconds and $\dot{P} = 4.73 \times 10^{-11}$ s s^{-1} leading to its classification as an AXP (Vasisht & Gotthelf 1997).

The first burst was detected on 6 May 2010 by Swift /BAT (Kumar & Safi-Harb 2010), followed by four additional bursts in February 2011, and six more bursts between 16 June and 2 July 2011 (Lin et al. 2011b). Over the next 13 years, the source exhibited only sporadic bursting activity, with only 6 bursts. A new period of high bursting activity began on 20 August 2024, with a total of 23 bursts detected by Swift (Dichiara et al. 2024), NICER (Ng et al. 2024), FERMI (Roberts et al. 2024), SVOM (SVOM/GRM Team et al. 2024b), GECAM-B (Zhang et al. 2024), and Insight-HXMT (Cai et al. 2024). An additional four bursts followed in November 2024 (Palm 2024; SVOM/GRM Team et al. 2024c; Mereghetti et al. 2024a), and the latest burst was observed on 23 January 2025 (Svinkin et al. 2025). ,

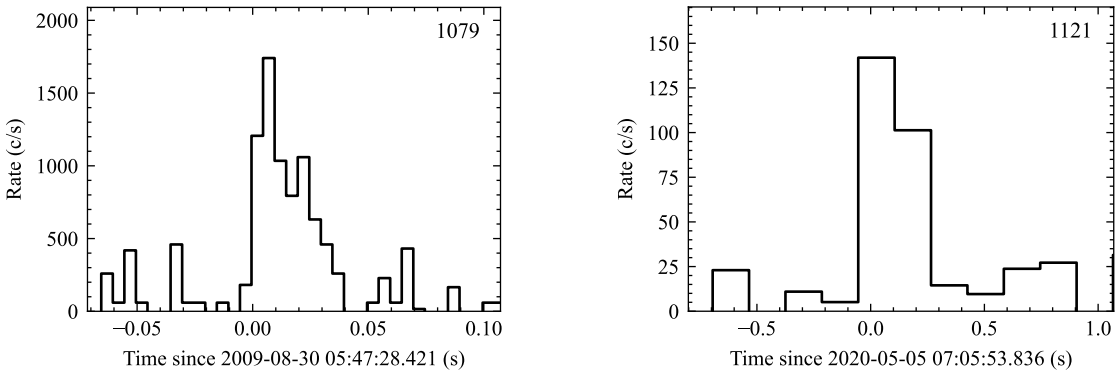

Figure 4.25: Light curves of the bursts from PSR J1846–0258.

Since its discovery, this magnetar has maintained a steady flux level. A glitch and and antiglitch were also observed, neither of which were associated with an outburst (Şaşmaz Muş et al. 2014). However, in August 2024, coinciding with its burst-active period, the persistent X-ray emission increased by a factor of ~ 1.6 (Younes et al. 2025). During this active period, 1E 1841–045 was observed by IXPE and it showed highly polarized X-ray emission. The spectrum, composed of a blackbody and two power-law components, exhibited polarization below approximately 25% in the soft thermal component, around 30% in the intermediate one, and exceeding 65% in the hard power-law component (Rigoselli et al. 2025).

I report the detection of the burst on 24 April 2011, between two bursting periods of the source. The burst has signal-to-noise ratio of 4.6. The fluence is equal to 8.4×10^{-09} erg cm^{-2} in a duration of 7.26 ms Additionally, IBAS reported the detection of the burst from this source on 2024 November 9; however, this burst is not included here, as the ScW in which it occurred was private at the time of analysis.

PSR J1846–0258

PSR J1846–0258 was the first rotation-powered pulsar found to display a magnetar-like behaviour. It was discovered in 2000 with a spin period of $P = 327$ ms and $\dot{P} = 7.1 \times 10^{-12}$ s s^{-1}, corresponding to a characteristic age of 723 years and a surface magnetic field of $B \approx 5 \times 10^{13}$ G (Gotthelf et al. 2000; Mereghetti et al. 2002a). It is located in the supernova remnant Kes 75. From its discovery until its first outburst in 2006, it behaved like a typical rotation-powered pulsar (Gavriil et al. 2008). During the 2006 outburst, however, it exhibited classic magnetar-like behaviour, including a large flux increase, significant bursting activity, and a glitch. A second outburst began in May/June 2020 (Blumer et al. 2021; Sathyaprakash et al. 2024), after 14 years of quiescence during which its X-ray emission had returned to the pre-outburst level (Livingstone et al. 2011a). Multiple bursts were detected from PSR J1846–0258 during both outbursts. In the first outburst, only five bursts were observed (Gavriil et al. 2008); however, during the second outburst, nearly 60 bursts were detected between July and October 2020 by FERMI and Swift (Uzuner et al. 2023).

INTEGRAL, FERMI, and RXTE confirmed the presence of hard X-rays and γ-rays

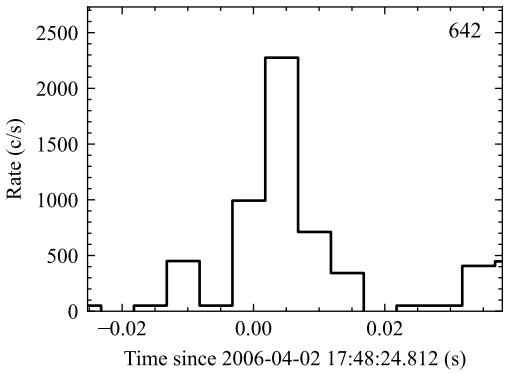

Figure 4.26: Light curve of the burst from SGR 1900+14.

not only during outbursts, but also in the pre- and post-outburst phases (Kuiper & Hermsen 2009; Kuiper et al. 2018). However, broad-band analysis showed that this emission originates both from the source and its pulsar wind nebula, with the latter component dominating the flux (McBride et al. 2008). In later observations, during the quiescent period in 2017, hard X-ray emission up to 55 keV was detected by NuSTAR, but was associated exclusively with the pulsar wind nebula (Gotthelf et al. 2021).

In my search, I identified two bursts associated with PSR J1846–0258. The first one was a short burst lasting ~ 36 ms, detected during the first post-outburst epoch, in 2009 with a high signal-to-noise ratio of 6.1 and fluence of 6.2×10^{-9} erg cm^{-2}. The second burst had a fluence of 1.0×10^{-8} erg cm^{-2}, but a signal-to-noise ratio of only 3.5, due to duration of 267.15 ms. It was detected in May 2020. Despite having a low signal-to-noise ratio, its timing may be significant because it coincides with the onset of the second outburst.

SGR 1900+14

SGR 1900+14 was the second magnetar observed to emit a Giant Flare, on 27 August 1998 (Feroci et al. 2001). It was discovered in 1979, when it emitted three bursts (Mazets et al. 1979a) detected by Venera 11 and Venera 12. The second detection occurred with the detection of the next three bursts in 1992 by BATSE (Kouveliotou et al. 1993; Aptekar et al. 2001).

The reactivation of the source happened just before the giant flare in May 1998 and lasted till 1999, during which over a thousand bursts were detected by RXTE, BATSE, and Konus experiment (GöğüŞ et al. 1999). After the giant flare, two bursting periods were observed, in November 2002 (Hurley et al. 2002) and March 2006 (Vetere et al. 2006; Golenetskii et al. 2006b).

I report detection of a burst on 2 April 2006, three days after the burst detected by Konus-Wind (Golenetskii et al. 2006a). The short, 12.6 ms long burst had a fluence of 4.4×10^{-9} erg cm^{-2} and a soft spectrum, with no counts detected above 100 keV.

Chapter 5

Giant flares from extragalactic magnetars

As mentioned in Section 1.6.1, Magnetar Giant Flares (MGFs) are the most powerful emission magnetars can produce. However, they are also very rare events, with only three confirmed MGFs observed in our Galaxy and the Magellanic Clouds in the last 45 years. The extreme luminosity of the initial peak of MGFs, reaching up to 10^{47} erg s^{-1}, allows us to observe them in nearby galaxies up to a few tens of Mpc away with current instruments (e.g., Trigg et al. 2025), but their pulsating tails would remain undetectable beyond ~ 3 Mpc. Thus, an MGF from a distant galaxy appears very similar to, and is difficult to distinguish from, a short GRB (Mazets et al. 1982a). Here I report on a search for MGFs in the INTEGRAL observations of the Virgo cluster and in a few other nearby galaxies with high star formation rates (SFRs). Then, I report the discovery of two extragalactic magnetar candidates, one in M82 and one in PGC 86046. The results obtained in the first part of the chapter have been published in the paper: *INTEGRAL search for magnetar giant flares from the Virgo Cluster and in nearby galaxies with high star formation rate*, by Pacholski, Arrigoni, Mereghetti, Salvaterra published on MNRAS in 2024. The second part of the chapter describes my contribution to two papers, published respectively on Nature and ApJ:

- *A magnetar giant flare in the nearby starburst galaxy M82*, by Mereghetti, Rigoselli, Salvaterra, Pacholski, et al., 2024.
- *GRB 241107A: A Giant Flare from a Close-by Extragalactic Magnetar?*, by Rodi, Pacholski, Mereghetti, et al., 2025.

5.1 Search for MGFs in Virgo and other nearby galaxies

A few candidate MGFs have been identified among short GRBs with positions consistent with bright galaxies outside the Local Group (see Chapter 1). Although an MGF origin cannot be proven with absolute certainty in all these cases, at least some of them appear very plausible (Svinkin et al. 2021; Roberts et al. 2021; Mereghetti et al. 2024c). Furthermore, significant evidence for a population of extragalactic MGFs emerges from

a collective statistical analysis of these candidates (Burns et al. 2021). Their main properties are compared to those of the three confirmed MGFs in Table 5.1.

During giant flares, magnetars emit a significant fraction of their total magnetic energy budget. This limits the number of the most energetic events that can be emitted in a magnetar's lifetime. It is therefore interesting to derive observational constraints on the rate of MGFs as a function of energy. Given the low rate of Galactic MGFs, it is clear that targeted searches in more distant galaxies could be a more promising way to enlarge the sample and derive constraints on the MGFs rate of occurrence. Galaxies with high star formation rate (SFR) offer the best prospects, since magnetars are believed to originate from massive stars undergoing core-collapse supernova explosions.

The procedure I used to search for MGFs is similar to that adopted for the search of short bursts from Galactic magnetars (see Section 2.2). At the extragalactic distances considered here, only the initial peak of MGFs can be detected with INTEGRAL as the pulsating tail would be too faint to be observable. Thus, I looked for short spikes of hard X-ray emission with durations of less than one second. Given the harder spectrum of MGFs compared to that of short bursts, I performed the search in the 15–300 keV energy range.

5.1.1 Virgo cluster

At a distance of ∼16.5 Mpc, Virgo is the closest cluster of galaxies and it has been extensively observed by INTEGRAL. I considered all the galaxies reported in the Extended Virgo Cluster Catalog (EVCC, Kim et al. 2014), excluding the dwarf galaxies. I then extracted from the INTEGRAL archive all the ScWs covering the positions of the 975 selected galaxies. This resulted in 10,886 ScWs obtained between May 2003 and August 2023, yielding a total observation time of 34.8 Ms. On average, a single galaxy was observed for 22 Ms in 6700 ScWs. Since in general each ScW contains several galaxies, I did not apply any spatial selection based on the PIF and extracted light curves in eight integration times with logarithmically spaced durations between 0.01 and 1.28 s using the counts from the whole detection plane of ISGRI. All the burst candidates found through the search in the light curves were examined by producing the sky images of the corresponding time intervals, but none of them could be confidently interpreted as a real burst from one of the Virgo galaxies in the field of view.

5.1.2 Nearby galaxies

In order to put constraints also on less energetic MGFs, I considered also the seven nearby galaxies with high SFR listed in Table 5.2 which are closer than the Virgo cluster. In contrast to the analysis done for the Virgo cluster, the light curves were filtered based on their PIF (see Section 2.2).

Also in this case, no significant bursts from the considered galaxies were found, with the exception of the rediscovery of GRB 231115A in M82 (see Section 5.2.1).

Table 5.1: Properties of the three confirmed MGFs and of the candidates found in external galaxies.

Source	Galaxy d (Mpc)	E_{GF} L_{peak}	α E_{peak}(keV)	T (s)	References
790305 SGR 0526−66	LMC 0.055	0.7 0.65	— 500	< 0.25	[3],[4]
980827 SGR 1900+14	Milky Way 0.0125	0.43 2.3	— 1200	< 1.0	[3],[4]
041227 SGR 1806−20	Milky Way 0.0087	7.7 12	−0.7 850	0.18	[1], [2]
051103	M81 3.7	53 180	−0.3 2300	0.14	[6]
070201	M31 0.78	1.5 12	−0.98 296	0.256	[3]
070222	M83 4.5	6.2 40	−1.0 1290	0.038	[4]
180128A	NGC 253 3.5	0.60 11	0.6 290	0.2	[8]
200415A	NGC 253 3.5	13 140	0.0 887	0.10	[5],[6]
231115A	M82 3.6	1 5.1	0.04 551	0.093	[7],[9]

Isotropic energy E_{GF} and peak luminosity L_{peak} are in the 1 keV − 10 MeV range.
References: [1] Frederiks et al. (2007a), [2] Bibby et al. (2008), [3] Mazets et al. (2008), [4] Burns et al. (2021), [5] Roberts et al. (2021), [6] Svinkin et al. (2021), [7] Mereghetti et al. (2024c), [8] Trigg et al. (2024), [9] Trigg et al. (2025).

5.1.3 Discussion

The results of the search for MGFs in the INTEGRAL data can be used to constrain the rate of occurrence of these events. To do this, it is necessary to know the energy distribution of MGFs and an estimate of the expected numbers of MGFs in the considered data sets.

Energy distribution of MGFs

Given that the energy distribution of MGFs is only poorly constrained by the three confirmed events seen up to now, I assumed that it can be described by a power law with index γ in the range [E_{min},E_{max}] and estimated the most likely parameters using a larger set of events selected among those listed in Table 5.1 as described below.

The expected number of MGF with energy in the range [E_1,E_2] detectable in an observation of duration T is given by

$$\mu_{12} = \tilde{k} \frac{\gamma - 1}{E_{min}^{1-\gamma} - E_{max}^{1-\gamma}} \int_{E_1}^{E_2} E^{-\gamma} N(E) T \mathrm{d}E, \tag{5.1}$$

Table 5.2: Nearby galaxies with high star formation rate

Galaxy	Distance (Mpc)	SFR ($M_\odot$ yr^{-1})	Exposure (Ms)
NGC 253	3.5	4.9	0.62
M81	3.7	0.5	25.5
M82	3.6	7.1	26.1
M83	4.5	4.2	5.2
NGC 4945	3.4	1.45	17.9
IC 342	2.3	1.9	7.2
PGC 50779	4.2	3.9	20.8

where the normalisation $\tilde{k}$ represents the total number of MGFs per year per magnetar and $N(E)$ is the number of magnetars from which an event of energy E would be detectable.

As discussed in Burns et al. (2021), the whole sky was covered down to a limiting fluence of $S_{\rm IPN} = 2 \times 10^{-6}$ erg cm^{-2} with the instruments of the InterPlanetary Network (IPN) during the last 30 yrs. Therefore, I set T=30 yrs in eq. (5.1) and selected from Table 5.1 the MGFs with fluence above $S_{\rm IPN}$ observed in this time period. Only 790305 and 231115A do not satisfy these two requirements and thus are excluded, leading to a complete sample of seven MGFs.

To estimate $N(E)$ I considered all the galaxies within $d_{\rm max} = \sqrt{E/4\pi S_{\rm IPN}}$ reported in the *z0MGS* catalog (Leroy et al. 2019), and assumed that each of them contains a number of magnetars N_i proportional to its SFR: $N_i = N_{\rm MW+MC}\ (SFR_i/SFR_{MW+MC}) = 30\ (SFR_i/\ 1.85 M_\odot\ {\rm yr}^{-1})$. I have assumed 30 magnetars in the Milky Way and Magellanic Clouds, based on the number of known magnetars. This is probably an underestimate due to the presence of still undiscovered quiescent magnetars. All the derived rates scale linearly with $N_{\rm MW+MC}$.

I then applied a maximum likelihood method to determine $\tilde{k}$ and γ values that best reproduce the observed data, considering that the observed number of MGFs with energy $E_1 < E < E_2$ follows a Poisson distribution with average μ_{12}. In this way, I found $\gamma = 1.97$ and $\tilde{k} = 3.5 \times 10^{-3}$ yr^{-1} magnetar^{-1}, with 90% c.l. intervals of [1.73,2.21] and [1.3,6.7]$\times 10^{-3}$, respectively. The corresponding distribution, in its integral form, is shown by the red line in Fig. 5.1, where the shaded area indicates the 90% c.l. uncertainty.

5.1.4 Expected number of MGFs

The expected number of MGFs in the INTEGRAL observations of the Virgo cluster can be calculated by summing the contributions of all the individual galaxies:

$$N_{\rm GF} = \sum_i N_i^{\rm GF} = \sum_i \int T_i(< S) R_{\rm GF}(S)\ N_i dS \tag{5.2}$$

where $R_{\rm GF}(S)$ is the rate of GF with fluence $S = \frac{E}{4\pi d_i^2}$ emitted by a single magnetar.

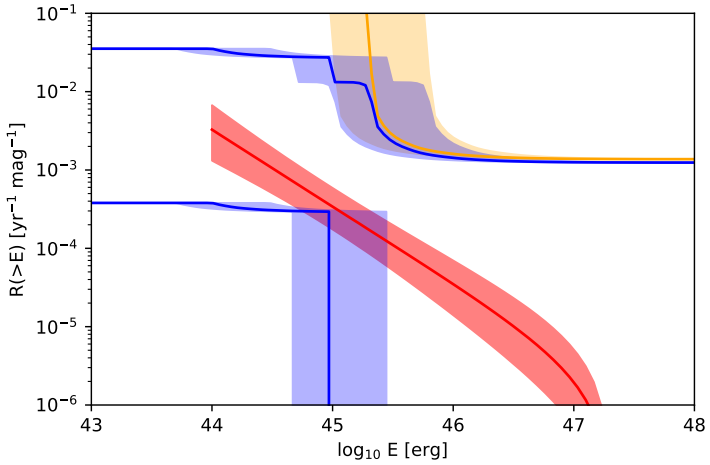

Figure 5.1: Rate of magnetar giant flares as a function of energy. The red line is the distribution I derived with a maximum likelihood analysis of seven MGF with fluence above 2×10^{-6} erg cm^{-2} observed in the last 30 yrs. The shaded area indicates the 90% c.l. interval. The upper limit (90% c.l.) derived from the INTEGRAL observations of the Virgo cluster of galaxies is indicated by the orange line. The blue lines give the lower and upper limits with the inclusion of seven nearby galaxies with high star formation rate. The shaded blue and orange areas indicate the uncertainty resulting from the spectral parameters assumed for the MGF.

The same distance d_i = 16.5 Mpc was used for all the Virgo cluster galaxies. $T_i(< S)$ is the total time in which galaxy i has been observed with sensitivity better than S. In the computation of $T_i(< S)$, I took into account the dependence of the ISGRI sensitivity on the galaxy position in the field of view and on the background level measured in each ScW. The instrument sensitivity in the energy range used for the search depends also on the spectral shape of the burst. An exponentially cut-off power law spectrum ($F(E) = kE^{\alpha}\exp(-(E(2+\alpha)/E_p))$ ph cm^{-2} s^{-1} keV^{-1}) was assumed.

The number of magnetars per galaxy is proportional to the rate $R_{\rm SN}$ of core collapse supernovae. Therefore, it can be estimated by scaling the number of Galactic magnetars: $N_i = N_{MW} R_i^{\rm SN}/R_{MW}^{\rm SN}$. The rate of core collapse supernovae depends on the luminosity and morphological type of each galaxy: $R^{SN} = k_{\rm morph} L_g$. I used the g band luminosities L_g reported in the EVCC and the values of $k_{\rm morph}$ given in Table 5.3.

As a representative spectral shape for an MGF initial spike, the parameters measured with INTEGRAL for 231115A in M82 were used: α=0.04 and E_p=551 keV (Mereghetti et al. 2024c). For these values, eq. 5.2 gives an expected number of $N_{\rm GF}$ = 0.15 in the Virgo cluster observations. By varying the spectral parameters in the range observed in other MGFs (α=[–1.0,0.6] and E_p=[300, 2300] keV), $N_{\rm GF}$ varies from 0.05 to 0.3.

5.1.5 Constraints on the MGF rate

Given that no MGFs were detected in Virgo, I computed the rate upper limit as

$$R_{\rm up}(S) = \frac{N_{\rm up}}{\sum_i T_i(< S) N_i}, \tag{5.3}$$

Table 5.3: Coefficients of proportionality between rate of core collapse supernovae (in units of SN/century) and galaxy luminosity (in units of $10^{10} L_{\odot}$) assumed in this work. See Svinkin et al. (2015).

Galaxy type		$k_{\rm morph}$
Elliptical		0.05
Spiral	S0	0.05
Spiral	Sa-b	0.89
Spiral	Sc-d	1.68
Spiral	Sm	1.46
Spiral	unclassified	1
Irregular		1.46
Dwarf		0

with $N_{\rm up} = 2.3$, which corresponds to the 90% c.l. (Gehrels 1986). The corresponding limit on the rate as a function of MGF energy E is indicated by the orange line in Figure 5.1, where the shaded region reflects the uncertainty given by varying the spectral parameters in the range mentioned above.

Owing to the relatively large distance of the Virgo cluster, these observations cannot constrain the rate of MGFs with energy below a few 10^{45} erg. On the other hand, this can be done with the results obtained for the seven galaxies in Table 5.2, which globally are expected to contain fewer magnetars, but are closer than the Virgo cluster. In this case, one MGF was detected with INTEGRAL (231115A in M82, see Section 5.2.1). Therefore, using the formalism described above, both an upper and a lower limit to the MGF rate can be derived. As indicated by the two blue lines in Figure 5.1, the limits (at 90% c.l.) obtained from these seven galaxies (plus those in the Virgo cluster) extend to lower values of E.

Fig. 5.2 compares the limits obtained in this work with the estimates derived by different authors (Popov & Stern 2006; Ofek 2007; Svinkin et al. 2015; Burns et al. 2021). I converted all these published measurements to the same units ($\rm yr^{-1}$ $\rm magnetar^{-1}$) and 90% c.l. for the upper limits and, when needed, I also renormalised them to the same number of assumed Galactic magnetars (30). The black histogram shows the constraints derived using only the three confirmed MGFs in the Milky Way and LMC.

5.1.6 Conclusions

I searched for MGFs in ∼35 Ms of INTEGRAL data on the Virgo cluster of galaxies with negative results. With the reasonable assumption that the number of active magnetars in each galaxy scales with the rate of star formation, a 90% c.l. upper limit of about one giant flare with $E > 3 \times 10^{45}$ erg every ∼500 yr per magnetar was derived. I also put some constraints on the rate of MGFs with lower energies, thanks to the INTEGRAL observations of a few nearby galaxies with high SFR. The analysis of this sample, with the detection of only one MGF in M82, implies a rate lower limit of $R(> E) > 4 \times 10^{-4}$ $\rm yr^{-1}$ $\rm magnetar^{-1}$, for energies $E < 10^{45}$ erg.

These findings are in agreement with those obtained in analysis based on data from

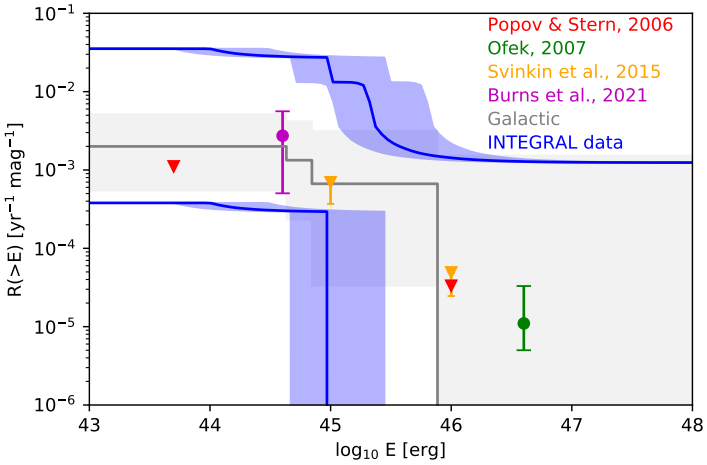

Figure 5.2: Lower and upper limits (90% c.l.) on the rate of MGFs as a function of emitted energy E derived in this work (blue lines, with shaded uncertainty regions resulting from the uncertainties on MGF spectra). The coloured symbols give the rate values (dots) or upper limits (triangles) reported by different authors (rescaled to the same assumptions to allow a proper comparison). The black histogram (with 90% c.l. uncertainty shaded) is the rate derived using only the three confirmed MGFs (790305 in the LMC, 980827 and 041227 in our Galaxy).

other satellites that were obtained with different methods and assumptions. Although the detection of pulsating tails, which would unambiguously confirm the MGF candidates, is difficult with the current instrumentation, the most recent discoveries show that quick and precise localisations with instruments providing good spectral/timing capabilities coupled to rapid multiwavelength follow-ups are key elements to advance in this field.

5.2 Discovery of two extragalactic MGFs

5.2.1 GRB 231115A

The IBIS instrument detected GRB 231115A on 2023 November 15 at 15:36:20.7 UT Mereghetti et al. (2023). This short burst was also seen by other satellites (Dalessi et al. 2023; Cheung et al. 2023; Xue et al. 2023; Frederiks et al. 2023; Wang et al. 2024a), but only INTEGRAL could promptly associate it to the M82 galaxy thanks to a localization at few arcmin level, publicly distributed by the INTEGRAL Burst Alert System (IBAS, Mereghetti et al. 2003) only 13 s after the burst detection. The burst occurred in the field of view of IBIS, at coordinates R.A.=149.0205 deg, Dec.=+69.6719 deg (J2000, 2 arcmin 90% c.l. radius).

Data analysis and results

The T_{90} of the burst was estimated in the same way as for the short bursts as described in Section 4.1.1, using the ISGRI data in the 30-250 keV energy range, resulting in T_{90} = 93 ms. The light curves plotted in Figure 5.3 show that GRB 231115A was clearly

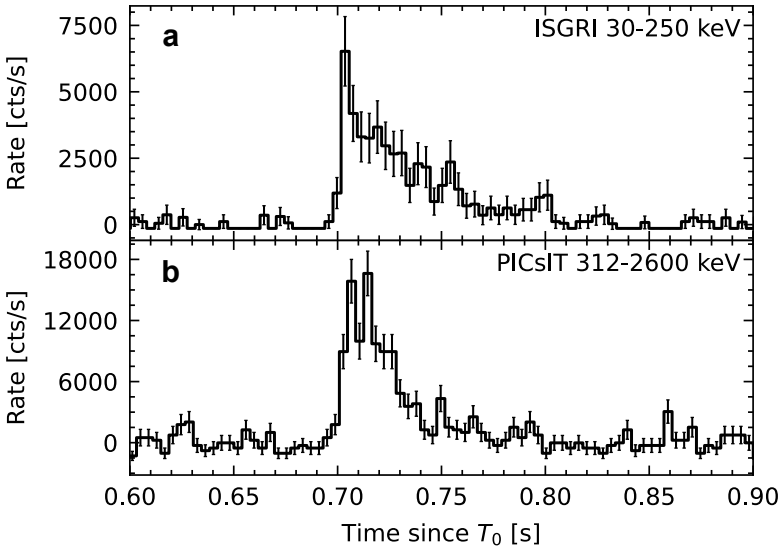

Figure 5.3: Light curves of GRB 231115A. Background-subtracted light curves (errors are at 1σ) obtained with the ISGRI detector in the $30-250$ keV energy range (**a**) and with the PICsIT detector in the $312-2600$ keV energy range (**b**). Time is referred to T_0 = 2023-11-15 15:36:20 UT (time at the INTEGRAL position; the burst reached instruments on low Earth orbit satellites about 0.4 s later).

visible in the two IBIS detectors (see Section 2.1).

I extracted an ISGRI spectrum in 14 logarithmically spaced energy channels between $30-500$ keV in two time intervals from 15:36:20.687 to 15:36:20.748 UT that corresponds to the peak of the burst, and the total spectrum from 15:36:20.687 to 15:36:20.833 UT, which includes the whole burst duration.

The PICsIT spectrum was extracted only for the peak time interval, from the spectral-timing data mode in 8 predefined energy channels spanning the $212-2600$ keV range. Data in spectral-timing mode (counts integrated over the whole detector in 3.9 ms time bins) do not provide imaging information (contrary to the ISGRI data). Therefore, the background count-rate in each PICsIT energy channel was calculated as the median count rate during the INTEGRAL science window (5013 s duration) containing the burst. A proper correction factor was applied to the PICsIT effective area to account for the angular distance between the IBIS pointing direction and GRB 231115A.

A 5% systematic uncertainty was added to both spectra. The ISGRI and PICsIT spectra were fitted simultaneously using XSPEC version 12.12.1 (Arnaud 1996). A fit with a power law was unacceptable ($\chi^2 = 59.4$ for 17 degrees of freedom), while a power law with exponential cut-off, defined as $F(E) = KE^{\alpha}\ \exp(-E(2+\alpha)/E_p)$, gave a good fit with photon index $\alpha = 0.04^{+0.27}_{-0.24}$, peak energy $E_p = 551^{+81}_{-59}$ keV, and $30-2600$ keV flux $F = (7.2^{+0.6}_{-0.7}) \times 10^{-6}$ erg cm^{-2} s^{-1}.

The ISGRI spectrum for the time interval corresponding to the whole GRB is less well constrained, but the best fit parameters are within the errors consistent with those of the ISGRI plus PICsIT spectrum. All the fit parameters are summarized in Table 5.4, where also the results obtained with a blackbody model are given.

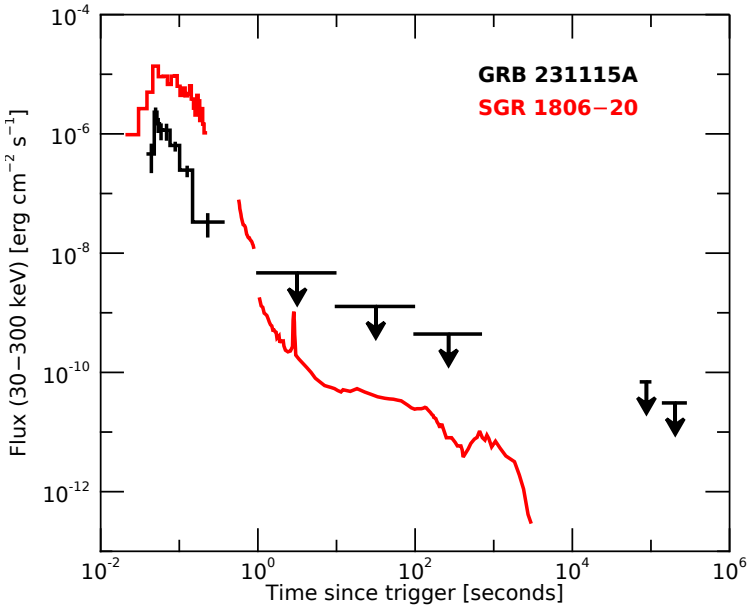

Figure 5.4: Comparison between GRB 231115A and the 2004 giant flare from SGR 1806–20. Errors are at 1σ, upper limits are at 3σ. The light curve of SGR 1806–20 (red) has been rescaled to the distance of M82 (data from Helicon-Coronas-F, Frederiks et al. (2007a), Konus-Wind, Frederiks et al. (2007a) and INTEGRAL, SPI-ACS Mereghetti et al. (2005b)). Note that the 5.2 s periodicity in the SGR 1806–20 light curve is not visible due to the used bin size.

Follow up observation. After the discovery of GRB 231115A INTEGRAL carried out a Target of Opportunity (ToO) observation that started only 21 hours after the burst and continued in the next satellite revolution. The first part of the ToO was done between 12:38 UT and 19:46 UT of November 16. The next one from 07:21 UT of November 17 to 23:09 UT of November 18, resulting in a total exposure of 162 ks divided in 57 science windows. Using the OSA 11.2 software, I produced the mosaics of the ISGRI images in the $30 - 100$ keV energy range for three periods: November 16, November 17-18, and November 16 to 18. No sources were detected at the position of GRB 231115A. The 3σ upper limits on the $30 - 100$ keV flux, derived assuming a thermal bremsstrahlung spectrum with temperature $kT = 30$ keV, are 6.5×10^{-11} erg cm^{-2} s^{-1} for November 16, 2.9×10^{-11} erg cm^{-2} s^{-1} for November 17-18, and 2.6×10^{-11} erg cm^{-2} s^{-1} for the sum of the two periods. I also derived an upper limit of 3.8×10^{-10} erg cm^{-2} s^{-1} on the flux in the time interval from $T_0 + 1.7$ s to $T_0 + 11.8$ min, during which the GRB 231115A position was in the IBIS field of view. All these upper limits are plotted in Figure 5.4, where it can be seen that, even a giant flare as energetic as the one emitted from SGR 1806–20, at the distance of M82 would have been undetectable by IBIS after the initial bright pulse.

Search for past activity from M82. The region of M82 has been repeatedly observed with INTEGRAL, starting in November 2003. I followed the procedure described in

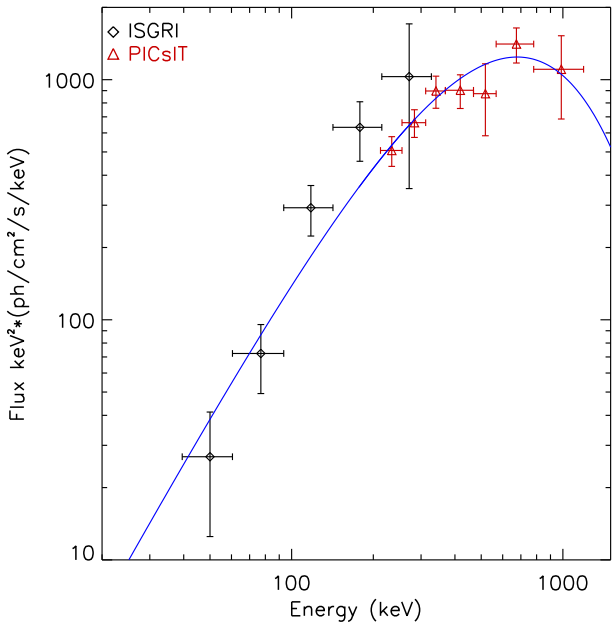

Figure 5.5: Time averaged IBIS spectrum of GRB 241107A (from T_0+0.17 s to T_0+0.40 s). ISGRI data are plotted as black diamonds and PICsIT data as red triangles. The best fit cutoff power-law model is overplotted as a solid blue line.

Section 2.2 to search for other possible bursts from this direction, however none was found. Through simulations I found that bursts down to a factor ∼5 fainter than GRB 231115A would have been detected in these data, assuming the same time profile and spectrum.

Discussion and conclusions

The position of GRB 231115A coincides with the nearby starburst galaxy M82 (Förster Schreiber et al. 2003). Notably, the central region of the galaxy, where most star formation activity occurred, is inside the INTEGRAL/IBIS error region. Considering that the total angular size of all the galaxies with apparent luminosity brighter than M82 (excluding the Magellanic Clouds and M31) is ∼6000 arcmin^2, the chance alignment with GRB 231115A is 4×10^{-5}. A more elaborate analysis of Burns (2023) indicates that the Bayes factor favouring a giant flare in M82 with respect to a chance alignment of a short GRB in the background is a factor 30 larger than that of the previous best MGF candidate (GRB 200415A possibly associated to NGC 253 Hurley et al. 2021), making GRB 231115A by far the most compelling case for an MGF outside the local group of galaxies.

M82 was in the field of view of IBIS starting from 9.2 hours before up to 11.8 minutes after the occurrence of GRB 231115A, but no other bursts were detected. The corresponding fluence upper limit of the order of 10^{-7} erg cm^{-2} for a 0.1 s duration does not exclude the possibility of precursor activity as seen in the Galactic MGFs (Hurley et al. 1999; Palmer et al. 2005). An INTEGRAL target of opportunity observation was

Table 5.4: Results of spectral fits of GRB 231115A. Errors are at 1σ, fluxes are in the $30-2600$ keV energy range. Time intervals are in seconds after T_0 = 15:36:20 UT.

Detectors	ISGRI+PICsIT	ISGRI
Time interval	0.687–0.748	0.687–0.833
Blackbody		
kT (keV)	108^{+7}_{-5}	68^{+12}_{-11}
Flux (10^{-6} erg cm^{-2} s^{-1})	$7.9^{+0.6}_{-0.7}$	$2.1^{+0.6}_{-0.7}$
χ^2 / d.o.f.	31.9/17	16.4/12
Cut-off power law		
α	$0.04^{+0.27}_{-0.24}$	$0.55^{+0.50}_{-0.42}$
E_p (keV)	551^{+81}_{-59}	355^{+158}_{-89}
Flux (10^{-6} erg cm^{-2} s^{-1})	$7.2^{+0.6}_{-0.7}$	2.7 ± 1.1
χ^2 / d.o.f.	17.2/16	14.9/11

performed in the following three days, but no other bursting or persistent emission was detected by IBIS from the direction of M82. Integrating all the data of the ToO observation, the upper limit on the persistent emission at the position of GRB 231115A is 2.6×10^{-11} erg cm^{-2} s^{-1} on the 30–100 keV.

At the distance of M82 (3.6 Mpc, Freedman et al. 1994), the GRB 231115A fluence measured with IBIS implies an emitted isotropic energy $E_{\rm iso} = 10^{45}$ erg (1 keV – 10 MeV), well below the typical value for a short GRB, but consistent with the one of the initial pulses of the three giant flares securely associated with magnetars (Hurley et al. 1999; Palmer et al. 2005; Mazets et al. 1979b). The short duration and hard spectrum of GRB 231115A are also in agreement with the properties seen in the initial pulses of MGFs. In the three giant flares securely associated with magnetars, the initial short and hard pulse was followed by a softer tail, with a duration of a few minutes and a maximum luminosity of $\sim 10^{42}$ erg s^{-1}, characterized by a periodic modulation induced by the neutron star rotation. A similar feature would be too faint to be visible by IBIS at the distance of M82. This is shown in Figure 5.4, which compares the limits obtained for GRB 231115A with the light curve of the most energetic Galactic giant flare ever observed (the one emitted by SGR 1806–20 in 2004; Palmer et al. 2005) rescaled to a distance of 3.6 Mpc.

The field of GRB 231115A was promptly observed with the Neil Gehrels Swift Observatory starting 9 ks after the burst (Osborne et al. 2023) and a deeper X-ray observation was carried out with the XMM-Newton satellite, starting 0.7 days after the burst (Rigoselli et al. 2023).

The comparison of the Swift and XMM-Newton images with those obtained in previous observations of M82 does not show evidence for new X-ray sources inside the GRB 231115A error region. Due to the presence of unresolved X-ray emission from the central part of the galaxy, the corresponding upper limit is position-dependent. The limit of 4×10^{-14} erg cm^{-2} s^{-1} derived from the XMM-Newton data, which applies to 60% of the error region, is inconsistent with the flux at T_0+1 day of the large majority of X-ray afterglows of short GRBs detected with the Swift/XRT instrument. Although a rapid

afterglow drop, as observed in the class of so-called short lived short GRBs (Sakamoto & Gehrels 2009), cannot be excluded, this X-ray upper limit disfavors the GRB interpretation. It is instead consistent with the quiescent X-ray emission of a magnetar in M82. In fact the X-ray luminosity of known magnetars, also considering the peak values reached during outbursts (Coti Zelati et al. 2018), never exceeds 10^{36} erg s^{-1}, corresponding to 6×10^{-16} erg cm^{-2} s^{-1} at the M82 distance.

Holding true the association of GRB 231115A with M82 on the basis of the remarkable spatial coincidence, the low value of $E_{\rm iso}$ could be reconciled with a short GRB origin only if the jet axis is pointed away from our direction, similar to the case of the gravitational wave event GRB 170817A (Abbott et al. 2017), which produced the bright kilonova AT2017gfo in the optical/NIR band. However, the deep upper limits of m > 20.0 – 24.0 mag (depending on the assumed position in the INTEGRAL error circle) on the optical counterpart that was obtained starting at T_0+0.2 days exclude this possibility, both for an AT2017gfo-like event and for even fainter kilonovae. Furthermore, an off-axis GRB event would likely display a longer duration than that observed for GRB 231115A. Finally note that the binary merger of two compact objects at 3.6 Mpc would have produced a strong signal in gravitational waves, at variance with the non-detection reported by the LIGO/Virgo/KAGRA Collaboration (Ligo Scientific Collaboration et al. 2023).

The discovery of a young, active magnetar in M82, a starburst galaxy characterized by a high star formation rate (Leroy et al. 2019) is consistent with the origin of magnetars in core collapse supernova explosions (Duncan & Thompson 1992). The volumetric rate of MGFs with $E_{\rm iso} > 4 \times 10^{44}$ erg has been recently estimated (Burns et al. 2021) as $(3.8^{+4.0}_{-3.1}) \times 10^5$ Gpc^{-3} yr^{-1}. Assuming a direct link with the young stellar population of core collapse progenitors and considering the total star formation rate of 4000 $M_\odot$ yr^{-1} within 50 Mpc, this corresponds to a rate of $R(E_{\rm iso} > 4\times 10^{44}) = 0.05^{+0.05}_{-0.04}$ yr^{-1} $(M_\odot\,{\rm yr}^{-1})^{-1}$. Given the star formation rate of 7.1 $M_\odot$ yr^{-1} in M82 (Leroy et al. 2019) and assuming a power-law distribution of the giant flares energies with slope 1.7, the expected rate of MGFs with $E_{\rm iso} > 10^{45}$ erg in M82 is $R_{\rm M82}(E_{\rm iso} > 10^{45}) = 0.19^{+0.19}_{-0.15}$ yr^{-1}.

GRB 051103 is another short GRB that has been proposed as a possible MGF in the M81 group of galaxies (Frederiks et al. 2007b). According to a detailed statistical analysis (Burns et al. 2021), M82 is the most likely host of GRB 051103, despite being slightly outside its 260 arcmin^2 localization region. The rate of MGFs derived above is fully consistent with the detection of two events from M82 in 20 years.

Therefore, starburst galaxies such as M82, which produce a significant population of young magnetars, appear as promising targets to constrain the energy distribution function of MGFs by means of long dedicated observations with future high sensitivity instruments.

5.2.2 GRB 241107A

The short GRB 241107A was first found in data from the *SVOM* and INTEGRAL satellites (Wang et al. 2024b; Rodi et al. 2024). An error box with area of about one square

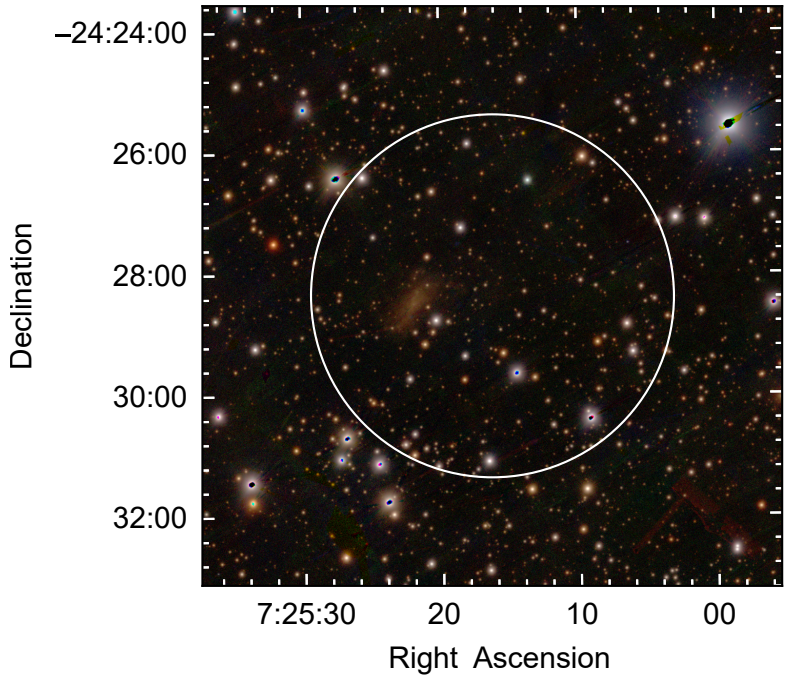

Figure 5.6: Pan-STARRS1 optical image of the location of GRB 241107A, with the i-band, r-band, and g-band used as RGB colours. The circle with radius 3 arcmin is the IBIS/ISGRI position (90% c.l.). The galaxy PGC 86046 is clearly visible at coordinates R.A.=7:25:22, Dec.=−24:28:23

degree was later obtained by triangulation of data from SVOM, INTEGRAL, Konus-WIND and Swift (Kozyrev et al. 2024). The only reported optical follow-up observation was performed 4.8 days after the trigger with the GROWTH-India Telescope, which derived upper limits of about 20.8 and 20.6 mag for r′ and i′ filters, respectively (Mohan et al. 2024). Although the burst was inside the fields of view of the INTEGRAL/IBIS and Swift/BAT imaging instruments, it was too faint to trigger the automatic burst searches. The offline analysis of these data provided positions with uncertainties of a few square arcmin (Mereghetti et al. 2024b; DeLaunay et al. 2024) at coordinates consistent with those of the galaxy PGC 86046 which has a distance of $4.1^{+1.2}_{-0.9}$ Mpc (Tully et al. 2016).

The burst has been detected with ISGRI with the highest significance (6.7σ) in the 30-180 keV energy range and in the time interval from T_0+0.17 s to T_0+0.40 s (with T_0=2024-11-07 23:30:00 UTC). The derived coordinates are R.A.= 111.3360 deg, Dec.= −24.4439 deg (J2000) with an uncertainty of 3 arcmin (90% c.l. radius). Fig. 5.6 shows the error region of GRB 241107A superimposed on an optical image from Pan-STARRS1 (Chambers et al. 2016), where the PGC 86046 galaxy is clearly visible.

Observations and Data Analysis

GRB 241107A was detected in the PICsIT data in spectral-timing mode, which have a time resolution of 3.9 ms with counts integrated over the entire detector in 8 pre-defined energy channels from 212 keV to 2.6 MeV. Therefore, no imaging information is available for this data type. The background count rate in each energy channel was taken to be the

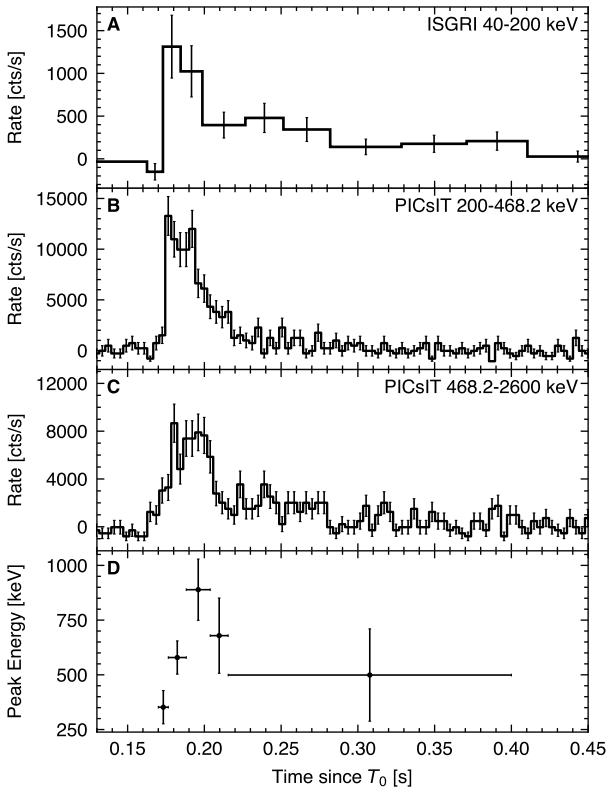

Figure 5.7: Background subtracted light curves of GRB 241107A in three energy bands, with T_0=2024-11-07 23:30:00 UT. The ISGRI (40-200 keV) light curve has been binned to have at least 18 counts in each bin (A panel). The PICsIT light curves (200-468.2 keV, B panel and 468.2-2600 keV, C panel) have the original bin size of 3.9 ms. Panel D shows the evolution of E_p during the burst.

median count rate during the INTEGRAL pointing (1800 s) including GRB 241107A . To account for the angular distance between GRB 241107A and the IBIS pointing direction (11.6 degrees), a correction was applied to the PICsIT effective area. This procedure is the same that was also used in the analysis of GRB 231115A in Section 5.2.1

Timing and spectral properties

The light curves of GRB 241107A as measured by IBIS in different energy ranges are plotted in Fig. 5.7. The burst had a total duration of ∼250 ms and consisted of an initial pulse lasting ∼50 ms followed by a fainter tail. An image extracted from the ISGRI data in the time interval from T_0+0.25 s to T_0+0.40 s confirms that the tail is indeed due to the burst. Based on the PICsIT light curve, the GRB rise occurred within a single time bin and thus it lasted less than 3.9 ms.

The time averaged spectrum of GRB 241107A , obtained from the ISGRI and PICsIT data of the whole duration of the burst, is shown in Fig. 5.5. A good fit is found with an exponentially cut off power law model with photon index $\alpha = 0.07^{+0.27}_{-0.24}$, peak energy $E_p = 678^{+125}_{+90}$ keV and 20 keV − 10 MeV flux of (3.4±0.5)×10^{-6} erg cm^{-2} s^{-1}. This corresponds to a fluence of $\sim 8 \times 10^{-7}$ erg cm^{-2}. A single blackbody model gives a temperature of $kT = 136^{+15}_{-11}$ keV, but the fit is worse. All the fit parameters are given

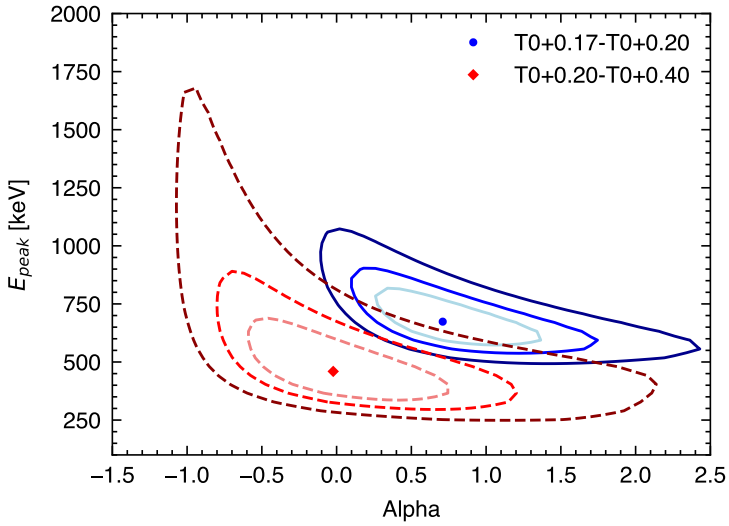

Figure 5.8: Confidence contours of the joint ISGRI+PICsIT spectra for the peak (T_0+0.17-T_0+0.20, solid blue line) and tail (T_0+0.20-T_0+0.40, dashed red line) of the burst. The contours represent confidence levels of 68%, 90%, and 99%.

in Table 5.5.

I also extracted ISGRI and PICsIT spectra for two time intervals corresponding to the main pulse and the tail. Although the best fit parameters have relatively large uncertainties, they seem to indicate that the spectrum of the tail is slightly softer than that of the peak (see Table 5.5). As shown by the contour plots of the errors on α and E_p in Fig. 5.8, the spectral variation can be better described by a reduction in the peak energy, rather than by a change in α.

To further investigate the burst spectral evolution I split the PICsIT data into the five time intervals indicated in Table 5.5 and performed a joint fit to an exponentially cutoff power law with α fixed to the time-averaged value (0.07). At the start of the burst E_p increases from $\sim$ 330 keV to a maximum value of $\sim$ 890 keV at the peak before decreasing to roughly 500 keV as the flux decays though the errors on the E_p values are large (see bottom panel of Figure 5.7 and Table 5.5).

The sky position of GRB 241107A was repeatedly observed by INTEGRAL starting from February 2003 to $T_0 + 5.7$ days. I extracted from the public data archive all the relevant IBIS pointings, totalling 9 Ms of exposure. Using the method described in Section 2.2, I searched for other possible bursts from this position, but none were found.

Discussion and conclusions

The chance coincidence of finding a galaxy brighter than magnitude m in an error circle of radius R is given by

$$P(< m) = 1 - \mathrm{e}^{-\pi R^2 \sigma(<m)} \tag{5.4}$$

where, $\sigma(< m)$ is the number density of galaxies brighter than m. $\sigma(< m)$ can be derived from the galaxy number counts plotted in Fig. 4 of Ferguson et al. (2000) and using the

Table 5.5: Results of spectral fits of GRB 241107A.

Interval	Start–Stop[a]	Model[b]	α	E_p	T_{BB}	Flux[c]	χ^2(dof)
Total	0.17–0.40	CPL	$0.07^{+0.27}_{-0.24}$	678^{+125}_{-90}	–	3.4 ± 0.5	8.8(9)
		BB	–	–	136^{+15}_{-11}	$2.7^{+0.4}_{-0.2}$	21.8(10)
Peak	0.17–0.20	CPL	$0.71^{+0.42}_{-0.31}$	674^{+85}_{-71}	–	$16.1^{+1.9}_{-1.8}$	14.3(9)
		BB	–	–	152^{+18}_{-9}	$14.7^{+1.4}_{-1.5}$	17.0(10)
Tail	0.20–0.40	CPL	$-0.02^{+0.48}_{-0.39}$	460^{+126}_{-88}	–	1.1 ± 0.2	13.9(8)
		BB	–	–	99^{+22}_{-20}	1.0 ± 0.2	19.3(9)
1	0.1700−0.1765	CPL	0.07[d]	352 ± 76		8^{+2}_{-2}	4.75(5)
2	0.1765−0.1882	CPL	0.07[d]	579 ± 76		24^{+5}_{-4}	9.80(5)
3	0.1882−0.2038	CPL	0.07[d]	889 ± 140		25^{+8}_{-6}	5.00(5)
4	0.2038−0.2155	CPL	0.07[d]	679 ± 172		9^{+3}_{-2}	3.10(5)
5	0.2155−0.4000	CPL	0.07[d]	499 ± 211		$0.6^{+0.4}_{-0.3}$	4.36(4)

[a] Times are relative to T_0 and expressed in seconds.
[b] CPL = cut off power law; BB = blackbody.
[c] Flux integrated over the 20 keV–10 MeV energy range, in units of 10^{-6} erg cm^{-2} s^{-1}.
E_p and T_{BB} are given in keV.
[d] Parameter fixed during the fit.

PGC 86046 magnitudes in the I and B bands, $m_B = 16.336$, $m_I = 14.634$, reported in the HIPASS catalogue (Doyle et al. 2005). For R=3 arcmin, the chance coincidence probabilities are equal to $P(< m_B)$=2.9% and $P(< m_I)$=5.5%.

At the PGC 86046 distance of 4.1 Mpc (Tully et al. 2016), the fluence derived above for GRB 241107A corresponds to an emitted isotropic energy $E_{iso} = 1.6 \times 10^{45}$ erg, that fits perfectly with the typical values of MGFs. This is illustrated in the $E_p - E_{iso}$ plot of Fig. 5.9, where the values of GRB 241107A for different assumed distances are compared with those of the other MGFs and of the short GRBs.

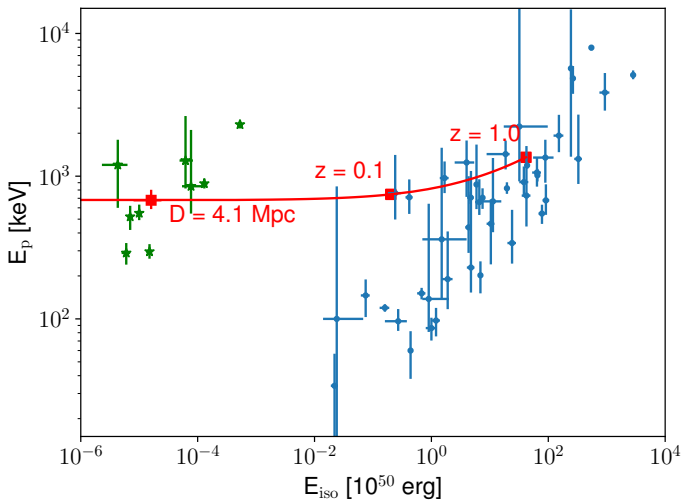

Figure 5.9: Position of GRB 241107A (red square) in the E_p versus E_{iso} plane. The sample of short GRBs (blue) is taken from Minaev & Pozanenko (2020). The three confirmed magnetar giant flares and the extragalactic MGF candidates are indicated by the green stars (data from Table 5.1 and references therein and Svinkin et al. (2016)).

It is interesting to compare GRB 241107A with the MGF candidate in the Sculptor Galaxy, GRB 200415A (Svinkin et al. 2021; Roberts et al. 2021), which, in the small sample of extragalactic MGFs, is probably the one with the best spectral information. During the initial ∼7 ms, its spectrum hardened, with E_p evolving from 430 keV to 1.8 MeV, and then it gradually softened with E_p tracing the downward flux evolution. A similar behavior is possibly seen also in GRB 231115A (Trigg et al. 2025), which is currently the most convincing extragalactic MGF and is associated to the M82 starburst galaxy (Mereghetti et al. 2024c). The spectral evolution of GRB 241107A shown in Fig. 5.7 is consistent with a similar behavior. These three bursts are also similar for their rise times $\lesssim$4 ms and some evidence for a double-peaked light curve.

For GRB 200415A time-resolved analysis of the relationship between E_p and the isotropic luminosity (L_{iso}) found $E_p \propto L_{iso}^{0.23\pm0.10}$ (Chand et al. 2021). The authors report a stronger correlation with an exponent of 0.31 ± 0.04 when excluding the three spectra before $T_0 - 0.001$s. In the case of GRB 231115A, the exponent is $0.35^{+0.11}_{-0.07}$ or $0.41^{+0.21}_{-0.08}$ depending on the time binning (Trigg et al. 2025). A fit to our values for GRB 241107A has an exponent of 0.32 ± 0.15, similar to that of the other two MGF candidates.

In conclusion, although it cannot be excluded that GRB 241107A is an ordinary short GRB at redshift $\gtrsim$0.1, its properties are consistent with an MGF origin, as it is suggested by the presence of a nearby galaxy with a chance probability of only a few percent of being in the burst error region. Unfortunately, GRB 241107A could not be localized precisely in near real time. Rapid follow-up observations at other wavelengths could have provided compelling evidence in favor of one of the two possibilities for the nature of GRB 241107A .

Summary and Conclusions

The work described in this thesis focused on the study of the hard X-ray emission from magnetars using all the currently (Fall 2025) available data from the INTEGRAL/IBIS instrument. I studied both the persistent emission, that could be examined in detail only for the few magnetars sufficiently bright in this energy range, and the bursting emission. For this latter aspect, I could analyse data for the whole sample of known magnetars in the Galaxy and Magellanic Clouds, thanks to the complete sky coverage and long exposure obtained by INTEGRAL. The public archival data I used represent virtually the totality of IBIS data on magnetars[1]. Important information on magnetars can also be obtained from the ones outside the Local Group, which can be detected only when they emit giant flares. I used the extensive INTEGRAL observations of the Virgo cluster and other nearby galaxies with high star formation rates to constrain the rate of giant flares emitted by magnetars as a function of their isotropic energy.

INTEGRAL discovered the persistent hard X-ray emission in magnetars, showing that it is an energetically relevant component. The persistent emission from magnetars has been extensively studied in the classical X-ray energy range (below ∼10 keV). However, progress in the hard X-rays has been more difficult, owing to the relatively faint fluxes in relation to the sensitivity of current instruments. I concentrated on data obtained with the IBIS/ISGRI detector, which led to the detection of eight magnetars during more than twenty years of observations. Five of them were detected multiple times, allowing the construction of long-term light curves. I revealed flux evolution SGR 1806–20 and PSR J1846–0258 that was previously unnoticed. For the first source, flux evolution after the outbursts, specifically after 2011, showed an increase followed by a decrease in 2016. For the latter, the analysis showed small, but statistically significant, long-term variability.

The great majority of the data I analysed were not published before. I used the most updated analysis software and calibrations and, in general, I found a good agreement with published results (which refer mostly to observation obtained before 2011). However, in some cases, small differences were also found in the spectral parameters and/or reported fluxes. These can be in part explained by the different methods, calibrations and data selections that were used. I also showed, through several tests based on ISGRI imaging and comparisons with NuSTAR observations, that systematic overestimations of the ISGRI fluxes can be obtained for detections at low signal-to-noise ratio. The relatively high threshold that I adopted to overcome this problem, resulted in the need for long exposures and/or a limited number of spectral channels. This was especially true for

[1] only a small number of observations could not be used because not yet public.

the second half of the INTEGRAL mission, owing to the gradual radiation damage experienced by the ISGRI detector, which caused an increase in the effective low energy threshold usable for the analysis. With this conservative approach, the obtained results on the persistent emission from the few detected magnetars, although limited, can be considered as reliable.

For what concerns the study of short bursts, I could consider the whole population of currently confirmed magnetars plus a few candidates (about 40 sources). I performed a systematic search for short bursts from all these sources using ISGRI data from the start of the mission through October 2024. The total exposure across all sources amounted to over 1,100 Ms. Essential for this analysis was the imaging capability of ISGRI, which allowed me to confirm the nature of burst candidates found in the analysis of light curves, especially in crowded regions such as the Galactic Centre. My analysis led to a final sample of 1,351 confirmed bursts from 21 different sources. 935 bursts were detected from SGR 1806–20, 233 bursts from SGR 1935+2154, and 146 bursts from 1E 1547.0–5408, and the remaining 37 bursts were detected from 18 other sources. This is the only systematic search for magnetar bursts using INTEGRAL data, so the sample includes many bursts that have never been reported before, including single bursts from sources that have not shown intensive bursting activity.

As with the persistent emission, the evolving low energy threshold of ISGRI influenced this part of the analysis. While most bursts had enough counts above ∼35 keV to be detected through the whole time period, some of the faintest ones would not be detected when the sensitivity at low energies decreased (as it was the case for SGR 1935+2154, which was active after 2015). Nevertheless, the overall effect should be limited to only the faintest bursts. This effect was visible, for example, in the results on the fluence distributions of the three source, where SGR 1935+2154 had a low energy cut-off (which is determined by the instrument's sensitivity limit) that was two times higher than that of SGR 1806–20.

INTEGRAL has also given important contributions to the study of extragalactic Magnetar Giant Flares. I carried out the spectral and timing analysis of the IBIS data of the two most recent extragalactic MGFs candidates: GRB 231115A, in the nearby starburst galaxy M82 and GRB 241107A, likely associated to the galaxy PGC 86046. While the precise position of GRB 241107A was determined with a delay of a few days, GRB 231115A was localised in real time by the INTEGRAL Burst Alert System at arcmin level. This prompted fast follow-up observations at other wavelengths, making this the most compelling case for an extragalactic MGF to date.

The rate of MGFs is poorly constrained, with only three confirmed events from local magnetars observed during the last 45 years. Even with the addition of extragalactic candidates, the sample remains small. As MGFs can release up to a significant fraction of the total magnetic energy available in a magnetar, better constraints on their rates are essential for a deeper understanding of the magnetic budget of magnetars and their evolution. Since it can be assumed that the number of magnetars in a galaxy scales with the star formation rate of the galaxy, the rate of MGFs can be constrained by searching

for them in galaxies with high star-formation rates. I applied a technique similar to that used for short bursts to systematically search for extragalactic MGFs in the archival INTEGRAL data. I selected the Virgo cluster, the closest cluster of galaxies (∼16.5 Mpc) which also contains multiple star-forming galaxies, as well as seven closer galaxies with high star-formation rates.

In about 35 Ms of INTEGRAL data on the Virgo cluster and a total of ~ 100 Ms on the nearby galaxies, I detected only one MGF (the one in M82 mentioned above). Using the non-detection of other MGFs, I derived an upper limit on the rate of MGFs. The obtained limit corresponds to about one giant flare with $E > 3 \times 10^{45}$ erg every ~ 500 yr per magnetar. The search for MGFs in nearby galaxies (at distances of 2–5 Mpc), which included the detection of the MGF in M82, allowed me to place constraints on the rate of lower-energy MGFs. I derived a lower limit of $R(> E) > 4 \times 10^{-4}$ yr^{-1} magnetar^{-1} for energies $E < 10^{45}$ erg.

These constraints are limited by two factors: the total available observation time and the instrumental sensitivity. The spectra of the initial spikes of MGF are harder than those of short SGR bursts, and this makes them easier to detect with ISGRI. However, its sensitivity still limited the search to only the closest galaxies for MGF energies below $\sim 10^{45}$ erg. Nevertheless, the constraints I obtained with this survey are the first systematic limits on MGF rates derived with hard X-ray monitoring with a wide field of view and good source location capability. Future instruments with higher sensitivity and a large field of view, such as the THESEUS satellite's X-Gamma-ray Imaging Spectrometer (Amati et al. 2022), will make it possible to improve these limits and detect more extragalactic MGFs at larger distances, enhancing our understanding of these extreme events. For the study of both persistent and bursting emission from magnetars, future progress will greatly benefit from instruments that provide broad energy coverage with high sensitivity. High-quality spectra and time-resolved spectroscopy during bursts across a wide energy range (from soft to hard X-rays) would allow systematic studies connecting short bursts, intermediate bursts, and giant flares.

Bibliography

Abbott, B. P., Abbott, R., Abbott, T. D., et al. 2017, ApJ, 848, L12

Alexander, R. & Fedorova, V. 2020, ATel, 14186, 1

Alford, J. A. J. & Halpern, J. P. 2016, ApJ, 818, 122

Amati, L., Labanti, C., Mereghetti, S., et al. 2022, in Society of Photo-Optical Instrumentation Engineers (SPIE) Conference Series, Vol. 12181, Space Telescopes and Instrumentation 2022: Ultraviolet to Gamma Ray, ed. den Herder, J.-W. A., Nikzad, S., & Nakazawa, K., 1218126

An, H., Archibald, R. F., Hascoët, R., et al. 2015, ApJ, 807, 93

An, H., Cumming, A., & Kaspi, V. M. 2018, ApJ, 859, 16

An, H., Hascoët, R., Kaspi, V. M., et al. 2013, ApJ, 779, 163

An, H., Kaspi, V. M., Beloborodov, A. M., et al. 2014, ApJ, 790, 60

Aptekar, R. L., Frederiks, D. D., Golenetskii, S. V., et al. 2001, ApJS, 137, 227

Archibald, R. F., Burgay, M., Lyutikov, M., et al. 2017a, ApJ, 849, L20

Archibald, R. F., Kaspi, V. M., Ng, C.-Y., et al. 2013, Nature, 497, 591

Archibald, R. F., Kaspi, V. M., Ng, C. Y., et al. 2015, ApJ, 800, 33

Archibald, R. F., Kaspi, V. M., Tendulkar, S. P., & Scholz, P. 2016, ApJ, 829, L21

Archibald, R. F., Scholz, P., & Kaspi, V. 2017b, ATel, 10107, 1

Archibald, R. F., Scholz, P., Kaspi, V. M., Tendulkar, S. P., & Beardmore, A. P. 2020, ApJ, 889, 160

Arnaud, K. A. 1996, in Astronomical Society of the Pacific Conference Series, Vol. 101, Astronomical Data Analysis Software and Systems V, ed. Jacoby, G. H. & Barnes, J., 17

Aschwanden, M. J., Crosby, N. B., Dimitropoulou, M., et al. 2016, Space Sci. Rev., 198, 47

Astropy Collaboration, Price-Whelan, A. M., Lim, P. L., et al. 2022, ApJ, 935, 167

Astropy Collaboration, Price-Whelan, A. M., Sipőcz, B. M., et al. 2018, AJ, 156, 123

Astropy Collaboration, Robitaille, T. P., Tollerud, E. J., et al. 2013, A&A, 558, A33

Bansal, K., Wharton, R. S., Pearlman, A. B., et al. 2023, MNRAS, 523, 2401

Barthelmy, S. D., Baumgartner, W. H., Beardmore, A. P., et al. 2008, ATel, 1676, 1

Beloborodov, A. M. 2009, ApJ, 703, 1044

Beloborodov, A. M. 2017, ApJ, 843, L26

Beloborodov, A. M. & Li, X. 2016, ApJ, 833, 261

Beniamini, P., Wadiasingh, Z., Trigg, A., et al. 2025, ApJ, 980, 211

Bernardini, F., Israel, G. L., Dall'Osso, S., et al. 2009, A&A, 498, 195

Bibby, J. L., Crowther, P. A., Furness, J. P., & Clark, J. S. 2008, MNRAS, 386, L23
Blumer, H., Safi-Harb, S., McLaughlin, M. A., & Fiore, W. 2021, ApJ, 911, L6
Bochenek, C. D., Ravi, V., Belov, K. V., et al. 2020, Nature, 587, 59
Borghese, A., Coti Zelati, F., Rea, N., et al. 2020, ApJ, 902, L2
Borghese, A., Rea, N., Turolla, R., et al. 2019, MNRAS, 484, 2931
Braithwaite, J. 2009, MNRAS, 397, 763
Burgay, M., Possenti, A., Kerr, M., et al. 2016a, ATel, 9286, 1
Burgay, M., Possenti, A., Kerr, M., et al. 2016b, ATel, 9366, 1
Burns, E. 2023, GCN, 35038, 1
Burns, E., Svinkin, D., Hurley, K., et al. 2021, ApJ, 907, L28
Cai, C., Li, X.-B., Xiong, S.-L., et al. 2024, GCN, 37606, 1
Cai, C., Xiong, S.-L., Lin, L., et al. 2022, ApJS, 260, 25
Caleb, M., Rajwade, K., Desvignes, G., et al. 2022, MNRAS, 510, 1996
Camero, A., Papitto, A., Rea, N., et al. 2014, MNRAS, 438, 3291
Camilo, F., Ransom, S. M., Halpern, J. P., & Reynolds, J. 2007a, ApJ, 666, L93
Camilo, F., Ransom, S. M., Halpern, J. P., et al. 2006, Nature, 442, 892
Camilo, F., Ransom, S. M., Peñalver, J., et al. 2007b, ApJ, 669, 561
Castro-Tirado, A. J., Østgaard, N., Göğüş, E., et al. 2021, Nature, 600, 621
Ćerri-Serim, D., Serim, M. M., Şahiner, Ş., Inam, S. ć., & Baykal, A. 2019, MNRAS, 485, 2
Chambers, K. C., Magnier, E. A., Metcalfe, N., et al. 2016, arXiv:1612.05560
Champion, D., Cognard, I., Cruces, M., et al. 2020, MNRAS, 498, 6044
Chand, V., Joshi, J. C., Gupta, R., et al. 2021, RAA, 21, 236
Chatterjee, R., Agrawal, V. K., & Nandi, A. 2021, MNRAS, 505, 3785
Cheng, B., Epstein, R. I., Guyer, R. A., & Young, A. C. 1996, Nature, 382, 518
Cheung, C. C., Kerr, M., Grove, J. E., et al. 2023, GCN, 35045, 1
CHIME/FRB Collaboration, Andersen, B. C., Bandura, K. M., et al. 2020, Nature, 587, 54
Clauset, A., Shalizi, C. R., & Newman, M. E. J. 2009, SIAM Review, 51, 661
Cline, T., Frederiks, D. D., Golenetskii, S., et al. 2000, ApJ, 531, 407
Cline, T. L., Desai, U. D., Pizzichini, G., et al. 1980, ApJ, 237, L1
Cline, T. L., Desai, U. D., Teegarden, B. J., et al. 1982, ApJ, 255, L45
Collazzi, A. C., Kouveliotou, C., van der Horst, A. J., et al. 2015, ApJS, 218, 11
Coti Zelati, F., Borghese, A., Rea, N., et al. 2021, ATel, 14674, 1
Coti Zelati, F., Rea, N., Pons, J. A., Campana, S., & Esposito, P. 2018, MNRAS, 474, 961
Courvoisier, T. J.-L., Walter, R., Beckmann, V., et al. 2003, A&A, 411, L53
Crawford, D. F., Jauncey, D. L., & Murdoch, H. S. 1970, ApJ, 162, 405
Şaşmaz Muş, S., Aydın, B., & Göğüş, E. 2014, MNRAS, 440, 2916
Şaşmaz Muş, S. & Göğüş, E. 2013, ApJ, 778, 156
Cummings, J. R., Burrows, D., Campana, S., et al. 2011, ATel, 3488, 1
Curran, P. A. 2014, arXiv:1411.3816

Dai, S., Johnston, S., Weltevrede, P., et al. 2018, MNRAS, 480, 3584
Dalessi, S., Roberts, O. J., Veres, P., Meegan, C., & Fermi Gamma-ray Burst Monitor Team. 2023, GCN, 35044, 1
Dall'Osso, S., Israel, G. L., Stella, L., Possenti, A., & Perozzi, E. 2003, ApJ, 599, 485
D'Avanzo, P. 2015, JHEAp, 7, 73
De Grandis, D., Rea, N., Kovlakas, K., et al. 2025, A&A, 701, A229
De Marco, G., Martin, J., Toma, L., et al. 2023, in Space Operations: Proceedings of the 17th International Conference on Space Operations (SpaceOps 2023) (Mohammed Bin Rashid Space Centre (MBRSC) on behalf of SpaceOps), paper ID #481, Copyright © 2023 European Space Agency
DeLaunay, J., Tohuvavohu, A., Ronchini, S., et al. 2024, GCN, 38177, 1
den Hartog, P. R., Hermsen, W., Kuiper, L., et al. 2006, A&A, 451, 587
den Hartog, P. R., Kuiper, L., & Hermsen, W. 2008a, A&A, 489, 263
den Hartog, P. R., Kuiper, L., Hermsen, W., et al. 2008b, A&A, 489, 245
den Hartog, P. R., Kuiper, L., Hermsen, W., et al. 2007, Ap&SS, 308, 647
Dhillon, V. S., Marsh, T. R., Hulleman, F., et al. 2005, MNRAS, 363, 609
Dhillon, V. S., Marsh, T. R., Littlefair, S. P., et al. 2011, MNRAS, 416, L16
Di Salvo, T., Burderi, L., Robba, N. R., & Guainazzi, M. 1998, ApJ, 509, 897
Dib, R. & Kaspi, V. M. 2014, ApJ, 784, 37
Dib, R., Kaspi, V. M., & Gavriil, F. P. 2008, ApJ, 673, 1044
Dib, R., Kaspi, V. M., & Gavriil, F. P. 2009, ApJ, 702, 614
Dichiara, S., Palmer, D. M., & Neil Gehrels Swift Observatory Team. 2024, GCN, 37222, 1
Dong, F. A. & Chime/Frb Collaboration. 2022, ATel, 15681, 1
Doyle, M. T., Drinkwater, M. J., Rohde, D. J., et al. 2005, MNRAS, 361, 34
Duncan, R. C. & Thompson, C. 1992, ApJ, 392, L9
Enoto, T., Nakazawa, K., Makishima, K., et al. 2010a, PASJ, 62, 475
Enoto, T., Nakazawa, K., Makishima, K., et al. 2010b, ApJ, 722, L162
Enoto, T., Ng, M., Hu, C.-P., et al. 2021, ApJ, 920, L4
Esposito, P., Israel, G. L., Turolla, R., et al. 2011, MNRAS, 416, 205
Esposito, P., Israel, G. L., Zane, S., et al. 2008, MNRAS, 390, L34
Esposito, P., Mereghetti, S., Tiengo, A., et al. 2007, A&A, 476, 321
Esposito, P., Rea, N., Borghese, A., et al. 2020, ApJ, 896, L30
Evans, D., Kiebesadel, R., Baros, J., et al. 1979, IAU Circ., 3356, 1
Evans, P. A., Beardmore, A. P., Page, K. L., et al. 2009, MNRAS, 397, 1177
Evans, P. A., Gropp, J. D., Kennea, J. A., et al. 2020, GCN, 27373, 1
Evans, W. D., Klebesadel, R. W., Laros, J. G., et al. 1980, ApJ, 237, L7
Fahlman, G. G. & Gregory, P. C. 1981, Nature, 293, 202
Ferguson, H. C., Dickinson, M., & Williams, R. 2000, ARA&A, 38, 667
Fermi-LAT Collaboration, Ajello, M., Atwood, W. B., et al. 2021, NatAs, 5, 385
Feroci, M., Costa, E., Amati, L., et al. 1998, IAU Circ., 6945, 3
Feroci, M., Frontera, F., Costa, E., et al. 1999, ApJ, 515, L9

Feroci, M., Hurley, K., Duncan, R. C., & Thompson, C. 2001, ApJ, 549, 1021
Ferrigno, C. 2025, GCN, 39563, 1
Förster Schreiber, N. M., Genzel, R., Lutz, D., & Sternberg, A. 2003, ApJ, 599, 193
Frederiks, D., Svinkin, D., Lysenko, A., et al. 2023, GCN, 35062, 1
Frederiks, D. D., Golenetskii, S. V., Palshin, V. D., et al. 2007a, AstL, 33, 1
Frederiks, D. D., Palshin, V. D., Aptekar, R. L., et al. 2007b, AstL, 33, 19
Freedman, W. L., Hughes, S. M., Madore, B. F., et al. 1994, ApJ, 427, 628
Gavriil, F. P., Gonzalez, M. E., Gotthelf, E. V., et al. 2008, Science, 319, 1802
Gavriil, F. P. & Kaspi, V. M. 2004, ApJ, 609, L67
Gavriil, F. P., Kaspi, V. M., & Woods, P. M. 2002, Nature, 419, 142
Gavriil, F. P., Kaspi, V. M., & Woods, P. M. 2004, ApJ, 607, 959
Gavriil, F. P., Kaspi, V. M., & Woods, P. M. 2006, ApJ, 641, 418
Gehrels, N. 1986, ApJ, 303, 336
Gehrels, N., Chincarini, G., Giommi, P., et al. 2004, ApJ, 611, 1005
Gelfand, J. D. & Gaensler, B. M. 2007, ApJ, 667, 1111
Gendreau, K. C., Arzoumanian, Z., Adkins, P. W., et al. 2016, in Society of Photo-Optical Instrumentation Engineers (SPIE) Conference Series, Vol. 9905, Space Telescopes and Instrumentation 2016: Ultraviolet to Gamma Ray, ed. den Herder, J.-W. A., Takahashi, T., & Bautz, M., 99051H
Giri, U., Andersen, B. C., Chawla, P., et al. 2023, arXiv:2310.16932
Göhler, E., Wilms, J., & Staubert, R. 2005, A&A, 433, 1079
Goldwurm, A., David, P., Foschini, L., et al. 2003, A&A, 411, L223
Golenetskii, S., Aptekar, R., Mazets, E., et al. 2006a, GCN, 4946, 1
Golenetskii, S., Aptekar, R., Mazets, E., et al. 2006b, GCN, 4936, 1
Golenetskii, S. V., Ilinskii, V. N., & Mazets, E. P. 1984, Nature, 307, 41
Good, D. & Chime/Frb Collaboration. 2020, ATel, 14074, 1
Gordon, C. & Arnaud, K. 2021, PyXspec: Python interface to XSPEC spectral-fitting program, Astrophysics Source Code Library, ascl:2101.014
Gotthelf, E. V., Halpern, J. P., Alford, J. A. J., et al. 2019a, ApJ, 874, L25
Gotthelf, E. V., Halpern, J. P., Mori, K., & Beloborodov, A. M. 2019b, ApJ, 882, 173
Gotthelf, E. V., Safi-Harb, S., Straal, S. M., & Gelfand, J. D. 2021, ApJ, 908, 212
Gotthelf, E. V., Vasisht, G., Boylan-Kolchin, M., & Torii, K. 2000, ApJ, 542, L37
Gotz, D., Mereghetti, S., Hurley, K., et al. 2008, in American Institute of Physics Conference Series, Vol. 983, 40 Years of Pulsars: Millisecond Pulsars, Magnetars and More, ed. Bassa, C., Wang, Z., Cumming, A., & Kaspi, V. M. (AIP), 289–291
Götz, D., Mereghetti, S., Mirabel, I. F., et al. 2004, in ESA Special Publication, Vol. 552, 5th INTEGRAL Workshop on the INTEGRAL Universe, ed. Schoenfelder, V., Lichti, G., & Winkler, C., 615
Götz, D., Mereghetti, S., Molkov, S., et al. 2006, A&A, 445, 313
Götz, D., Rea, N., Israel, G. L., et al. 2007a, A&A, 475, 317
Götz, O., Mereghetti, S., Hurley, K., et al. 2007b, in ESA Special Publication, Vol. 622, The Obscured Universe. Proceedings of the VI INTEGRAL Workshop, 533

Göğüş, E., Lin, L., Kaneko, Y., et al. 2016, ApJ, 829, L25
GöğüŞ , E., Woods, P. M., Kouveliotou, C., et al. 1999, ApJ, 526, L93
Göğüş, E., Cusumano, G., Levan, A. J., et al. 2010, ApJ, 718, 331
Göğüş, E., Kouveliotou, C., Woods, P. M., et al. 2001, ApJ, 558, 228
Göğüş, E., Woods, P. M., Kouveliotou, C., et al. 2000, ApJ, 532, L121
Grefenstette, B., Bhargava, Y., Fuerst, F., et al. 2025, NuSTAR/nustar-gen-utils: The one with Zenodo, v0.7
Gregory, P. C. & Fahlman, G. G. 1980, Nature, 287, 805
Gros, A., Goldwurm, A., Soldi, S., et al. 2013, arXiv:1302.6915
Guo, Y.-J., Dai, S., Li, Z.-S., et al. 2015, RAA, 15, 525
Harrison, F. A., Craig, W. W., Christensen, F. E., et al. 2013, ApJ, 770, 103
Heasarc. 2014, HEAsoft: Unified Release of FTOOLS and XANADU, Astrophysics Source Code Library, ascl:1408.004
Helfand, D. J. & Long, K. S. 1979, Nature, 282, 589
Holland, S. T., Barthelmy, S. D., Baumgartner, W. H., et al. 2008, GCN, 8112, 1
Hotan, A. W., Long, S. R., Dickey, J. M., & Dolley, T. J. 2007, ApJ, 668, 449
Hu, C.-P., Begiçarslan, B., Güver, T., et al. 2020, ApJ, 902, 1
Hurley, K., Boggs, S. E., Smith, D. M., et al. 2005, Nature, 434, 1098
Hurley, K., Cline, T., Mazets, E., et al. 1999, Nature, 397, 41
Hurley, K., Mazets, E., Golenetskii, S., & Cline, T. 2002, GCN, 1715, 1
Hurley, K., Svinkin, D., Frederiks, D., et al. 2021, in American Astronomical Society Meeting Abstracts, Vol. 237, American Astronomical Society Meeting Abstracts, 340.06
Ibrahim, A. I., Markwardt, C. B., Swank, J. H., et al. 2004, ApJ, 609, L21
Ibrahim, A. Y., Borghese, A., Coti Zelati, F., et al. 2024, ApJ, 965, 87
Ibrahim, A. Y., Borghese, A., Rea, N., et al. 2023, ApJ, 943, 20
Ioka, K. 2020, ApJ, 904, L15
Israel, G. L., Covino, S., Stella, L., et al. 1999, ApJ, 518, L107
Israel, G. L., Götz, D., Zane, S., et al. 2007, A&A, 476, L9
Jackson, M. S. & Halpern, J. P. 2005, ApJ, 633, 1114
Jensen, P. L., Clausen, K., Cassi, C., et al. 2003, A&A, 411, L7
Kaastra, J. S. & Bleeker, J. A. M. 2016, A&A, 587, A151
Kaneko, Y., Göğüş, E., Baring, M. G., et al. 2021, ApJ, 916, L7
Kargaltsev, O., Kouveliotou, C., Pavlov, G. G., et al. 2012, ApJ, 748, 26
Kaspi, V. M. & Beloborodov, A. M. 2017, ARA&A, 55, 261
Kaspi, V. M. & Gavriil, F. P. 2003, ApJ, 596, L71
Kaspi, V. M., Gavriil, F. P., Woods, P. M., et al. 2003, ApJ, 588, L93
Kaspi, V. M., Lackey, J. R., & Chakrabarty, D. 2000, ApJ, 537, L31
Kern, B. & Martin, C. 2002, Nature, 417, 527
Kim, S., Rey, S.-C., Jerjen, H., et al. 2014, ApJS, 215, 22
Kirsten, F., Marcote, B., Nimmo, K., et al. 2022, Nature, 602, 585
Klose, S., Henden, A. A., Geppert, U., et al. 2004, ApJ, 609, L13

Kouveliotou, C., Dieters, S., Strohmayer, T., et al. 1998a, Nature, 393, 235
Kouveliotou, C., Fishman, G. J., Meegan, C. A., et al. 1993, Nature, 362, 728
Kouveliotou, C., Kippen, M., Woods, P., et al. 1998b, IAU Circ., 6944, 2
Kouveliotou, C., Strohmayer, T., Hurley, K., et al. 1999, ApJ, 510, L115
Kouveliotou, C., Tennant, A., Woods, P. M., et al. 2001, ApJ, 558, L47
Koyama, K., Hoshi, R., & Nagase, F. 1987, PASJ, 39, 801
Kozyrev, A. S., Golovin, D. V., Litvak, M. L., et al. 2024, GCN, 38165, 1
Kriss, G. A., Becker, R. H., Helfand, D. J., & Canizares, C. R. 1985, ApJ, 288, 703
Kuiper, L. & Hermsen, W. 2009, A&A, 501, 1031
Kuiper, L. & Hermsen, W. 2010, ATel, 2509, 1
Kuiper, L., Hermsen, W., & Dekker, A. 2018, MNRAS, 475, 1238
Kuiper, L., Hermsen, W., den Hartog, P. R., & Collmar, W. 2006, ApJ, 645, 556
Kuiper, L., Hermsen, W., & Mendez, M. 2004, ApJ, 613, 1173
Kulkarni, S. R. & Frail, D. A. 1993, Nature, 365, 33
Kulkarni, S. R., Kaplan, D. L., Marshall, H. L., et al. 2003, ApJ, 585, 948
Kumar, H. S. & Safi-Harb, S. 2010, ApJ, 725, L191
Labanti, C., Di Cocco, G., Ferro, G., et al. 2003, A&A, 411, L149
Lamb, R. C., Fox, D. W., Macomb, D. J., & Prince, T. A. 2002, ApJ, 574, L29
Lanza, M. L., Atteia, J.-L., Guillot, S., et al. 2024, ATel, 16837, 1
Laros, J. G., Fenimore, E. E., Fikani, M. M., Klebesadel, R. W., & Barat, C. 1986, Nature, 322, 152
Laros, J. G., Fenimore, E. E., Klebesadel, R. W., et al. 1987, ApJ, 320, L111
Lebrun, F., Leray, J. P., Lavocat, P., et al. 2003, A&A, 411, L141
Leroy, A. K., Sandstrom, K. M., Lang, D., et al. 2019, ApJS, 244, 24
Levin, L., Bailes, M., Bates, S., et al. 2010, ApJ, 721, L33
Li, C. K., Lin, L., Xiong, S. L., et al. 2021, NatAs, 5, 378
Ligo Scientific Collaboration, VIRGO Collaboration, & Kagra Collaboration. 2023, GCN, 35049, 1
Lin, L., Göğüş, E., Roberts, O. J., et al. 2020a, ApJ, 902, L43
Lin, L., Göğüş, E., Roberts, O. J., et al. 2020b, ApJ, 893, 156
Lin, L., Göğüş, E., Baring, M. G., et al. 2012, ApJ, 756, 54
Lin, L., Kouveliotou, C., Baring, M. G., et al. 2011a, ApJ, 739, 87
Lin, L., Kouveliotou, C., Göğüş, E., et al. 2011b, ApJ, 740, L16
Lin, L., Kouveliotou, C., & van der Horst, A. J. 2011c, in American Institute of Physics Conference Series, Vol. 1358, Gamma Ray Bursts 2010, ed. McEnery, J. E., Racusin, J. L., & Gehrels, N. (AIP), 313–316
Livingstone, M. A., Ng, C. Y., Kaspi, V. M., Gavriil, F. P., & Gotthelf, E. V. 2011a, ApJ, 730, 66
Livingstone, M. A., Scholz, P., Kaspi, V. M., Ng, C. Y., & Gavriil, F. P. 2011b, ApJ, 743, L38
Lund, N., Budtz-Jørgensen, C., Westergaard, N. J., et al. 2003, A&A, 411, L231
Lynch, R. S., Archibald, R. F., Kaspi, V. M., & Scholz, P. 2015, ApJ, 806, 266

Lyutikov, M. 2003, MNRAS, 346, 540
Maan, Y., Leeuwen, J. v., Straal, S., & Pastor-Marazuela, I. 2022, ATel, 15697, 1
Manchester, R. N., Hobbs, G. B., Teoh, A., & Hobbs, M. 2005, AJ, 129, 1993
Mazets, E. P., Aptekar, R. L., Butterworth, P. S., et al. 1999, ApJ, 519, L151
Mazets, E. P., Aptekar, R. L., Cline, T. L., et al. 2008, ApJ, 680, 545
Mazets, E. P., Golenetskii, S. V., Gurian, I. A., & Ilinskii, V. N. 1982a, Ap&SS, 84, 173
Mazets, E. P., Golenetskii, S. V., Ilinskii, V. N., et al. 1982b, Ap&SS, 82, 261
Mazets, E. P., Golenetskii, S. V., Ilinskii, V. N., et al. 1981, Ap&SS, 80, 3
Mazets, E. P., Golenetskij, S. V., & Guryan, Y. A. 1979a, Soviet Astronomy Letters, 5, 343
Mazets, E. P., Golentskii, S. V., Ilinskii, V. N., Aptekar, R. L., & Guryan, I. A. 1979b, Nature, 282, 587
McBride, V. A., Dean, A. J., Bazzano, A., et al. 2008, A&A, 477, 249
McGarry, M. B., Gaensler, B. M., Ransom, S. M., Kaspi, V. M., & Veljkovik, S. 2005, ApJ, 627, L137
Mereghetti, S. 1995, ApJ, 455, 598
Mereghetti, S. 2008, A&A Rev., 15, 225
Mereghetti, S., Bandiera, R., Bocchino, F., & Israel, G. L. 2002a, ApJ, 574, 873
Mereghetti, S., Chiarlone, L., Israel, G. L., & Stella, L. 2002b, in Neutron Stars, Pulsars, and Supernova Remnants, ed. Becker, W., Lesch, H., & Trümper, J., 29
Mereghetti, S., Esposito, P., Tiengo, A., et al. 2012, A&A, 546, A30
Mereghetti, S., Esposito, P., Tiengo, A., et al. 2006, A&A, 450, 759
Mereghetti, S., Götz, D., Borkowski, J., Walter, R., & Pedersen, H. 2003, A&A, 411, L291
Mereghetti, S., Gotz, D., Ferrigno, C., et al. 2023, GCN, 35037, 1
Mereghetti, S., Gotz, D., Ferrigno, C., et al. 2024a, GCN, 38148, 1
Mereghetti, S., Götz, D., Mirabel, I. F., & Hurley, K. 2005a, A&A, 433, L9
Mereghetti, S., Götz, D., von Kienlin, A., et al. 2005b, ApJ, 624, L105
Mereghetti, S., Götz, D., Weidenspointner, G., et al. 2009, ApJ, 696, L74
Mereghetti, S., Pacholski, D. P., Gotz, D., et al. 2024b, GCN, 38172, 1
Mereghetti, S., Pons, J. A., & Melatos, A. 2015, Space Sci. Rev., 191, 315
Mereghetti, S., Rigoselli, M., Salvaterra, R., et al. 2024c, Nature, 629, 58
Mereghetti, S., Savchenko, V., Ferrigno, C., et al. 2020, ApJ, 898, L29
Mereghetti, S. & Stella, L. 1995, ApJ, 442, L17
Mereghetti, S., Stella, L., & Israel, G. L. 1999, Nuclear Physics B Proceedings Supplements, 69, 253
Mereghetti, S., Tiengo, A., Esposito, P., et al. 2005c, ApJ, 628, 938
Mereghetti, S., Tiengo, A., Stella, L., et al. 2004, ApJ, 608, 427
Minaev, P. Y. & Pozanenko, A. S. 2020, MNRAS, 492, 1919
Mohan, T., Waratkar, G., Saikia, A. P., et al. 2024, GCN, 38187, 1
Molkov, S., Hurley, K., Sunyaev, R., et al. 2005, A&A, 433, L13
Molkov, S. V., Cherepashchuk, A. M., Lutovinov, A. A., et al. 2004, AstL, 30, 534

Mong, Y. L. & Ng, C. Y. 2018, ApJ, 852, 86
Morii, M., Sato, R., Kataoka, J., & Kawai, N. 2003, PASJ, 55, L45
Muno, M. P., Clark, J. S., Crowther, P. A., et al. 2006, ApJ, 636, L41
Murakami, T., Tanaka, Y., Kulkarni, S. R., et al. 1994, Nature, 368, 127
Nakar, E., Gal-Yam, A., Piran, T., & Fox, D. B. 2006, ApJ, 640, 849
Ng, M., Younes, G., Hu, C. P., et al. 2024, ATel, 16789, 1
Ofek, E. O. 2007, ApJ, 659, 339
Ofek, E. O., Muno, M., Quimby, R., et al. 2008, ApJ, 681, 1464
Olausen, S. A. & Kaspi, V. M. 2014, ApJS, 212, 6
Olive, J.-F., Hurley, K., Sakamoto, T., et al. 2004, ApJ, 616, 1148
Osborne, J. P., Sbarufatti, B., D'Ai, A., et al. 2023, GCN, 35064, 1
Page, K. L., Barthelmy, S., & Cummings, J. R. 2015, GCN, 18632, 1
Palm, D. M. 2024, ATel, 16927, 1
Palmer, D. M., Barthelmy, S., Gehrels, N., et al. 2005, Nature, 434, 1107
Palmer, D. M., Barthelmy, S. D., Cummings, J. R., et al. 2015, GCN, 18634, 1
Pearlman, A. B., Majid, W. A., Prince, T. A., et al. 2020, arXiv:2005.08410
Pintore, F., Mereghetti, S., Esposito, P., et al. 2019, MNRAS, 483, 3832
Pons, J. A. & Rea, N. 2012, ApJ, 750, L6
Popov, S. B. & Postnov, K. A. 2010, in Evolution of Cosmic Objects through their Physical Activity, ed. Harutyunian, H. A., Mickaelian, A. M., & Terzian, Y., 129–132
Popov, S. B. & Stern, B. E. 2006, MNRAS, 365, 885
Prieskorn, Z. & Kaaret, P. 2012, ApJ, 755, 1
Qu, Z., Li, Z., Chen, Y., et al. 2015, PASP, 127, 211
Rajwade, K. M., Stappers, B. W., Lyne, A. G., et al. 2022, MNRAS, 512, 1687
Rea, N., Esposito, P., Turolla, R., et al. 2010, Science, 330, 944
Rea, N., Israel, G. L., Esposito, P., et al. 2012, ApJ, 754, 27
Rea, N., Israel, G. L., Turolla, R., et al. 2009, MNRAS, 396, 2419
Rea, N., Oosterbroek, T., Zane, S., et al. 2005, MNRAS, 361, 710
Rea, N., Turolla, R., Zane, S., et al. 2007, ApJ, 661, L65
Rehan, N. S. & Ibrahim, A. I. 2025, ApJS, 276, 60
Revnivtsev, M. G., Sunyaev, R. A., Varshalovich, D. A., et al. 2004, AstL, 30, 382
Ridnaia, A., Svinkin, D., Frederiks, D., et al. 2021, NatAs, 5, 372
Rigoselli, M., Pacholski, D. P., Mereghetti, S., Salvaterra, R., & Campana, S. 2023, GCN, 35175, 1
Rigoselli, M., Taverna, R., Mereghetti, S., et al. 2025, ApJ, 985, L34
Roberts, O. J., Veres, P., Baring, M. G., et al. 2021, Nature, 589, 207
Roberts, O. J., Veres, P., de Barra, C., et al. 2024, GCN, 37234, 1
Rodi, J., Ubertini, P., Bazzano, A., & Natalucci, L. 2024, GCN, 38164, 1
Rodi, J. C., Pacholski, D. P., Mereghetti, S., et al. 2025, ApJ, 979, L25
Rothschild, R. E., Kulkarni, S. R., & Lingenfelter, R. E. 1994, Nature, 368, 432
Rothschild, R. E. & Lingenfelter, R. E. 1984, Nature, 312, 737
Sakamoto, T. & Gehrels, N. 2009, in American Institute of Physics Conference Series, Vol.

1133, Gamma-ray Burst: Sixth Huntsville Symposium, ed. Meegan, C., Kouveliotou, C., & Gehrels, N. (AIP), 112–114
Sathyaprakash, R., Rea, N., Coti Zelati, F., et al. 2024, ApJ, 976, 56
Sato, T., Bamba, A., Nakamura, R., & Ishida, M. 2010, PASJ, 62, L33
Savchenko, V., Ferrigno, C., Bozzo, E., et al. 2018, ATel, 11270, 1
Savchenko, V., Neronov, A., Beckmann, V., Produit, N., & Walter, R. 2010, A&A, 510, A77
Scargle, J. D. 1998, ApJ, 504, 405
Scargle, J. D., Norris, J. P., Jackson, B., & Chiang, J. 2013, ApJ, 764, 167
Scaringi, S., Bird, A. J., Hill, A. B., et al. 2010, A&A, 516, A75
Scholz, P. & Kaspi, V. M. 2011, ApJ, 739, 94
Scholz, P., Kaspi, V. M., & Cumming, A. 2014, ApJ, 786, 62
Scholz, P., Ng, C. Y., Livingstone, M. A., et al. 2012, ApJ, 761, 66
Serim, M. M., Inam, S. Ç., & Baykal, A. 2012, in Astronomical Society of the Pacific Conference Series, Vol. 466, Electromagnetic Radiation from Pulsars and Magnetars, ed. Lewandowski, W., Maron, O., & Kijak, J., 255
Seward, F. D., Charles, P. A., & Smale, A. P. 1986, ApJ, 305, 814
Shannon, R. M. & Johnston, S. 2013, MNRAS, 435, L29
Spruit, H. C. 2009, in IAU Symposium, Vol. 259, Cosmic Magnetic Fields: From Planets, to Stars and Galaxies, ed. Strassmeier, K. G., Kosovichev, A. G., & Beckman, J. E., 61–74
Sugizaki, M., Nagase, F., Yamauchi, S., et al. 1997, IAU Circ., 6585, 2
Svinkin, D., Frederiks, D., Hurley, K., et al. 2021, Nature, 589, 211
Svinkin, D., Ridnaia, A., Frederiks, D., et al. 2025, GCN, 39022, 1
Svinkin, D. S., Frederiks, D. D., Aptekar, R. L., et al. 2016, ApJS, 224, 10
Svinkin, D. S., Hurley, K., Aptekar, R. L., Golenetskii, S. V., & Frederiks, D. D. 2015, MNRAS, 447, 1028
SVOM/GRM Team, Wang, C.-W., Dong, Y.-W., et al. 2024a, GCN, 37647, 1
SVOM/GRM Team, Wang, C.-W., Dong, Y.-W., et al. 2024b, GCN, 37297, 1
SVOM/GRM Team, Zhang, W.-L., Tan, W.-J., et al. 2024c, GCN, 38192, 1
Thompson, C. & Duncan, R. C. 1993, ApJ, 408, 194
Thompson, C. & Duncan, R. C. 1995, MNRAS, 275, 255
Thompson, C. & Duncan, R. C. 1996, ApJ, 473, 322
Thompson, C., Lyutikov, M., & Kulkarni, S. R. 2002, ApJ, 574, 332
Tiengo, A., Esposito, P., & Mereghetti, S. 2008, ApJ, 680, L133
Tiengo, A., Esposito, P., Mereghetti, S., et al. 2009, MNRAS, 399, L74
Tiengo, A., Esposito, P., Mereghetti, S., et al. 2013, Nature, 500, 312
Torne, P., Eatough, R. P., Karuppusamy, R., et al. 2015, MNRAS, 451, L50
Trigg, A. C., Burns, E., Roberts, O. J., et al. 2024, A&A, 687, A173
Trigg, A. C., Stewart, R., Van Kooten, A., et al. 2025, A&A, 694, A323
Tsang, D. & Gourgouliatos, K. N. 2013, ApJ, 773, L17
Tully, R. B., Courtois, H. M., & Sorce, J. G. 2016, AJ, 152, 50

Ubertini, P., Lebrun, F., Di Cocco, G., et al. 2003, A&A, 411, L131
Uzuner, M., Keskin, Ö., Kaneko, Y., et al. 2023, ApJ, 942, 8
van der Horst, A. J., Connaughton, V., Kouveliotou, C., et al. 2010, ApJ, 711, L1
van der Horst, A. J., Kouveliotou, C., Gorgone, N. M., et al. 2012, ApJ, 749, 122
van Paradijs, J., Taam, R. E., & van den Heuvel, E. P. J. 1995, A&A, 299, L41
Vasisht, G. & Gotthelf, E. V. 1997, ApJ, 486, L129
Vedrenne, G., Roques, J. P., Schönfelder, V., et al. 2003, A&A, 411, L63
Vetere, L., Barthelmy, S. D., Kennea, J. A., Markwardt, C. B., & Palmer, D. M. 2006, GCN, 4922, 1
Voges, W., Aschenbach, B., Boller, T., et al. 1998, in IAU Symposium, Vol. 179, New Horizons from Multi-Wavelength Sky Surveys, ed. McLean, B. J., Golombek, D. A., Hayes, J. J. E., & Payne, H. E., 433
von Kienlin, A., Gruber, D., Kouveliotou, C., et al. 2012, ApJ, 755, 150
Wang, W., Tong, H., & Guo, Y.-J. 2014, RAA, 14, 673
Wang, Y., Wei, Y.-J., Zhou, H., et al. 2024a, ApJ, 969, 127
Wang, Y., Xie, W.-J., Atteia, J. L., et al. 2024b, GCN, 38125, 1
Weng, S.-S. & Göğüş, E. 2015, ApJ, 815, 15
Winkler, C., Courvoisier, T. J. L., Di Cocco, G., et al. 2003, A&A, 411, L1
Woltjer, L. 1964, ApJ, 140, 1309
Woods, P. M., Kouveliotou, C., Gavriil, F. P., et al. 2005, ApJ, 629, 985
Woods, P. M., Kouveliotou, C., Göğüş, E., et al. 2001, ApJ, 552, 748
Woods, P. M., Kouveliotou, C., van Paradijs, J., et al. 1999, ApJ, 519, L139
Wu, Y., Yang, Y.-P., Wang, F.-Y., & Dai, Z.-G. 2025, ApJ, 988, 274
Xue, W. C., Xiong, S. L., Li, X. B., Li, C. K., & Insight-HXMT Team. 2023, GCN, 35060, 1
Younes, G., Baring, M. G., Kouveliotou, C., et al. 2017a, ApJ, 851, 17
Younes, G., Baring, M. G., Kouveliotou, C., et al. 2020a, ApJ, 889, L27
Younes, G., Güver, T., Kouveliotou, C., et al. 2020b, ApJ, 904, L21
Younes, G., Kouveliotou, C., Jaodand, A., et al. 2017b, ApJ, 847, 85
Younes, G., Lander, S. K., Baring, M. G., et al. 2025, ApJ, 989, 89
Younes, G., Lander, S. K., Baring, M. G., et al. 2022, ApJ, 924, L27
Zhang, C. F., Jiang, J. C., Men, Y. P., et al. 2020, ATel, 13699, 1
Zhang, W.-L., Xiong, S.-L., Tan, W.-J., Huang, Y., & Gecam Team. 2024, GCN, 37240, 1

Appendix A

Tables of burst timing and spectral parameters

Table A.1: Bursts from 1E 1547.0–5408.

No	T_{start} (UTC)	T_{BB} (ms)	T_{90} (ms)	COD	CTS[a]	CTS[b]	CTS[c]
0	2003-03-14 00:09:42.553	68.0	—	0.74	1.7	39.0	16.5
934	2008-10-09 07:24:59.094	16.4	—	0.97	40.5	31.3	0.0
935	2009-01-24 15:41:14.098	85.3	—	0.89	37.9	30.6	2.3
936	2009-01-24 15:48:32.241	280.5	—	0.89	179.1	86.4	15.4
937	2009-01-24 16:28:28.556	278.1	—	1.00	31.7	35.0	5.0
938	2009-01-24 16:28:31.640	1665.5	—	1.00	148.0	116.8	26.6
939	2009-01-24 16:48:19.454	50.3	—	0.98	39.0	63.8	7.4
940	2009-01-24 18:44:30.202	232.7	—	1.00	46.2	71.1	1.5
941	2009-01-24 22:29:42.471	124.3	109.7	1.00	88.5	137.7	23.8
942	2009-01-24 22:39:38.976	9.8	—	1.00	8.9	12.4	3.7
943	2009-01-24 22:43:01.409	34.5	—	1.00	42.1	40.8	4.5
944	2009-01-24 23:20:51.673	92.4	—	1.00	40.1	58.2	13.2
945	2009-01-24 23:41:21.587	11.7	—	1.00	25.6	14.0	3.5
946	2009-01-24 23:54:44.462	54.4	—	1.00	18.7	21.6	7.8
947	2009-01-25 00:01:19.130	74.2	—	1.00	32.7	38.7	7.2
948	2009-01-25 03:07:20.863	999.3	850.5	1.00	142.8	108.2	4.4
949	2009-01-25 03:36:54.729	131.9	—	0.98	34.6	49.5	8.7
950	2009-01-25 04:17:16.375	89.8	84.6	0.89	349.7	297.8	18.9
951	2009-01-25 05:05:52.874	63.6	—	0.98	32.2	49.8	9.3
952	2009-01-25 05:13:54.312	31.2	—	0.98	22.5	13.7	0.8
953	2009-01-25 05:22:04.539	18.0	—	0.98	23.0	30.3	3.1
954	2009-01-25 05:22:04.383	358.1	—	0.98	75.7	102.3	37.0
955	2009-01-25 05:22:08.690	420.4	226.4	0.98	657.8	648.9	77.7
956	2009-01-25 05:25:05.497	39.5	36.1	0.98	129.7	115.3	13.0
957	2009-01-25 05:35:08.447	152.2	—	1.00	125.8	121.4	14.9
958	2009-01-25 06:38:58.622	245.1	86.0	0.93	540.3	474.4	30.7
959	2009-01-25 07:18:47.691	51.0	—	1.00	22.2	36.8	3.6

Table A.1: (continued)

No	T_{start} (UTC)	T_{BB} (ms)	T_{90} (ms)	COD	CTS[a]	CTS[b]	CTS[c]
960	2009-01-25 08:03:12.539	226.0	162.6	0.99	22.9	47.3	10.7
961	2009-01-25 08:15:36.374	52.6	—	0.99	16.1	41.0	3.1
962	2009-01-25 08:19:12.466	100.0	—	0.99	61.1	90.4	17.6
963	2009-01-25 08:23:52.358	73.6	—	0.99	34.0	33.7	11.0
964	2009-01-25 08:32:08.566	48.5	—	0.95	55.5	37.2	1.8
965	2009-01-25 08:32:14.398	79.4	—	0.95	48.6	33.1	6.1
966	2009-01-25 08:43:41.543	173.4	67.3	0.95	873.6	707.2	53.4
967	2009-01-25 10:31:08.957	28.7	—	0.95	35.6	58.7	7.3
968	2009-01-25 10:57:27.523	87.2	72.0	1.00	219.4	266.5	18.8
969	2009-01-25 10:58:06.617	140.0	—	1.00	53.9	145.5	30.1
970	2009-01-25 11:07:41.675	71.6	—	1.00	63.1	53.0	7.1
971	2009-01-25 12:06:09.843	339.3	—	1.00	20.7	58.5	12.4
972	2009-01-25 12:55:21.610	93.3	57.1	1.00	695.0	598.9	47.3
973	2009-01-25 13:38:31.302	272.9	262.3	1.00	103.4	140.3	14.5
974	2009-01-25 13:51:54.651	246.6	132.3	1.00	35.5	85.7	30.7
975	2009-01-25 15:46:12.929	546.5	—	0.91	29.2	64.2	24.1
976	2009-01-25 16:14:40.136	55.9	—	0.85	20.7	28.3	5.4
977	2009-01-25 17:01:52.799	24.3	—	1.00	14.9	22.6	1.5
978	2009-01-25 17:01:53.955	75.7	—	1.00	104.3	123.1	9.0
979	2009-01-25 18:21:27.702	134.2	119.4	1.00	72.7	69.6	12.0
980	2009-01-25 18:25:22.137	323.6	227.9	1.00	87.9	149.2	37.8
981	2009-01-25 18:25:22.682	117.1	76.8	1.00	101.7	115.9	26.9
982	2009-01-25 18:49:32.474	31.1	—	1.00	46.5	32.6	2.2
983	2009-01-25 19:08:54.039	408.4	300.2	0.89	492.6	651.6	106.8
984	2009-01-25 19:10:06.028	80.8	—	0.89	19.7	41.9	6.1
985	2009-01-25 19:29:11.899	248.3	235.9	0.89	59.7	122.8	24.9
986	2009-01-25 20:27:24.259	58.5	49.6	0.92	80.6	56.3	5.0
987	2009-01-25 21:36:05.380	286.1	217.3	1.00	218.3	186.2	32.9
988	2009-01-25 21:38:22.511	35.4	—	1.00	22.4	30.1	3.5
989	2009-01-25 21:38:38.738	42.4	—	1.00	12.8	20.4	4.6
990	2009-01-25 21:42:26.017	403.1	392.2	0.81	201.7	184.3	29.7
991	2009-01-25 21:52:13.299	357.2	100.0	0.81	795.4	655.6	85.6
992	2009-01-28 18:09:21.076	54.2	—	0.94	14.5	20.5	0.4
993	2009-01-28 19:47:51.620	53.3	—	1.00	30.4	42.4	7.0
994	2009-01-29 00:49:12.436	406.8	98.9	0.95	238.6	197.8	36.6
995	2009-01-29 15:40:45.322	91.4	66.4	1.00	15.9	42.6	6.8
996	2009-01-29 16:46:13.675	54.1	—	1.00	17.9	28.5	1.9
997	2009-01-29 16:51:40.794	106.8	82.0	1.00	137.5	159.0	19.0
998	2009-01-29 16:59:59.090	58.7	—	1.00	16.4	29.2	9.6
999	2009-01-29 18:02:18.055	62.3	—	0.96	17.2	19.8	6.7
1000	2009-01-29 18:42:12.902	37.6	—	1.00	17.9	33.9	4.8
1001	2009-01-29 22:04:21.056	30.3	—	1.00	20.4	25.9	8.8
1002	2009-01-29 22:27:24.547	88.8	—	0.89	16.7	35.8	11.0
1003	2009-01-29 22:27:27.046	156.1	83.9	0.89	535.5	497.4	46.8

Table A.1: (continued)

No	T_{start} (UTC)	T_{BB} (ms)	T_{90} (ms)	COD	CTS[a]	CTS[b]	CTS[c]
1004	2009-01-30 02:34:25.223	92.3	71.8	0.93	109.2	191.2	25.2
1005	2009-01-30 06:33:10.654	126.8	115.9	0.93	21.7	53.3	7.5
1006	2009-01-30 06:58:16.955	124.4	97.0	0.93	251.2	320.9	22.3
1007	2009-01-30 06:58:32.557	50.2	—	0.93	25.9	38.5	3.5
1008	2009-01-30 07:34:44.425	92.9	—	0.88	65.3	86.7	14.9
1009	2009-01-30 14:30:54.712	87.8	—	1.00	34.9	71.0	7.3
1010	2009-01-30 16:31:11.387	314.2	—	1.00	24.8	71.3	1.1
1011	2009-01-30 18:09:38.679	81.8	50.3	0.91	88.4	64.2	7.7
1012	2009-01-30 19:02:08.753	28.6	—	0.85	35.0	47.9	3.5
1013	2009-01-30 19:24:21.156	163.9	—	0.85	23.4	37.9	18.5
1014	2009-01-30 19:29:41.596	502.2	319.0	0.85	779.9	1019.1	168.7
1015	2009-01-30 20:25:03.641	7.8	—	1.00	13.3	17.7	1.0
1016	2009-01-30 20:41:39.151	58.3	—	1.00	15.0	39.1	7.1
1017	2009-01-31 00:49:04.831	42.7	—	0.90	12.1	20.3	6.6
1018	2009-01-31 01:54:36.019	81.7	67.3	0.94	73.4	134.7	20.0
1019	2009-01-31 04:53:14.353	50.1	—	0.81	21.5	26.7	7.0
1020	2009-01-31 06:32:58.701	57.2	—	1.00	16.1	33.3	7.2
1021	2009-01-31 07:53:28.209	54.7	—	1.00	22.3	36.6	8.0
1022	2009-01-31 08:48:26.391	45.8	—	1.00	39.5	74.2	20.3
1023	2009-01-31 10:02:21.149	99.2	—	0.98	74.4	82.0	13.6
1024	2009-01-31 10:40:26.013	39.8	—	1.00	13.1	31.5	3.4
1025	2009-01-31 13:02:59.226	83.7	—	1.00	25.9	45.7	14.1
1026	2009-01-31 13:03:20.263	67.3	58.4	1.00	43.9	54.1	9.6
1027	2009-01-31 13:33:22.855	12.2	—	1.00	10.0	16.4	3.8
1028	2009-01-31 14:01:42.462	116.7	—	1.00	37.5	49.6	4.6
1029	2009-01-31 14:08:55.103	145.9	109.8	1.00	176.7	233.8	31.4
1030	2009-01-31 18:19:47.483	42.6	—	1.00	17.6	40.2	9.1
1031	2009-01-31 19:23:07.878	41.8	—	1.00	27.9	44.6	15.9
1032	2009-02-01 16:25:16.586	116.9	82.2	0.93	114.8	193.4	19.0
1033	2009-02-01 17:10:45.394	263.7	230.3	0.89	890.3	902.5	70.9
1034	2009-02-01 19:44:31.172	103.8	—	0.93	28.5	18.4	0.5
1035	2009-02-01 20:33:49.174	186.0	114.0	0.89	67.5	69.6	10.1
1036	2009-02-01 21:12:56.463	287.1	250.9	0.85	744.4	839.9	92.7
1037	2009-02-01 23:13:56.642	246.4	83.6	0.95	807.9	775.6	69.2
1038	2009-02-01 23:16:20.525	30.9	—	0.95	32.2	17.8	5.8
1039	2009-02-01 23:51:28.246	59.6	—	0.95	9.5	32.9	7.2
1040	2009-02-01 23:58:45.769	208.5	130.2	0.95	73.1	116.6	15.6
1041	2009-02-02 00:43:01.228	260.7	226.7	0.99	57.5	70.8	7.5
1042	2009-02-02 05:06:52.230	28.0	—	1.00	36.7	28.8	6.3
1043	2009-02-04 20:27:21.107	158.1	94.0	1.00	1119.5	817.7	73.0
1044	2009-02-05 04:34:03.288	8.4	—	0.95	12.0	17.4	0.0
1045	2009-02-05 04:34:03.496	15.1	—	0.95	9.1	13.7	0.0
1046	2009-02-05 06:12:22.360	53.9	—	0.92	128.4	68.4	6.4
1047	2009-02-05 07:22:15.354	364.7	—	0.87	38.6	58.1	7.9

Table A.1: (continued)

No	T_{start} (UTC)	T_{BB} (ms)	T_{90} (ms)	COD	CTS[a]	CTS[b]	CTS[c]
1048	2009-02-05 08:16:45.773	112.0	—	0.85	40.9	51.6	19.4
1049	2009-02-05 08:18:16.088	135.4	—	0.85	59.4	102.4	26.2
1050	2009-02-05 19:35:40.122	75.7	54.7	0.91	353.2	304.6	37.4
1051	2009-02-06 05:38:46.044	13.5	—	0.87	7.9	12.9	2.5
1052	2009-02-06 09:32:07.690	9.4	—	0.91	6.8	15.5	2.4
1053	2009-02-06 13:22:22.553	108.9	93.3	1.00	51.2	80.6	12.6
1054	2009-02-06 14:32:33.619	26.9	—	1.00	51.4	56.4	4.2
1055	2009-02-06 15:08:26.004	101.7	67.6	1.00	91.1	140.0	22.6
1056	2009-02-06 17:13:12.581	234.8	—	1.00	10.0	56.1	4.4
1057	2009-02-06 18:01:22.444	71.0	58.6	1.00	37.8	63.8	9.6
1058	2009-02-06 19:39:42.226	53.5	—	1.00	19.2	32.5	8.0
1059	2009-02-06 20:42:36.312	60.8	45.8	1.00	45.5	77.6	18.4
1060	2009-02-06 20:49:39.518	165.1	—	1.00	12.8	34.1	10.1
1061	2009-02-06 21:32:19.007	71.3	49.6	1.00	239.0	226.6	27.9
1062	2009-02-07 00:54:55.798	56.1	56.0	1.00	74.2	68.1	12.4
1063	2009-02-07 17:09:40.584	124.3	108.3	1.00	67.2	123.3	26.7
1064	2009-02-07 18:59:04.342	79.8	—	0.95	37.1	58.5	12.0
1065	2009-02-07 20:01:20.342	109.7	35.8	1.00	264.6	323.6	45.1
1066	2009-02-07 20:04:13.577	100.5	—	1.00	20.6	31.8	2.5
1067	2009-02-08 02:36:17.667	24.6	—	1.00	27.6	40.7	3.8
1068	2009-02-08 02:52:46.515	40.2	—	1.00	8.9	27.9	14.4
1069	2009-02-08 03:17:26.571	85.6	47.5	1.00	107.1	92.3	16.0
1070	2009-02-08 08:09:52.373	66.6	41.5	1.00	142.1	145.0	14.6
1071	2009-02-08 11:06:28.295	99.6	53.7	1.00	201.1	220.4	34.0
1072	2009-03-10 04:00:43.067	76.9	58.4	1.00	108.1	72.6	6.4
1073	2009-03-22 15:17:42.410	575.8	508.5	0.31	288.2	212.7	33.8
1074	2009-03-22 18:56:17.955	936.3	896.3	0.60	121.0	145.3	36.0
1075	2009-03-22 18:56:24.079	851.3	197.4	0.60	529.9	477.4	66.6
1076	2009-03-22 22:39:16.162	585.9	409.0	1.00	3441.9	2235.6	152.5
1077	2009-03-28 13:05:12.471	105.0	101.7	0.30	140.8	222.4	7.4
1078	2009-04-07 13:31:27.707	495.6	—	0.64	172.6	124.9	39.0

[a] Counts in 20–40 keV.

[b] Counts in 40–100 keV.

[c] Counts in 100–150 keV.

Table A.2: Bursts from SGR 1806–20.

No	T_{start} (UTC)	T_{BB} (ms)	T_{90} (ms)	COD	CTS[a]	CTS[b]	CTS[c]
5	2003-08-23 17:32:11.718	216.1	121.8	0.73	104.0	190.8	29.8
6	2003-08-23 22:05:01.450	129.5	91.3	0.40	171.2	138.1	4.8
7	2003-08-23 22:05:01.776	87.6	—	0.40	85.5	97.6	10.1
8	2003-08-24 15:01:11.846	213.0	189.9	0.86	48.4	55.7	11.8
9	2003-08-24 15:30:44.152	254.8	177.2	0.86	240.0	172.6	19.8
10	2003-08-24 15:57:14.658	123.8	—	0.96	30.3	44.4	0.2
11	2003-08-24 16:33:24.855	293.2	112.4	0.96	42.6	52.0	17.6
12	2003-08-24 17:50:20.050	224.4	159.7	0.97	292.8	196.4	11.1
13	2003-08-24 17:56:31.863	201.2	—	0.78	43.5	64.8	1.4
14	2003-08-24 19:03:48.664	101.7	87.2	0.78	129.4	93.7	2.7
15	2003-08-24 19:03:48.981	112.5	77.7	0.78	35.0	35.1	2.5
16	2003-08-25 00:40:36.002	140.7	107.4	0.41	47.6	60.1	0.0
17	2003-08-25 00:42:04.417	398.7	271.8	0.41	272.7	233.1	7.6
18	2003-08-25 03:40:35.719	81.7	74.4	0.59	31.6	29.4	5.9
19	2003-08-25 03:55:00.918	479.8	259.1	0.59	447.3	338.6	27.8
20	2003-08-25 04:34:33.886	64.4	—	0.39	38.9	32.5	6.8
21	2003-08-26 00:16:18.960	350.0	302.4	0.40	132.5	96.4	12.0
22	2003-09-04 00:53:43.988	27.1	—	1.00	25.9	14.7	0.4
23	2003-09-04 01:15:56.972	49.9	—	1.00	77.8	34.6	0.0
24	2003-09-05 07:46:15.329	70.4	56.2	1.00	28.1	27.4	0.0
25	2003-09-10 18:16:41.740	51.0	—	0.69	35.4	34.0	0.0
26	2003-09-19 19:44:28.487	35.2	—	0.16	66.9	69.6	0.0
27	2003-09-20 03:53:12.915	69.9	52.1	0.26	50.9	35.9	0.0
28	2003-09-20 13:57:54.791	142.9	128.6	0.69	418.8	238.1	17.5
29	2003-10-06 18:51:27.378	82.6	55.5	0.26	187.9	113.1	7.2
30	2003-10-07 22:54:51.703	157.2	—	0.12	225.7	65.0	0.0
31	2003-10-08 03:27:03.899	368.9	147.2	0.17	2966.5	1281.4	84.7
32	2003-10-08 03:27:56.145	252.3	142.8	0.17	2045.6	846.0	43.0
33	2003-10-08 14:09:38.558	45.4	—	0.71	37.3	26.1	0.0
34	2003-10-08 20:22:06.545	135.7	88.9	0.67	254.2	125.5	13.3
35	2003-10-09 04:27:48.099	304.4	226.6	0.97	232.8	146.9	8.1
36	2003-10-11 01:26:27.082	106.0	—	1.00	74.0	64.6	6.9
37	2003-10-11 16:01:57.655	48.8	43.3	0.18	196.8	132.9	5.5
38	2003-10-14 14:31:45.431	159.7	77.3	0.76	225.1	156.4	4.7
39	2003-10-15 02:35:19.682	149.4	102.1	0.86	111.8	81.7	3.9
40	2003-10-15 04:55:00.829	263.9	174.1	0.55	957.5	484.6	32.2
41	2003-10-15 07:25:04.299	23.0	—	0.83	14.8	18.6	3.3
42	2003-10-15 07:37:47.822	145.0	118.7	1.00	127.0	102.1	6.8
43	2003-10-15 07:39:33.049	73.5	—	1.00	18.0	43.4	2.0
44	2003-10-15 07:55:53.000	102.2	—	1.00	114.5	82.3	3.1
45	2003-10-15 07:56:21.101	111.6	59.6	1.00	72.2	51.6	9.3
46	2003-10-15 07:56:21.404	76.8	—	1.00	66.3	45.0	2.3
47	2003-10-15 08:43:19.232	43.9	—	0.80	27.9	35.6	1.7
48	2003-10-15 08:44:15.829	83.2	—	0.80	35.8	52.7	6.1

Table A.2: (continued)

No	T_{start} (UTC)	T_{BB} (ms)	T_{90} (ms)	COD	CTS[a]	CTS[b]	CTS[c]
49	2003-10-15 10:19:31.967	89.5	54.0	0.43	132.9	134.7	11.8
50	2003-10-15 11:00:28.774	139.7	113.8	0.57	160.0	111.7	10.9
51	2003-10-15 11:08:52.839	52.1	—	0.57	33.6	22.7	1.9
52	2003-10-15 11:16:16.175	117.0	—	0.71	103.4	86.2	3.4
53	2003-10-15 11:17:05.342	209.7	165.8	0.71	77.6	92.8	6.3
54	2003-10-15 11:28:31.131	133.4	91.3	0.71	48.8	58.0	1.0
55	2003-10-15 12:08:26.065	114.1	58.7	0.82	123.3	115.6	13.3
56	2003-10-15 12:37:32.455	93.8	—	0.92	92.1	57.2	6.1
57	2003-10-15 12:51:33.098	89.3	56.5	0.77	142.7	103.0	11.2
58	2003-10-15 13:05:27.778	25.2	—	0.77	31.7	32.8	2.4
59	2003-10-15 13:08:04.032	88.0	—	0.77	45.4	43.1	2.0
60	2003-10-15 13:18:26.742	93.6	—	0.77	69.7	67.8	5.2
61	2003-10-15 13:18:27.091	144.8	134.2	0.77	219.2	163.6	20.0
62	2003-10-15 13:33:21.560	129.5	—	0.59	69.9	61.9	4.5
63	2003-10-15 14:29:51.820	14.8	—	0.22	10.4	31.4	0.0
64	2003-10-15 15:55:12.779	265.6	133.1	0.62	1194.1	671.1	19.8
65	2003-10-15 18:05:34.730	82.2	74.3	0.54	67.0	59.6	0.0
66	2003-10-15 19:23:38.540	411.1	52.2	0.33	1408.3	670.1	53.8
67	2003-10-15 21:47:07.520	175.8	151.5	0.78	150.6	104.7	5.3
68	2004-02-18 01:28:48.530	17.5	—	0.89	37.7	17.1	0.8
70	2004-03-08 21:15:42.744	83.6	53.6	0.60	74.2	96.2	0.9
71	2004-03-09 10:24:08.362	215.0	165.8	0.56	936.8	575.6	15.0
72	2004-03-15 15:38:35.187	160.2	126.5	0.40	440.7	261.9	24.3
73	2004-03-16 13:02:06.468	145.3	—	0.59	114.5	70.0	0.0
74	2004-03-20 06:34:35.067	523.3	398.1	0.86	231.4	218.7	13.0
75	2004-03-20 11:39:30.947	112.7	106.8	1.00	19.1	29.4	1.0
76	2004-03-20 17:57:01.923	228.2	103.9	0.71	60.2	66.1	4.9
77	2004-03-29 06:15:40.976	54.7	52.8	0.47	115.6	98.4	11.5
78	2004-03-29 11:46:47.527	152.3	—	0.67	85.6	77.3	2.3
79	2004-03-30 17:03:05.829	296.1	150.4	0.67	3372.3	1312.2	26.5
80	2004-03-30 20:37:14.431	57.4	41.3	0.32	418.0	213.7	14.1
81	2004-03-31 03:29:18.319	19.7	—	0.32	132.0	65.9	0.0
82	2004-04-01 18:14:29.419	32.2	—	0.32	23.2	35.2	3.0
83	2004-04-07 20:37:44.026	252.5	230.0	0.52	462.4	392.0	42.7
84	2004-04-07 21:27:11.167	282.0	186.2	0.52	232.5	167.7	24.6
85	2004-04-08 13:53:57.015	319.6	288.6	0.96	129.6	116.6	11.0
87	2004-08-17 04:56:18.618	63.4	—	1.00	40.6	34.7	8.8
88	2004-08-17 05:59:52.248	116.6	83.3	1.00	42.4	60.1	1.9
89	2004-08-17 08:01:28.205	627.6	—	1.00	35.7	65.5	2.3
90	2004-08-17 08:09:26.297	29.8	—	1.00	32.7	32.2	1.0
91	2004-08-17 12:45:54.936	74.1	70.1	1.00	45.5	52.4	6.0
92	2004-08-17 15:05:31.622	39.2	—	1.00	123.2	64.7	4.5
93	2004-08-17 16:43:48.631	146.5	—	1.00	34.8	11.2	3.3
94	2004-08-17 19:35:54.088	675.9	317.8	1.00	477.9	257.1	32.9

Table A.2: (continued)

No	T_{start} (UTC)	T_{BB} (ms)	T_{90} (ms)	COD	CTS[a]	CTS[b]	CTS[c]
95	2004-08-18 00:07:18.687	48.7	—	1.00	60.8	64.2	0.0
96	2004-08-18 00:22:01.859	532.0	—	1.00	95.1	44.9	0.0
97	2004-08-18 02:31:16.258	187.7	—	1.00	65.1	32.3	6.7
98	2004-08-18 04:52:04.548	29.6	—	1.00	14.6	22.8	4.9
99	2004-08-18 05:23:48.375	193.1	203.7	1.00	69.5	58.4	12.9
100	2004-08-18 05:24:03.388	210.7	130.8	1.00	91.8	37.0	6.9
101	2004-08-18 05:40:03.836	230.3	126.8	1.00	139.5	71.2	11.9
102	2004-08-18 05:40:35.233	312.3	211.0	1.00	77.2	96.9	9.1
103	2004-08-18 06:26:55.888	315.6	—	1.00	103.5	56.0	14.8
104	2004-08-18 07:03:55.411	103.7	83.5	1.00	82.7	64.4	5.3
105	2004-08-18 07:09:26.976	366.5	—	1.00	86.8	74.6	6.5
106	2004-08-18 07:48:38.654	253.7	122.7	1.00	200.1	148.0	13.5
107	2004-08-18 07:49:29.845	1223.5	—	1.00	61.5	94.8	2.1
108	2004-08-18 07:58:50.231	343.0	265.2	1.00	210.7	119.7	2.4
109	2004-08-18 08:29:27.235	515.6	358.1	1.00	174.2	121.6	5.1
110	2004-08-18 10:44:30.115	344.7	317.3	1.00	132.0	68.5	3.5
111	2004-08-18 13:02:33.872	150.2	90.5	1.00	137.6	69.7	5.6
112	2004-08-18 14:02:26.920	111.7	—	1.00	34.9	18.7	6.1
113	2004-08-18 14:04:01.277	151.3	—	1.00	72.4	26.6	1.2
114	2004-08-18 14:48:43.892	276.8	239.6	1.00	93.2	51.0	1.3
115	2004-08-18 14:50:55.515	175.8	—	1.00	43.7	26.2	7.9
116	2004-08-18 15:53:12.697	921.3	—	1.00	92.2	52.3	0.0
117	2004-08-18 16:23:51.730	194.8	—	1.00	33.2	32.1	7.6
118	2004-08-18 17:10:27.153	150.2	72.7	1.00	325.4	102.7	12.4
119	2004-08-18 19:56:28.190	190.5	—	1.00	59.5	36.8	12.5
120	2004-08-18 20:30:10.105	450.3	264.3	1.00	636.1	213.6	8.1
121	2004-08-18 20:37:31.907	55.8	—	1.00	58.7	39.1	4.2
122	2004-08-18 21:52:49.776	177.3	80.1	1.00	804.5	257.9	10.9
123	2004-08-18 21:57:04.216	151.8	68.1	1.00	764.0	386.2	14.1
124	2004-08-18 22:40:26.818	82.5	49.0	1.00	401.2	201.4	7.7
125	2004-08-18 23:13:35.376	50.0	—	1.00	21.2	20.0	0.3
126	2004-08-18 23:40:11.894	207.5	—	1.00	70.5	39.3	9.7
127	2004-08-18 23:56:30.972	131.1	119.6	1.00	48.4	24.9	0.0
128	2004-08-19 00:02:59.376	101.1	95.9	1.00	87.4	56.1	8.7
129	2004-08-19 00:04:22.823	248.2	—	1.00	194.0	100.0	17.2
130	2004-08-19 00:09:22.853	140.3	83.1	1.00	233.1	80.7	8.8
131	2004-08-19 00:11:15.925	153.4	125.7	1.00	596.7	289.8	16.0
132	2004-08-19 00:13:32.264	96.7	77.0	1.00	120.8	106.7	8.2
133	2004-08-19 00:28:46.129	47.2	—	1.00	13.6	22.2	5.0
134	2004-08-19 00:35:36.254	316.4	—	1.00	87.5	57.3	5.6
135	2004-08-19 01:02:58.725	410.5	—	1.00	62.4	61.7	4.7
136	2004-08-19 01:05:26.712	494.7	480.0	1.00	377.2	208.8	17.0
137	2004-08-19 01:29:25.441	76.0	—	1.00	46.4	39.8	8.0
138	2004-08-19 02:01:50.831	402.2	316.6	1.00	51.6	29.3	7.0

Table A.2: (continued)

No	T_{start} (UTC)	T_{BB} (ms)	T_{90} (ms)	COD	CTS[a]	CTS[b]	CTS[c]
139	2004-08-19 02:36:30.901	626.7	360.0	1.00	80.0	62.4	5.3
140	2004-08-19 03:05:55.161	79.7	—	1.00	57.4	39.3	1.9
141	2004-08-21 02:30:46.076	77.8	—	0.70	40.7	45.9	0.0
142	2004-08-21 02:37:53.251	248.8	163.4	0.70	839.7	541.4	21.8
143	2004-08-21 02:47:46.577	370.5	364.1	0.70	121.5	99.3	20.7
144	2004-08-21 04:49:32.336	120.0	101.3	0.36	419.3	232.7	3.5
145	2004-08-21 20:56:46.755	232.9	185.8	0.21	16.3	87.7	0.0
146	2004-08-21 21:17:31.428	370.6	347.8	0.21	79.6	130.2	0.0
147	2004-08-21 22:16:04.544	790.0	—	0.21	58.9	44.2	22.4
148	2004-08-21 22:20:22.156	1084.0	114.1	0.21	81.8	195.6	24.0
149	2004-08-21 22:27:24.959	291.9	137.5	0.22	452.8	182.4	5.8
150	2004-08-22 00:07:08.481	740.3	168.4	0.19	543.8	401.5	17.3
151	2004-08-22 15:33:08.318	185.1	117.8	0.34	2371.2	852.1	23.7
152	2004-08-22 16:07:38.996	311.8	117.7	0.34	181.5	182.7	1.4
153	2004-08-22 18:15:57.184	62.1	—	0.40	54.4	49.1	0.0
154	2004-08-22 21:32:16.628	205.8	142.9	0.41	330.8	205.4	18.9
155	2004-08-23 00:26:13.258	326.7	120.7	0.40	346.4	201.8	17.1
156	2004-08-23 00:37:25.680	126.4	110.4	0.55	74.5	45.4	4.9
157	2004-08-23 00:44:29.688	246.7	—	0.55	117.4	80.8	14.0
158	2004-08-23 01:09:46.592	92.7	88.6	0.55	402.9	228.7	10.8
159	2004-08-23 01:20:54.647	37.1	—	0.55	30.5	37.2	1.2
160	2004-08-23 02:50:26.201	67.4	—	0.78	94.7	118.2	1.0
161	2004-08-23 03:26:26.055	744.3	494.1	0.78	2165.6	1274.9	65.5
162	2004-08-23 03:35:11.453	289.3	—	0.78	96.7	101.7	2.9
163	2004-08-23 04:04:49.236	95.2	—	0.78	73.2	56.3	4.4
164	2004-08-23 04:46:10.011	280.6	273.5	0.97	125.9	116.3	17.0
165	2004-08-23 04:46:14.693	70.3	—	0.97	73.1	52.2	9.5
166	2004-08-23 05:13:15.650	154.9	123.1	0.97	213.8	159.6	14.8
167	2004-08-23 05:51:10.985	133.8	—	0.96	90.6	100.4	9.4
168	2004-08-23 06:13:45.443	102.5	—	0.96	22.3	42.9	2.8
169	2004-08-23 06:14:16.532	323.6	146.4	0.96	1924.3	815.2	33.9
170	2004-08-23 06:40:47.715	270.0	167.5	0.96	53.3	75.0	3.0
171	2004-08-23 06:43:37.713	233.1	—	0.96	101.8	106.2	11.8
172	2004-08-23 06:44:19.856	330.7	173.2	0.96	57.2	43.8	16.4
173	2004-08-23 08:39:42.530	232.3	—	0.68	29.4	43.3	16.1
174	2004-08-23 08:56:29.666	98.0	71.8	0.51	387.6	177.2	16.9
175	2004-08-23 09:02:09.696	168.4	93.8	0.51	202.8	173.8	4.8
176	2004-08-23 09:16:05.832	37.5	—	0.51	61.1	28.7	0.0
177	2004-08-23 09:27:49.922	183.0	57.8	0.51	256.9	123.2	1.6
178	2004-08-23 09:31:11.253	38.3	—	0.51	69.9	22.1	8.4
179	2004-08-23 09:31:43.655	444.6	260.8	0.51	330.1	212.3	22.0
180	2004-08-23 09:31:44.304	53.6	79.6	0.51	31.6	43.2	10.3
181	2004-08-23 10:04:09.688	66.1	—	0.68	23.9	42.8	0.0
182	2004-08-23 10:12:29.957	514.9	128.4	0.68	1604.6	833.5	46.3

Table A.2: (continued)

No	T_{start} (UTC)	T_{BB} (ms)	T_{90} (ms)	COD	CTS[a]	CTS[b]	CTS[c]
183	2004-08-23 10:24:04.887	61.0	—	0.68	48.1	25.5	5.4
184	2004-08-23 10:38:24.930	418.2	325.7	0.68	1209.1	551.5	37.8
185	2004-08-23 10:58:46.421	35.6	—	0.86	35.0	25.5	0.4
186	2004-08-23 11:08:30.298	88.6	78.3	0.86	182.0	101.8	16.9
187	2004-08-23 11:20:48.262	60.0	—	0.86	43.1	68.7	0.4
188	2004-08-23 11:23:10.248	489.4	185.7	0.86	3400.1	1592.3	59.4
189	2004-08-23 11:27:18.171	184.5	—	0.86	90.4	62.5	5.1
190	2004-08-23 12:08:35.558	106.1	57.6	0.96	83.2	76.5	5.6
191	2004-08-23 12:35:03.138	37.5	—	0.96	21.7	19.9	3.6
192	2004-08-23 12:43:31.478	55.9	—	0.96	57.7	43.3	1.9
193	2004-08-23 13:21:09.647	807.9	588.1	0.97	15244.9	6191.5	91.6
194	2004-08-23 13:21:32.080	112.1	—	0.97	58.0	35.9	5.2
195	2004-08-23 13:21:32.780	132.3	—	0.97	106.3	102.4	9.1
196	2004-08-23 13:21:33.770	821.4	185.3	0.97	153.5	137.3	15.8
197	2004-08-23 13:22:20.846	29.6	—	0.97	26.0	18.9	2.1
198	2004-08-23 13:25:16.130	215.9	170.5	0.97	230.9	188.4	13.1
199	2004-08-23 13:26:03.610	372.7	160.5	0.97	3162.2	1613.4	64.9
200	2004-08-23 13:26:20.667	90.6	89.7	0.97	41.8	37.7	4.1
201	2004-08-23 13:26:58.526	142.8	109.4	0.97	350.3	217.8	14.6
202	2004-08-23 13:35:41.124	352.3	183.5	0.97	119.3	119.3	7.7
203	2004-08-23 13:47:55.213	42.4	—	0.97	49.4	39.5	4.7
204	2004-08-23 14:21:12.312	107.3	—	0.78	115.3	110.7	12.2
205	2004-08-23 14:58:02.301	262.3	—	0.78	65.4	47.3	6.1
206	2004-08-23 15:15:29.636	318.2	183.3	0.78	129.2	128.9	6.6
207	2004-08-23 15:48:29.448	102.0	—	0.78	33.2	25.4	0.0
208	2004-08-23 16:17:57.946	336.0	124.0	0.69	1462.7	608.8	43.5
209	2004-08-23 16:18:42.934	48.4	—	0.68	28.2	16.7	1.4
210	2004-08-23 16:46:03.551	389.6	153.7	0.69	94.3	62.3	12.4
211	2004-08-23 16:48:42.156	53.7	—	0.68	37.2	32.1	0.0
212	2004-08-23 16:48:53.904	278.3	145.3	0.69	73.0	69.5	2.6
213	2004-08-23 17:00:54.829	91.8	85.0	0.69	30.8	24.3	4.7
214	2004-08-23 17:14:56.967	47.9	—	0.55	59.5	46.5	3.1
215	2004-08-23 17:48:55.201	309.5	—	0.55	68.3	82.4	5.5
216	2004-08-23 17:52:48.511	813.7	751.2	0.55	105.6	99.7	8.4
217	2004-08-23 17:57:00.453	29.4	24.8	0.55	119.8	107.5	11.7
218	2004-08-23 18:03:09.092	134.3	—	0.55	259.4	135.5	4.7
219	2004-08-23 18:03:23.417	101.4	—	0.55	65.4	47.2	0.0
220	2004-08-23 18:03:28.022	80.5	—	0.55	71.2	49.0	5.4
221	2004-08-23 18:13:36.186	256.5	230.2	0.40	59.8	67.8	26.0
222	2004-08-23 18:19:31.874	144.8	—	0.40	108.0	91.3	11.6
223	2004-08-23 18:19:32.563	292.1	129.8	0.40	79.2	68.6	14.1
224	2004-08-23 18:37:02.999	116.0	73.4	0.40	43.5	34.6	0.0
225	2004-08-23 18:41:04.061	40.1	—	0.40	66.6	40.9	0.0
226	2004-08-23 18:57:30.968	44.2	—	0.40	15.0	34.0	1.8

Table A.2: (continued)

No	T_{start} (UTC)	T_{BB} (ms)	T_{90} (ms)	COD	CTS[a]	CTS[b]	CTS[c]
227	2004-08-23 18:58:51.377	1080.4	378.8	0.40	712.7	673.3	44.7
228	2004-08-23 19:02:48.416	605.0	454.6	0.40	349.8	319.6	21.1
229	2004-08-23 19:11:21.128	330.1	148.4	0.29	270.2	183.1	3.1
230	2004-08-23 20:30:14.308	34.7	—	0.41	35.2	35.6	2.0
231	2004-08-23 20:48:17.321	501.8	448.2	0.41	434.0	214.2	12.8
232	2004-08-23 21:44:00.274	126.7	—	0.50	95.0	79.3	0.0
233	2004-08-23 22:22:20.029	124.7	—	0.50	43.0	61.4	1.3
234	2004-08-23 22:25:44.820	137.9	—	0.51	56.1	37.4	0.0
235	2004-08-23 22:25:47.423	130.3	—	0.51	32.2	20.6	7.9
236	2004-08-23 22:37:08.892	494.4	330.1	0.51	1543.0	438.1	16.2
237	2004-08-23 23:01:40.315	71.3	49.4	0.60	208.9	143.6	12.5
238	2004-08-24 00:05:25.989	38.1	—	0.59	40.7	43.0	0.0
239	2004-08-24 00:12:57.396	322.6	178.3	0.59	855.8	432.9	30.4
240	2004-08-24 01:03:11.049	26.9	—	0.39	66.0	30.8	0.0
241	2004-08-24 01:42:16.759	92.9	85.0	0.40	95.7	119.6	16.1
242	2004-08-24 02:33:06.633	68.5	—	0.41	72.6	38.1	7.2
243	2004-08-24 02:35:22.335	122.0	52.1	0.41	1125.6	471.2	20.7
244	2004-08-24 02:36:41.818	65.2	—	0.41	47.7	33.9	0.9
245	2004-08-24 03:30:36.608	234.7	172.6	0.34	90.6	52.1	3.7
246	2004-08-24 03:54:07.973	127.6	96.7	0.35	489.6	345.2	6.9
247	2004-08-24 03:58:56.466	31.1	—	0.35	83.3	44.0	2.6
248	2004-08-24 04:05:31.283	107.2	87.5	0.34	61.4	53.7	4.1
249	2004-08-24 04:06:28.203	307.8	294.2	0.35	453.2	220.4	17.3
250	2004-08-24 04:06:29.849	101.3	—	0.35	87.9	40.6	2.5
251	2004-08-24 04:14:12.751	93.4	—	0.35	34.3	50.6	7.7
252	2004-08-24 04:59:04.677	267.6	218.9	0.27	166.9	114.8	9.8
253	2004-08-24 05:37:56.545	100.1	60.6	0.27	374.9	267.9	33.1
254	2004-08-24 05:41:35.596	33.5	—	0.27	30.0	20.3	3.7
255	2004-08-24 05:44:15.710	155.0	—	0.27	158.5	100.7	5.0
256	2004-08-24 05:55:30.221	680.4	40.5	0.19	205.9	142.5	0.0
257	2004-08-24 06:10:50.441	132.2	100.8	0.19	97.0	29.1	6.1
258	2004-08-24 07:04:35.017	163.7	96.9	0.20	422.6	135.4	7.6
259	2004-08-24 08:10:15.713	32.8	29.2	0.10	82.8	43.5	0.0
260	2004-08-24 08:39:19.375	55.3	—	0.10	153.3	95.9	0.0
261	2004-08-24 08:56:20.267	321.4	—	0.15	212.6	75.9	40.9
262	2004-08-24 09:08:16.908	32.3	—	0.13	36.3	63.8	0.0
263	2004-08-24 09:11:47.261	450.0	—	0.13	186.1	82.9	2.9
264	2004-08-29 01:16:59.901	52.2	33.7	1.00	101.7	80.2	0.5
265	2004-08-30 12:03:31.325	263.6	83.9	0.52	218.8	128.5	0.0
266	2004-08-30 12:56:31.011	156.3	—	0.69	32.5	53.2	12.0
267	2004-08-30 14:49:37.391	206.8	75.1	0.35	986.5	512.6	22.5
268	2004-08-30 17:11:03.529	14.4	—	0.50	111.4	71.7	2.1
269	2004-08-30 18:06:50.110	170.6	—	0.69	244.7	147.2	5.1
270	2004-08-30 18:18:46.387	295.9	85.8	0.52	227.0	130.1	5.1

Table A.2: (continued)

No	T_{start} (UTC)	T_{BB} (ms)	T_{90} (ms)	COD	CTS[a]	CTS[b]	CTS[c]
271	2004-08-30 18:58:57.552	156.3	—	0.52	170.6	96.0	10.5
272	2004-08-30 20:01:25.361	36.5	—	0.69	38.2	26.8	0.8
273	2004-08-30 20:05:12.420	53.2	—	0.69	27.1	35.8	3.7
274	2004-08-30 21:07:06.659	41.9	41.3	0.49	70.6	28.2	3.7
275	2004-08-30 21:46:14.725	102.2	77.0	0.35	120.6	137.1	10.0
276	2004-08-31 13:45:58.506	245.1	189.3	0.52	808.1	468.9	18.7
277	2004-08-31 14:25:26.392	41.0	34.7	0.52	54.4	34.7	8.6
278	2004-08-31 14:26:27.401	10.5	—	0.52	23.7	22.8	0.0
279	2004-08-31 14:26:52.775	55.4	—	0.52	54.6	48.0	0.6
280	2004-08-31 15:05:07.881	184.5	157.7	0.68	121.9	118.3	12.1
281	2004-08-31 16:42:38.372	99.8	—	0.35	45.8	75.1	8.4
282	2004-08-31 17:11:51.668	52.7	39.4	0.35	598.7	254.1	0.0
283	2004-08-31 17:31:52.802	20.7	—	0.34	34.3	16.2	0.0
284	2004-08-31 18:32:17.875	102.2	86.5	0.35	445.8	182.2	19.8
285	2004-08-31 20:05:10.690	146.7	—	0.69	101.4	109.7	6.5
286	2004-08-31 20:28:24.647	66.1	—	0.69	43.8	55.7	2.6
287	2004-08-31 20:28:57.203	194.2	107.3	0.69	366.9	264.6	31.7
288	2004-08-31 21:55:10.217	265.8	—	0.68	52.1	70.7	0.0
289	2004-08-31 22:37:16.069	17.5	—	0.68	47.8	22.6	1.3
290	2004-08-31 22:44:40.467	226.1	93.3	0.68	297.5	218.8	23.8
291	2004-09-01 01:21:19.797	28.9	—	0.34	59.4	51.4	0.0
292	2004-09-01 01:34:30.000	84.3	—	0.35	63.2	45.4	6.7
293	2004-09-01 03:32:22.748	109.3	89.8	0.69	115.9	92.4	4.0
294	2004-09-01 05:37:09.200	75.8	—	0.68	13.5	32.6	4.8
295	2004-09-01 06:29:52.968	17.6	—	0.49	31.0	51.5	4.4
296	2004-09-01 07:37:02.056	124.4	121.4	0.35	131.9	99.6	0.0
297	2004-09-01 08:50:31.822	138.9	—	0.35	122.7	70.0	0.0
298	2004-09-01 09:40:48.496	153.8	—	0.49	45.5	43.2	10.0
299	2004-09-01 10:07:11.900	147.0	—	0.69	85.9	56.9	14.8
300	2004-09-01 10:21:28.062	706.0	—	0.69	118.6	122.3	1.0
301	2004-09-01 10:26:22.863	103.2	—	0.69	44.1	31.3	9.2
302	2004-09-01 11:25:00.202	28.2	—	0.52	105.2	59.4	9.8
303	2004-09-01 12:14:49.521	75.8	56.3	0.68	123.9	80.5	1.3
304	2004-09-01 14:29:08.462	84.7	78.7	0.35	85.0	78.1	3.8
305	2004-09-01 17:52:21.591	180.8	102.7	0.69	1505.4	748.4	23.7
306	2004-09-01 17:57:38.886	123.4	—	0.69	146.8	110.5	6.5
307	2004-09-01 20:25:09.849	771.1	299.4	0.21	1821.8	1011.5	42.6
308	2004-09-01 21:06:01.744	337.5	61.5	0.20	132.7	116.0	6.3
309	2004-09-01 21:07:55.338	917.3	123.7	0.20	72.4	160.2	25.0
310	2004-09-01 21:07:56.090	165.2	—	0.20	24.9	57.4	17.5
311	2004-09-01 23:31:05.849	132.8	130.1	0.18	112.9	96.5	3.5
312	2004-09-02 03:58:51.079	35.8	—	0.52	31.2	25.8	3.8
313	2004-09-02 07:44:50.788	75.8	—	0.35	197.0	82.0	1.5
314	2004-09-02 07:46:46.650	66.5	36.4	0.35	260.1	193.7	0.0

Table A.2: (continued)

No	T_{start} (UTC)	T_{BB} (ms)	T_{90} (ms)	COD	CTS[a]	CTS[b]	CTS[c]
315	2004-09-02 10:52:19.643	32.2	—	0.69	27.4	23.0	6.3
316	2004-09-02 13:58:12.937	108.1	90.9	0.49	61.3	39.8	6.7
317	2004-09-03 12:17:33.077	68.9	—	0.91	17.8	37.3	5.3
318	2004-09-03 13:07:25.334	67.8	55.2	0.68	34.5	41.6	1.1
319	2004-09-03 13:36:22.578	499.5	—	0.68	162.3	163.7	3.8
320	2004-09-03 19:00:58.539	160.3	—	0.69	61.8	55.1	6.1
321	2004-09-03 21:01:50.548	56.2	—	0.66	18.3	25.5	4.8
322	2004-09-04 00:06:02.296	97.4	—	0.35	15.0	58.5	6.6
323	2004-09-04 00:44:47.672	70.1	—	0.49	94.7	57.9	3.1
324	2004-09-04 02:19:56.811	214.7	173.3	0.69	69.1	52.7	1.9
325	2004-09-04 02:35:04.438	64.6	43.8	0.69	158.6	77.5	0.0
326	2004-09-04 07:36:03.547	123.7	—	0.35	60.6	58.4	7.2
327	2004-09-04 08:42:10.387	186.6	78.4	0.49	359.3	222.6	13.7
328	2004-09-08 02:45:44.327	297.1	82.8	0.42	766.8	398.9	8.2
329	2004-09-08 10:26:46.933	145.1	—	0.24	170.0	77.4	3.6
330	2004-09-09 21:18:15.384	296.9	93.9	0.66	438.4	198.1	3.2
331	2004-09-11 19:50:40.164	192.1	118.0	0.21	409.5	133.0	0.0
332	2004-09-11 20:11:23.165	111.9	88.7	0.32	226.7	157.7	15.4
333	2004-09-15 00:40:05.494	117.8	85.5	0.29	444.0	168.7	4.9
334	2004-09-15 00:50:19.819	39.3	—	0.29	80.0	64.5	3.2
335	2004-09-15 12:39:04.235	91.6	67.1	0.50	146.9	110.9	7.0
336	2004-09-17 09:34:31.913	26.3	—	0.42	35.0	53.7	2.2
337	2004-09-17 11:23:21.450	170.9	—	1.00	36.9	22.3	0.0
338	2004-09-17 13:42:35.172	79.7	—	0.40	121.2	83.7	4.3
339	2004-09-17 16:26:12.572	149.4	—	0.74	100.1	55.0	10.4
340	2004-09-17 17:51:04.198	109.3	—	0.34	113.7	57.8	4.2
341	2004-09-17 20:37:37.971	128.8	110.1	0.79	48.7	37.1	7.3
342	2004-09-18 15:36:08.835	183.5	127.0	0.28	187.5	174.6	11.9
343	2004-09-18 18:16:25.458	56.7	—	0.60	19.9	40.6	2.1
344	2004-09-18 18:20:37.599	181.2	—	0.60	97.4	93.8	11.0
345	2004-09-19 00:22:33.589	233.6	—	0.86	135.1	110.1	17.0
346	2004-09-19 16:38:25.824	304.0	116.1	0.24	709.1	259.8	36.6
347	2004-09-20 07:48:09.137	109.9	—	1.00	57.8	41.0	10.6
348	2004-09-20 09:30:53.389	98.1	76.7	0.85	78.7	64.2	5.8
349	2004-09-20 13:51:57.205	177.9	—	0.65	108.8	79.4	1.2
350	2004-09-20 14:18:09.787	69.4	63.4	0.65	344.0	133.7	4.1
351	2004-09-22 02:40:22.825	208.0	192.9	0.25	87.0	98.5	4.4
352	2004-09-22 02:40:23.349	351.3	339.0	0.25	311.7	196.5	7.6
353	2004-09-22 06:51:22.181	182.2	—	0.29	130.4	66.2	14.2
354	2004-09-22 08:04:31.889	42.4	—	0.56	54.4	16.2	0.0
355	2004-09-22 19:30:54.316	37.6	—	0.49	94.4	37.1	3.7
356	2004-09-22 20:12:16.812	165.6	94.7	0.52	1027.0	803.8	54.6
357	2004-09-22 20:49:16.651	48.6	—	0.32	87.1	46.6	4.2
358	2004-09-22 21:13:15.018	1286.3	—	0.30	147.7	139.0	25.5

Table A.2: (continued)

No	T_{start} (UTC)	T_{BB} (ms)	T_{90} (ms)	COD	CTS[a]	CTS[b]	CTS[c]
359	2004-09-23 07:05:46.378	117.3	—	0.40	101.0	60.5	2.4
360	2004-09-23 08:15:45.675	33.6	—	0.67	59.4	63.3	0.7
361	2004-09-23 18:01:02.436	49.3	—	0.85	45.6	22.3	6.5
362	2004-09-23 21:19:41.112	86.2	61.4	0.31	121.6	65.5	4.7
363	2004-09-30 13:03:42.191	201.9	—	1.00	123.2	101.3	2.2
364	2004-09-30 15:42:19.068	77.7	—	0.23	128.5	126.6	3.3
365	2004-10-01 01:51:12.423	81.7	58.9	0.23	122.1	105.2	33.3
366	2004-10-01 06:03:29.826	125.1	92.3	0.58	145.3	120.4	9.5
367	2004-10-01 10:44:14.220	51.8	49.7	0.65	30.6	37.8	0.3
368	2004-10-01 14:18:33.397	167.2	153.3	0.58	80.8	78.4	8.0
369	2004-10-01 16:23:47.485	125.4	—	0.85	34.7	37.7	5.7
370	2004-10-01 18:12:58.064	127.7	—	0.25	116.3	123.8	5.7
371	2004-10-01 18:17:51.999	64.7	47.1	0.25	119.3	80.1	3.3
372	2004-10-01 18:45:53.294	75.8	69.6	0.23	330.4	161.4	3.3
373	2004-10-01 22:03:13.302	70.3	62.4	0.69	454.0	269.3	21.6
374	2004-10-01 22:28:00.873	25.1	—	0.52	27.9	37.7	0.0
375	2004-10-02 02:02:19.406	125.4	66.2	0.69	50.6	70.2	8.7
376	2004-10-02 02:47:29.140	72.1	68.4	0.85	529.2	223.5	15.3
377	2004-10-02 10:10:27.014	128.3	93.1	0.39	1788.9	741.1	5.3
378	2004-10-02 22:18:51.543	1222.9	—	0.23	123.5	188.0	31.4
379	2004-10-04 01:30:44.448	213.7	—	0.39	63.2	45.0	6.3
380	2004-10-04 07:49:49.847	49.4	—	0.33	72.4	68.0	6.0
381	2004-10-04 12:23:46.584	73.7	—	0.23	77.7	45.5	3.4
382	2004-10-04 12:23:46.885	186.2	79.3	0.23	781.2	435.5	37.7
383	2004-10-04 20:38:27.136	71.8	59.9	0.74	81.6	61.1	6.7
384	2004-10-05 02:24:37.368	139.7	91.7	0.90	150.7	116.6	12.2
385	2004-10-05 06:04:06.439	46.1	—	0.42	65.1	53.3	1.4
386	2004-10-05 12:57:20.124	142.7	129.3	0.85	204.5	171.7	19.8
387	2004-10-05 13:56:47.323	18841.6	—	0.77	293632.6	7679.8	198.8
388	2004-10-05 13:57:17.308	168.9	—	0.77	108.5	119.2	13.8
389	2004-10-05 13:57:23.285	1152.1	—	0.77	200.0	277.4	42.6
390	2004-10-05 13:57:43.089	323.0	349.7	0.77	120.9	100.2	10.0
391	2004-10-05 13:57:52.706	49.0	—	0.77	27.9	21.5	5.6
392	2004-10-05 13:57:53.124	40.3	37.8	0.77	42.0	46.4	1.7
393	2004-10-05 13:57:56.563	300.4	—	0.77	176.1	128.2	17.9
394	2004-10-05 13:58:00.955	244.2	—	0.77	66.7	64.4	14.5
395	2004-10-05 13:58:34.114	157.2	—	0.77	156.8	118.6	12.6
396	2004-10-05 13:58:44.827	291.9	—	0.77	191.4	125.5	4.3
397	2004-10-05 13:58:45.818	122.0	103.6	0.77	404.0	287.6	20.7
398	2004-10-05 13:58:46.111	21.0	—	0.77	37.6	34.3	0.9
399	2004-10-05 13:58:47.452	151.1	130.6	0.77	43.8	64.9	8.1
400	2004-10-05 13:58:49.047	222.7	271.2	0.77	68.1	55.0	1.6
401	2004-10-05 13:58:50.059	44.0	53.5	0.77	32.7	24.7	4.9
402	2004-10-05 13:59:06.671	1427.3	1046.6	0.77	484.9	414.6	30.3

Table A.2: (continued)

No	T_{start} (UTC)	T_{BB} (ms)	T_{90} (ms)	COD	CTS[a]	CTS[b]	CTS[c]
403	2004-10-05 13:59:10.195	47.7	—	0.77	27.7	27.0	6.1
404	2004-10-05 13:59:14.895	103.1	122.7	0.77	106.7	88.3	3.8
405	2004-10-05 13:59:15.700	834.4	691.3	0.77	974.0	835.9	37.4
406	2004-10-05 13:59:16.933	137.4	128.5	0.77	80.2	92.6	6.2
407	2004-10-05 13:59:18.706	80.2	—	0.77	63.3	45.0	5.2
408	2004-10-05 13:59:19.734	786.0	160.2	0.77	101.5	78.8	5.0
409	2004-10-05 13:59:22.997	1159.4	—	0.77	367.6	401.0	36.8
410	2004-10-05 13:59:31.059	30.1	—	0.77	25.1	14.6	0.7
411	2004-10-05 13:59:31.854	1317.4	—	0.77	216.7	300.5	58.9
412	2004-10-05 13:59:33.977	1074.7	832.2	0.77	500.9	342.4	93.6
413	2004-10-05 13:59:36.363	116.8	—	0.77	145.8	119.5	0.0
414	2004-10-05 13:59:39.043	33125.3	—	0.77	14718.8	8336.7	443.6
415	2004-10-05 14:00:18.554	305.6	549.0	0.77	50.3	68.5	19.4
416	2004-10-05 14:00:19.517	144.4	185.1	0.77	167.6	95.1	7.9
417	2004-10-05 14:00:26.646	79.7	64.6	0.77	25.9	36.9	9.9
418	2004-10-05 14:00:28.949	1273.7	—	0.77	92.2	140.7	9.6
419	2004-10-05 14:00:31.461	740.3	—	0.77	88.0	102.8	0.0
420	2004-10-05 14:00:34.364	522.6	433.5	0.77	155.8	123.6	23.1
421	2004-10-05 14:00:36.675	39.7	—	0.77	8.4	29.2	0.0
422	2004-10-05 14:00:47.665	365.5	243.1	0.77	91.1	137.2	12.7
423	2004-10-05 14:00:50.757	144.0	—	0.77	129.5	100.1	6.5
424	2004-10-05 14:01:01.530	486.3	295.8	0.77	81.2	89.7	13.3
425	2004-10-05 14:01:02.680	128.2	—	0.77	25.9	61.6	15.1
426	2004-10-05 14:01:05.157	16.6	—	0.77	10.9	21.0	0.0
427	2004-10-05 14:01:22.183	814.5	—	0.77	171.0	124.7	8.0
428	2004-10-05 14:01:34.321	541.6	439.3	0.77	103.4	116.4	2.9
429	2004-10-05 14:01:38.352	27.6	—	0.77	45.5	35.8	5.0
430	2004-10-05 14:01:39.936	128.6	—	0.77	98.6	90.3	20.4
431	2004-10-05 14:02:04.577	170.0	154.6	0.77	28.4	33.0	0.9
432	2004-10-05 14:02:05.291	195.3	101.3	0.77	162.8	95.4	11.7
433	2004-10-05 14:02:24.559	510.7	—	0.77	78.5	72.2	9.3
434	2004-10-05 14:02:36.699	333.3	253.8	0.77	68.1	69.3	8.5
435	2004-10-05 14:03:49.710	403.4	—	0.77	60.2	68.7	14.9
436	2004-10-05 14:03:51.259	541.5	114.3	0.77	44.6	69.5	8.6
437	2004-10-05 14:04:36.956	308.5	411.4	0.77	27.0	78.4	1.0
438	2004-10-05 14:04:38.963	429.1	331.8	0.77	399.5	370.3	28.7
439	2004-10-05 14:05:48.748	762.7	—	0.77	96.2	102.3	0.0
440	2004-10-05 14:07:30.620	52.8	—	0.77	11.6	27.2	1.4
441	2004-10-05 14:07:34.561	1186.2	203.9	0.77	184.3	203.5	30.7
442	2004-10-05 14:08:00.705	245.9	164.1	0.77	345.9	242.4	24.1
443	2004-10-05 14:28:01.499	699.2	220.3	0.60	76.6	110.0	24.6
444	2004-10-05 14:38:08.942	84.7	—	0.60	18.5	42.8	5.2
445	2004-10-05 14:47:05.368	940.1	797.4	0.60	30.4	72.5	33.9
446	2004-10-05 14:55:33.733	352.5	—	0.60	68.7	51.5	9.0

Table A.2: (continued)

No	T_{start} (UTC)	T_{BB} (ms)	T_{90} (ms)	COD	CTS[a]	CTS[b]	CTS[c]
447	2004-10-05 15:11:18.650	26.1	—	0.42	49.1	49.4	1.9
448	2004-10-05 16:49:52.968	278.9	186.5	0.42	1961.2	790.4	41.8
449	2004-10-05 16:51:31.178	192.9	—	0.42	74.1	68.7	15.2
450	2004-10-05 17:47:33.032	37.3	31.4	0.85	20.0	17.2	1.1
451	2004-10-05 17:58:41.089	86.9	—	0.85	50.9	29.7	4.2
452	2004-10-05 19:18:27.336	594.0	540.3	0.79	616.5	359.4	39.9
453	2004-10-05 19:38:56.986	217.2	108.2	0.79	415.3	184.2	11.6
454	2004-10-05 20:00:33.031	247.9	117.6	0.57	161.4	153.6	16.2
455	2004-10-05 20:04:14.000	240.1	125.3	0.57	180.4	125.0	13.5
456	2004-10-05 20:04:16.067	167.8	167.6	0.57	48.9	41.0	0.0
457	2004-10-06 19:52:03.330	108.0	97.5	0.43	132.9	89.5	14.7
458	2004-10-06 20:05:44.898	20.5	—	0.43	25.6	23.0	0.0
459	2004-10-06 23:01:37.739	359.8	—	0.48	58.8	82.1	18.1
460	2004-10-08 08:31:18.013	361.5	241.7	0.34	82.7	134.7	1.4
461	2004-10-08 17:39:20.200	131.2	122.0	1.00	67.8	81.5	5.3
462	2004-10-08 20:33:21.456	54.0	36.1	1.00	44.8	44.0	6.8
463	2004-10-08 22:24:00.058	23.4	—	1.00	29.8	12.6	0.0
464	2004-10-09 12:04:35.717	34.5	—	0.72	38.2	27.1	0.0
465	2004-10-09 12:36:51.798	36.9	—	0.76	46.9	54.4	2.2
466	2004-10-09 12:58:10.293	159.5	87.5	0.66	1520.7	775.1	19.5
467	2004-10-09 13:08:16.308	79.9	49.0	0.66	41.2	49.1	8.6
468	2004-10-09 13:31:17.425	46.9	—	0.86	52.3	34.8	4.0
469	2004-10-09 19:18:32.972	69.5	—	0.98	62.9	65.7	4.0
470	2004-10-09 22:46:05.223	37.0	—	0.98	9.9	16.1	3.9
471	2004-10-09 23:04:21.631	37.5	—	0.91	19.4	25.9	5.6
472	2004-10-09 23:08:21.396	22.5	—	0.91	41.5	28.2	2.0
473	2004-10-09 23:51:52.574	35.5	—	0.79	5.1	17.7	6.3
474	2004-10-10 02:13:35.189	40.0	—	0.55	28.9	41.3	2.2
475	2004-10-10 10:12:33.821	138.0	—	0.06	254.7	108.4	0.0
476	2004-10-11 12:21:26.351	44.8	—	0.16	52.7	70.5	14.5
477	2004-10-11 16:43:00.827	22.2	—	0.71	24.5	14.6	4.2
478	2004-10-11 19:03:11.735	81.9	—	0.95	39.3	35.2	0.8
479	2004-10-14 06:06:35.315	91.0	73.8	0.80	167.5	177.6	15.5
480	2004-10-14 15:29:40.651	87.1	79.2	0.39	33.8	52.8	13.2
481	2004-10-16 03:08:41.452	285.6	254.3	0.06	261.7	182.3	28.0
482	2004-10-16 07:48:28.243	48.2	—	0.35	37.0	32.2	5.6
483	2004-10-16 10:12:39.895	249.5	—	0.64	276.5	177.0	6.0
484	2004-10-16 10:51:33.975	155.9	—	0.51	171.9	128.3	18.6
485	2004-10-16 19:50:16.408	145.9	—	1.00	35.5	50.4	4.9
486	2004-10-16 20:55:26.123	67.5	—	0.83	38.5	31.9	1.5
487	2004-10-17 01:51:57.382	56.9	—	0.64	28.4	25.9	1.0
488	2004-10-17 06:38:49.384	56.3	75.3	0.23	254.5	134.1	7.6
489	2004-10-17 06:41:10.131	52.3	—	0.21	132.4	78.4	23.0
490	2004-10-17 06:43:53.750	155.1	147.9	0.21	56.7	93.2	32.3

Table A.2: (continued)

No	T_{start} (UTC)	T_{BB} (ms)	T_{90} (ms)	COD	CTS[a]	CTS[b]	CTS[c]
491	2004-10-17 06:45:07.761	42.1	—	0.21	242.5	78.9	3.2
492	2004-10-17 07:03:07.740	179.9	—	0.23	234.4	129.9	9.1
493	2004-10-17 11:17:49.570	36.7	—	0.22	122.6	27.9	0.0
494	2004-10-17 12:29:49.420	139.2	80.4	0.29	171.4	94.1	8.2
495	2004-10-17 12:48:53.656	80.2	—	0.30	87.6	60.5	5.3
496	2004-10-17 13:31:36.178	62.0	—	0.49	80.6	85.1	19.4
497	2004-10-17 13:34:22.483	286.3	187.3	0.49	94.7	97.5	6.0
498	2004-10-17 14:58:59.692	41.6	35.3	0.37	138.5	101.5	11.3
499	2004-10-19 15:10:54.134	67.0	—	1.00	102.1	54.9	4.5
500	2004-10-19 16:24:30.335	123.7	48.0	0.84	135.6	90.4	1.8
501	2004-10-19 18:49:24.868	31.3	28.7	0.38	106.7	88.6	0.0
502	2004-10-19 19:02:25.867	164.6	120.2	0.38	619.9	305.1	13.8
503	2004-10-19 19:34:41.802	97.6	65.6	0.51	166.6	118.0	8.5
504	2004-10-19 20:23:20.180	151.0	—	0.64	208.9	191.0	11.5
505	2004-10-19 20:30:23.649	43.7	—	0.64	50.8	33.2	6.4
506	2004-10-19 20:38:13.679	115.1	105.4	0.64	84.7	70.7	12.2
507	2004-10-19 20:56:48.870	99.5	79.0	0.67	102.1	91.7	5.3
508	2004-10-19 21:41:24.337	71.1	—	0.47	52.6	51.0	5.8
509	2004-10-19 22:17:09.877	118.7	87.2	0.44	145.7	108.4	3.4
510	2004-10-19 22:50:20.842	219.4	66.3	0.42	196.9	143.2	12.0
511	2004-10-19 22:53:21.545	56.7	40.8	0.42	162.4	102.2	4.1
512	2004-10-20 01:20:27.801	191.3	—	0.22	231.7	172.2	3.8
513	2004-10-20 05:39:33.422	152.1	81.6	0.07	435.7	281.1	10.9
514	2004-10-20 06:53:40.620	71.7	—	0.25	155.1	82.7	0.0
515	2004-10-20 13:50:27.802	64.5	43.7	0.72	145.4	73.6	7.2
516	2004-10-20 15:37:10.398	85.5	—	0.89	66.1	42.9	4.8
517	2004-10-20 19:44:16.878	574.1	493.2	0.94	129.6	161.5	10.1
518	2004-10-20 20:12:18.591	161.3	128.3	0.94	247.8	233.3	28.3
519	2004-10-20 20:15:56.754	18.2	—	0.94	12.3	13.7	4.6
520	2004-10-20 21:43:15.807	53.5	—	0.94	40.6	27.9	0.0
521	2004-10-27 23:11:33.888	87.8	—	0.89	49.1	50.1	6.5
522	2004-10-27 23:11:52.479	187.0	110.4	0.89	156.8	139.8	11.0
523	2005-02-16 07:52:15.973	69.7	—	0.28	96.9	75.0	6.7
524	2005-02-16 17:37:58.167	120.8	114.9	0.64	41.4	32.6	0.0
525	2005-02-16 17:39:33.834	769.0	696.9	0.64	88.9	54.4	23.8
526	2005-02-16 23:09:17.089	104.7	80.2	1.00	215.1	131.3	14.7
527	2005-02-17 00:19:56.791	199.3	89.2	0.74	288.1	151.0	13.4
528	2005-02-17 08:01:11.537	257.4	245.1	0.48	209.6	156.0	16.1
529	2005-03-02 07:47:25.870	139.9	86.5	1.00	242.9	156.1	5.4
530	2005-03-02 12:59:18.696	169.7	85.7	0.33	213.7	96.3	8.5
531	2005-03-11 10:09:32.765	90.0	—	0.23	171.1	102.9	8.2
532	2005-03-11 15:40:00.827	11.3	—	0.53	50.7	38.1	4.5
533	2005-03-12 04:11:37.751	522.5	112.4	0.13	315.2	261.5	9.1
534	2005-03-12 06:39:25.669	103.9	95.7	0.56	78.0	40.3	9.2

Table A.2: (continued)

No	T_{start} (UTC)	T_{BB} (ms)	T_{90} (ms)	COD	CTS[a]	CTS[b]	CTS[c]
535	2005-03-12 09:11:33.399	293.2	—	0.67	126.7	70.6	11.6
536	2005-03-17 19:32:26.289	63.8	—	0.47	160.6	91.2	7.7
537	2005-03-19 06:13:55.697	29.7	—	0.91	51.8	22.7	0.4
538	2005-03-19 08:01:29.633	50.8	—	0.80	68.2	45.7	2.7
539	2005-03-20 11:06:04.195	409.2	128.5	0.15	333.6	274.6	8.7
540	2005-03-20 11:06:04.723	279.6	161.6	0.15	639.2	583.1	14.2
541	2005-03-21 02:31:14.619	40.4	—	0.64	16.4	27.2	2.7
542	2005-03-21 12:15:22.115	242.8	128.1	0.45	312.1	194.8	4.2
543	2005-03-22 00:16:20.523	189.8	137.1	0.52	1034.7	648.7	17.9
544	2005-03-22 03:06:40.144	77.7	53.6	0.70	131.5	81.3	6.6
545	2005-03-22 07:23:08.186	91.9	73.2	0.49	488.3	187.5	9.2
546	2005-03-23 02:38:20.436	865.2	302.1	0.39	4848.7	2309.9	57.1
547	2005-03-23 19:56:25.586	118.5	—	0.55	68.1	59.3	0.8
548	2005-03-23 22:49:24.141	242.5	166.9	0.99	375.3	142.8	3.9
549	2005-03-24 16:37:15.840	237.8	135.9	0.20	400.5	162.6	7.9
550	2005-03-24 23:16:57.853	21.1	—	0.34	169.6	95.9	0.0
551	2005-03-25 03:12:57.549	589.7	304.7	0.54	2202.0	2008.3	178.9
552	2005-03-26 13:25:07.031	144.3	118.5	0.32	98.9	96.6	6.2
553	2005-03-28 03:32:34.944	309.1	154.6	0.53	2153.2	1291.5	49.2
554	2005-03-28 05:56:41.990	72.0	62.2	0.77	228.1	138.8	8.1
555	2005-03-28 07:08:30.728	28.1	—	0.93	33.3	15.0	0.4
556	2005-03-28 11:19:17.170	72.1	—	0.45	56.9	56.0	0.7
557	2005-04-02 05:52:02.712	20.6	—	0.19	25.2	35.4	4.0
558	2005-04-03 23:31:44.874	55.4	—	0.69	42.9	28.0	1.8
559	2005-04-14 18:56:00.743	1198.4	752.6	0.18	7598.1	2695.2	57.0
560	2005-04-14 20:17:56.134	303.5	281.3	0.22	2508.1	1068.4	29.6
561	2005-04-15 03:12:00.936	288.0	—	0.48	94.7	43.0	1.0
562	2005-04-15 04:45:16.052	90.7	—	0.81	46.6	42.2	8.0
563	2005-04-16 15:36:59.730	178.2	131.6	0.28	372.8	230.6	8.1
564	2005-04-16 22:38:02.226	260.7	—	0.92	44.3	62.3	0.0
565	2005-04-16 22:57:22.419	272.1	167.2	0.92	1971.4	818.1	22.6
566	2005-04-16 22:58:50.991	95.5	—	0.92	155.4	76.4	0.0
567	2005-04-17 20:55:33.146	163.3	160.8	0.56	313.0	198.2	11.9
568	2005-04-19 15:45:40.162	60.6	—	0.33	77.4	41.2	9.9
569	2005-04-19 16:05:15.779	599.1	—	0.33	90.8	88.6	30.5
570	2005-04-20 03:44:55.683	785.4	219.9	0.38	2131.2	985.7	34.8
571	2005-04-20 07:44:52.694	17.0	—	0.83	32.2	20.6	0.0
572	2005-04-20 10:31:15.915	73.2	60.4	0.70	142.4	98.3	0.0
573	2005-04-20 11:55:04.493	350.5	193.3	0.88	1087.2	400.1	7.5
574	2005-04-20 21:40:32.443	75.0	68.7	0.05	752.1	100.0	38.3
575	2005-04-21 05:31:37.293	986.8	—	0.49	11853.4	4461.0	25.9
576	2005-04-22 09:38:26.235	75.1	—	0.95	47.4	24.3	0.0
577	2005-04-22 15:03:40.570	96.7	—	0.53	64.4	24.3	0.0
578	2005-04-22 16:58:03.486	27.7	—	0.39	34.2	32.1	7.9

Table A.2: (continued)

No	T_{start} (UTC)	T_{BB} (ms)	T_{90} (ms)	COD	CTS[a]	CTS[b]	CTS[c]
579	2005-04-22 17:03:06.484	96.7	—	0.40	197.4	65.0	0.0
580	2005-04-22 19:28:49.563	17.2	—	0.34	31.1	20.4	0.0
581	2005-04-22 22:35:19.337	36.4	—	0.14	112.0	56.2	0.0
582	2005-04-23 01:29:24.702	46.4	—	0.08	271.7	89.0	0.0
583	2005-04-24 06:29:54.898	58.0	—	0.25	103.3	103.3	3.4
584	2005-04-24 09:11:10.829	13.7	—	0.40	25.8	18.8	2.8
585	2005-04-25 03:26:06.474	18.6	—	0.81	27.7	11.6	2.1
586	2005-04-25 04:40:14.998	775.6	176.3	0.98	617.1	298.2	10.1
587	2005-04-25 11:03:55.816	84.3	78.4	0.74	618.9	202.2	0.0
588	2005-04-25 12:07:15.056	225.2	—	0.44	316.5	178.4	6.3
589	2005-04-25 15:59:30.324	43.2	—	0.34	47.5	34.4	6.0
590	2005-04-27 01:27:13.690	257.5	—	0.09	856.0	369.0	0.0
591	2005-04-27 23:35:44.787	54.1	—	0.81	50.0	24.8	0.0
592	2005-04-28 05:47:31.023	29.2	—	0.65	23.5	18.2	0.0
593	2005-04-28 09:50:56.444	353.3	274.3	0.52	232.2	154.1	8.8
594	2005-04-28 11:26:39.702	167.4	164.1	0.46	441.9	200.5	8.3
595	2005-08-17 00:03:23.034	9.5	—	0.51	57.9	20.7	0.0
596	2005-08-17 00:50:17.836	88.0	74.5	0.71	212.0	87.8	4.2
597	2005-08-20 15:55:02.324	57.9	—	1.00	32.8	36.6	2.7
598	2005-08-20 23:38:47.096	11.1	—	1.00	41.0	21.4	0.0
599	2005-08-21 08:31:53.862	111.2	—	0.52	46.2	36.5	3.6
600	2005-08-21 08:31:54.547	403.9	338.9	0.52	487.3	291.3	35.0
601	2005-08-21 10:31:23.174	22.1	—	0.67	42.9	26.4	0.6
602	2005-08-22 13:03:34.708	62.7	41.6	0.68	39.7	24.8	3.5
603	2005-08-22 14:04:57.899	20.2	—	0.81	19.1	20.6	3.5
604	2005-08-22 15:06:49.232	21.4	—	0.84	24.5	21.3	0.0
605	2005-08-22 15:12:54.528	44.4	—	0.85	19.4	32.6	3.8
606	2005-08-22 16:06:40.240	99.1	78.9	0.89	41.9	42.0	0.4
607	2005-08-24 18:04:08.562	200.4	174.1	0.95	345.9	185.7	9.7
608	2005-08-25 12:52:16.894	42.1	—	0.51	30.9	14.2	6.1
609	2005-08-28 12:40:19.735	50.7	45.3	0.55	64.9	69.4	3.0
610	2005-08-28 19:10:00.378	31.5	—	0.95	22.7	12.7	2.9
611	2005-08-29 00:49:59.792	69.7	—	0.99	189.9	94.1	0.0
612	2005-09-03 12:35:02.662	103.4	81.4	0.69	83.1	84.9	7.6
613	2005-09-06 13:07:59.537	57.6	57.4	0.91	81.6	31.7	1.4
614	2005-09-06 13:08:59.394	43.7	34.2	0.91	171.5	112.1	5.2
615	2005-09-15 18:42:18.354	111.8	69.3	0.90	564.8	255.2	7.6
616	2005-09-16 17:08:29.665	20.3	—	0.34	42.3	25.9	0.0
617	2005-09-23 19:38:14.696	141.3	—	0.64	65.9	39.0	0.0
618	2005-10-01 07:47:10.048	169.4	104.6	1.00	163.2	106.4	3.1
619	2005-10-02 12:44:54.805	31.4	—	0.63	27.9	15.0	2.9
620	2005-10-02 22:06:21.211	28.9	—	0.94	40.0	36.7	0.2
621	2005-10-04 01:21:03.447	76.6	66.0	0.84	51.8	25.9	1.1
622	2005-10-04 02:54:14.028	92.4	82.3	0.92	71.2	47.9	2.4

Table A.2: (continued)

No	T_{start} (UTC)	T_{BB} (ms)	T_{90} (ms)	COD	CTS[a]	CTS[b]	CTS[c]
623	2005-10-04 03:30:22.962	20.0	—	0.92	27.9	24.5	4.6
624	2005-10-10 21:26:55.686	29.4	—	0.66	20.2	28.6	0.0
625	2005-10-10 22:49:57.937	26.2	—	0.35	48.3	30.2	0.0
626	2005-10-15 11:36:33.613	44.3	—	0.68	27.0	19.9	0.0
627	2005-10-22 03:43:39.858	48.6	—	0.89	115.8	85.2	5.0
628	2005-10-22 07:25:36.606	332.7	264.8	0.67	1587.7	828.6	45.1
629	2005-10-22 08:52:42.266	39.3	—	1.00	62.7	39.7	4.7
630	2005-10-22 08:52:46.776	19.2	—	1.00	31.4	20.7	0.5
631	2005-10-22 09:02:05.167	15.0	—	1.00	18.8	14.7	0.0
632	2005-10-25 03:02:13.000	51.8	—	0.59	60.6	31.8	1.7
633	2005-10-25 04:48:30.976	46.3	—	0.95	65.8	35.4	2.3
634	2005-10-25 09:42:53.721	49.8	40.2	0.33	212.5	73.9	17.5
635	2005-10-25 17:48:10.777	26.7	—	0.68	24.0	22.4	2.8
636	2005-10-25 22:07:00.148	66.5	—	0.73	23.7	26.0	0.6
637	2005-10-26 00:32:47.895	340.3	—	1.00	40.0	19.3	7.2
638	2005-10-28 00:21:52.917	4.4	—	0.20	43.9	35.0	0.0
639	2005-10-28 07:53:25.376	47.2	—	0.37	105.5	44.5	0.0
640	2006-02-15 19:11:07.285	162.1	—	0.41	259.2	133.8	6.4
641	2006-03-27 05:37:55.856	182.3	142.0	0.76	764.9	369.6	11.5
644	2006-04-22 11:27:16.813	157.0	93.3	0.94	482.3	310.9	4.2
645	2006-04-22 13:30:50.916	5.1	—	0.65	12.9	9.1	0.0
646	2006-04-22 15:59:12.235	199.9	118.0	0.54	431.9	224.2	13.0
647	2006-08-16 06:32:02.110	180.1	93.2	0.35	25.0	66.4	2.7
648	2006-08-19 04:45:05.512	22.9	—	0.52	64.9	21.0	0.8
649	2006-08-19 05:57:48.282	119.5	101.9	0.52	1055.2	390.4	3.4
650	2006-08-19 05:57:49.051	22.0	—	0.52	51.9	17.8	4.0
651	2006-08-25 20:24:40.410	17.3	—	0.51	28.3	16.3	2.0
652	2006-08-25 20:24:41.769	152.3	149.4	0.51	67.1	66.8	0.0
653	2006-08-25 20:40:16.691	42.5	—	0.51	48.3	22.9	1.0
654	2006-08-25 21:03:31.752	36.2	31.1	0.71	104.3	48.5	6.2
655	2006-08-25 22:17:04.645	273.8	—	0.34	69.4	79.0	0.0
656	2006-08-26 02:13:37.761	510.8	325.7	0.25	2568.3	1059.5	35.7
657	2006-08-26 03:23:35.338	66.6	—	0.46	122.9	79.2	0.0
658	2006-08-26 04:13:22.560	315.5	157.3	0.46	360.6	154.0	1.0
659	2006-08-26 04:25:25.333	1182.8	974.8	0.53	12387.7	4724.7	70.9
660	2006-08-26 05:42:36.056	128.4	99.9	0.32	161.0	56.3	7.7
661	2006-08-26 12:32:54.991	317.1	167.7	0.18	1528.5	448.7	56.9
662	2006-08-26 18:48:45.993	650.2	267.6	0.28	3689.3	1608.4	39.8
663	2006-08-26 22:07:23.726	702.0	585.7	0.40	12755.9	5430.7	74.1
664	2006-08-27 03:14:45.564	295.4	—	0.88	193.6	151.2	13.0
665	2006-08-27 04:20:10.313	56.9	52.1	0.69	158.4	98.1	1.7
666	2006-08-27 08:49:52.705	177.4	91.9	0.53	226.0	113.3	4.7
667	2006-08-27 12:19:25.948	18.8	—	1.00	51.9	20.5	0.6
668	2006-08-27 12:25:26.815	47.4	—	1.00	93.3	58.0	0.1

Table A.2: (continued)

No	T_{start} (UTC)	T_{BB} (ms)	T_{90} (ms)	COD	CTS[a]	CTS[b]	CTS[c]
669	2006-08-27 12:41:34.972	124.7	—	1.00	69.2	53.7	0.8
670	2006-08-28 13:38:30.955	161.0	93.8	0.58	111.3	106.3	12.3
671	2006-08-28 16:07:53.514	119.8	—	0.30	68.5	58.6	12.3
672	2006-08-28 16:38:37.156	69.1	56.3	0.14	132.4	94.9	0.0
673	2006-08-28 20:01:24.152	19.0	—	0.31	63.9	31.3	0.0
674	2006-08-29 18:44:02.123	16.9	—	0.85	21.9	5.8	0.0
675	2006-08-29 21:57:43.184	668.5	—	0.71	16242.5	6914.0	170.5
676	2006-08-29 22:10:28.093	1058.5	576.9	0.51	8469.1	3158.2	34.7
677	2006-08-29 22:19:55.183	19.9	—	0.51	45.1	28.2	0.0
678	2006-08-29 22:48:00.808	328.2	87.6	0.51	372.2	185.1	15.1
679	2006-08-30 00:15:37.850	56.7	—	0.34	54.1	45.2	1.8
680	2006-08-30 03:16:47.448	25.8	32.2	0.74	13.0	31.6	0.8
681	2006-08-30 03:16:47.703	74.8	26.3	0.74	87.3	55.1	5.2
682	2006-08-30 04:10:47.318	35.0	—	0.95	30.3	19.8	0.0
683	2006-08-30 04:16:23.049	111.5	80.5	0.95	153.4	78.5	4.6
684	2006-08-30 06:46:31.590	122.6	—	0.90	65.0	73.5	1.6
685	2006-08-30 07:19:08.743	44.1	—	0.90	38.4	33.9	3.8
686	2006-08-30 07:50:09.095	67.9	—	0.90	57.3	54.8	8.8
687	2006-08-30 09:28:02.598	78.8	67.8	0.49	48.6	25.5	10.7
688	2006-08-30 14:58:39.237	34.1	—	0.85	68.3	39.0	0.2
689	2006-08-30 15:11:36.237	20.0	—	0.85	31.4	35.1	2.3
690	2006-08-30 16:37:40.576	94.3	—	0.83	387.8	125.2	1.6
691	2006-08-31 04:59:52.535	103.6	86.5	0.34	614.0	298.6	0.0
692	2006-09-01 11:58:20.382	41.8	36.4	0.62	67.9	41.9	7.0
693	2006-09-04 15:58:43.891	189.3	157.9	0.68	382.1	246.0	17.6
694	2006-09-04 16:13:43.783	112.4	99.7	0.55	130.2	61.8	4.3
695	2006-09-04 23:00:08.688	474.0	81.0	0.51	198.1	99.8	11.8
696	2006-09-05 08:36:09.347	21.8	—	0.30	68.5	16.9	0.0
697	2006-09-05 12:04:23.138	42.1	—	0.48	52.8	29.6	3.5
698	2006-09-05 12:04:23.640	618.8	611.3	0.48	134.3	90.6	3.7
699	2006-09-06 20:56:01.662	293.2	—	0.30	250.4	134.7	14.2
700	2006-09-06 23:07:07.261	148.2	147.8	0.54	133.3	109.0	12.2
701	2006-09-07 02:40:53.846	15.3	—	1.00	26.4	19.8	0.7
702	2006-09-07 02:40:54.323	62.8	—	1.00	39.1	29.5	4.7
703	2006-09-07 10:36:09.842	475.4	365.9	0.56	4035.4	1449.3	80.6
704	2006-09-09 02:55:21.372	173.3	163.3	0.50	248.1	131.1	5.3
705	2006-09-09 07:10:20.719	73.1	—	0.42	182.7	75.9	0.0
706	2006-09-09 07:44:41.837	66.8	—	0.57	67.4	53.2	7.1
707	2006-09-09 11:12:52.056	41.6	—	0.41	109.1	78.0	0.8
708	2006-09-09 12:29:37.464	76.5	61.8	0.21	105.2	83.3	1.1
709	2006-09-12 12:25:43.530	34.7	—	0.65	27.0	30.6	0.0
710	2006-09-12 16:30:41.266	129.9	—	0.74	73.3	42.4	1.9
711	2006-09-12 18:01:53.040	48.9	—	0.98	53.6	41.3	3.1
712	2006-09-13 01:49:33.552	124.4	—	1.00	72.8	32.3	3.3

Table A.2: (continued)

No	T_{start} (UTC)	T_{BB} (ms)	T_{90} (ms)	COD	CTS[a]	CTS[b]	CTS[c]
713	2006-09-14 11:01:03.876	104.2	—	1.00	31.2	29.7	1.5
714	2006-09-14 11:52:05.925	55.7	41.8	0.91	57.8	28.7	2.9
715	2006-09-15 10:29:58.367	155.5	124.1	0.78	58.3	33.5	10.2
716	2006-09-15 10:30:25.792	88.5	65.6	0.78	291.1	140.8	7.0
717	2006-09-15 13:53:58.073	37.7	—	0.74	50.0	28.1	0.0
718	2006-09-15 17:00:01.473	266.1	160.9	0.68	276.1	195.2	12.8
719	2006-09-15 17:07:47.944	30.4	—	0.68	41.6	11.0	0.0
720	2006-09-15 17:17:07.616	26.9	—	0.65	24.0	5.0	0.0
721	2006-09-15 18:15:15.287	688.0	463.8	0.52	4789.0	1684.1	48.7
722	2006-09-15 18:58:32.882	485.3	305.8	0.35	737.8	419.3	24.5
723	2006-09-16 15:18:17.684	73.4	—	0.74	72.7	32.8	0.1
724	2006-09-16 16:37:43.096	510.9	197.1	0.71	1477.1	738.5	28.3
725	2006-09-16 23:42:55.453	831.0	630.7	1.00	13731.3	5086.9	170.5
726	2006-09-17 03:09:49.267	197.4	159.1	1.00	1487.2	684.4	20.0
727	2006-09-17 05:30:48.849	59.6	—	0.82	32.6	8.6	0.2
728	2006-09-17 08:16:59.079	241.2	79.3	1.00	394.8	194.1	15.2
729	2006-09-18 08:24:38.414	285.2	220.8	0.56	113.4	141.2	11.9
730	2006-09-18 08:40:54.183	61.1	—	0.52	93.3	37.7	7.2
731	2006-09-18 09:58:38.949	168.0	—	0.49	243.8	112.9	1.6
732	2006-09-19 04:06:53.025	370.1	338.1	1.00	338.8	184.1	6.9
733	2006-09-19 05:09:02.323	41.8	—	0.91	48.7	44.4	5.7
734	2006-09-19 08:33:00.535	99.4	—	1.00	67.7	38.0	2.8
735	2006-09-19 11:41:00.967	346.5	199.9	1.00	245.2	120.2	4.9
736	2006-09-19 17:18:55.400	555.9	469.5	0.90	169.9	96.5	15.0
737	2006-09-19 17:18:56.300	47.3	—	0.90	48.0	30.5	2.5
738	2006-09-19 20:27:01.948	330.4	168.0	0.74	356.7	204.1	8.8
739	2006-09-19 20:33:20.974	645.9	240.5	0.74	3155.2	1256.4	15.2
740	2006-09-20 05:38:29.381	381.1	135.9	0.32	547.6	339.1	14.6
741	2006-09-20 13:36:40.081	40.7	—	0.09	177.7	147.1	13.9
742	2006-09-21 08:31:40.263	57.6	—	0.58	93.2	42.7	1.9
743	2006-09-21 08:39:02.823	483.4	213.7	0.58	2108.5	801.8	18.5
744	2006-09-21 10:45:21.682	226.1	202.5	0.84	134.6	89.9	6.2
745	2006-09-21 15:37:38.648	697.6	592.7	0.64	621.7	323.2	15.9
746	2006-09-21 15:39:36.799	59.0	55.3	0.64	112.0	68.6	9.9
747	2006-09-21 17:01:33.116	91.9	—	0.89	29.1	29.6	2.0
748	2006-09-21 18:08:16.165	11.2	—	1.00	18.7	8.1	2.2
749	2006-09-21 18:59:59.753	70.1	—	1.00	31.1	39.8	0.0
750	2006-09-22 01:15:40.089	163.1	137.1	1.00	230.2	119.6	8.3
751	2006-09-22 02:10:51.808	1031.1	—	1.00	105.4	105.9	0.7
752	2006-09-22 14:33:50.792	368.3	223.2	0.07	2427.4	838.1	0.0
753	2006-09-22 16:13:46.361	85.6	54.7	0.30	131.6	53.5	1.2
754	2006-09-22 22:18:00.785	108.5	—	0.22	107.9	51.0	0.0
755	2006-09-22 23:02:54.509	224.6	—	0.42	127.0	99.5	16.4
756	2006-09-23 02:06:16.308	303.3	238.0	1.00	561.0	365.6	29.9

Table A.2: (continued)

No	T_{start} (UTC)	T_{BB} (ms)	T_{90} (ms)	COD	CTS[a]	CTS[b]	CTS[c]
757	2006-09-23 02:07:44.778	555.7	38.2	1.00	271.1	236.5	6.8
758	2006-09-23 06:45:59.936	227.6	—	1.00	49.9	41.5	0.0
759	2006-09-23 08:42:46.989	72.1	67.7	1.00	115.8	61.0	0.6
760	2006-09-23 08:43:18.601	620.1	261.1	1.00	2447.0	1082.3	15.7
761	2006-09-24 04:48:03.431	249.4	225.5	0.68	478.7	312.6	26.5
762	2006-09-26 12:08:39.830	25.8	—	0.67	28.4	17.5	4.1
763	2006-09-30 10:07:47.409	33.7	27.9	0.67	22.8	18.4	0.7
764	2006-09-30 13:07:58.053	196.6	128.4	0.69	454.2	183.5	8.1
765	2006-09-30 14:20:46.703	20.4	—	0.98	36.7	17.5	3.4
766	2006-09-30 15:31:36.893	82.2	—	0.77	63.0	46.4	2.8
767	2006-10-02 03:16:03.998	390.7	65.5	0.64	122.8	62.9	0.0
768	2006-10-04 06:01:06.950	81.5	71.2	1.00	65.6	39.6	0.4
769	2006-10-04 08:59:13.057	209.7	136.0	1.00	1304.4	584.9	15.6
770	2006-10-04 11:45:48.369	153.8	60.7	1.00	780.1	379.1	3.5
771	2006-11-02 06:38:12.163	216.9	108.7	0.77	354.0	160.0	6.1
772	2007-02-26 15:13:27.525	11.5	—	0.33	12.5	20.4	0.0
773	2007-02-26 19:54:27.177	20.3	—	1.00	44.5	14.2	0.0
774	2007-02-26 21:07:54.330	88.0	—	1.00	65.0	43.1	2.9
775	2007-02-26 21:08:36.491	124.0	93.2	1.00	276.7	139.0	3.4
776	2007-02-27 07:27:48.588	130.6	94.2	1.00	546.8	168.4	11.9
777	2007-02-27 13:10:21.490	365.9	135.6	1.00	303.0	187.3	5.2
778	2007-02-28 04:44:02.665	265.0	137.9	1.00	745.3	273.4	9.1
780	2007-03-06 15:59:29.199	181.4	151.2	0.08	1530.4	612.4	17.1
781	2007-03-15 00:54:21.735	54.4	37.0	0.74	241.0	148.0	8.1
782	2007-03-16 15:27:15.705	292.5	102.7	0.57	1004.2	472.1	12.8
783	2007-03-18 20:29:12.955	60.1	—	0.73	257.9	103.6	0.0
784	2007-03-18 23:09:38.826	11.3	—	1.00	34.3	18.0	3.4
785	2007-03-22 23:51:26.373	110.0	—	1.00	68.7	59.5	7.1
786	2007-03-24 09:52:17.365	31.2	27.6	0.97	67.5	22.7	5.2
787	2007-03-24 20:37:33.247	721.7	491.9	1.00	347.8	234.9	0.2
788	2007-04-01 13:44:31.606	132.7	—	1.00	66.3	45.0	7.1
789	2007-04-02 14:54:11.428	20.1	—	0.43	29.3	16.3	5.3
790	2007-04-03 14:51:32.619	549.6	50.9	0.99	109.8	83.2	11.1
791	2007-04-03 19:12:13.178	159.5	108.3	0.33	410.5	270.5	11.9
792	2007-04-04 16:24:41.193	92.1	—	0.31	190.9	164.3	8.9
793	2007-04-04 22:35:18.365	360.6	171.5	0.70	157.4	109.0	16.3
794	2007-04-06 17:40:10.729	246.7	—	1.00	52.5	51.2	10.1
795	2007-04-07 08:39:36.736	33.4	—	1.00	51.9	23.4	0.0
796	2007-04-07 18:52:24.708	250.3	232.3	0.98	204.5	125.4	4.2
797	2007-04-08 14:43:16.539	401.9	213.1	1.00	2042.1	963.4	27.8
798	2007-04-18 13:42:09.521	379.7	159.8	0.69	127.3	84.7	5.0
799	2007-08-22 06:38:06.097	22.9	—	0.67	27.1	15.0	1.1
800	2007-08-23 07:25:34.780	43.0	—	0.32	143.0	75.3	2.5
801	2007-08-24 14:04:46.912	10.4	—	0.38	28.3	19.7	0.0

Table A.2: (continued)

No	T_{start} (UTC)	T_{BB} (ms)	T_{90} (ms)	COD	CTS[a]	CTS[b]	CTS[c]
802	2007-08-29 05:14:27.489	16.9	—	1.00	17.6	30.5	1.9
803	2007-08-29 14:03:27.426	738.8	505.6	0.99	2202.6	1575.4	105.7
804	2007-08-29 22:40:18.273	329.0	116.1	0.35	751.9	417.0	2.9
805	2007-08-29 23:22:21.438	150.5	102.6	0.47	591.1	278.1	16.1
806	2007-08-30 14:33:07.771	238.6	—	0.24	51.9	80.0	0.0
807	2007-08-31 11:01:55.318	16.8	—	0.76	18.1	19.0	0.0
808	2007-08-31 23:10:37.220	76.0	61.6	0.67	258.5	116.1	0.0
809	2007-08-31 23:10:50.203	24.3	—	0.67	36.4	21.6	0.9
810	2007-09-09 13:35:10.786	134.1	88.7	1.00	168.4	93.3	9.4
811	2007-09-09 18:23:05.878	13.8	—	0.25	73.5	41.3	0.0
812	2007-09-09 22:45:36.465	53.8	43.1	1.00	112.7	66.8	0.0
813	2007-09-10 05:31:06.629	24.9	—	0.61	112.4	60.6	2.4
814	2007-09-13 06:02:17.404	39.9	—	0.09	327.2	123.2	0.0
815	2007-09-13 22:19:53.852	602.2	151.2	0.47	1011.5	595.4	21.6
816	2007-09-14 03:23:55.512	127.8	123.2	0.34	166.2	88.4	2.7
817	2007-09-14 10:37:21.018	138.8	80.5	0.40	152.0	97.8	12.0
818	2007-09-14 10:46:01.100	494.6	373.9	0.40	4391.7	1762.4	10.9
819	2007-09-15 01:38:39.379	655.2	409.5	0.52	1389.9	712.4	13.5
820	2007-09-15 02:17:17.460	141.8	100.2	0.48	156.7	77.5	4.2
821	2007-09-15 03:34:16.773	507.0	203.7	0.34	436.9	209.4	0.0
822	2007-09-15 04:31:53.891	68.0	—	0.69	34.1	61.2	0.0
823	2007-09-15 12:21:31.730	114.8	100.7	0.66	121.5	81.7	0.0
824	2007-09-15 12:58:26.656	393.2	—	0.86	66.1	60.0	11.4
825	2007-09-15 13:25:35.595	107.9	77.2	0.86	170.6	89.4	0.2
826	2007-09-15 14:41:44.083	216.7	—	0.86	259.7	193.9	10.0
827	2007-09-15 14:41:44.689	128.4	71.8	0.86	557.2	182.4	18.6
828	2007-09-15 17:07:59.770	47.3	—	0.45	39.6	42.0	4.2
829	2007-09-15 17:12:43.777	27.3	—	0.44	51.3	14.7	5.0
830	2007-09-15 17:34:26.881	113.0	85.4	0.45	88.0	72.8	9.7
831	2007-09-15 21:34:07.363	166.4	115.8	0.61	275.3	146.4	6.7
832	2007-09-16 07:08:36.607	393.1	236.1	0.36	2151.7	996.4	43.2
833	2007-09-16 07:14:27.290	253.6	108.8	0.36	241.6	134.2	1.4
834	2007-09-16 09:16:59.379	48.6	—	0.57	58.4	41.6	2.9
835	2007-09-16 09:48:03.579	305.5	253.8	0.57	3345.3	1131.1	33.9
836	2007-09-16 19:02:43.795	553.5	335.4	0.57	557.0	344.3	39.9
837	2007-09-17 05:07:39.470	20.1	—	0.78	25.0	13.6	0.9
838	2007-09-18 04:38:05.398	1363.0	—	0.69	79.2	93.5	8.1
839	2007-09-19 10:01:51.679	702.9	519.5	0.35	6717.4	2604.3	73.9
840	2007-09-19 11:01:42.082	294.0	—	0.38	110.7	39.6	6.1
841	2007-09-19 11:03:28.066	46.8	35.9	0.39	54.8	61.3	5.1
842	2007-09-19 11:46:07.734	42.9	—	0.18	130.0	84.3	0.0
843	2007-09-19 19:25:02.188	66.3	—	0.20	188.9	115.1	0.0
844	2007-09-19 19:34:48.023	86.3	70.4	0.41	151.1	73.2	3.1
845	2007-09-19 19:34:48.423	661.1	338.2	0.41	3378.7	1429.6	59.8

Table A.2: (continued)

No	T_{start} (UTC)	T_{BB} (ms)	T_{90} (ms)	COD	CTS[a]	CTS[b]	CTS[c]
846	2007-09-19 19:37:29.443	316.2	221.8	0.41	1469.8	617.5	27.0
847	2007-09-19 19:50:04.703	35.8	—	0.41	79.1	30.9	1.9
848	2007-09-19 19:55:34.020	131.0	102.7	0.41	141.5	106.0	13.2
849	2007-09-19 20:19:33.775	44.6	—	0.41	66.5	37.4	1.7
850	2007-09-19 20:34:40.541	683.6	582.8	0.20	737.6	532.8	0.0
851	2007-09-19 20:45:10.620	1726.0	795.7	0.20	20079.4	7288.7	99.0
852	2007-09-19 20:45:15.280	139.3	59.6	0.20	200.7	134.8	1.1
853	2007-09-19 20:45:24.956	629.1	183.5	0.20	2577.3	977.8	17.2
854	2007-09-19 20:45:29.523	35.4	65.3	0.20	37.5	72.6	11.0
855	2007-09-19 20:45:29.781	215.2	104.7	0.20	1171.4	666.4	36.1
856	2007-09-19 20:45:51.520	221.7	—	0.19	123.4	24.3	5.9
857	2007-09-19 20:45:57.703	107.7	99.8	0.20	501.6	244.6	7.4
858	2007-09-19 20:45:58.447	323.0	127.3	0.20	215.4	144.8	4.5
859	2007-09-19 20:46:08.717	26.7	26.4	0.20	82.8	69.6	5.8
860	2007-09-19 20:47:02.732	197.6	193.1	0.20	400.3	239.0	4.6
861	2007-09-19 20:47:07.696	457.5	—	0.19	149.4	119.1	0.0
862	2007-09-19 20:47:11.597	147.0	79.8	0.20	317.5	171.9	1.5
863	2007-09-19 20:47:30.601	77.0	66.2	0.20	634.1	176.5	4.1
864	2007-09-19 20:48:13.519	40.4	—	0.19	128.6	29.5	0.0
865	2007-09-19 20:48:56.718	309.1	198.7	0.20	1206.4	379.5	48.4
866	2007-09-19 20:50:14.969	152.9	113.6	0.20	444.3	179.8	2.3
867	2007-09-19 20:51:03.647	193.3	124.1	0.20	689.7	279.7	23.4
868	2007-09-19 20:52:28.048	166.4	—	0.20	296.7	170.2	28.7
869	2007-09-19 21:02:19.734	99.1	89.7	0.20	495.7	212.4	3.0
870	2007-09-19 21:02:20.747	240.2	219.2	0.20	291.0	183.4	17.0
871	2007-09-19 21:02:22.811	190.2	93.8	0.20	448.0	328.5	13.4
872	2007-09-19 21:13:17.322	257.7	231.8	0.19	117.5	87.3	19.0
873	2007-09-19 21:20:32.357	155.8	—	0.19	290.9	97.8	0.0
874	2007-09-19 21:25:25.122	480.3	275.5	0.20	1610.2	566.4	31.1
875	2007-09-20 04:30:08.928	550.5	468.9	0.18	5536.0	3163.8	154.7
876	2007-09-20 04:30:10.742	456.0	398.6	0.18	2323.4	1057.3	41.0
877	2007-09-20 05:05:26.951	286.9	230.2	0.18	242.1	118.8	1.3
878	2007-09-20 05:24:03.624	115.1	—	0.18	87.6	41.4	18.7
879	2007-09-20 06:21:03.008	148.3	136.4	0.39	1212.7	451.0	0.6
880	2007-09-21 07:12:01.925	464.6	394.3	0.49	3248.7	1333.1	23.3
881	2007-09-21 14:52:22.636	120.4	111.5	0.26	713.4	282.2	0.0
882	2007-09-21 23:15:06.469	78.5	50.2	0.26	356.6	169.5	1.2
883	2007-09-22 10:40:24.697	99.0	77.9	0.39	105.2	44.1	3.3
884	2007-09-24 02:31:13.995	64.8	—	0.23	88.3	43.2	0.0
885	2007-09-24 04:28:30.738	164.7	153.6	0.24	1190.0	395.0	7.5
886	2007-09-24 05:11:26.753	199.2	—	0.24	11.4	44.8	51.2
887	2007-09-24 07:02:30.474	35.3	—	0.56	52.4	55.3	3.7
888	2007-09-24 07:22:56.188	39.6	35.6	0.70	169.3	96.0	4.3
889	2007-09-24 09:00:48.544	70.6	—	0.91	181.2	91.3	3.3

Table A.2: (continued)

No	T_{start} (UTC)	T_{BB} (ms)	T_{90} (ms)	COD	CTS[a]	CTS[b]	CTS[c]
890	2007-09-24 13:25:14.670	43.0	—	0.14	282.1	98.1	7.7
891	2007-09-24 14:11:00.416	105.7	81.7	0.14	111.8	57.8	15.0
892	2007-09-24 16:48:21.532	65.3	—	0.77	68.3	51.8	8.1
893	2007-09-24 16:59:03.189	58.4	—	0.75	39.4	35.2	3.7
894	2007-09-24 18:02:55.713	353.9	—	0.97	59.0	49.0	12.1
895	2007-09-24 21:57:24.515	1991.2	—	0.41	1302.9	829.7	28.4
896	2007-09-24 22:08:08.700	73.1	—	0.41	101.3	38.5	0.3
897	2007-09-25 05:04:35.902	674.1	429.7	0.78	481.8	380.3	26.3
898	2007-09-25 05:10:23.475	50.2	—	0.78	271.3	107.2	4.8
899	2007-09-25 07:08:24.335	67.7	—	0.47	45.4	31.3	3.1
900	2007-09-25 13:28:00.174	112.4	85.6	0.45	136.8	31.3	2.4
901	2007-09-25 16:38:34.927	1440.8	268.0	0.30	1827.8	860.0	1.6
902	2007-09-25 23:12:43.767	29.2	—	0.25	41.0	27.1	1.8
903	2007-09-26 09:24:44.282	117.7	—	0.52	144.3	73.4	0.3
904	2007-09-26 11:20:34.021	131.0	50.8	0.85	258.7	147.3	12.6
905	2007-09-30 01:10:40.846	128.4	68.9	1.00	65.8	59.6	12.2
906	2007-09-30 02:29:00.436	167.6	—	1.00	54.3	48.5	4.3
907	2007-09-30 05:13:49.085	142.3	72.1	1.00	178.7	107.7	9.7
908	2007-09-30 09:39:40.993	246.8	93.4	1.00	63.0	51.2	7.1
910	2007-10-01 11:56:22.498	74.6	73.7	1.00	63.1	42.7	10.3
911	2007-10-01 13:22:32.418	448.7	318.3	1.00	224.1	194.2	21.9
912	2007-10-01 13:22:33.298	835.4	375.1	1.00	279.9	279.1	26.7
913	2007-10-02 03:29:13.702	176.3	103.9	1.00	279.1	120.7	5.6
914	2007-10-02 06:31:49.617	74.4	—	1.00	182.6	113.1	1.0
915	2007-10-03 19:15:23.682	34.5	—	0.31	2.1	31.3	7.4
916	2007-10-05 02:45:28.698	310.3	117.6	0.35	698.5	279.3	17.1
918	2007-10-17 02:33:56.366	45.2	—	0.34	126.3	59.4	0.0
919	2007-10-29 08:23:36.823	148.1	—	0.30	537.6	288.9	17.3
920	2007-10-29 08:25:23.649	20.6	17.3	0.30	128.1	61.3	3.5
921	2008-02-23 22:43:30.064	129.8	76.8	0.26	224.6	189.7	2.9
922	2008-02-29 19:41:19.034	83.6	—	0.18	199.9	113.4	2.4
923	2008-03-19 15:12:23.152	106.5	66.9	0.31	615.8	297.1	41.2
924	2008-04-03 02:53:17.605	25.8	—	1.00	18.3	16.5	5.6
925	2008-04-03 08:43:39.037	349.5	129.5	1.00	771.8	355.9	11.1
1081	2010-03-29 12:53:04.477	235.0	156.7	0.49	213.4	150.1	5.9
1086	2012-09-19 07:08:00.344	222.0	—	0.83	20.1	22.6	10.7
1087	2013-02-26 10:09:29.160	43.4	23.6	0.83	31.2	42.3	6.6
1088	2013-02-28 02:43:19.384	55.5	31.2	0.91	93.5	67.5	5.9
1089	2013-09-19 02:57:51.143	23.0	—	0.66	24.7	10.1	4.8
1090	2014-09-02 05:55:29.963	563.6	168.2	0.63	302.0	347.6	69.8
1092	2014-09-28 10:02:29.548	184.8	—	0.39	81.3	46.6	14.4
1095	2014-10-23 15:52:18.912	89.1	—	0.47	93.0	60.1	9.0
1096	2014-10-25 11:27:52.568	203.3	179.8	0.84	46.9	52.0	6.7
1098	2015-02-18 22:51:26.490	93.5	74.3	1.00	—	77.8	3.0

Table A.2: (continued)

No	T_{start} (UTC)	T_{BB} (ms)	T_{90} (ms)	COD	CTS[a]	CTS[b]	CTS[c]
1099	2015-04-02 06:41:44.664	1099.0	1045.2	0.49	—	58.1	32.4
1108	2018-10-20 19:00:40.576	8.4	—	1.00	—	8.2	2.0
1110	2020-03-12 23:34:36.667	116.7	—	0.90	—	32.8	6.8
1111	2020-03-15 23:22:00.071	29.9	—	0.61	—	55.8	9.2
1129	2021-08-18 22:00:40.849	693.3	156.1	0.31	—	225.4	15.3
1130	2021-10-16 10:00:06.996	490.4	202.6	0.97	—	203.5	25.9
1150	2022-03-19 21:44:21.768	3.8	—	0.73	—	35.6	1.6
1345	2023-03-21 06:12:20.010	42.8	28.5	0.98	—	269.5	67.1
1347	2023-09-02 17:08:21.408	1674.7	—	0.92	—	100.1	22.9
1348	2024-02-09 10:33:02.836	33.6	—	0.33	—	59.9	6.9

[a] Counts in 20–40 keV.

[b] Counts in 40–100 keV.

[c] Counts in 100–150 keV.

Table A.3: Bursts from SGR 1935+2154.

No	T_{start} (UTC)	T_{BB} (ms)	T_{90} (ms)	COD	CTS[a]	CTS[b]	CTS[c]
1100	2015-05-11 01:31:20.484	630.3	—	0.71	—	24.1	43.2
1101	2015-12-21 02:51:12.494	85.4	38.1	0.78	—	347.8	28.6
1102	2016-05-30 00:46:25.402	273.7	156.4	0.20	—	336.8	63.2
1109	2019-11-14 00:30:46.498	50.2	—	0.27	—	63.5	14.5
1112	2020-04-28 03:47:52.135	47.0	27.4	0.11	—	203.0	34.2
1113	2020-04-28 04:09:47.290	73.3	42.6	0.11	—	230.9	43.8
1114	2020-04-28 05:56:30.451	114.8	37.2	0.29	—	268.0	70.2
1115	2020-04-28 06:07:46.818	156.6	—	0.29	—	205.8	41.6
1116	2020-04-28 08:03:34.210	116.4	84.4	0.15	—	87.0	7.8
1117	2020-04-28 09:51:04.730	371.4	174.5	0.48	—	192.3	25.0
1118	2020-04-28 14:34:24.002	728.1	205.8	0.72	—	1302.9	533.3
1119	2020-04-28 19:01:59.661	64.6	61.6	1.00	—	48.9	19.9
1120	2020-05-03 23:25:13.252	285.4	146.3	0.05	—	1950.6	456.2
1122	2021-02-02 12:54:26.687	201.3	41.6	0.16	—	766.7	136.7
1123	2021-07-06 17:14:49.085	72.8	47.1	0.18	—	1071.5	179.0
1124	2021-07-07 00:20:35.948	116.8	—	0.32	—	68.0	17.7
1125	2021-07-07 00:33:31.305	198.7	103.0	0.32	—	2446.9	429.0
1126	2021-07-12 04:32:39.244	502.9	33.1	0.27	—	467.7	45.1
1127	2021-07-12 16:58:50.470	286.7	55.5	0.14	—	280.5	120.3
1128	2021-07-12 18:04:28.018	45.0	42.5	0.18	—	209.6	63.7
1131	2021-11-03 01:52:58.882	393.6	—	0.61	—	59.3	35.1
1132	2021-11-19 01:20:53.614	193.9	—	0.50	—	20.1	46.9
1133	2021-12-20 16:16:09.112	74.2	55.8	0.39	—	101.8	41.2
1134	2022-01-10 15:55:38.241	473.5	125.2	0.36	—	721.4	79.6
1135	2022-01-13 06:36:43.697	797.4	151.1	0.16	—	1325.1	285.2
1136	2022-01-16 10:04:32.942	147.0	—	0.47	—	75.2	21.8
1137	2022-01-16 10:07:37.146	600.0	—	0.47	—	183.5	97.7
1138	2022-01-16 10:34:42.085	41.2	—	0.38	—	49.8	9.0
1139	2022-01-16 10:40:32.949	125.1	—	0.38	—	78.3	7.4
1140	2022-01-16 10:48:37.470	372.4	102.4	0.38	—	631.5	108.6
1141	2022-01-16 10:59:28.558	91.3	82.8	0.38	—	91.9	26.4
1142	2022-01-16 11:15:52.615	560.4	460.2	0.26	—	213.5	56.8
1143	2022-01-16 11:17:35.296	134.2	71.0	0.26	—	282.4	63.9
1144	2022-01-16 11:20:30.354	299.6	—	0.26	—	209.5	21.1
1145	2022-01-16 11:39:42.602	172.4	36.7	0.26	—	517.9	81.2
1146	2022-01-16 11:45:43.700	40.5	35.9	0.26	—	419.9	80.1
1147	2022-01-16 14:09:38.698	375.9	138.8	0.36	—	3244.9	525.8
1148	2022-01-16 14:10:00.921	168.2	—	0.36	—	106.5	0.8
1149	2022-01-16 18:46:30.063	37.1	—	0.41	—	51.1	12.8
1152	2022-04-26 02:53:03.880	62.8	—	0.73	—	21.4	13.3
1153	2022-05-10 10:17:20.864	2.7	—	0.79	—	24.1	3.2
1154	2022-05-10 10:17:22.423	3.4	—	0.79	—	34.5	0.0
1155	2022-05-10 10:22:25.201	2.6	—	0.79	—	31.0	0.0
1156	2022-05-10 10:23:20.339	3.3	—	0.79	—	30.9	0.0

Table A.3: (continued)

No	T_{start} (UTC)	T_{BB} (ms)	T_{90} (ms)	COD	CTS[a]	CTS[b]	CTS[c]
1157	2022-06-09 12:17:37.707	72.7	66.7	0.40	—	67.8	25.6
1158	2022-06-19 12:46:20.922	149.0	102.7	0.55	—	240.2	65.4
1159	2022-10-10 14:45:56.459	194.1	201.4	1.00	—	95.3	21.9
1160	2022-10-10 21:08:56.178	297.4	57.2	0.89	—	523.5	115.6
1161	2022-10-10 21:28:25.000	20.0	—	0.94	—	7.7	8.9
1162	2022-10-10 21:28:25.857	237.7	129.2	0.94	—	128.5	80.1
1163	2022-10-10 23:20:17.018	159.1	138.5	1.00	—	53.0	29.9
1164	2022-10-10 23:32:48.997	389.1	—	1.00	—	72.2	32.0
1165	2022-10-11 16:42:31.028	56.4	42.9	0.88	—	20.6	10.3
1166	2022-10-11 23:22:48.894	290.1	252.3	0.88	—	130.0	28.8
1167	2022-10-12 12:47:03.905	524.2	85.7	1.00	—	846.0	226.2
1168	2022-10-12 13:32:18.649	79.2	—	0.93	—	37.9	11.7
1169	2022-10-12 14:01:00.556	60.2	48.8	0.93	—	18.8	12.5
1170	2022-10-12 14:22:46.784	79.1	—	0.77	—	163.4	27.0
1171	2022-10-12 14:22:45.835	671.9	106.3	0.77	—	177.0	71.2
1172	2022-10-12 14:22:46.784	676.0	629.6	0.77	—	329.7	105.5
1173	2022-10-12 14:40:49.770	874.4	94.6	0.77	—	592.4	163.3
1174	2022-10-12 14:43:19.720	291.3	180.4	0.77	—	1173.5	220.5
1175	2022-10-12 14:44:45.253	971.9	—	0.77	—	12917.5	1945.8
1176	2022-10-12 14:46:33.670	21.9	—	0.77	—	20.5	9.6
1177	2022-10-12 14:48:48.223	68.8	—	0.77	—	34.3	5.3
1178	2022-10-12 14:49:01.891	97.2	73.4	0.77	—	99.8	15.7
1179	2022-10-12 14:49:59.908	780.0	264.6	0.77	—	244.0	90.4
1180	2022-10-12 14:51:14.859	888.9	702.2	0.77	—	251.7	75.0
1181	2022-10-12 14:52:50.266	47.9	—	0.77	—	34.6	14.4
1182	2022-10-12 14:54:37.715	136.1	71.9	0.77	—	104.5	34.7
1183	2022-10-12 14:55:46.673	224.6	—	0.77	—	36.0	28.3
1184	2022-10-12 14:56:30.334	167.7	110.0	0.77	—	110.1	15.8
1185	2022-10-12 14:59:59.248	29.7	—	0.77	—	18.6	8.2
1186	2022-10-12 15:05:35.597	780.9	584.8	0.77	—	222.6	105.4
1187	2022-10-12 15:06:50.702	650.3	175.4	0.77	—	208.5	80.0
1188	2022-10-12 15:09:33.074	209.1	202.5	0.77	—	33.8	7.5
1189	2022-10-12 15:10:40.509	42.5	—	0.77	—	58.7	15.8
1190	2022-10-12 15:11:18.753	552.0	67.4	0.77	—	460.5	77.1
1191	2022-10-12 15:14:03.911	668.2	—	0.77	—	2682.7	444.1
1192	2022-10-12 15:14:34.289	283.1	148.0	0.77	—	667.3	166.2
1193	2022-10-12 15:14:51.100	78.2	—	0.77	—	59.6	11.3
1194	2022-10-12 15:14:58.205	570.2	—	0.77	—	259.2	88.1
1195	2022-10-12 15:15:02.168	189.5	125.0	0.77	—	87.1	46.4
1196	2022-10-12 15:15:32.441	718.8	308.3	0.77	—	119.2	37.2
1197	2022-10-12 15:15:58.280	107.1	82.9	0.77	—	95.9	42.9
1198	2022-10-12 15:16:21.098	52.7	—	0.77	—	21.9	30.8
1199	2022-10-12 15:16:22.511	477.6	175.3	0.77	—	355.2	120.1
1200	2022-10-12 15:16:23.588	451.4	213.8	0.77	—	1229.2	361.2

Table A.3: (continued)

No	T_{start} (UTC)	T_{BB} (ms)	T_{90} (ms)	COD	CTS[a]	CTS[b]	CTS[c]
1201	2022-10-12 15:16:27.243	85.2	—	0.77	—	41.4	12.6
1202	2022-10-12 15:16:45.741	78.7	50.5	0.77	—	50.3	11.5
1203	2022-10-12 15:17:15.993	460.1	—	0.77	—	128.8	69.3
1204	2022-10-12 15:17:18.261	359.8	—	0.77	—	113.0	23.7
1205	2022-10-12 15:18:13.642	1200.2	418.5	0.77	—	552.7	193.3
1206	2022-10-12 15:18:51.614	147.6	41.6	0.77	—	302.0	66.5
1207	2022-10-12 15:18:56.395	91.2	—	0.77	—	64.6	17.7
1208	2022-10-12 15:19:41.930	402.1	—	0.77	—	65.9	41.0
1209	2022-10-12 15:20:08.459	321.6	—	0.77	—	76.3	27.4
1210	2022-10-12 15:20:30.654	1636.1	716.5	0.77	—	12116.5	1462.1
1211	2022-10-12 15:20:46.894	40.8	—	0.77	—	33.2	6.8
1212	2022-10-12 15:21:39.644	48.7	44.1	0.77	—	53.7	5.2
1213	2022-10-12 15:22:04.312	150.3	—	0.77	—	71.8	28.4
1214	2022-10-12 15:22:24.955	422.8	122.0	0.77	—	357.3	62.1
1215	2022-10-12 15:22:25.674	421.3	136.0	0.77	—	231.1	63.1
1216	2022-10-12 15:22:37.961	463.2	169.1	0.77	—	169.2	46.3
1217	2022-10-12 15:25:34.450	56.3	47.7	0.77	—	42.6	13.1
1218	2022-10-12 15:25:49.925	123.4	117.3	0.77	—	50.6	16.8
1219	2022-10-12 15:26:23.371	543.0	—	0.77	—	123.6	55.2
1220	2022-10-12 15:27:32.514	426.6	—	0.77	—	96.9	42.0
1221	2022-10-12 15:29:01.819	151.1	88.0	0.77	—	91.4	24.8
1222	2022-10-12 15:29:48.196	822.1	219.7	0.77	—	758.7	236.0
1223	2022-10-12 15:30:39.855	728.0	119.4	0.77	—	1051.3	193.2
1224	2022-10-12 15:31:15.289	90.8	—	0.77	—	51.1	11.4
1225	2022-10-12 15:33:34.801	249.1	—	0.77	—	61.8	35.0
1226	2022-10-12 15:33:40.242	347.4	65.1	0.77	—	489.8	113.1
1227	2022-10-12 15:34:10.908	95.9	—	0.77	—	41.4	21.0
1228	2022-10-12 15:35:32.424	283.0	—	0.77	—	74.8	20.7
1229	2022-10-12 15:36:11.187	212.2	99.5	0.77	—	128.7	29.8
1230	2022-10-12 15:37:43.253	217.9	159.3	0.77	—	111.5	58.4
1231	2022-10-12 15:37:43.724	4.9	—	0.77	—	9.3	4.2
1232	2022-10-12 15:38:42.282	278.6	197.0	0.77	—	84.8	14.5
1233	2022-10-12 15:39:02.423	213.0	54.6	0.77	—	136.2	26.8
1234	2022-10-12 15:39:42.181	469.5	165.0	0.77	—	2148.9	359.1
1235	2022-10-12 15:39:43.344	24.8	—	0.77	—	35.4	6.7
1236	2022-10-12 15:40:10.013	269.4	94.9	0.77	—	175.2	63.0
1237	2022-10-12 15:40:39.630	936.7	834.2	0.77	—	223.8	119.5
1238	2022-10-12 15:41:18.460	112.0	98.2	0.77	—	67.0	25.0
1239	2022-10-12 15:41:29.381	94.5	—	0.77	—	37.4	14.4
1240	2022-10-12 15:41:32.747	455.4	—	0.77	—	87.8	27.9
1241	2022-10-12 15:41:42.434	565.0	507.2	0.77	—	165.3	67.9
1242	2022-10-12 15:42:06.400	153.4	—	0.77	—	62.2	28.1
1243	2022-10-12 15:42:16.106	59.0	—	0.77	—	30.7	16.5
1244	2022-10-12 15:42:30.807	615.6	329.2	0.77	—	5079.8	886.1

Table A.3: (continued)

No	T_{start} (UTC)	T_{BB} (ms)	T_{90} (ms)	COD	CTS[a]	CTS[b]	CTS[c]
1245	2022-10-12 15:42:32.078	8.0	—	0.77	—	12.2	0.0
1246	2022-10-12 15:42:50.406	205.3	—	0.77	—	75.0	37.5
1247	2022-10-12 15:43:05.416	176.0	46.6	0.77	—	310.9	58.5
1248	2022-10-12 15:43:10.464	184.3	—	0.77	—	32.2	25.6
1249	2022-10-12 15:43:14.703	102.9	61.5	0.77	—	40.5	23.8
1250	2022-10-12 15:43:17.054	279.3	258.3	0.77	—	86.9	33.3
1251	2022-10-12 15:43:24.600	56.6	—	0.77	—	71.9	21.8
1252	2022-10-12 15:43:36.144	124.3	—	0.77	—	43.6	7.0
1253	2022-10-12 15:43:45.146	54.9	—	0.77	—	39.2	12.0
1254	2022-10-12 15:43:52.557	34.0	—	0.77	—	29.4	10.9
1255	2022-10-12 15:43:56.941	165.0	113.7	0.77	—	84.5	16.6
1256	2022-10-12 15:44:02.622	130.0	—	0.77	—	43.7	13.3
1257	2022-10-12 15:44:24.952	438.9	317.0	0.77	—	138.4	65.7
1258	2022-10-12 15:44:52.130	39.9	36.0	0.77	—	42.6	8.2
1259	2022-10-12 15:45:00.931	94.6	—	0.77	—	53.7	3.5
1260	2022-10-12 15:45:08.333	1852.5	—	0.77	—	4314.1	1050.8
1261	2022-10-12 15:45:19.178	77.7	71.5	0.77	—	62.6	17.0
1262	2022-10-12 15:45:35.080	244.4	55.1	0.77	—	125.7	44.3
1263	2022-10-12 15:45:46.823	57.7	—	0.77	—	32.5	9.3
1264	2022-10-12 15:45:47.818	292.1	—	0.77	—	63.5	24.5
1265	2022-10-12 15:46:03.254	297.3	124.3	0.77	—	161.2	45.7
1266	2022-10-12 15:46:36.044	97.4	97.0	0.77	—	57.2	19.0
1267	2022-10-12 15:47:09.885	235.9	98.3	0.77	—	126.2	45.3
1268	2022-10-12 15:47:51.782	422.9	258.9	0.77	—	406.2	109.3
1269	2022-10-12 15:48:09.234	267.2	—	0.77	—	51.6	23.0
1270	2022-10-12 15:48:15.725	357.0	216.9	0.77	—	1041.9	286.2
1271	2022-10-12 15:49:13.165	430.5	106.9	0.77	—	848.2	223.0
1272	2022-10-12 15:51:02.336	270.6	129.6	0.77	—	109.9	24.3
1273	2022-10-12 15:51:22.262	35.4	—	0.77	—	30.6	8.9
1274	2022-10-12 15:52:11.031	109.9	—	0.77	—	50.4	24.5
1275	2022-10-12 15:52:17.848	65.7	—	0.77	—	70.2	13.8
1276	2022-10-12 15:55:34.700	55.8	51.0	0.77	—	41.2	10.0
1277	2022-10-12 15:55:35.517	59.5	—	0.77	—	44.9	13.5
1278	2022-10-12 15:57:22.197	77.5	73.1	0.77	—	41.6	16.4
1279	2022-10-12 15:57:22.918	90.0	—	0.77	—	30.8	14.8
1280	2022-10-12 16:00:48.482	316.3	152.4	0.77	—	259.2	61.4
1281	2022-10-12 16:07:11.340	132.3	126.7	0.77	—	84.3	30.4
1282	2022-10-12 16:07:37.875	106.3	—	0.77	—	52.4	16.1
1283	2022-10-12 16:11:14.050	240.6	—	0.94	—	33.5	24.9
1284	2022-10-12 16:11:14.700	406.2	65.1	0.94	—	238.9	74.0
1285	2022-10-12 16:13:01.640	94.6	83.4	0.94	—	50.4	10.9
1286	2022-10-12 16:13:38.978	107.2	73.7	0.94	—	106.3	30.0
1287	2022-10-12 16:25:46.115	438.0	391.1	0.94	—	187.6	51.5
1288	2022-10-12 16:35:05.532	315.2	138.1	0.94	—	104.2	40.7

Table A.3: (continued)

No	T_{start} (UTC)	T_{BB} (ms)	T_{90} (ms)	COD	CTS[a]	CTS[b]	CTS[c]
1289	2022-10-12 16:35:42.592	212.6	122.9	0.94	—	33.7	15.1
1290	2022-10-12 16:37:45.436	88.0	83.9	0.94	—	104.9	26.2
1291	2022-10-12 16:41:31.683	75.2	71.1	0.94	—	52.0	15.2
1292	2022-10-12 16:41:32.707	370.0	—	0.94	—	155.0	34.6
1293	2022-10-12 16:43:56.886	662.4	195.2	0.94	—	306.6	110.2
1294	2022-10-12 16:46:42.514	146.3	92.6	0.94	—	31.0	8.2
1295	2022-10-12 16:57:13.399	357.4	—	0.94	—	170.0	64.3
1296	2022-10-12 17:00:46.681	63.8	61.8	0.94	—	29.2	20.3
1297	2022-10-12 17:00:47.061	255.0	79.9	0.94	—	862.8	187.8
1298	2022-10-12 17:06:40.479	102.4	—	0.94	—	22.4	14.4
1299	2022-10-12 17:17:56.566	477.2	703.6	0.88	—	122.1	57.6
1300	2022-10-12 17:17:57.291	67.8	43.3	0.88	—	41.7	24.1
1301	2022-10-12 17:19:33.031	93.4	—	0.88	—	37.2	14.1
1302	2022-10-12 17:36:24.250	196.4	—	0.88	—	31.0	17.5
1303	2022-10-12 17:36:25.194	241.9	—	0.88	—	35.9	21.1
1304	2022-10-12 17:39:25.743	402.0	199.2	0.88	—	249.6	75.2
1305	2022-10-12 17:39:26.638	39.4	—	0.88	—	36.9	11.0
1306	2022-10-12 17:43:10.833	125.4	62.4	0.88	—	505.8	86.5
1307	2022-10-12 17:52:22.334	96.8	—	0.88	—	31.3	6.7
1308	2022-10-12 17:52:46.192	279.3	183.3	0.88	—	160.6	49.6
1309	2022-10-12 18:09:32.087	66.8	63.4	0.88	—	19.8	16.2
1310	2022-10-12 18:33:43.257	281.2	68.3	1.00	—	993.1	207.8
1311	2022-10-12 18:47:49.744	119.4	—	1.00	—	47.5	4.4
1312	2022-10-12 19:03:00.380	300.0	—	1.00	—	32.1	16.2
1313	2022-10-12 19:26:08.232	618.3	354.6	1.00	—	71.3	22.2
1314	2022-10-12 19:39:06.217	371.5	—	1.00	—	72.4	39.7
1315	2022-10-12 19:39:06.780	232.4	101.0	1.00	—	75.0	15.5
1316	2022-10-12 19:54:56.628	330.8	198.5	1.00	—	54.5	33.5
1317	2022-10-12 20:00:20.726	189.1	127.1	1.00	—	73.2	17.2
1318	2022-10-12 20:06:05.870	251.2	135.0	1.00	—	66.0	11.3
1319	2022-10-12 20:22:11.549	164.2	—	1.00	—	37.1	14.0
1320	2022-10-12 20:22:12.271	217.6	—	1.00	—	36.6	20.4
1321	2022-10-12 20:32:22.207	1086.5	1141.0	1.00	—	96.6	30.7
1322	2022-10-12 20:32:28.806	31.9	20.0	1.00	—	69.6	11.5
1323	2022-10-12 20:38:05.907	252.9	—	1.00	—	33.8	28.3
1324	2022-10-12 20:50:31.674	98.1	97.6	1.00	—	80.0	14.6
1325	2022-10-12 20:58:49.287	1334.7	232.2	0.87	—	1122.4	300.8
1326	2022-10-12 21:09:06.286	403.8	101.7	0.87	—	330.2	108.1
1327	2022-10-12 21:10:45.622	157.9	—	0.87	—	43.7	15.7
1328	2022-10-12 21:10:46.055	206.3	—	0.87	—	64.1	19.6
1329	2022-10-12 21:12:10.333	78.0	42.8	0.87	—	345.8	92.3
1330	2022-10-12 21:44:18.220	227.7	47.1	0.87	—	300.4	72.0
1331	2022-10-12 21:49:36.947	350.2	202.2	0.87	—	139.0	50.6
1332	2022-10-12 22:10:27.649	277.5	—	0.72	—	62.9	44.4

Table A.3: (continued)

No	T_{start} (UTC)	T_{BB} (ms)	T_{90} (ms)	COD	CTS[a]	CTS[b]	CTS[c]
1333	2022-10-12 22:34:56.653	267.6	201.4	0.72	—	204.5	38.4
1334	2022-10-12 23:26:41.992	750.7	85.7	0.72	—	2357.7	510.0
1335	2022-10-12 23:45:45.705	355.8	94.2	0.72	—	193.3	70.9
1336	2022-10-13 00:00:53.164	541.4	263.9	0.88	—	2584.5	461.1
1337	2022-10-13 00:52:37.923	335.9	49.6	0.88	—	533.9	111.7
1338	2022-10-13 00:55:25.978	34.5	—	0.88	—	39.4	1.1
1339	2022-10-14 20:48:47.191	118.0	—	0.98	—	54.9	12.7
1340	2022-10-14 22:41:25.843	221.4	163.1	1.00	—	227.5	91.4
1341	2022-10-15 02:09:05.136	72.6	—	0.98	—	72.4	7.5
1342	2022-10-15 02:13:54.349	115.0	74.3	0.98	—	239.6	31.1
1343	2022-10-15 15:40:28.394	110.3	—	1.00	—	30.1	20.6
1344	2022-10-16 03:51:09.829	29.2	—	0.77	—	19.9	15.7

[a] Counts in 20–40 keV.

[b] Counts in 40–100 keV.

[c] Counts in 100–150 keV.

Table A.4: Results of the time-averaged spectral analysis of the bursts from 1E 1547.0–5408.

	Power law			Cutoff power law			
No	α	χ^2_r(dof)	Flux	α	E_{peak}	χ^2_r(dof)	Flux
936	-2.3 ± 0.2	1.7(7)	1.2 ± 0.2	—	—	—	—
938	-2.4 ± 0.3	0.5(6)	0.3 ± 0.1	—	—	—	—
941	-1.6 ± 0.2	1.5(7)	$2.6^{+0.3}_{-0.4}$	$0.4^{+1.9}_{-0.8}$	$67.7^{+14.7}_{-11.6}$	0.7(6)	2.6 ± 0.4
950	-2.3 ± 0.1	0.3(8)	8.3 ± 0.7	$-1.8^{+0.5}_{-0.2}$	< 32.2	0.2(7)	8.2 ± 0.7
954	-1.6 ± 0.3	0.6(7)	0.8 ± 0.2	—	—	—	—
955	—	—	—	$-0.8^{+0.5}_{-0.4}$	$46.6^{+4.2}_{-1.9}$	1.1(8)	$3.8^{+0.2}_{-0.3}$
956	-2.2 ± 0.2	0.5(5)	$7.1^{+1.1}_{-1.3}$	—	—	—	—
957	-1.7 ± 0.2	1.5(7)	2.8 ± 0.4	—	—	—	—
958	—	—	—	$-0.7^{+0.5}_{-0.4}$	$41.2^{+3.3}_{-4.2}$	1.6(8)	5.2 ± 0.3
962	-1.2 ± 0.2	1.1(6)	$2.7^{+0.4}_{-0.5}$	—	—	—	—
966	—	—	—	-0.2 ± 0.4	$40.1^{+1.9}_{-2.2}$	0.7(8)	10.3 ± 0.5
968	—	—	—	$0.5^{+1.0}_{-0.5}$	$53.2^{+4.0}_{-3.6}$	0.3(7)	$7.4^{+0.6}_{-0.7}$
969	$-0.6^{+0.3}_{-0.2}$	1.0(5)	$3.3^{+0.4}_{-0.5}$	—	—	—	—
972	—	—	—	$0.2^{+0.5}_{-0.4}$	$44.9^{+2.1}_{-2.0}$	0.8(7)	16.6 ± 0.9
973	-1.6 ± 0.3	0.5(7)	$1.2^{+0.2}_{-0.3}$	—	—	—	—
974	-0.9 ± 0.3	1.2(3)	1.1 ± 0.2	$1.2^{+3.4}_{-1.2}$	$91.1^{+48.8}_{-18.3}$	0.2(2)	1.1 ± 0.2
978	-1.7 ± 0.2	0.4(7)	$4.6^{+0.6}_{-0.7}$	—	—	—	—
979	-2.0 ± 0.3	0.1(5)	1.5 ± 0.4	—	—	—	—
980	-1.3 ± 0.2	1.7(7)	1.3 ± 0.2	$0.7^{+2.0}_{-0.8}$	$77.2^{+16.9}_{-12.3}$	1.1(6)	1.3 ± 0.2
981	-1.7 ± 0.2	1.7(6)	2.4 ± 0.4	—	—	—	—
985	-0.8 ± 0.2	0.6(7)	$2.0^{+0.3}_{-0.4}$	—	—	—	—
987	$-1.9^{+0.1}_{-0.2}$	1.2(8)	1.9 ± 0.2	—	—	—	—
990	-1.7 ± 0.2	0.9(6)	1.5 ± 0.3	—	—	—	—
991	-2.2 ± 0.1	1.0(9)	$5.5^{+0.3}_{-0.4}$	$-1.2^{+0.4}_{-0.5}$	$36.7^{+4.6}_{-10.2}$	0.4(8)	$5.3^{+0.3}_{-0.4}$
1003	—	—	—	-0.4 ± 0.4	$45.6^{+3.2}_{-3.0}$	0.4(8)	9.1 ± 0.6
1004	-1.3 ± 0.2	1.2(8)	$6.6^{+0.8}_{-0.9}$	—	—	—	—
1008	-1.4 ± 0.3	1.3(4)	$3.2^{+0.6}_{-0.7}$	$0.9^{+2.7}_{-1.1}$	$55.4^{+13.6}_{-8.4}$	0.6(3)	2.3 ± 0.5
1011	-2.4 ± 0.3	0.9(6)	$2.3^{+0.4}_{-0.5}$	—	—	—	—
1014	—	—	—	-0.6 ± 0.3	$63.1^{+4.2}_{-4.6}$	1.4(9)	5.9 ± 0.3
1018	-1.0 ± 0.2	0.3(7)	$6.9^{+1.0}_{-1.2}$	—	—	—	—
1023	-1.4 ± 0.3	0.4(4)	$3.0^{+0.6}_{-0.7}$	$0.3^{+2.0}_{-1.6}$	$58.6^{+132.2}_{-11.9}$	0.1(3)	$2.2^{+0.7}_{-0.5}$
1029	-1.5 ± 0.1	1.0(9)	4.4 ± 0.4	-0.6 ± 0.6	$91.7^{+74.9}_{-18.8}$	0.8(8)	$4.4^{+0.4}_{-0.5}$
1032	-1.6 ± 0.2	1.6(8)	$3.8^{+0.4}_{-0.5}$	$0.0^{+1.1}_{-0.9}$	$64.4^{+16.6}_{-8.0}$	1.3(7)	$3.7^{+0.4}_{-0.5}$
1033	—	—	—	-0.4 ± 0.3	$44.8^{+2.2}_{-1.3}$	0.7(8)	9.3 ± 0.4
1037	—	—	—	-0.1 ± 0.4	45.6 ± 2.1	0.6(9)	8.3 ± 0.4
1040	-1.6 ± 0.3	0.6(6)	1.5 ± 0.3	—	—	—	—
1043	—	—	—	-0.2 ± 0.4	$37.4^{+2.0}_{-2.4}$	0.8(8)	11.8 ± 0.6
1046	-2.3 ± 0.3	1.1(4)	$4.8^{+1.2}_{-1.3}$	—	—	—	—
1049	-1.3 ± 0.2	0.5(7)	$2.8^{+0.4}_{-0.5}$	—	—	—	—
1050	-2.2 ± 0.1	1.1(8)	$11.1^{+0.9}_{-1.0}$	—	—	—	—
1053	-1.8 ± 0.3	0.6(4)	$1.9^{+0.4}_{-0.5}$	—	—	—	—
1055	—	—	—	$0.0^{+1.2}_{-0.6}$	$76.8^{+19.6}_{-12.6}$	1.6(7)	3.8 ± 0.5
1059	-0.9 ± 0.3	0.6(3)	$4.3^{+0.7}_{-0.9}$	—	—	—	—

Table A.4: (continued)

	Power law			Cutoff power law			
No	α	χ^2_r(dof)	Flux	α	E_{peak}	χ^2_r(dof)	Flux
1062	-1.5 ± 0.3	0.5(4)	$4.7^{+0.9}_{-1.0}$	—	—	—	—
1063	-1.0 ± 0.2	1.5(6)	$3.2^{+0.5}_{-0.6}$	—	—	—	—
1065	—	—	—	$0.0^{+0.7}_{-0.6}$	$47.7^{+3.7}_{-3.3}$	0.6(7)	$6.6^{+0.5}_{-0.6}$
1070	-1.8 ± 0.2	0.7(7)	$5.5^{+0.7}_{-0.8}$	$0.1^{+1.2}_{-1.0}$	$50.4^{+8.6}_{-5.6}$	0.2(6)	4.9 ± 0.7
1073	$-2.2^{+0.3}_{-0.4}$	1.6(6)	$1.0^{+0.2}_{-0.3}$	—	—	—	—
1074	-1.3 ± 0.3	0.8(9)	0.6 ± 0.1	—	—	—	—
1075	-2.1 ± 0.1	0.7(9)	1.9 ± 0.2	—	—	—	—
1076	—	—	—	0.3 ± 0.3	$38.3^{+1.2}_{-1.4}$	1.2(8)	13.0 ± 0.5
1078	-1.7 ± 0.3	1.0(8)	1.1 ± 0.2	—	—	—	—

Flux is in units of 10^{-7} erg cm^{-2} s^{-1}.
E_{peak} is in units of keV.

Table A.5: Results of the time-averaged spectral analysis of the bursts from SGR 1806–20.

	Power law			Cutoff power law			
No	α	χ^2_r(dof)	Flux	α	E_{peak}	χ^2_r(dof)	Flux
6	-2.2 ± 0.2	1.6(8)	2.9 ± 0.4	$-0.5^{+1.3}_{-1.0}$	$46.3^{+8.6}_{-9.6}$	1.3(7)	$3.0^{+0.4}_{-0.5}$
9	—	—	—	$-0.4^{+1.0}_{-0.9}$	$40.0^{+5.2}_{-8.8}$	1.5(6)	1.6 ± 0.2
14	-2.1 ± 0.3	0.8(6)	3.3 ± 0.6	—	—	—	—
17	-2.1 ± 0.2	0.8(9)	1.6 ± 0.2	—	—	—	—
19	-2.1 ± 0.1	0.8(9)	2.1 ± 0.2	—	—	—	—
28	-2.6 ± 0.1	1.5(8)	4.4 ± 0.4	—	—	—	—
32	—	—	—	$-0.6^{+0.5}_{-0.9}$	$24.9^{+3.2}_{-10.8}$	0.6(8)	12.0 ± 0.8
34	-2.8 ± 0.2	1.4(7)	2.2 ± 0.3	—	—	—	—
35	-2.4 ± 0.2	1.3(7)	1.1 ± 0.2	—	—	—	—
36	$-2.1^{+0.3}_{-0.4}$	0.7(4)	1.3 ± 0.3	—	—	—	—
38	-2.1 ± 0.2	0.6(7)	3.1 ± 0.4	—	—	—	—
39	$-2.1^{+0.2}_{-0.3}$	0.5(6)	$1.6^{+0.2}_{-0.3}$	—	—	—	—
40	-2.7 ± 0.1	1.3(9)	4.9 ± 0.3	$-1.8^{+0.5}_{-0.2}$	< 23.5	0.9(8)	4.8 ± 0.3
44	-2.3 ± 0.2	1.4(6)	1.9 ± 0.3	—	—	—	—
45	-2.5 ± 0.3	1.0(5)	$1.1^{+0.2}_{-0.3}$	—	—	—	—
52	-2.2 ± 0.3	0.6(6)	1.8 ± 0.4	—	—	—	—
53	-1.2 ± 0.4	0.5(6)	$1.6^{+0.4}_{-0.5}$	—	—	—	—
55	—	—	—	$-0.2^{+1.1}_{-0.9}$	$55.5^{+10.2}_{-6.9}$	1.7(6)	2.5 ± 0.3
56	-2.3 ± 0.2	0.2(6)	1.9 ± 0.3	—	—	—	—
64	—	—	—	$-1.2^{+0.5}_{-0.4}$	$25.0^{+5.3}_{-9.0}$	0.9(7)	$6.5^{+0.3}_{-0.4}$
66	—	—	—	-1.0 ± 0.6	$24.3^{+4.5}_{-9.1}$	1.3(8)	4.5 ± 0.3
67	-2.2 ± 0.2	0.4(6)	$2.1^{+0.3}_{-0.4}$	—	—	—	—
71	—	—	—	-0.5 ± 0.6	$34.1^{+3.1}_{-5.8}$	0.8(7)	$6.9^{+0.4}_{-0.5}$
80	-2.4 ± 0.2	1.7(7)	$11.5^{+1.5}_{-1.6}$	—	—	—	—
83	-2.1 ± 0.1	0.9(9)	$4.6^{+0.3}_{-0.4}$	—	—	—	—
84	-2.1 ± 0.2	0.8(9)	1.8 ± 0.2	—	—	—	—
85	-2.2 ± 0.2	0.6(7)	0.8 ± 0.1	—	—	—	—
92	-2.9 ± 0.3	1.6(4)	$3.3^{+0.6}_{-0.7}$	$3.7^{+2.0}_{-3.6}$	$31.1^{+2.0}_{-6.0}$	0.1(3)	2.8 ± 0.4
94	-2.6 ± 0.2	0.7(8)	0.9 ± 0.1	—	—	—	—
96	-2.3 ± 0.4	0.7(6)	0.3 ± 0.1	—	—	—	—
99	-1.6 ± 0.4	1.3(5)	1.0 ± 0.2	—	—	—	—
100	-2.6 ± 0.4	1.2(4)	$0.5^{+0.1}_{-0.2}$	$3.1^{+5.2}_{-3.3}$	$32.4^{+3.6}_{-5.5}$	0.5(3)	0.4 ± 0.1
102	-1.4 ± 0.3	0.6(6)	0.9 ± 0.2	—	—	—	—
103	$-3.0^{+0.5}_{-0.6}$	0.9(4)	0.3 ± 0.1	—	—	—	—
104	-1.9 ± 0.3	0.4(5)	$1.7^{+0.3}_{-0.4}$	—	—	—	—
105	-1.7 ± 0.6	0.8(4)	0.6 ± 0.2	$1.8^{+3.8}_{-2.6}$	$42.2^{+9.7}_{-5.6}$	0.3(3)	0.4 ± 0.1
106	-2.0 ± 0.2	1.1(8)	1.4 ± 0.2	—	—	—	—
107	$-0.8^{+0.5}_{-0.4}$	0.6(6)	0.3 ± 0.1	—	—	—	—
108	-2.6 ± 0.2	0.9(6)	0.8 ± 0.1	—	—	—	—
109	-2.1 ± 0.3	0.2(6)	0.6 ± 0.1	—	—	—	—
110	-1.6 ± 0.3	1.7(6)	0.9 ± 0.2	—	—	—	—
114	-2.8 ± 0.5	1.4(3)	0.3 ± 0.1	$7.5^{+7.5}_{-6.4}$	$28.8^{+2.5}_{-2.4}$	0.4(2)	0.2 ± 0.1
116	-2.2 ± 0.5	0.5(5)	$0.2^{+0.0}_{-0.1}$	—	—	—	—

Table A.5: (continued)

	Power law			Cutoff power law			
No	α	χ^2_r(dof)	Flux	α	E_{peak}	χ^2_r(dof)	Flux
118	-3.1 ± 0.2	0.9(6)	1.7 ± 0.2	—	—	—	—
120	-3.1 ± 0.1	1.7(7)	1.2 ± 0.1	$-0.9^{+1.2}_{-1.0}$	$17.7^{+6.2}_{-14.8}$	1.0(6)	1.1 ± 0.1
124	-2.6 ± 0.1	0.7(7)	6.4 ± 0.6	—	—	—	—
128	-2.3 ± 0.3	0.8(4)	$1.2^{+0.2}_{-0.3}$	—	—	—	—
129	-2.6 ± 0.2	1.7(6)	1.0 ± 0.1	—	—	—	—
130	-3.0 ± 0.2	0.9(6)	1.4 ± 0.2	—	—	—	—
131	-2.7 ± 0.1	1.1(8)	4.1 ± 0.3	—	—	—	—
132	-2.0 ± 0.3	0.2(6)	$2.6^{+0.4}_{-0.5}$	—	—	—	—
134	-2.1 ± 0.3	0.7(4)	0.4 ± 0.1	$-0.0^{+5.2}_{-1.5}$	$40.9^{+11.4}_{-8.9}$	0.3(3)	0.4 ± 0.1
135	-1.3 ± 0.4	0.4(3)	0.4 ± 0.1	—	—	—	—
139	-1.2 ± 0.5	0.5(5)	0.5 ± 0.2	—	—	—	—
142	-2.5 ± 0.1	0.5(8)	$5.7^{+0.3}_{-0.4}$	—	—	—	—
143	-2.0 ± 0.3	0.4(7)	$0.8^{+0.1}_{-0.2}$	—	—	—	—
144	-3.0 ± 0.2	0.2(7)	$4.5^{+0.6}_{-0.7}$	—	—	—	—
154	-2.5 ± 0.2	1.6(8)	3.0 ± 0.4	—	—	—	—
155	-3.1 ± 0.3	1.6(6)	1.3 ± 0.2	—	—	—	—
160	-1.9 ± 0.3	1.1(6)	$4.4^{+0.8}_{-0.9}$	—	—	—	—
162	-1.6 ± 0.3	1.1(7)	1.0 ± 0.2	—	—	—	—
164	-2.0 ± 0.2	0.6(7)	1.1 ± 0.2	—	—	—	—
165	-2.1 ± 0.3	0.8(5)	2.1 ± 0.4	$0.2^{+3.0}_{-1.6}$	$40.6^{+7.0}_{-9.1}$	0.5(4)	$1.8^{+0.3}_{-0.4}$
167	-1.9 ± 0.3	0.4(5)	$1.7^{+0.3}_{-0.4}$	—	—	—	—
169	—	—	—	-0.0 ± 0.5	$27.9^{+2.0}_{-2.6}$	0.9(8)	6.4 ± 0.3
175	-2.1 ± 0.3	1.4(7)	$2.7^{+0.4}_{-0.5}$	—	—	—	—
177	$-3.4^{+0.3}_{-0.4}$	1.7(6)	1.3 ± 0.3	—	—	—	—
179	-2.4 ± 0.2	1.3(8)	1.4 ± 0.2	—	—	—	—
182	—	—	—	-1.3 ± 0.4	$20.7^{+5.8}_{-10.3}$	0.5(7)	4.0 ± 0.2
184	-2.9 ± 0.1	0.7(9)	3.3 ± 0.2	—	—	—	—
186	-2.3 ± 0.2	0.9(6)	4.1 ± 0.6	—	—	—	—
188	—	—	—	$-0.7^{+0.3}_{-0.5}$	$28.2^{+2.2}_{-4.9}$	1.6(9)	7.5 ± 0.3
189	-2.4 ± 0.4	1.3(5)	0.8 ± 0.2	—	—	—	—
190	-1.5 ± 0.2	0.6(7)	$2.2^{+0.3}_{-0.4}$	$0.0^{+1.4}_{-1.2}$	$69.0^{+37.2}_{-12.6}$	0.5(6)	$2.0^{+0.3}_{-0.4}$
193	—	—	—	$0.8^{+0.6}_{-0.3}$	$32.4^{+1.5}_{-0.6}$	1.6(8)	16.4 ± 0.6
195	—	—	—	$4.5^{+4.1}_{-3.7}$	$37.2^{+2.9}_{-2.7}$	1.3(4)	1.1 ± 0.2
196	-1.8 ± 0.3	0.6(8)	0.5 ± 0.1	$-2.7^{+0.7}_{-0.6}$	$66.0^{+31.4}_{-27.7}$	0.4(7)	$0.3^{+0.1}_{-0.2}$
198	-2.1 ± 0.1	0.9(8)	2.1 ± 0.2	—	—	—	—
201	$-2.3^{+0.1}_{-0.2}$	0.8(7)	4.2 ± 0.4	—	—	—	—
202	-1.9 ± 0.2	1.5(7)	0.9 ± 0.1	$0.0^{+2.0}_{-0.9}$	$50.9^{+8.2}_{-6.7}$	1.0(6)	0.8 ± 0.1
204	-1.6 ± 0.3	0.6(7)	3.6 ± 0.6	—	—	—	—
208	-3.0 ± 0.1	1.3(10)	6.0 ± 0.3	—	—	—	—
217	$-2.3^{+0.3}_{-0.4}$	1.6(6)	$8.4^{+1.8}_{-2.1}$	—	—	—	—
218	-3.0 ± 0.2	1.6(6)	2.4 ± 0.4	—	—	—	—
227	-2.0 ± 0.1	0.4(9)	$1.8^{+0.1}_{-0.2}$	—	—	—	—
228	-2.1 ± 0.1	1.2(9)	$1.6^{+0.1}_{-0.2}$	$-0.5^{+0.6}_{-0.8}$	$52.3^{+6.7}_{-7.5}$	0.5(8)	1.7 ± 0.2
231	-2.7 ± 0.2	1.2(8)	1.4 ± 0.2	—	—	—	—

Table A.5: (continued)

	Power law			Cutoff power law			
No	α	χ^2_r(dof)	Flux	α	E_{peak}	χ^2_r(dof)	Flux
237	-2.2 ± 0.2	1.3(9)	$6.7^{+0.7}_{-0.8}$	—	—	—	—
239	-2.6 ± 0.1	0.4(9)	3.8 ± 0.3	—	—	—	—
246	—	—	—	$-0.1^{+0.9}_{-0.8}$	$34.2^{+3.9}_{-4.8}$	1.1(6)	$6.8^{+0.6}_{-0.7}$
264	-2.2 ± 0.3	0.4(5)	$4.0^{+0.7}_{-0.8}$	—	—	—	—
265	—	—	—	$9.0^{+9.0}_{-3.7}$	35.7 ± 1.4	1.2(5)	1.2 ± 0.1
267	-2.7 ± 0.1	0.7(9)	$7.4^{+0.5}_{-0.6}$	—	—	—	—
269	-2.5 ± 0.2	0.3(7)	$2.6^{+0.3}_{-0.4}$	—	—	—	—
271	-2.3 ± 0.3	1.1(6)	$2.3^{+0.4}_{-0.5}$	—	—	—	—
280	-1.9 ± 0.2	1.0(7)	1.8 ± 0.3	—	—	—	—
284	-3.3 ± 0.2	1.1(8)	$4.5^{+0.6}_{-0.7}$	—	—	—	—
285	-2.0 ± 0.2	0.4(7)	2.0 ± 0.3	$-0.7^{+1.3}_{-1.1}$	$50.9^{+20.5}_{-17.9}$	0.2(6)	$1.9^{+0.3}_{-0.4}$
290	$-2.1^{+0.1}_{-0.2}$	0.5(9)	3.1 ± 0.3	—	—	—	—
293	-1.9 ± 0.3	1.0(6)	$2.4^{+0.5}_{-0.6}$	—	—	—	—
300	—	—	—	$2.6^{+3.0}_{-2.9}$	$50.2^{+9.0}_{-5.2}$	1.4(5)	0.5 ± 0.1
303	-2.5 ± 0.2	0.9(7)	$3.1^{+0.5}_{-0.6}$	—	—	—	—
305	—	—	—	$-1.1^{+0.4}_{-0.5}$	$23.2^{+3.8}_{-9.8}$	1.3(7)	11.7 ± 0.6
306	-2.0 ± 0.2	0.5(6)	$3.2^{+0.5}_{-0.6}$	—	—	—	—
314	-2.2 ± 0.3	1.1(7)	$7.6^{+1.3}_{-1.5}$	—	—	—	—
319	-2.0 ± 0.2	1.2(7)	0.8 ± 0.1	$0.2^{+2.1}_{-1.3}$	$49.4^{+9.0}_{-7.1}$	0.9(6)	0.8 ± 0.1
325	-2.9 ± 0.3	1.0(6)	3.5 ± 0.6	—	—	—	—
328	-2.8 ± 0.1	0.7(9)	3.6 ± 0.3	—	—	—	—
330	-2.6 ± 0.2	1.3(7)	2.0 ± 0.2	—	—	—	—
335	-2.3 ± 0.2	1.5(7)	$3.4^{+0.5}_{-0.6}$	—	—	—	—
345	-2.0 ± 0.2	0.5(7)	1.5 ± 0.2	—	—	—	—
346	-3.0 ± 0.2	1.3(9)	3.1 ± 0.4	—	—	—	—
350	-3.3 ± 0.2	1.5(7)	5.2 ± 0.6	—	—	—	—
352	$-2.3^{+0.2}_{-0.3}$	0.7(8)	1.7 ± 0.3	—	—	—	—
363	-1.7 ± 0.2	0.6(7)	1.6 ± 0.3	—	—	—	—
373	-2.3 ± 0.1	0.7(8)	$11.8^{+1.0}_{-1.1}$	—	—	—	—
382	-2.8 ± 0.2	0.7(9)	$6.3^{+0.7}_{-0.8}$	—	—	—	—
384	-1.9 ± 0.2	1.6(7)	$2.6^{+0.3}_{-0.4}$	—	—	—	—
386	-2.2 ± 0.2	1.1(7)	3.2 ± 0.4	—	—	—	—
387	—	—	—	-1.8 ± 0.2	< 19.5	0.2(10)	3.0 ± 0.1
388	-1.9 ± 0.2	1.3(8)	1.8 ± 0.3	—	—	—	—
389	-1.7 ± 0.2	0.6(10)	0.7 ± 0.1	—	—	—	—
390	-2.1 ± 0.3	0.1(6)	0.9 ± 0.2	—	—	—	—
395	-2.1 ± 0.2	0.7(8)	2.4 ± 0.3	—	—	—	—
396	-2.3 ± 0.2	1.4(7)	1.2 ± 0.2	—	—	—	—
397	-2.3 ± 0.1	0.7(10)	6.1 ± 0.5	$-1.3^{+0.5}_{-0.6}$	< 41.0	0.4(9)	6.2 ± 0.5
402	-2.0 ± 0.1	1.1(10)	0.9 ± 0.1	—	—	—	—
404	-1.9 ± 0.2	1.2(6)	2.8 ± 0.4	$0.2^{+2.6}_{-1.0}$	$46.8^{+6.9}_{-5.7}$	0.7(5)	2.3 ± 0.4
405	—	—	—	-0.6 ± 0.4	$43.5^{+2.8}_{-3.5}$	1.4(9)	2.7 ± 0.1
406	-1.5 ± 0.3	1.0(7)	2.1 ± 0.4	—	—	—	—
408	$-1.9^{+0.2}_{-0.3}$	0.9(8)	0.5 ± 0.1	—	—	—	—

Table A.5: (continued)

	Power law			Cutoff power law			
No	α	χ^2_r(dof)	Flux	α	E_{peak}	χ^2_r(dof)	Flux
409	-1.9 ± 0.1	1.6(9)	1.2 ± 0.1	—	—	—	—
411	-1.6 ± 0.2	1.0(10)	0.6 ± 0.1	—	—	—	—
413	-2.0 ± 0.2	1.0(7)	2.9 ± 0.4	—	—	—	—
414	—	—	—	-1.3 ± 0.2	$36.4^{+2.7}_{-3.3}$	1.2(11)	2.3 ± 0.0
416	-2.7 ± 0.3	0.9(7)	1.7 ± 0.3	—	—	—	—
418	-1.4 ± 0.3	1.1(7)	0.5 ± 0.1	$2.1^{+1.8}_{-2.7}$	$59.6^{+26.3}_{-6.4}$	0.9(6)	0.4 ± 0.1
419	-1.5 ± 0.3	0.8(7)	$0.6^{+0.1}_{-0.2}$	—	—	—	—
420	-2.2 ± 0.2	0.1(7)	0.8 ± 0.1	—	—	—	—
424	-1.3 ± 0.3	1.5(5)	$0.8^{+0.1}_{-0.2}$	—	—	—	—
427	-2.1 ± 0.3	0.9(7)	0.5 ± 0.1	$0.2^{+3.5}_{-1.5}$	$39.9^{+7.0}_{-5.2}$	0.6(6)	0.4 ± 0.1
428	-1.5 ± 0.2	0.7(9)	0.8 ± 0.1	—	—	—	—
430	-1.7 ± 0.3	0.2(6)	$2.1^{+0.3}_{-0.4}$	—	—	—	—
432	-2.5 ± 0.2	0.2(6)	$1.5^{+0.2}_{-0.3}$	—	—	—	—
438	-2.1 ± 0.1	1.3(9)	2.2 ± 0.2	$-0.6^{+0.7}_{-0.6}$	$48.0^{+5.6}_{-5.3}$	0.5(8)	2.2 ± 0.2
441	-1.3 ± 0.3	0.7(8)	0.6 ± 0.1	$-2.7^{+0.7}_{-0.5}$	$61.5^{+42.9}_{-37.6}$	0.4(7)	$0.3^{+0.1}_{-0.2}$
442	-2.5 ± 0.1	1.4(8)	$2.7^{+0.2}_{-0.3}$	—	—	—	—
453	—	—	—	$-1.4^{+1.0}_{-0.7}$	$14.8^{+9.4}_{-14.3}$	1.7(5)	1.9 ± 0.2
455	2.3 ± 0.2	0.5(6)	$1.5^{+0.2}_{-0.3}$	—	—	—	—
461	-1.1 ± 0.3	0.2(5)	2.3 ± 0.5	—	—	—	—
466	—	—	—	$-0.2^{+0.5}_{-0.4}$	$31.4^{+2.2}_{-2.8}$	1.2(7)	11.9 ± 0.6
483	-2.5 ± 0.2	1.5(7)	$1.9^{+0.2}_{-0.3}$	—	—	—	—
484	-2.3 ± 0.3	1.2(7)	2.3 ± 0.4	—	—	—	—
500	-3.1 ± 0.3	0.2(5)	1.5 ± 0.3	—	—	—	—
503	$-2.2^{+0.2}_{-0.3}$	0.8(7)	$3.7^{+0.6}_{-0.7}$	—	—	—	—
504	-2.3 ± 0.2	1.1(8)	2.9 ± 0.4	—	—	—	—
507	-1.7 ± 0.3	1.2(6)	$3.5^{+0.8}_{-0.9}$	—	—	—	—
510	-2.6 ± 0.2	1.0(6)	1.6 ± 0.3	$-0.0^{+3.5}_{-1.4}$	$33.2^{+6.0}_{-11.4}$	0.5(5)	1.5 ± 0.2
515	$-2.6^{+0.2}_{-0.3}$	1.4(5)	$2.8^{+0.5}_{-0.6}$	$0.0^{+3.0}_{-1.4}$	$32.1^{+6.0}_{-11.8}$	0.9(4)	$2.5^{+0.4}_{-0.5}$
518	-1.9 ± 0.1	0.7(9)	$3.7^{+0.3}_{-0.4}$	—	—	—	—
522	-2.0 ± 0.2	0.9(6)	2.2 ± 0.3	—	—	—	—
526	-2.7 ± 0.2	0.6(7)	$2.9^{+0.3}_{-0.4}$	—	—	—	—
527	-2.6 ± 0.2	1.1(7)	$2.0^{+0.2}_{-0.3}$	—	—	—	—
528	-2.2 ± 0.2	0.9(8)	1.8 ± 0.3	—	—	—	—
529	-2.5 ± 0.1	0.6(7)	2.8 ± 0.3	—	—	—	—
535	—	—	—	$1.4^{+3.6}_{-1.4}$	33.3 ± 4.0	0.8(4)	0.7 ± 0.1
540	-1.9 ± 0.2	0.5(8)	$6.9^{+0.8}_{-0.9}$	—	—	—	—
543	-2.5 ± 0.1	1.1(8)	$9.4^{+0.6}_{-0.7}$	$-1.7^{+0.5}_{-0.4}$	< 28.6	0.8(7)	$9.1^{+0.6}_{-0.7}$
544	$-3.0^{+0.4}_{-0.5}$	1.2(6)	$2.0^{+0.5}_{-0.6}$	—	—	—	—
545	-3.0 ± 0.2	1.7(7)	$5.6^{+0.6}_{-0.7}$	—	—	—	—
548	-3.3 ± 0.2	0.8(6)	$1.3^{+0.1}_{-0.2}$	—	—	—	—
551	—	—	—	-0.3 ± 0.3	47.2 ± 2.0	0.8(10)	9.2 ± 0.4
553	—	—	—	-0.3 ± 0.4	$32.0^{+2.2}_{-2.8}$	0.9(7)	10.2 ± 0.5
554	-2.5 ± 0.2	0.6(7)	$5.7^{+0.7}_{-0.8}$	—	—	—	—
559	—	—	—	$-1.5^{+0.4}_{-0.3}$	$13.5^{+6.1}_{-8.3}$	1.0(10)	11.3 ± 0.5

Table A.5: (continued)

	Power law			Cutoff power law			
No	α	χ^2_r(dof)	Flux	α	E_{peak}	χ^2_r(dof)	Flux
560	—	—	—	-1.4 ± 0.5	< 24.4	0.7(8)	$11.1^{+0.7}_{-0.8}$
565	—	—	—	$-0.9^{+0.4}_{-0.5}$	$20.8^{+3.2}_{-7.1}$	1.0(7)	7.5 ± 0.4
566	-2.7 ± 0.3	0.7(5)	2.0 ± 0.4	—	—	—	—
567	-2.5 ± 0.2	1.3(7)	3.2 ± 0.4	—	—	—	—
570	—	—	—	-1.4 ± 0.6	$16.9^{+6.5}_{-13.6}$	0.9(8)	3.6 ± 0.2
572	$-2.7^{+0.2}_{-0.3}$	1.1(6)	$3.1^{+0.5}_{-0.6}$	—	—	—	—
573	-3.1 ± 0.1	1.3(7)	3.4 ± 0.2	—	—	—	—
575	—	—	—	$-0.5^{+0.3}_{-0.4}$	$22.6^{+1.9}_{-3.8}$	1.0(7)	13.8 ± 0.5
586	—	—	—	$-0.1^{+0.8}_{-1.0}$	$30.5^{+2.6}_{-3.5}$	0.7(5)	1.0 ± 0.1
587	—	—	—	-0.4 ± 0.9	$20.6^{+3.9}_{-8.2}$	1.2(5)	$6.7^{+0.5}_{-0.6}$
588	-2.9 ± 0.2	1.5(7)	1.9 ± 0.3	—	—	—	—
596	-3.3 ± 0.3	0.6(6)	$2.0^{+0.4}_{-0.5}$	—	—	—	—
611	-3.0 ± 0.2	0.7(5)	$3.1^{+0.4}_{-0.5}$	—	—	—	—
614	-2.0 ± 0.2	1.5(5)	$9.0^{+1.6}_{-1.7}$	—	—	—	—
615	—	—	—	$0.3^{+1.1}_{-0.9}$	$27.8^{+3.1}_{-4.3}$	0.8(6)	5.4 ± 0.4
627	-2.2 ± 0.2	1.5(6)	$4.7^{+0.7}_{-0.8}$	—	—	—	—
628	—	—	—	$-1.0^{+0.4}_{-0.5}$	$25.4^{+3.2}_{-7.6}$	0.6(7)	6.2 ± 0.3
640	—	—	—	$5.3^{+2.4}_{-3.7}$	$34.3^{+2.1}_{-2.6}$	0.4(4)	2.0 ± 0.3
641	-2.6 ± 0.1	1.5(8)	$6.4^{+0.4}_{-0.5}$	$-1.3^{+0.5}_{-0.6}$	< 29.1	0.8(7)	6.1 ± 0.4
644	—	—	—	$-0.4^{+0.5}_{-0.9}$	$33.4^{+2.8}_{-7.8}$	0.7(6)	4.7 ± 0.4
646	—	—	—	$0.5^{+1.8}_{-0.7}$	$33.7^{+3.1}_{-2.5}$	0.3(5)	3.2 ± 0.3
649	-3.1 ± 0.1	1.6(7)	8.5 ± 0.8	—	—	—	—
656	—	—	—	$-1.0^{+0.5}_{-0.6}$	$19.3^{+4.4}_{-8.2}$	1.0(7)	6.1 ± 0.4
658	—	—	—	$2.4^{+3.1}_{-2.5}$	$34.5^{+3.2}_{-2.6}$	1.7(6)	$1.4^{+0.2}_{-0.3}$
659	—	—	—	$-1.1^{+0.5}_{-0.3}$	$18.9^{+4.7}_{-3.9}$	1.5(8)	10.5 ± 0.4
661	-3.2 ± 0.2	1.1(8)	$4.9^{+0.5}_{-0.6}$	$-1.3^{+1.6}_{-0.7}$	< 22.2	0.7(7)	4.5 ± 0.5
664	—	—	—	$0.2^{+1.3}_{-1.0}$	$42.9^{+5.0}_{-4.9}$	1.1(6)	1.3 ± 0.2
665	-2.4 ± 0.2	0.3(6)	$5.2^{+0.8}_{-0.9}$	—	—	—	—
666	-2.4 ± 0.2	0.5(7)	$2.2^{+0.3}_{-0.4}$	—	—	—	—
668	—	—	—	3.3 ± 3.7	$40.0^{+3.1}_{-7.6}$	1.5(3)	$2.6^{+0.4}_{-0.5}$
670	$-2.7^{+0.3}_{-0.4}$	0.5(6)	$1.3^{+0.3}_{-0.4}$	—	—	—	—
675	—	—	—	$1.2^{+0.7}_{-0.4}$	$30.6^{+1.3}_{-1.0}$	0.5(7)	$19.3^{+0.7}_{-0.8}$
676	—	—	—	-0.2 ± 0.4	$25.2^{+1.8}_{-2.6}$	1.4(8)	6.9 ± 0.3
678	-2.7 ± 0.2	0.4(8)	1.8 ± 0.2	—	—	—	—
683	$-2.9^{+0.2}_{-0.3}$	0.9(5)	1.5 ± 0.3	—	—	—	—
690	—	—	—	$3.0^{+1.2}_{-2.3}$	$31.7^{+1.5}_{-3.2}$	0.6(4)	4.9 ± 0.5
693	$-2.3^{+0.1}_{-0.2}$	0.6(8)	3.8 ± 0.4	—	—	—	—
695	$-2.2^{+0.2}_{-0.3}$	0.6(7)	1.0 ± 0.2	—	—	—	—
700	$-2.2^{+0.2}_{-0.3}$	0.8(6)	$2.3^{+0.4}_{-0.5}$	—	—	—	—
704	$-3.0^{+0.2}_{-0.3}$	1.0(6)	1.8 ± 0.3	—	—	—	—
716	-2.7 ± 0.2	0.8(7)	$4.4^{+0.5}_{-0.6}$	—	—	—	—
718	-2.0 ± 0.2	0.9(8)	2.4 ± 0.3	—	—	—	—
721	—	—	—	$-1.1^{+0.3}_{-0.5}$	$18.4^{+3.0}_{-7.2}$	0.6(8)	8.0 ± 0.3
722	-2.6 ± 0.1	0.8(9)	$2.5^{+0.2}_{-0.3}$	$-1.5^{+0.8}_{-0.5}$	< 30.3	0.5(8)	2.4 ± 0.3

Table A.5: (continued)

	Power law			Cutoff power law			
No	α	χ^2_r(dof)	Flux	α	E_{peak}	χ^2_r(dof)	Flux
724	—	—	—	$-0.9^{+0.4}_{-0.6}$	$25.1^{+3.4}_{-8.1}$	1.0(8)	3.4 ± 0.2
725	—	—	—	$-0.6^{+0.3}_{-0.5}$	$23.4^{+2.0}_{-4.3}$	0.8(7)	8.1 ± 0.3
726	—	—	—	$-0.7^{+0.4}_{-0.6}$	$25.4^{+2.5}_{-6.3}$	0.8(7)	7.8 ± 0.4
728	—	—	—	-0.3 ± 1.0	$26.4^{+4.0}_{-9.5}$	0.9(5)	1.8 ± 0.2
729	-1.6 ± 0.2	1.5(8)	$1.5^{+0.2}_{-0.3}$	—	—	—	—
731	$-3.0^{+0.3}_{-0.4}$	0.7(6)	$1.5^{+0.3}_{-0.4}$	—	—	—	—
732	-2.5 ± 0.1	0.8(8)	$1.4^{+0.1}_{-0.2}$	—	—	—	—
735	-2.7 ± 0.2	0.5(7)	$0.9^{+0.1}_{-0.2}$	—	—	—	—
736	$-2.5^{+0.3}_{-0.4}$	0.5(5)	0.4 ± 0.1	$-0.1^{+2.7}_{-2.0}$	< 33.1	0.3(4)	0.3 ± 0.1
740	—	—	—	$1.8^{+1.7}_{-2.1}$	$37.6^{+2.8}_{-2.5}$	1.3(8)	2.1 ± 0.3
744	-1.8 ± 0.2	1.3(6)	1.5 ± 0.3	—	—	—	—
745	—	—	—	$-0.6^{+0.9}_{-0.7}$	$28.0^{+4.4}_{-7.4}$	1.0(6)	1.1 ± 0.1
750	-2.5 ± 0.2	0.9(7)	$2.1^{+0.2}_{-0.3}$	—	—	—	—
751	-1.7 ± 0.3	0.8(7)	0.3 ± 0.1	—	—	—	—
756	-2.3 ± 0.1	0.8(8)	3.1 ± 0.2	$-1.6^{+0.5}_{-0.4}$	< 36.6	0.5(7)	3.0 ± 0.2
759	-2.4 ± 0.4	0.3(4)	2.3 ± 0.7	—	—	—	—
760	—	—	—	$-1.2^{+0.3}_{-0.5}$	$20.6^{+3.6}_{-8.8}$	1.4(7)	3.6 ± 0.2
761	-2.3 ± 0.1	1.6(8)	$3.7^{+0.3}_{-0.4}$	—	—	—	—
764	$-2.7^{+0.1}_{-0.2}$	0.4(7)	2.8 ± 0.3	$-1.6^{+0.9}_{-0.4}$	< 26.1	0.1(6)	2.6 ± 0.3
769	—	—	—	$-0.7^{+0.4}_{-0.5}$	$25.5^{+2.6}_{-5.3}$	1.2(7)	6.6 ± 0.3
770	—	—	—	$-0.0^{+0.7}_{-0.6}$	$28.2^{+2.5}_{-3.7}$	0.3(6)	5.9 ± 0.4
771	-2.5 ± 0.1	1.1(7)	$2.4^{+0.2}_{-0.3}$	-0.7 ± 0.9	$30.3^{+4.6}_{-11.3}$	0.4(6)	2.2 ± 0.2
775	-2.6 ± 0.2	0.4(6)	3.3 ± 0.4	—	—	—	—
778	-3.1 ± 0.1	0.6(6)	2.7 ± 0.3	—	—	—	—
782	—	—	—	$-0.7^{+0.5}_{-0.9}$	$24.4^{+3.0}_{-11.0}$	0.8(7)	4.2 ± 0.3
783	-2.8 ± 0.2	1.1(6)	$4.9^{+0.8}_{-0.9}$	—	—	—	—
785	-2.2 ± 0.3	1.1(5)	1.2 ± 0.3	—	—	—	—
787	-2.4 ± 0.2	0.3(7)	0.8 ± 0.1	—	—	—	—
790	$-2.2^{+0.7}_{-0.8}$	0.9(3)	$0.5^{+0.2}_{-0.3}$	—	—	—	—
791	-2.0 ± 0.4	0.7(8)	$5.4^{+1.4}_{-1.7}$	—	—	—	—
793	-2.0 ± 0.5	0.6(7)	$0.9^{+0.3}_{-0.4}$	—	—	—	—
796	$-2.4^{+0.2}_{-0.3}$	1.3(7)	1.4 ± 0.3	$2.0^{+2.1}_{-3.1}$	$38.1^{+3.8}_{-7.5}$	1.0(6)	1.3 ± 0.2
797	—	—	—	$0.5^{+1.4}_{-0.5}$	$29.2^{+2.6}_{-2.0}$	1.1(7)	5.4 ± 0.4
798	$-2.1^{+0.4}_{-0.5}$	1.0(6)	$0.8^{+0.2}_{-0.3}$	—	—	—	—
803	—	—	—	$-0.9^{+0.3}_{-0.4}$	$34.9^{+3.8}_{-5.6}$	0.9(8)	5.2 ± 0.2
804	—	—	—	$0.6^{+1.7}_{-0.7}$	$30.4^{+3.4}_{-2.8}$	0.9(6)	3.0 ± 0.3
805	—	—	—	$-0.8^{+1.1}_{-1.0}$	$25.4^{+5.2}_{-17.0}$	1.4(7)	5.5 ± 0.6
810	-2.1 ± 0.2	1.0(6)	2.4 ± 0.4	$0.0^{+1.4}_{-1.2}$	$40.8^{+5.9}_{-6.3}$	0.5(5)	2.1 ± 0.3
815	-2.6 ± 0.1	0.7(9)	$2.8^{+0.2}_{-0.3}$	—	—	—	—
818	—	—	—	$-1.0^{+0.3}_{-0.5}$	$19.7^{+3.0}_{-6.4}$	1.3(7)	$9.6^{+0.4}_{-0.5}$
821	-2.4 ± 0.3	0.5(7)	1.4 ± 0.3	—	—	—	—
831	-2.4 ± 0.2	1.4(6)	2.9 ± 0.5	—	—	—	—
839	—	—	—	$-1.1^{+0.4}_{-0.3}$	$18.4^{+3.5}_{-4.9}$	1.5(10)	10.7 ± 0.4
846	—	—	—	$-1.5^{+0.5}_{-0.4}$	< 21.1	1.3(8)	6.2 ± 0.4

Table A.5: (continued)

	Power law			Cutoff power law			
No	α	χ^2_r(dof)	Flux	α	E_{peak}	χ^2_r(dof)	Flux
851	—	—	—	$-0.6^{+0.2}_{-0.4}$	$21.8^{+1.7}_{-3.4}$	1.1(9)	17.1 ± 0.5
853	—	—	—	-1.2 ± 0.6	$16.2^{+5.4}_{-9.7}$	1.2(7)	5.1 ± 0.3
855	—	—	—	$-0.3^{+0.8}_{-0.9}$	$31.4^{+3.0}_{-6.2}$	1.4(6)	9.5 ± 0.9
857	-2.6 ± 0.2	1.7(6)	$7.8^{+1.1}_{-1.2}$	—	—	—	—
865	-2.9 ± 0.1	1.6(9)	5.1 ± 0.5	—	—	—	—
867	—	—	—	$-0.2^{+1.2}_{-1.3}$	< 28.2	1.2(7)	$4.5^{+0.5}_{-0.6}$
869	-2.5 ± 0.2	1.3(6)	$9.1^{+1.3}_{-1.5}$	—	—	—	—
871	-2.4 ± 0.2	1.1(7)	5.3 ± 0.7	-0.9 ± 1.0	$34.1^{+6.9}_{-26.0}$	0.8(6)	$5.1^{+0.6}_{-0.7}$
875	—	—	—	$-0.4^{+0.3}_{-0.4}$	$30.7^{+1.8}_{-3.2}$	1.1(8)	17.7 ± 0.7
876	—	—	—	-1.5 ± 0.5	< 21.9	1.1(7)	7.0 ± 0.5
879	—	—	—	$-0.8^{+0.8}_{-0.7}$	$19.3^{+4.8}_{-8.8}$	1.4(5)	9.0 ± 0.7
880	—	—	—	0.2 ± 0.5	$26.6^{+1.9}_{-2.4}$	0.7(7)	9.0 ± 0.4
882	—	—	—	$1.2^{+2.0}_{-1.7}$	$25.8^{+3.8}_{-6.5}$	1.1(4)	$4.7^{+0.6}_{-0.7}$
885	-3.4 ± 0.2	1.3(8)	6.7 ± 0.8	$-0.8^{+1.9}_{-1.2}$	< 24.7	0.9(7)	6.4 ± 0.8
888	$-2.6^{+0.2}_{-0.3}$	1.4(6)	$6.8^{+1.2}_{-1.4}$	—	—	—	—
889	-3.0 ± 0.2	1.2(5)	2.9 ± 0.5	$0.2^{+3.1}_{-1.6}$	< 28.9	0.8(4)	2.4 ± 0.4
895	—	—	—	-0.3 ± 0.7	$34.8^{+3.1}_{-4.2}$	0.7(7)	1.1 ± 0.1
897	—	—	—	$-1.2^{+0.5}_{-0.7}$	< 37.5	1.6(7)	$1.5^{+0.1}_{-0.2}$
898	-3.0 ± 0.2	0.6(6)	$5.9^{+0.9}_{-1.0}$	—	—	—	—
901	—	—	—	$-0.5^{+0.5}_{-0.8}$	$30.0^{+2.6}_{-7.3}$	1.3(7)	2.0 ± 0.2
904	-2.6 ± 0.2	0.9(7)	3.4 ± 0.4	$-1.0^{+0.9}_{-1.0}$	< 31.3	0.5(6)	3.1 ± 0.4
905	$-2.0^{+0.3}_{-0.4}$	0.8(4)	$1.5^{+0.3}_{-0.4}$	—	—	—	—
907	—	—	—	$1.5^{+2.9}_{-1.1}$	$34.5^{+3.2}_{-2.9}$	1.3(4)	$1.5^{+0.2}_{-0.3}$
911	-1.9 ± 0.2	1.4(8)	$1.1^{+0.1}_{-0.2}$	$0.1^{+1.4}_{-1.0}$	$49.2^{+7.6}_{-5.5}$	1.0(7)	$1.0^{+0.1}_{-0.2}$
912	-2.0 ± 0.2	1.0(8)	0.8 ± 0.1	—	—	—	—
913	-2.9 ± 0.3	0.8(6)	1.5 ± 0.3	—	—	—	—
914	—	—	—	$2.3^{+2.6}_{-1.0}$	$33.4^{+2.7}_{-2.0}$	1.7(4)	$3.0^{+0.3}_{-0.4}$
919	-2.5 ± 0.2	1.0(6)	6.5 ± 0.9	—	—	—	—
923	-2.8 ± 0.2	0.4(9)	$8.9^{+0.9}_{-1.0}$	—	—	—	—
1081	-2.0 ± 0.2	0.8(7)	$2.4^{+0.3}_{-0.4}$	$-0.4^{+1.4}_{-1.3}$	$43.6^{+8.7}_{-9.7}$	0.6(6)	2.1 ± 0.3
1088	$-3.2^{+0.3}_{-0.4}$	0.9(3)	$3.1^{+0.5}_{-0.6}$	—	—	—	—
1090	-2.4 ± 0.2	1.6(7)	2.1 ± 0.2	—	—	—	—
1098	-2.8 ± 0.3	0.3(4)	2.4 ± 0.4	—	—	—	—
1347	-1.2 ± 0.7	0.6(4)	0.2 ± 0.1	—	—	—	—

Flux is in units of 10^{-7} erg cm^{-2} s^{-1}.

E_{peak} is in units of keV.

Table A.6: Results of the time-averaged spectral analysis of the bursts from SGR 1935+2154.

	Power law			Cutoff power law			
No	α	χ^2_r(dof)	Flux	α	E_{peak}	χ^2_r(dof)	Flux
1101	-3.1 ± 0.2	0.6(4)	9.6 ± 0.8	—	—	—	—
1118	-2.0 ± 0.1	1.4(8)	6.1 ± 0.3	-1.1 ± 0.5	$66.4^{+11.4}_{-7.7}$	1.1(7)	6.0 ± 0.3
1122	—	—	—	> 6.3	39.8 ± 1.7	1.0(4)	$7.3^{+0.8}_{-0.9}$
1123	—	—	—	> 4.6	44.4 ± 1.6	1.3(5)	$35.3^{+2.8}_{-2.9}$
1125	—	—	—	$-0.1^{+0.9}_{-1.1}$	$31.7^{+4.4}_{-10.5}$	0.8(6)	26.9 ± 1.3
1135	-3.1 ± 0.3	1.6(5)	4.3 ± 0.4	—	—	—	—
1140	-3.7 ± 0.3	0.8(5)	$3.6^{+0.3}_{-0.4}$	—	—	—	—
1145	-3.0 ± 0.3	0.7(5)	$6.3^{+0.7}_{-0.8}$	—	—	—	—
1147	—	—	—	$0.8^{+1.5}_{-0.9}$	$30.4^{+4.8}_{-5.2}$	1.3(5)	17.7 ± 0.7
1158	-2.7 ± 0.3	0.4(5)	4.4 ± 0.5	—	—	—	—
1160	-3.6 ± 0.2	1.0(5)	3.3 ± 0.2	—	—	—	—
1162	-1.8 ± 0.3	0.2(5)	2.1 ± 0.2	—	—	—	—
1166	-3.1 ± 0.4	0.4(3)	1.1 ± 0.2	$-0.0^{+4.6}_{-2.1}$	< 43.8	0.0(2)	1.1 ± 0.2
1167	—	—	—	-0.5 ± 1.0	$30.6^{+8.0}_{-14.8}$	1.0(4)	3.3 ± 0.2
1170	—	—	—	> 1.3	$37.7^{+2.6}_{-8.5}$	0.4(1)	2.9 ± 0.4
1171	-2.2 ± 0.3	0.5(4)	0.8 ± 0.1	—	—	—	—
1172	$-2.6^{+0.2}_{-0.3}$	1.3(6)	1.3 ± 0.1	—	—	—	—
1173	-2.7 ± 0.2	0.5(7)	1.6 ± 0.1	—	—	—	—
1174	—	—	—	$-1.6^{+1.1}_{-0.5}$	< 26.8	1.1(4)	8.3 ± 0.4
1175	—	—	—	$0.7^{+1.0}_{-0.7}$	32.7 ± 3.7	1.2(5)	15.9 ± 0.5
1179	-2.5 ± 0.3	0.4(5)	0.8 ± 0.1	$-0.4^{+2.2}_{-1.1}$	< 52.8	0.2(4)	0.8 ± 0.1
1180	-2.5 ± 0.3	1.3(5)	0.7 ± 0.1	—	—	—	—
1186	$-2.4^{+0.2}_{-0.3}$	0.9(5)	0.9 ± 0.1	—	—	—	—
1187	—	—	—	$4.3^{+2.3}_{-3.4}$	$53.9^{+4.0}_{-3.9}$	1.1(3)	0.8 ± 0.1
1190	-3.5 ± 0.3	1.6(5)	1.5 ± 0.1	—	—	—	—
1191	—	—	—	$0.7^{+1.0}_{-1.1}$	$31.9^{+3.3}_{-6.2}$	1.2(4)	7.0 ± 0.3
1192	-3.2 ± 0.2	1.4(6)	5.0 ± 0.3	—	—	—	—
1199	$-2.2^{+0.2}_{-0.3}$	1.2(5)	1.9 ± 0.2	—	—	—	—
1200	—	—	—	$0.0^{+1.0}_{-0.9}$	$40.0^{+4.3}_{-8.0}$	0.1(4)	5.9 ± 0.3
1203	-2.2 ± 0.6	0.5(4)	0.9 ± 0.2	—	—	—	—
1205	-2.3 ± 0.2	0.8(7)	1.3 ± 0.1	—	—	—	—
1206	$-3.6^{+0.3}_{-0.4}$	0.7(4)	4.2 ± 0.4	—	—	—	—
1210	—	—	—	$-0.1^{+0.8}_{-0.7}$	$27.3^{+4.4}_{-6.3}$	0.1(5)	7.5 ± 0.2
1214	$-3.7^{+0.3}_{-0.4}$	0.7(5)	1.6 ± 0.2	—	—	—	—
1215	-2.4 ± 0.3	0.3(4)	1.4 ± 0.2	—	—	—	—
1216	-2.7 ± 0.3	1.3(4)	1.0 ± 0.1	—	—	—	—
1219	-2.2 ± 0.3	1.1(4)	0.8 ± 0.1	—	—	—	—
1222	-2.8 ± 0.2	0.7(6)	2.1 ± 0.1	—	—	—	—
1223	—	—	—	$0.1^{+1.6}_{-1.4}$	$27.5^{+6.4}_{-13.1}$	1.4(3)	2.5 ± 0.1
1226	-2.8 ± 0.2	0.6(4)	3.4 ± 0.3	—	—	—	—
1234	—	—	—	$0.2^{+1.2}_{-0.8}$	$30.0^{+5.3}_{-5.9}$	0.1(4)	8.2 ± 0.3
1236	-2.8 ± 0.4	0.7(4)	1.4 ± 0.2	—	—	—	—
1237	-1.7 ± 0.3	1.0(5)	0.8 ± 0.1	—	—	—	—

Table A.6: (continued)

	Power law			Cutoff power law			
No	α	χ^2_r(dof)	Flux	α	E_{peak}	χ^2_r(dof)	Flux
1241	-2.0 ± 0.3	1.6(5)	0.8 ± 0.1	—	—	—	—
1244	—	—	—	$0.2^{+1.1}_{-0.7}$	30.1 ± 4.9	0.6(5)	12.7 ± 0.4
1247	—	—	—	$2.2^{+2.3}_{-2.7}$	$40.2^{+3.2}_{-12.8}$	0.9(3)	3.5 ± 0.3
1257	-2.0 ± 0.3	0.7(5)	$1.0^{+0.1}_{-0.2}$	—	—	—	—
1260	—	—	—	$0.2^{+0.8}_{-0.7}$	$37.1^{+3.3}_{-5.0}$	1.2(6)	3.7 ± 0.1
1265	$-2.4^{+0.4}_{-0.5}$	0.3(3)	1.4 ± 0.3	—	—	—	—
1268	-2.8 ± 0.3	0.5(4)	2.1 ± 0.2	—	—	—	—
1270	—	—	—	$1.3^{+1.5}_{-1.0}$	$41.7^{+3.2}_{-3.6}$	1.7(4)	6.1 ± 0.3
1271	-2.9 ± 0.2	0.2(5)	4.4 ± 0.3	—	—	—	—
1280	-2.6 ± 0.3	0.8(4)	1.9 ± 0.2	—	—	—	—
1287	-2.5 ± 0.3	0.9(4)	$1.2^{+0.1}_{-0.2}$	$3.1^{+3.1}_{-3.3}$	$46.5^{+3.7}_{-13.2}$	0.5(3)	1.0 ± 0.1
1288	$-1.9^{+0.4}_{-0.5}$	1.1(3)	1.2 ± 0.3	—	—	—	—
1292	-2.6 ± 0.4	0.7(4)	$1.0^{+0.1}_{-0.2}$	—	—	—	—
1293	—	—	—	$2.7^{+2.0}_{-2.7}$	$48.8^{+3.2}_{-6.7}$	0.9(3)	1.1 ± 0.1
1295	$-2.5^{+0.4}_{-0.5}$	1.4(3)	1.3 ± 0.2	—	—	—	—
1297	—	—	—	$0.2^{+1.4}_{-0.9}$	$34.1^{+5.6}_{-7.4}$	1.6(4)	6.3 ± 0.3
1304	—	—	—	> 2.9	$49.8^{+2.7}_{-2.6}$	1.4(3)	1.3 ± 0.1
1306	-3.7 ± 0.2	0.6(4)	7.1 ± 0.5	—	—	—	—
1308	-2.8 ± 0.3	0.9(4)	1.4 ± 0.2	—	—	—	—
1310	—	—	—	$0.5^{+1.5}_{-1.0}$	$33.7^{+4.9}_{-6.7}$	0.7(4)	6.7 ± 0.3
1325	-2.9 ± 0.1	0.8(6)	2.0 ± 0.1	—	—	—	—
1326	$-3.0^{+0.2}_{-0.3}$	1.7(4)	2.0 ± 0.2	$0.5^{+3.1}_{-1.7}$	$36.3^{+6.6}_{-14.5}$	1.0(3)	1.9 ± 0.2
1329	—	—	—	$0.6^{+2.8}_{-1.6}$	$32.1^{+6.9}_{-11.3}$	1.6(3)	$9.0^{+0.6}_{-0.7}$
1330	-3.2 ± 0.2	1.1(5)	3.1 ± 0.2	—	—	—	—
1331	—	—	—	< 4.3	$50.5^{+2.8}_{-2.7}$	0.7(3)	1.0 ± 0.1
1333	-3.3 ± 0.4	0.3(4)	1.4 ± 0.2	—	—	—	—
1334	—	—	—	$-1.6^{+0.8}_{-0.4}$	< 26.2	0.6(5)	6.0 ± 0.2
1335	-2.4 ± 0.3	1.1(5)	1.5 ± 0.2	—	—	—	—
1337	-3.1 ± 0.2	0.5(5)	2.9 ± 0.2	—	—	—	—
1340	$-2.4^{+0.2}_{-0.3}$	1.0(6)	2.6 ± 0.3	—	—	—	—
1342	$-4.8^{+0.4}_{-0.5}$	0.6(2)	3.3 ± 0.3	—	—	—	—

Flux is in units of 10^{-7} erg cm^{-2} s^{-1}.

E_{peak} is in units of keV.